COSMIC IMPRINTS OF QUANTUM JITTERS: STOCHASTIC INFLATION, SPECTRAL DISTORTIONS AND PRIMORDIAL BLACK HOLES

Von der Fakultät für Mathematik, Informatik und Naturwissenschaften der RWTH Aachen University zur Erlangung des akademischen Grades eines Doktors der Naturwissenschaften genehmigte Dissertation

vorgelegt von

Devanshu Sharma, M. Sc.

aus

Mehsana, Gujarat, India

Berichter: Prof. Dr. Julien Lesgourgues
Prof. Dr. Philipp Mertsch

Tag der mündlichen Prüfung: Dienstag, 23 September, 2025

Diese Dissertation ist auf den Internetseiten der Universtätsbiblothek online verfügbar.

RWTH Aachen University

Doctoral Thesis

COSMIC IMPRINTS OF QUANTUM JITTERS: STOCHASTIC INFLATION, SPECTRAL DISTORTIONS AND PRIMORDIAL BLACK HOLES

---

by

Devanshu Sharma

Supervisor and first examiner
Prof. Dr. Julien Lesgourgues

Second examiner
Prof. Dr. Philipp Mertsch

Institute for Theoretical Particle Physics and Cosmology

Aachen, Tuesday 23rd September, 2025

Abstract

In recent years, cosmology has rapidly advanced to become one of the most dynamic and popular fields in physics, propelled by both theoretical breakthroughs and the advent of high-precision observational missions. The latter includes a wide array of space-based experiments—such as Planck, Euclid, JWST, and GAIA—alongside powerful ground-based instruments like gravitational wave observatories (LIGO, VIRGO, KAGRA, and future detectors), as well as DESI, ACT, and SDSS. To accurately interpret observations of cosmic structures, anisotropies in the Cosmic Microwave Background (CMB), the epoch of reionization, and the stochastic gravitational wave background, it is essential to develop a comprehensive understanding of the primordial perturbations that laid the groundwork for these late-time phenomena. This thesis centers precisely on that foundational topic: primordial perturbations.

The theory of cosmic inflation is widely regarded as the most compelling explanation for the origin of these perturbations. Accordingly, the first part of this thesis provides an overview of inflation and its role in generating perturbations, the perturbative framework used to study their dynamics, the statistical properties of primordial black holes (PBHs) as byproducts of inflationary fluctuations, and the influence of these perturbations on the observed features of CMB anisotropies.

In the second part, the focus shifts to the quantum origin of primordial perturbations and their transition to classical behavior on superhorizon scales. We explore the role of stochastic processes in this context, particularly the analogy with Brownian motion, which enables a numerical treatment of quantum-enhanced evolution during inflation. A robust, non-perturbative numerical algorithm is developed to compute the statistical properties of these perturbations, and its validity is tested by recovering their two-point statistics.

Chapters three, four, and five are thematically interlinked and constitute the third part of the thesis. Chapter three presents a detailed investigation of CMB spectral distortions; frequency-dependent deviations from the blackbody spectrum of the CMB caused by energy injection into the photon-baryon plasma. Particular attention is given to distortions arising from the dissipation of small-scale primordial perturbations, and how the absence of detected distortions can be used to place constraints on their amplitude. Chapter four examines the impact of relaxing the assumption of Gaussian initial conditions by introducing local-type non-Gaussianity. We formulate a method to compute both the leading and next-to-leading-order corrections to spectral distortions due to such non-Gaussian features, and derive updated constraints on the amplitude of non-Gaussian primordial perturbations.

Chapter five is devoted to the study of primordial black holes. We investigate how CMB

spectral distortions constrain the scenario in which supermassive black holes originate from a primordial seed population. Building on the framework developed in earlier chapters, we analyze the relaxation of these constraints in the presence of non-Gaussian initial conditions. By considering various orders of non-Gaussianity, we demonstrate that higher-order non-Gaussianity can significantly enhance the permissible abundance of PBHs, potentially allowing them to serve as seeds for supermassive black holes.

Finally, chapter six concludes the thesis with a summary of all key findings and contributions.

Acknowledgements

First and foremost, I would like to express my deepest gratitude to my supervisor, Prof. Julien Lesgourgues, for his unwavering guidance, encouragement, and support throughout this journey. His deep insights, clarity of thought, and patient mentorship have been invaluable at every stage of my PhD. Beyond helping me become a better researcher, Julien has also inspired me to grow as a person and to communicate ideas with greater precision and confidence.

I am also sincerely thankful to Prof. Phillip Mertsch, for kindly agreeing to serve both as my second supervisor and one of the reviewers of this thesis.

I am very grateful to my collaborators, Prof. Christian Byrnes, Xav Pritchard, Prof. Ruth Durrer, and Dr. Anish Ghoshal, for the opportunity to work and learn alongside them. Their support has enhanced my perspective and deepened my understanding across various areas of cosmology. A special thank you goes to Chris, who has been more than a collaborator; his mentorship and encouragement have played an important role in my development as a researcher.

I would also like to thank my master's supervisors, Prof. Matthew Choptuik, Prof. Mayukh Gangopadhyay, and Dr. Yogesh, whose early guidance laid the foundation for my research path.

I am thankful to all my past and present colleagues at TTK, whose support made this experience both productive and enjoyable. In particular, I would like to thank Dr. Christian Fidler for our many insightful discussions, both in physics and beyond. I am also grateful to Dr. Markus Mosbech and Tobias Thrien for their help with computational matters, and to my friends and office-mates, Sven and Giona, for all the engaging conversations and shared moments over the years.

My sincere thanks to RWTH Aachen University for providing the infrastructure, resources, and support needed for the smooth and timely completion of my PhD. I also wish to extend my gratitude to Frau. Ina Vogel and Dr. Uwe Kahlert for their kind assistance with administrative and technical matters. The work was made possible with the support of the the German Academic Exchange Service (DAAD) scholarship. I wish to also acknowledge International Exchanges Schemes and COST Action Scheme for supporting my research visits to the University of Sussex and the University of Geneva, respectively.

I am grateful to Fynn Janssen, Dr. Markus Mosbech, and Dr. Ravi Sharma for generously taking the time to proofread my thesis and for offering thoughtful feedback.

Finally, I would like to thank my friends and family for their constant and unconditional support. A special thanks to all my cousins for their ongoing encouragement. Thank you would be an understatement for my parents for their sacrifices and support. I would be forever indebted to them.

Declaration of Authorship

I, Devanshu Sharma declare that this thesis and the work presented in it are my own and has been generated by me as the result of my own original research.

I do solemnely swear that:

- This work was done wholly or mainly while in candidature for the doctoral degree at this faculty and university;
- Where any part of this thesis has previously been submitted for a degree or any other qualification at this university or any other institution, this has been clearly stated;
- Where I have consulted the published work of others or myself, this is always clearly attributed;
- Where I have quoted from the work of others or myself, the source is always given. This thesis is entirely my own work, with the exception of such quotations;
- I have acknowledged all major sources of assistance;
- Where the thesis is based on work done by myself jointly with others, I have made clear exactly what was done by others and what I have contributed myself;
- Parts of this work have been published in the papers listed in the section *List of Publications*.

Date: June 19, 2025

Signature: Devanshu Sharma

List of Publications

1. Xavier Pritchard, Christian T. Byrnes, Julien Lesgourgues, **Devanshu Sharma**, *"Robust μ-distortion constraints on primordial supermassive black holes from cubic ($g_{\rm NL}$) non-Gaussian perturbations"*, [arXiv:2505.08442 [astro-ph.CO]], *Accepted for publication in JCAP.*

2. **Devanshu Sharma**, *"Stochastic inflation and non-perturbative power spectrum beyond slow roll"*, JCAP 03 (2025) 017, [arXiv:2411.08854 [astro-ph.CO]].

3. Christian T. Byrnes, Julien Lesgourgues, **Devanshu Sharma**, *"Robust μ-distortion constraints on primordial supermassive black holes from non-Gaussian perturbations"*, JCAP 09 (2024) 012, [arXiv:2404.18475 [astro-ph.CO]].

4. **Devanshu Sharma**, Julien Lesgourgues, Christian T. Byrnes, *"Spectral distortions from acoustic dissipation with non-Gaussian (or not) perturbations"*, JCAP 07 (2024) 090, [arXiv:2404.18474 [astro-ph.CO]].

Contents

List of Figures

List of Tables

1 Introduction **1**
- 1.1 Einstein Field Equations and FLRW Universe . . . 2
- 1.2 Hot Big Bang Model and Limitations . . . 4
  - 1.2.1 Horizon Problem . . . 4
  - 1.2.2 Flatness Problem . . . 6
  - 1.2.3 Monopole Problem . . . 6
- 1.3 Motivation For Cosmic Inflation . . . 7
- 1.4 Background Dynamics During Inflation . . . 9
  - 1.4.1 Slow-roll and Ultra-slow roll approximations . . . 10
- 1.5 Cosmological Perturbations: The Mukhanov-Sasaki Equation . . . 11
- 1.6 Primordial Black Holes . . . 16
  - 1.6.1 Statistics of PBH Abundance . . . 18
- 1.7 Reheating to Recombination . . . 21
- 1.8 Cosmic Microwave Background . . . 25

2 Stochastic Inflation **29**
- 2.1 Brownian Motion and Langevin Equation . . . 29
- 2.2 Stochastic Approach to Inflation . . . 32
- 2.3 Why a Non-Perturbative Approach? . . . 37
- 2.4 Classical ΔN Formalism . . . 39
- 2.5 Stochastic ΔN Formalism . . . 43
  - 2.5.1 Derivation . . . 43
  - 2.5.2 Numerical Implementation . . . 46
- 2.6 Obtaining the Statistics . . . 51
  - 2.6.1 Probability Distribution Function . . . 51
  - 2.6.2 Power Spectrum . . . 55
    - 2.6.2.1 Quadratic Potential . . . 56
    - 2.6.2.2 Realistic Potential . . . 58

3 CMB Spectral Distortions **61**

3.1 Background . . . 61
3.1.1 Blackbody Radiation . . . 62
3.1.2 Categorizing the Spectral Distortions . . . 64
3.1.2.1 Temperature Shift . . . 65
3.1.2.2 Chemical Potential (μ) Distortions . . . 66
3.1.2.3 y Distortions . . . 67
3.1.2.4 Residual Distortions . . . 69
3.2 Introduction to Acoustic Dissipation . . . 70
3.2.1 Expansion into Temperature Anisotropies . . . 72
3.2.2 Mathematical Formulation of Acoustic Dissipation . . . 74
3.2.3 Various Approximation Schemes . . . 79
3.2.4 Integrating the Source Function over Redshift . . . 80
3.3 Observational Constraints For a Peaked Spectrum . . . 81

4 Non-Gaussianity in Spectral Distortions 85
4.1 Local Non-Gaussianity and Its Limits . . . 87
4.2 Spectral Distortions in Perturbative Non-Gaussianity . . . 88
4.2.1 χ^2 Power Spectrum . . . 89
4.2.2 Window Function For Leading-Order Correction . . . 89
4.2.3 Window Function For Next-to-Leading-Order Correction . . . 91
4.3 Spectral Distortions in Non-Perturbative Non-Gaussianity . . . 95

5 PBH Constraints From Spectral Distortions 97
5.1 Gaussian Constraints . . . 99
5.2 Constraints From χ^2 Non-Gaussianity . . . 101
5.2.1 Perturbative Limit . . . 102
5.2.2 Non-Perturbative Limit . . . 103
5.3 Constraints From Cubic Non-Gaussianity . . . 105
5.3.1 Spectral Distortion Constraints . . . 108
5.3.2 PBH Constraints . . . 109
5.4 Stronger Non-Gaussianities . . . 110

6 Conclusions 113

Appendices 117
Appendix A: Two Point Correlators in Legendre Space . . . 119
Appendix B: Locally Non-Gaussian Bispectrum . . . 120
Appendix C: Noise Plots For Stochastic Inflation . . . 122
Appendix D: Accuracy Check of Stochastic Inflation . . . 122
D.1 M1 Model . . . 123
D.2 M3 Model . . . 123
Appendix E: Large Non-Gaussianity and PBH Abundance . . . 124

Bibliography 127

List of Figures

1.1 Evolution of the physical horizon and the physical scales . . . 8
1.2 Overview of the PBH constraints . . . 20
1.3 Binding energy per nucleon . . . 24
1.4 CMB temperature anisotropy map . . . 26
1.5 CMB angular power spectrum . . . 27

2.1 Brownian motion and Ornstein-Uhlenbeck process . . . 30
2.2 Fokker-Planck equation . . . 32
2.3 Squeezed perturbation in phase space . . . 33
2.4 Quantum to classical transformation of perturbations . . . 37
2.5 Worldlines of locally FLRW separate universes . . . 41
2.6 Stochastic ΔN formalism . . . 44
2.7 Numerical algorithm for the Stochastic inflation code . . . 47
2.8 Comparison between RK4 and SRK2 . . . 50
2.9 Inflationary potential models for simulation . . . 52
2.10 Probability Distribution Function (PDF) for the model M2 . . . 53
2.11 PBH abundance sensitivity to the tail of the PDF . . . 55
2.12 PDF for the model M3 . . . 56
2.13 Curvature power spectrum for the model M1 . . . 57
2.14 Curvature power spectrum for the model M3 . . . 59

3.1 Blackbody spectrum . . . 63
3.2 Integration kernels for s distortions . . . 66
3.3 Blackbody spectrum variation with μ amplitude . . . 68
3.4 Spectral shapes of spectral distortions . . . 70
3.5 Individual contributions to source function . . . 78
3.6 Comparison of the oscillatory source function . . . 82
3.7 FIRAS bounds on the curvature power spectrum amplitude in Gaussian case . . . 84

4.1 FIRAS bounds on the curvature power spectrum amplitude in χ^2 non-Gaussian case 90
4.2 Comparison between monopole and quadrupole transfer functions . . . 92
4.3 Comparison between the Gaussian and non-Gaussian window functions . . . 95
4.4 Ratio of non-Gaussian to Gaussian window functions . . . 96

5.1 Accretion constraints on PBHs . . . 99

5.2 PBH and μ constraints for Gaussian perturbations 101
5.3 PBH and μ constraints for perturbative non-Gaussian perturbations 103
5.4 PBH and μ constraints for non-perturbative non-Gaussian perturbations 105
5.5 Ratio of non-Gaussian to Gaussian variances 106
5.6 PBH and μ constraints for χ^2 and cubic non-Gaussian perturbations 108
5.7 PBH and μ constraints for Gaussian and cubic non-Gaussian perturbations 110
5.8 PBH and μ constraints for higher-order non-Gaussian perturbations 111
5.9 Sunset diagram contribution to the curvature power spectrum amplitude 112

C.1 Variances of the field and momentum noise for the model M2 123
C.2 Variances of the field and momentum noise for the model M3 124
D.1 Accuracy check of non-perturbative power spectrum for the model M1 125
D.2 Accuracy check of non-perturbative power spectrum for the model M3 125

List of Tables

1.1 Evolution of universe expansion for different energy components 3

2.1 Parameters of the Model potentials 53

3.1 Coefficients for the numerical fitting of window function $W_\mu(k)$ 81

4.1 Conditions for Gaussian and Non-Gaussian perturbations 87
4.2 Coefficients for the numerical fitting of window function $W_\mu^{(\mathrm{NG2})}(k)$ 91

CHAPTER 1

Introduction

Astronomy is perhaps the oldest of the sciences, dating back to around 1000 BCE. Over the course of human history, a vast number of intellectuals have contributed to the development of astronomy, including, but not limited to, Plato, Aristotle, Aryabhata, Ptolemy, Galileo, Copernicus, Kepler, and Newton. The growth of cosmology as a distinct branch of astronomy is comparatively more recent. The foundation of modern cosmology was arguably laid when Einstein published the theory of relativity more than a century ago. General Relativity was a much-needed alternative to Newton's laws of motion, providing physicists with a precise geometrical description of gravity at very large scales. Thereafter, the likes of Hubble, Friedmann, Eddington, Lemaître, De Sitter, and many others ensured rapid progress in theoretical and observational cosmology.

The discovery of the Cosmic Microwave Background (CMB) by Arno Penzias and Robert Wilson marked the beginning of a new era in cosmology. With the launch of the COBE satellite a few decades later, the world came to know about the copious amount of information contained in the CMB in the form of its (small)large-scale (in)homogeneity(ies). This provided a further boost to cosmology, along with confirmation that the cosmological principle could be applied at large scales—the more accurate mapping by the successor missions of COBE, namely WMAP, BICEP and PLANCK, led to the emergence of precision cosmology.

The primary content of this thesis begins from Chapter 2, where we introduce the stochastic formalism applied to the theory of cosmic inflation. In the same chapter, we explain the importance of quantum diffusion on the evolution of primordial perturbations, the need for a non-perturbative treatment of the perturbations, and design a numerical algorithm to construct the perturbations statistics. In Chapter 3, we describe the phenomenon of spectral distortions in the blackbody spectrum of the Cosmic Microwave Background (CMB) and essential processes associated with them. We introduce a new approximation scheme, while also discussing the existing ones, to compute spectral distortions from the dissipation of primordial perturbations. This helps us in setting up the most robust constraints on the (Gaussian) primordial curvature power spectrum from spectral distortions.

We reserve Chapter 4 and Chapter 5 for understanding the primordial non-Gaussianity in depth. Starting with Chapter 4, we construct a procedure to embody the non-Gaussian nature of

inflationary perturbations in the calculation of spectral distortions using the accurate scheme from Chapter 3. Using this procedure, we constrain the primordial perturbations in different limits of non-Gaussianity. The results of this procedure pave the way for Chapter 5, where we explain how non-Gaussianity affects our perception about Primordial Black Holes (PBHs). The conventional constraints on PBHs come under Gaussian-perturbations assumption; our study extends this perception for various limits of Gaussianity and also for various orders (or strengths) of non-Gaussianity. We end the discussion by summarizing everything in Chapter 6. The appendices have also been provided as a supplement to several discussions within the main sections that require either an accuracy check or a tedious calculation.

In the rest of this introduction, we will outline the homogeneous and isotropic description of the universe that can be understood from the exact solutions to Einstein's equations, the brief era of inflation in the early universe that seeded the cosmological perturbations, information encoded in the CMB temperature anisotropies, and finally, an overview of Primordial Black Holes (PBHs).

1.1 Einstein Field Equations and FLRW Universe

The assumption of the cosmological principle simplifies the mathematical description of the universe at large scales. In the standard ΛCDM model, the line element, which describes the interval between two events, of a homogeneous and isotropic spacetime is given by the Friedmann–Lemaître–Robertson–Walker metric given as [1]

$$ds^2 = -dt^2 + a^2(t)\left(\frac{dr^2}{1-Kr^2} + r^2 d\theta^2 + r^2 sin^2\theta d\phi^2\right) , \tag{1.1.1}$$

where t is the physical time coordinate of the three-dimensional space (r, θ, ϕ) represented in the spherical coordinate system and the factor $a(t)$ scales the expansion of the spatial hypersurface with t. The quantity K is called the spatial curvature of the universe, which has three discrete values $\{-1, 0, 1\}$ representing the open, flat and closed geometries of the spacetime, respectively [2]. In this thesis, we will use the sign convention $(-+++)$ and work in the natural units, i.e. $m_p = c = \hbar = 1$ unless otherwise stated. The Einstein equations are a set of non-linear coupled partial differential equations that can be expressed in reduced-index notation as [3]

$$R_{\mu\nu} - R\frac{g_{\mu\nu}}{2} + \Lambda g_{\mu\nu} = 8\pi G T_{\mu\nu} , \tag{1.1.2}$$

where

$$\begin{aligned} T_{\mu\nu} &= \text{Stress} - \text{Energy tensor} , \\ g_{\mu\nu} &= \text{Metric tensor} , \\ R_{\mu\nu} &= \text{Ricci tensor} , \\ R &= \text{Ricci scalar} , \\ \Lambda &= \text{Cosmological constant} . \end{aligned} \tag{1.1.3}$$

Computing the aforementioned quantities for the FLRW metric and substituting them in Eq. (1.1.2), one gets two exact solutions [1], one corresponding to the off-diagonal term, $\mu \neq \nu$,

$$\frac{\ddot{a}}{a} = \frac{-4\pi G}{3}(3p + \rho) , \tag{1.1.4}$$

and other corresponding to the diagonal term $\mu = \nu$

$$\left(\frac{\dot{a}}{a}\right)^2 = -\frac{K}{a(t)^2} + \frac{8\pi G\rho}{3} \ , \tag{1.1.5}$$

where p and ρ are, respectively, the pressure and energy density of the system. Note that the system of equations Eq. (1.1.2) is closed only after specifying the nature of the 'matter' content of the universe, together with its equation of state. For a perfect fluid with vanishing anisotropic stress, the off-diagonal terms are zero, and hence, after raising the index, the stress-energy tensor becomes

$$T^{\mu}_{\nu} = \text{diag}(-\rho, p, p, p) \ , \tag{1.1.6}$$

$$p = w\rho \ . \tag{1.1.7}$$

The set of Eqs. (1.1.4) and (1.1.5) is known as the Friedmann equations, named after Alexander Friedmann, who derived them shortly after the concept of General Relativity was introduced. The right-hand side of Eqs. (1.1.4) and (1.1.5) is the answer to 'What governs the dynamics of the universe' and the left-hand side is the answer to 'How does the right-hand side govern the dynamics of the universe?' Invoking the energy conservation condition $\delta_\mu T^\mu_0 = 0$, one finds

$$-\frac{\dot{\rho}}{p+\rho} = 3H \ , \tag{1.1.8}$$

with $H(t) = \frac{\dot{a(t)}}{a(t)}$ being the Hubble parameter. Depending on the constituting matter, Eq. (1.1.8) takes different forms summarized in Table 1.1. It is convenient to express the energy densities as

Scenario	$\boldsymbol{\rho(t) \propto}$	$\boldsymbol{a(t) \propto}$	$\boldsymbol{w}$
R.D	a^{-4}	$t^{1/2}$	1/3
M.D	a^{-3}	$t^{2/3}$	0
C.C.D	*Constant*	$\sinh^{2/3}\left(\frac{(3\Lambda t)^{1/2}}{2}\right)$	-1
K	a^{-2}	t	-1/3

Table 1.1: *Evolution of universe expansion for different energy components. R.D: radiation domination; M.D: matter domination (baryonic + CDM); C.C.D: cosmological constant domination; K: curvature domination.*

we observe them today

$$\Omega_{l,0} = \frac{\rho_{l,0}}{\rho_c} \ , \tag{1.1.9}$$

where the subscript 'l' denotes different types of matter and '0' implies their value today, and ρ_c is the critical energy density required to maintain the flat geometry of the universe. Several observations from either late-time measurement of H_0 through Supernovae and Baryon Acoustic Oscillations [4] or from early-time observations from the CMB anisotropies have given us the following data with finite but low uncertainty [5]

$$[\Omega_{r,0}, \Omega_{m,0}, \Omega_{\Lambda,0}] = \left[9 \times 10^{-5}, 3.1 \times 10^{-1}, 6.9 \times 10^{-1}\right] \ . \tag{1.1.10}$$

1.2 Hot Big Bang Model and Limitations

By the late 1920s, growing theoretical and observational evidence began to challenge the long-held view of a static universe. Influential contributions by Einstein, Friedmann, Slipher, and Wirtz laid the groundwork for a dynamic cosmological model [6–8]. Building on these developments, Georges Lemaître proposed in 1927 the idea of a universe that is expanding over time. This theoretical framework gained strong observational support following Edwin Hubble's 1929 discovery that galaxies exhibit redshifts proportional to their distances [9], implying a systematic cosmic expansion.

Motivated by these findings, Lemaître suggested that if the universe is expanding today, it must have originated from an initially hot and extremely dense state, or, a spacetime singularity, giving rise to what would later be termed the Big Bang [10]. This explosive origin was followed by a radiation-dominated era, during which the dynamics of the universe were governed by relativistic particles, including both fermions and bosons, at temperatures exceeding $T \gtrsim 200\text{GeV}$.

As the universe expanded and cooled, conditions became favorable for the formation of atomic nuclei and neutral atoms, marking the transition to a matter-dominated era. During this epoch, non-relativistic matter began to cluster under gravity, leading to the formation of large-scale structures such as galaxy clusters, dark matter halos, stars, and planetary systems [11].

In more recent cosmological history, observations have revealed that the universe has entered a phase of accelerated expansion, driven by an enigmatic energy component known as dark energy, often modeled as a cosmological constant. This discovery was confirmed in 1998 by two independent teams measuring the luminosity-distance relationship of Type Ia supernovae [12, 13], establishing the presence of a dominant dark energy component in the present-day universe. This discovery was awarded the Nobel Prize in Physics in 2011.

The hot Big Bang model was supported and further developed by George Gamow, who also laid the foundation for Big Bang nucleosynthesis calculations, along with Ralph Alpher and Hans Bethe [14]. Over the next few decades, Lemaître's Big Bang model (although the name 'Big Bang' was coined much later) overshadowed the existing alternative theories at that time, such as Fred Hoyle's steady-state universe [15], and the oscillating universe by Richard Tolman [16]. After the discovery of the CMB in 1964, the Big Bang theory firmly strengthened its ground among the majority of physicists as it correctly predicted the temperature and black-body spectrum of the CMB radiation filling the entire universe.

Despite its tremendous success, the hot Big Bang model could not satisfactorily answer several key questions. Primarily, it could not explain why the initial conditions had to be highly well-picked to the universe to have evolved in the state as we see it today. This motivated several physicists, including Guth, Starobinsky, Linde, Steinhardt, and Albrecht [17–19], in the 1970s and 1980s, to introduce a brief period of rapid expansion in the early universe, known as inflation. First, we will examine the three major problems that the hot Big Bang model has not solved, and then discuss how inflation was able to address them.

1.2.1 Horizon Problem

The causal horizon is determined by the geodesics of the massless species, i.e. photons, since the fastest information that can travel from one region to another is the speed of light. Following the

FLRW line element Eq. (1.1.1), one can easily get the null geodesics i.e. $ds^2 = 0$

$$dr = \frac{dt}{a(t)} \left(1 - Kr^2\right)^{1/2} \ , \tag{1.2.1}$$

where we assume a purely radial motion ($d\theta = d\phi = 0$). As we will see in the next subsection, the spatial curvature is of little importance in the discussion, and thus we set it to zero for convenience. Suppose a photon is emitted at time t_i and spatial position $(r_i, 0, 0)$ then at an arbitrary time t in the future, it would have travelled a distance

$$r(t) - r_i = \int_{t_i}^{t} \frac{dt}{a(t)} \ , \tag{1.2.2}$$

in the comoving coordinate system. To get the distance travelled in the physical coordinates, one scales the comoving distance with the expansion factor given by

$$r_{\rm phy}(t) = a(t) r(t) \ . \tag{1.2.3}$$

The upper limit on the causal horizon in the present time would be the distance travelled by the earliest emitted photon till its detection. To get a rough estimate of this upper limit, we assume that a photon was emitted just after the Big Bang and let $t = t_f$ be the time where it imprints its observational signature

$$R_{\rm hor}(t_f) = a(t_f) \int_{t_i}^{t_f} \frac{dt}{a(t)} \ . \tag{1.2.4}$$

We will see in Section 1.7 that the observations of the CMB give us the information about the last scattering surface at the time when recombination took place. This is because, after recombination, the photons begin to freestream and are barely influenced by the environment along their path, except for the redshifting due to expansion and the Sunyaev-Zeldovich effect.

On the other hand, the present-day physical horizon would have the following length at the time of recombination

$$R_{\rm hor,0} = a(t_0) \int_{t_{\rm rec}}^{t_0} \frac{dt}{a(t)} \ , \tag{1.2.5}$$

where $t_0, t_{\rm rec}$ denote the present time and the time at recombination, respectively. Taking the ratio of Eq. (1.2.5) with respect to Eq. (1.2.4) and considering $t_f = t_{\rm rec}$

$$\left.\frac{R_{\rm hor,0}}{R_{\rm hor,rec}}\right|_{t=t_{\rm rec}} = \frac{a(t_{\rm rec}) \int_{t_i}^{t_{\rm rec}} \frac{dt}{a(t)}}{a(t_0) \int_{t_{\rm rec}}^{t_0} \frac{dt}{a(t)}} = \frac{a_{\rm rec} \int_{a_i}^{a_{\rm rec}} \frac{da}{a^2 H(a)}}{a_0 \int_{a_{\rm rec}}^{a_0} \frac{da}{a^2 H(a)}} = \mathcal{O}(10^2) \ , \tag{1.2.6}$$

where the numerical estimate has been found after using Eqs. (1.1.8) and (1.1.10) together with the redshift at recombination $z_{\rm rec} \approx 10^3$. On an angular map of the CMB temperature spanning the whole sky, this would correspond to hundreds of thousands of causally disconnected regions that never exchanged any information. If that is the case, then how come the photon temperature is uniform across the sky today, differing only by one part in 10^5 parts? This is the horizon problem that was discovered after the first-ever measurement of the CMB anisotropies [20].

1.2.2 Flatness Problem

We can also decode the information about the spatial curvature of the universe from the angular power spectrum of the CMB anisotropies. The current understanding points towards a spatially flat universe $|\Omega_{K,0}| < 5 \times 10^{-3}$ up to 95% accuracy [5]. As already mentioned in Table 1.1, the curvature energy density scales as $1/a^2$. This effectively means that during the radiation ($\Omega_r \propto 1/a^4$) and matter-dominated era ($\Omega_r \propto 1/a^3$), the curvature energy would keep growing if its initial value were even slightly away from zero. For simplicity, if we consider the universe to be composed of only radiation and curvature energy throughout history, we have

$$\rho_r(t) = \rho_{r,0}\ a(t)^{-4} \qquad \rho_K(t) = \rho_{K,0}\ a(t)^{-2}\ , \tag{1.2.7}$$

and hence, their ratio would scale as a^2

$$\frac{\rho_K(t)}{\rho_r(t)} = \frac{\rho_{K,0}}{\rho_{r,0}} a^2 \tag{1.2.8}$$

$$\approx \frac{\rho_{r,0}}{\rho_{r,t}}\ . \tag{1.2.9}$$

In the second step, we assume that the energy densities of radiation and curvature are of the same order today. Moreover, expressing the ratio in terms of radiation energy density is helpful because we have precise measurements for $\rho_{r,0} \sim (10^{-4}\text{GeV})^4$. We know that general relativity breaks down near the Planck energy scales $\sim (10^{18}\text{GeV})^4$ [21]; hence, we restrict ourselves to scales smaller than or equal to the Planck energy scales. The ratio Eq. (1.2.9) at such scales becomes

$$\frac{\rho_K}{\rho_r} \approx 10^{-62}\ , \tag{1.2.10}$$

meaning that even to have the curvature energy density of the same magnitude as radiation energy density today, it would have to start as much suppressed as 10^{-62} times the radiation energy in the early times. Even a slightly higher value of ρ_K than this crude estimate would have driven it to values larger than the radiation energy density today, and the geometry of the universe would be far from the flat Euclidean geometry we see today. More precisely, the present energy density of the spatial curvature is two orders of magnitude lower than the energy density of the radiation, which exacerbates the fine-tuning issue. This is known as the flatness problem. The hot Big Bang model cannot explain the need for this fine-tuning in the early universe to shape the present universe.

1.2.3 Monopole Problem

Numerous extensions to the Standard Model of particle physics have been proposed in pursuit of a Grand Unified Theory (GUT)—a framework that unifies the fundamental interactions of nature within a single theoretical structure [22–24]. These GUTs predict that, at extremely high temperatures (on the order of 10^{16} GeV), a spontaneous symmetry breaking occurs [25], giving rise to the distinct fundamental forces of the Standard Model: the strong nuclear, weak nuclear, and electromagnetic forces.

An important consequence of such symmetry breaking is the predicted formation of topological defects in the early universe, including cosmic strings, domain walls, and magnetic monopoles

[26–28]. Moreover, several other theoretical frameworks in particle physics also support the existence of magnetic monopoles in significant abundance [29]. If such monopoles had indeed been produced in the early universe, the energy stored in their associated magnetic fields would have vastly exceeded the energy densities of both radiation and matter. This would have profoundly influenced the geometry of spacetime and the subsequent history of cosmic structure formation.

However, current observations reveal no evidence of magnetic monopoles in the universe today, nor do they indicate any monopole-induced effects on large-scale structures [30–32]. This stark contradiction between robust theoretical predictions and observational null results constitutes the so-called monopole problem. In fact, addressing this problem was one of the original motivations for the development of the inflationary paradigm, as first proposed by Alan Guth in his pioneering models of cosmic inflation [17, 33].

1.3 Motivation For Cosmic Inflation

The proposed solution to the three problems faced by the hot Big Bang model involved a de Sitter phase where the expansion was accelerated for a brief period in the early universe. From the second Friedmann equation Eq. (1.1.4), one gets the condition for a de Sitter universe

$$\ddot{a} > 0 \quad \Leftrightarrow \quad \frac{\rho}{p} < -\frac{1}{3} \, . \tag{1.3.1}$$

To achieve accelerated expansion, one requires a component with a negative equation of state, specifically $w < -\frac{1}{3}$. As indicated in Table 1.1, a cosmological constant with $w = -1$ satisfies this condition. However, a true cosmological constant—with constant energy density—would drive eternal inflation, preventing a graceful exit into the radiation-dominated era. Thus, it is not suitable for a transient inflationary phase.

A more viable alternative is to introduce a dynamical scalar field whose equation of state can evolve with time. Such a field can temporarily dominate the energy budget of the universe, driving the required phase of accelerated expansion. Crucially, it can decay at the end of this phase, naturally reheating the universe and initiating the radiation-dominated epoch. In what follows, we will revisit how this scalar field, commonly referred to as the inflaton, governs the evolution of the background universe during inflation.

Solution to the Horizon problem : We saw how the two diametrically opposite patches of the sky share (nearly) the same temperature despite the fact that the physical horizon at the last scattering surface is much smaller than the observable radius of the universe today. Now, suppose that we introduce a phase of inflationary expansion ($\dot{a} > 0$) prior to the onset of the radiation-dominated era. In this case, the physical scales would expand exponentially, while the physical horizon would remain constant as long as the universe is in the de Sitter stage (see Fig. 1.1). This provides us with the opportunity to generate arbitrarily large physical scales before the universe reaches recombination. The only necessary condition is that inflation should last long enough so that $R_{\rm hor,rec} \geq R_{\rm hor,0}$.

Solution to the Flatness problem : A similar argument to the solution to the Horizon problem can be applied to the solution to the Flatness problem. Since the quantity rescaled energy density Eq. (1.1.9) for the spatial curvature is proportional to the scale factor as $\Omega_K \propto \frac{1}{\dot{a}^2}$, an accelerating de Sitter phase before the radiation-dominated era would rapidly dissolve the

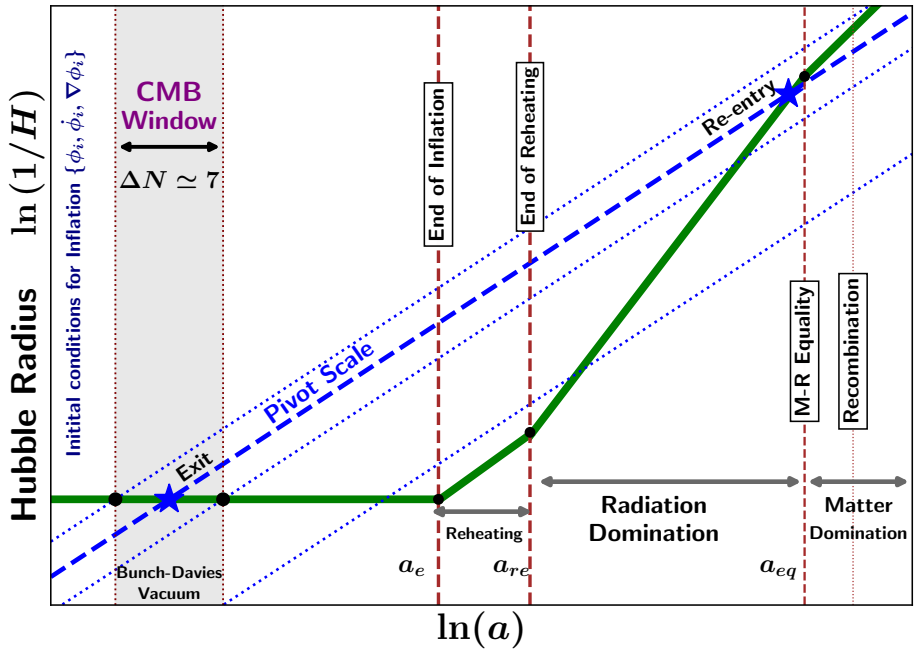

Figure 1.1: *The plot shows how the physical scales and the physical horizon evolve with the scale factor from the beginning of inflation until the matter-dominated era. The window of scales which is visible in the CMB corresponds to a narrow range of scales that exited in roughly the first few e-folds of inflation. The physical horizon, which remains nearly constant during inflation, starts increasing according to different powers of the scale factor shown in Table 1.1. Figure taken from the lecture notes [35].*

curvature to a negligible value, regardless of how large it was before the beginning of the phase. Therefore, we are free to choose initial conditions with an arbitrary value of curvature. Still, inflation will flatten the geometry of the universe before the energy from the scalar field of inflation is fully transferred to the radiation.

Once again, the only necessary condition is that inflation should last sufficiently long to drive Ω_k very close to zero, and with a bit of calculation, one can find that the minimum duration of inflation to solve the flatness problem is $\mathcal{O}(60)$ e-folds, assuming that inflation happened at the Planck energy scales. This number is lower if inflation happened at lower energy scales [34]. We will define the 'e-folds' of inflation shortly.

Solution to the Monopole problem : The monopole problem can also be solved by inflation if the magnetic monopoles were generated before the inflation. In such a situation, even if the energy density of the monopoles were significant before the beginning of inflation, the phase of the exponentially growing scale of the homogeneous background universe would dilute the energy density of non-relativistic monopoles as e^{-3Ht}, well before the onset of radiation-dominated era. Thus, the energy density of the monopoles would be so diluted that they would not affect the dynamics of the universe at all.

1.4 Background Dynamics During Inflation

First, let us consider the simplest scenario of a single-field model. The action of an inflaton field ϕ minimally coupled to gravity is

$$S = \int \sqrt{-g}\left(R - \left[\frac{1}{2}g^{\alpha\beta}\partial_\alpha\phi\partial_\beta\phi + V(\phi)\right]\right) d^4x \ , \tag{1.4.1}$$

where $g^{\alpha\beta}$ is the metric tensor defined over an FLRW background and $V(\phi)$ accounts for the potential energy of inflaton during inflation. The potential energy is a unique characteristic of the inflationary models. The associated Lagrangian energy densities of the inflaton and gravity are

$$\mathcal{L}_\phi = -\frac{1}{2}g^{\alpha\beta}\partial_\alpha\phi\partial_\beta\phi - V(\phi) \ , \tag{1.4.2}$$

$$\mathcal{L}_{\rm G} = R \ . \tag{1.4.3}$$

Varying the inflaton energy component of the action Eq. (1.4.1) with respect to the covariant metric tensor gives the stress-energy tensor

$$T_{\alpha\beta} = \partial_\alpha\phi\partial_\beta\phi - g_{\alpha\beta}\mathcal{L}_\phi \ . \tag{1.4.4}$$

One can raise the index of Eq. (1.4.4) and compare with the diagonal stress-energy tensor of mixed form in Eq. (1.1.6) to get the expressions for the energy density and pressure of the inflaton

$$\bar{\rho} = \frac{\bar{\phi}^2}{2} + V(\bar{\phi}) \ , \tag{1.4.5}$$

$$\bar{p} = \frac{\bar{\phi}^2}{2} - V(\bar{\phi}) \ , \tag{1.4.6}$$

where the bar on the variables means that the quantities are computed for the homogeneous and isotropic background. This notation will be important when we start considering perturbations over the background quantities in Section 1.5. Once we have the energy density and pressure, they can be plugged into the Friedmann equations Eqs. (1.1.4) and (1.1.5) to get the background dynamics governed by the inflaton

$$\bar{H}^2 = \frac{8\pi G}{3}\left(\frac{\bar{\phi}^2}{2} + V(\bar{\phi})\right) \ , \tag{1.4.7}$$

$$\bar{H}^2 + \dot{\bar{H}} = -\frac{8\pi G}{3}\left(\frac{\bar{\phi}^2}{2} - V(\bar{\phi})\right) \ . \tag{1.4.8}$$

On the other hand, we can also vary the action Eq. (1.4.1) with respect to the background inflaton that would give us the scalar field equation of motion or the Klein-Gordon equation given by

$$\ddot{\bar{\phi}} + 3\bar{H}\dot{\bar{\phi}} + \frac{\partial V}{\partial\bar{\phi}} = 0 \ . \tag{1.4.9}$$

We recall that the condition that the scalar field must lead to an accelerated expansion is $w_{\bar{\phi}} < -1/3$. Using Eqs. (1.4.5) and (1.4.6) one gets

$$V(\bar{\phi}) > \dot{\bar{\phi}}^2 \ , \tag{1.4.10}$$

1.4.1 Slow-roll and Ultra-slow roll approximations

Inflation lasts as long as the inequality Eq. (1.4.10) is satisfied. At the beginning of inflation, the inflaton sits at the top of the potential symbolizing an unstable state and, rolls down the potential as inflation progresses, converting its potential energy into its kinetic energy. Since the potential energy has to be larger than the kinetic term, one must ensure that the field rolls down slowly so that the condition Eq. (1.4.10) stays true to obtain the desired duration of inflation. For this purpose, a slow-roll approximation (SRA) scheme is generally accompanied by the inflationary setup Eqs. (1.4.7) to (1.4.9). The slow-roll parameters that control the rolling down of the field are given by

$$\epsilon = -\frac{\dot{\bar{H}}}{\bar{H}^2} \ , \tag{1.4.11}$$

$$\eta = -\frac{\ddot{\bar{H}}}{2\bar{H}\dot{\bar{H}}} \ , \tag{1.4.12}$$

where ϵ and η are the first and second slow-roll parameters, respectively. For a sufficiently long period of inflation, we need a stronger version of the inequality Eq. (1.4.10), i.e. $V(\bar{\phi}) \gg \dot{\bar{\phi}}^2$. In that case, the slow-roll parameters follow $\epsilon, |\eta| \ll 1$. When one of these parameters becomes of the order of unity, inflation is concluded. Moreover, under the SRA, the field kinetic energy is negligible, and the background equations Eqs. (1.4.7) and (1.4.9) can be approximated as

$$\bar{H}^2 \simeq \frac{8\pi G}{3} V(\bar{\phi}_{\rm SR}) \ , \tag{1.4.13}$$

$$3\bar{H}\dot{\bar{\phi}}_{\rm SR} + \frac{\partial V}{\partial \bar{\phi}} \simeq 0 \ , \tag{1.4.14}$$

which implies that if the potential energy is flat enough, the field rolls down slowly relative to the expansion rate of the background, and the Hubble parameter is approximately constant throughout the inflation. Thus, the physical scales of the universe exponentially grow with time, $a(t) = e^{Ht}$. It is more convenient to rescale the time variable because of the rapidly expanding background. This is done by introducing the e-fold parameter N such that $\frac{dN}{dt} = H$. The duration and progress of inflation are expressed in terms of the number of e-folds that have lapsed. The SRA simplifies the Klein-Gordon equation into a first-order ordinary differential equation Eq. (1.4.14). The SR parameters can also be written as functions of the potential slope

$$\epsilon = \frac{1}{2}\left(\frac{V'}{V}\right)^2 \ , \tag{1.4.15}$$

$$\eta = \frac{V''}{V} \ . \tag{1.4.16}$$

Enforcing both the SR conditions simultaneously means that the potential has a slowly varying slope and, at the same time, the rate of change of this slope is also slow. Moreover, to get the e-folds as a function of the field,

$$\bar{N}(\bar{\phi}) = \int_{\bar{\phi}_i}^{\bar{\phi}} \bar{H} dt = \int_{\bar{\phi}_i}^{\bar{\phi}} \frac{\bar{H}}{\dot{\bar{\phi}}} d\bar{\phi} \ . \tag{1.4.17}$$

Generally, the initial value of the field $\bar{\phi}_i$ is chosen to be at the beginning of inflation.

Suppose a certain section of the potential features an exactly flat region in which case, the potential gradient vanishes and there is no push on the field to further roll down from this region. The Klein-Gordon equation becomes

$$\ddot{\bar{\phi}}_{\rm USR} + 3\bar{H}\dot{\bar{\phi}}_{\rm USR} \simeq 0 \ , \tag{1.4.18}$$

and hence, whatever momentum the field had acquired before entering this region would only push it to escape the region. The Hubble parameter is exactly constant in this region, and the first SR parameter rapidly approaches zero. Such a section of potential is called an ultra-slow roll regime (USR). An USR regime enhances the growth of perturbations by orders of magnitude, because the super-Hubble perturbations keep on growing during the USR phase. Consequently, one expects that these perturbations are large enough to withstand the radiation pressure at horizon reentry and collapse gravitationally to black holes [36].

1.5 Cosmological Perturbations: The Mukhanov-Sasaki Equation

If the universe had only a homogeneous and isotropic background, the large inhomogeneities present today in the form of Large-scale Structures and galaxies would not have existed. The foundation for such inhomogeneities was laid by the tiny fluctuations in the inflaton's local values inherited from the vacuum fluctuations. These fluctuations were then pushed outside the causal horizon during the inflationary period. After the end of inflation, they reentered the horizon, and the field fluctuations were essentially transferred to the relativistic and subsequently non-relativistic species under adiabatic initial conditions.

One of the major achievements of inflation is that it provides a satisfactory origin of the observed anisotropies in the temperature of the CMB. A standard single-field slow roll model of inflation predicts a nearly scale-invariant power spectrum of the scalar perturbations, which has been successfully verified at the scales probed by the CMB missions [37, 38]. A powerful property of slow-roll models is their attractor nature, which basically drives the fluctuations towards the same solution regardless of their initial conditions.

In this subsection, we will cover the mathematical formulation of inflationary perturbations using linear perturbation theory and derive the so-called Mukhanov-Sasaki equation, which is extensively used to study the evolution of perturbations from their generation until their horizon reentry. Let us introduce a small perturbation in the homogeneous and isotropic inflaton variable that can be linearized,

$$\phi(x,t) \approx \bar{\phi}(t) + \delta\phi(x,t) \ . \tag{1.5.1}$$

The perturbed inflaton represents a localized variable. Since the energy of the field is the sole contributor to the matter content of the universe during inflation, the field fluctuations would also induce fluctuations in the stress-energy tensor Eq. (1.4.4) and eventually affect the geometry of the universe via the left-hand side of Eq. (1.1.2). In its most general form, one can write a perturbed FLRW metric as

$$ds^2 = (1+2A)dt^2 + 2a^2(t)\partial_\mu B dx^\mu dt + a^2(t)([1-2\psi]\,\gamma_{\mu\nu} + 2\partial_\mu\partial_\nu E)dx^\mu dx^\nu \ , \tag{1.5.2}$$

where the scalar sector has four degrees of perturbations, viz. the timelapse function A and three spatial perturbations B, ψ and E; moreover, $\gamma_{\mu\nu}$ is the spatial part of the background metric tensor.

First, we write the Klein-Gordon equation Eq. (1.4.9) in explicit notation [39]:

$$\left(\frac{\partial}{\partial t^2}+\frac{\partial}{\partial x^{i2}}\right)\phi(\mathrm{x}^i,t)+3H(t)\frac{\partial\phi(\mathrm{x}^i,t)}{\partial t}=\frac{\partial V(\phi(\mathrm{x}^i,t))}{\partial\phi}\ . \tag{1.5.3}$$

We drop the variable dependency inside the braces for convenience. Next, we need a linearized version of Eq. (1.5.3) that would tell us how the linear fluctuation '$\delta\phi$' propagates in space and time. If we replace the linearlized perturbed inflaton definition Eq. (1.5.1) in Eq. (1.5.3), and take the solution to Fourier space, we get [39, 40]

$$\begin{aligned}\delta\ddot{\phi}_{\mathbf{k}}+3H\delta\dot{\phi}_{\mathbf{k}}+\left(\frac{k^2}{a^2}+\frac{\partial^2V}{\partial\phi_{\mathbf{k}}^2}\right)\delta\phi_{\mathbf{k}}&=-2\frac{\partial V}{\partial\phi_{\mathbf{k}}}A\\&\quad+\dot{\phi}_k\left(\dot{A}+3\dot{\psi}+\frac{k^2}{a^2}(a^2\dot{E}-aB)\right)\ ,\end{aligned} \tag{1.5.4}$$

where we neglect the lapse function A, which signifies that one is working in a gauge where the fluctuation in time is switched off. If we choose the number of e-folds (N) as the time variable, this gauge choice would be called the uniform-N gauge.
We can solve for the metric perturbations using the constraint equations of the Einstein equations

$$\begin{aligned}3H(\dot{\psi}+HA)+\frac{k^2}{a^2}\left(\psi-H(aB-a^2\dot{E})\right)\\+4\pi G\left(\frac{\partial V}{\partial\phi_{\mathbf{k}}}\delta\phi_{\mathbf{k}}+(\delta\dot{\phi}_{\mathbf{k}}-\dot{\phi}A)\dot{\phi}_{\mathbf{k}}\right)=0\ ,\end{aligned} \tag{1.5.5}$$

$$\dot{\psi}+HA+4\pi G\dot{\phi}_{\mathbf{k}}\delta\phi_{\mathbf{k}}=0\ , \tag{1.5.6}$$

where Eq. (1.5.5) is the energy constraint and Eq. (1.5.6) is the momentum constraint. The metric perturbation can be set to zero in the spatially flat gauge so that the field perturbations are equal to a new variable Q, defined as [41, 42],

$$Q_{\mathbf{k}}=\delta\phi_{\mathbf{k}}+\frac{\dot{\phi}_{\mathbf{k}}\psi}{H}\ . \tag{1.5.7}$$

This variable is called the Mukhanov-Sasaki variable. The constraint equations Eqs. (1.5.5) and (1.5.6) in this gauge are as follows

$$3H^2A+\frac{k^2}{a^2}\left(-H(aB-a^2\dot{E})\right)+4\pi G\left(\frac{\partial V}{\partial\phi_{\mathbf{k}}}\delta\phi_{\mathbf{k}}+(\delta\dot{\phi}_{\mathbf{k}}-\dot{\phi}A)\dot{\phi}_{\mathbf{k}}\right)=0\ , \tag{1.5.8}$$

$$HA+4\pi G\dot{\phi}_{\mathbf{k}}\delta\phi_{\mathbf{k}}=0\ . \tag{1.5.9}$$

We can utilize Eqs. (1.5.8) and (1.5.9) to simplify the right-hand side of Eq. (1.5.4) to eventually give

$$\delta\ddot{\phi}_{\mathbf{k}}+3H\delta\dot{\phi}_{\mathbf{k}}+\left[\frac{k^2}{a^2}+\frac{\partial^2V}{\partial\phi_{\mathbf{k}}^2}-\frac{8\pi G}{a^3}\frac{d}{dt}\left(\frac{a^3\dot{\phi}_{\mathbf{k}}^2}{H}\right)\right]\delta\phi_{\mathbf{k}}=0\ . \tag{1.5.10}$$

The above equation is also commonly referred to as the Mukhanov-Sasaki equation. As an additional step, we can perform a change of variable from $dt \to dN$

$$\delta\phi''_{\mathbf{k}} + (3 + H'/H)\delta\phi'_{\mathbf{k}} + \left(k^2/(aH)^2 + \bar{\phi'_{\mathbf{k}}}^2 (3 + H'/H) + 2\phi'_{\mathbf{k}} V_{,\bar{\phi}}/H^2 + V_{,\bar{\phi}\bar{\phi}}/H^2\right)\delta\phi_{\mathbf{k}} = 0 \ . \tag{1.5.11}$$

It is more convenient to work with the Mukhanov-Sasaki equation in terms of N as the time variable, particularly when working with the stochastic inflation approach. We will study the stochastic inflation in detail in Chapter 2. One can rewrite Eq. (1.5.10) in a more functional form after rescaling the Mukhanov-Sasaki variable, $\nu_k = aQ_k$,

$$\nu''_k + \omega^2(\tau, k)\nu_k = 0 \ , \tag{1.5.12}$$

where the prime denotes the derivative with respect to the conformal time $\tau = \int \frac{dt}{a(t)}$. It is evident that Eq. (1.5.12) resembles the equation of motion for a harmonic oscillator with a time-dependent frequency [43]

$$\omega^2(\tau, k) = k^2 - \frac{z''}{z} \ . \tag{1.5.13}$$

It is often preferred to specify the scalar perturbations from inflation through a gauge-invariant variable $\mathcal{R}_k = \frac{\nu_k}{z}$, also known as the comoving curvature perturbation. The variable z is given by

$$z = a\sqrt{2\epsilon} \ , \tag{1.5.14}$$

$$\frac{z''}{z} = a^2\bar{H}^2\left(2 - \epsilon + \frac{3\eta}{2} - \frac{\epsilon\eta}{2} + \frac{\eta^2}{4} + \frac{\eta\epsilon_3}{4}\right) \ , \tag{1.5.15}$$

where ϵ_3 is the third SR parameter. Hence, each Fourier mode of the perturbation can be perceived as an independent harmonic oscillator. As we will see, $\mathcal{R}_k$ is a more desirable variable to work with, mainly for two reasons: (1) At super-Hubble scales ($k \ll aH$), the curvature perturbation freezes i.e. $\dot{\mathcal{R}}_k = 0$ [34]. In other words, the curvature perturbation corresponding to certain scales retains the information from the moment it crosses the physical horizon during inflation until it reenters the physical horizon during either the radiation era or the matter era, (2) With the assumption that the adiabatic initial condition holds [43, 44], it becomes trivial to transfer the curvature perturbation to the energy fluctuations in the standard model species.

At the beginning of inflation, a perturbation mode lies well within the physical horizon, with its scale much smaller than the horizon size. As inflation proceeds, these scales grow exponentially with the number of e-folds, while the Hubble parameter remains nearly constant. Eventually, the mode crosses the causal horizon when the condition $k = a\bar{H}$ is satisfied, and continues to stretch beyond the horizon as long as the universe remains in the de Sitter phase. Following the end of inflation—through the process of reheating, which we will discuss shortly, the universe enters the radiation-dominated era. During this phase, the physical horizon grows as τ^2, while the comoving scales increase only as τ. Consequently, the previously super-Hubble perturbation modes begin to reenter the horizon one after another, becoming sub-Hubble again. Assuming a de Sitter expansion throughout inflation, the scale factor evolves as $a(\tau) = -\frac{1}{\bar{H}\tau}$. Since ϵ varies slowly during this period, we can express the oscillation frequency as

$$\omega^2(\tau, k) \simeq k^2 - \frac{a''}{a} = k^2 - \frac{2}{\tau^2} \ , \tag{1.5.16}$$

substituting which in Eq. (1.5.12), one can compute the general solution as [43]

$$\nu(k,\tau) = \frac{\sqrt{\frac{2}{\pi}}A\sqrt{\tau}\left(\frac{\sin(k\tau)}{k\tau} - \cos(k\tau)\right)}{\sqrt{k\tau}} + \frac{\sqrt{\frac{2}{\pi}}B\sqrt{\tau}\left(-\sin(k\tau) - \frac{\cos(k\tau)}{k\tau}\right)}{\sqrt{k\tau}} \ , \tag{1.5.17}$$

Using the Euler's formula, Eq. (1.5.17) can also be written as

$$\nu_k(\tau) = e^{-ik\tau}\frac{C}{\sqrt{2k}}\left(1 - \frac{i}{k\tau}\right) + e^{ik\tau}\frac{D}{\sqrt{2k}}\left(1 + \frac{i}{k\tau}\right) \ , \tag{1.5.18}$$

with the new constants $C+B+iA = 0$ and $D+B-iA = 0$. The solution to the Mukhanov-Sasaki equation Eq. (1.5.12) can then be approximated in two different limits:

Sub-Hubble limit: In the sub-Hubble regime, we know that $k \gg a\bar{H}$ which translates to $k \gg 1/\tau$ and hence, $\omega \sim k$ i.e. the modes oscillate with a constant frequency when they are sufficiently smaller than the horizon. In this case, Eq. (1.5.12) becomes

$$\nu_k'' + k^2\nu_k = 0 \ , \tag{1.5.19}$$

whose solution is just a harmonic oscillator with a frequency proportional to the product $k\tau$. To obtain the exact solution for ν_k, it is necessary to specify the initial conditions, which are provided as the Bunch-Davies vacuum conditions. In the limit of very early time, Eq. (1.5.18) can be approximated as

$$v_k(\tau) = \lim_{\tau\to-\infty}\frac{e^{-k\tau}}{\sqrt{2k}} \ , \tag{1.5.20}$$

and hence, $C = 1$ and $D = 0$.

Super-Hubble limit : In the super-Hubble limit, one finds that $k \ll 1/\tau$ or $\omega \sim -\frac{2}{\tau^2}$ such that

$$\nu_k'' - \frac{2}{\tau^2}\nu_k = 0 \quad \Rightarrow \quad \nu_k(\tau) = \frac{E_1}{\tau} + E_2\tau^2 \ , \tag{1.5.21}$$

which implies that the solution in the super-Hubble limit consists of a growing solution ($\propto 1/\tau$) and a decaying solution ($\propto \tau^2$) since $\tau \in [-\infty, 0]$. After putting the limit $k\tau \to 0$ in Eq. (1.5.18) and comparing the coefficients, we get $E_1 = \frac{-i}{\sqrt{2k}k}$ so that

$$\nu_k(\tau) = \frac{-i}{\sqrt{2k}k}\frac{1}{\tau} \ . \tag{1.5.22}$$

It is also evident that the comoving curvature perturbation $\mathcal{R}_k$ is constant on super-Hubble scales. Finally, we get the expression for $\mathcal{R}_k$ from Eq. (1.5.22) at the horizon exit, which is [43]

$$\mathcal{R}_k|_{k=a\bar{H}} == \frac{-i}{\sqrt{2k}k}\frac{H}{\sqrt{2\epsilon}} \ , \tag{1.5.23}$$

which is indeed a constant value.

Power spectrum: As previously discussed, the quantum fluctuations in the vacuum expectation value of the inflaton were transmitted as spatial perturbations in the energy density of the inflaton. Hence, we expect $\delta\phi(x,t)$ to be a Gaussian random variable, and also $\mathcal{R}(x,t)$

($\propto \delta\phi^1(x,t)$). The statistical properties of a random Gaussian variable are fully explained using its first two moments, viz., its mean and variance. By its definition, the ensemble of all the possible values of $\delta\phi(x,t)$ is centred at zero, so from the ergodic hypothesis,

$$\langle \mathcal{R}(x,t) \rangle = 0 \ , \tag{1.5.24}$$

and hence, it is sufficient to compute only the variance of the fluctuations, which, in Fourier space, becomes

$$\langle \mathcal{R}_{k_1} \mathcal{R}_{k_2} \rangle = |\mathcal{R}_k(t)|^2 \, \delta(k_1 + k_2) = \left(\frac{\bar{H}}{\dot{\bar{\phi}}} \right)^2 |\delta\phi(k,t)|^2 \, \delta(k_1 + k_2) \ , \tag{1.5.25}$$

and define the dimensionless curvature power spectrum as

$$\mathcal{P}_{\mathcal{R}}(k) = \frac{k^3}{2\pi^2} |\mathcal{R}_k(t)|^2 \ . \tag{1.5.26}$$

If we wish to find the frozen power spectrum at super-Hubble scales, we can use Eq. (1.5.23) to get

$$\mathcal{P}_{\mathcal{R}}(k)|_{k=a\bar{H}} = \frac{\bar{H}^2}{8\pi^2 \epsilon} \tag{1.5.27}$$

In the slow-roll limit, the Hubble parameter can be replaced with the potential energy using Eq. (1.4.13) and the power spectrum in this approximation is given by [43]

$$\mathcal{P}_{\mathcal{R},\mathrm{SR}}(k)|_{k=a\bar{H}} = \frac{8\pi G V}{24\pi^2 \epsilon} \ . \tag{1.5.28}$$

The correlation of the curvature perturbations can be connected with the angular spectrum of the CMB anisotropies. Hence, it is possible to constrain the amplitude of the power spectrum at the scales in the neighbourhood of $k_{\mathrm{CMB}} = 0.05\mathrm{Mpc}^{-1}$. For this purpose, we can express Eq. (1.5.27) as a power law of the comoving scale in the following way

$$\mathcal{P}_{\mathcal{R}}(k)|_{k=a\bar{H}} = A_{\mathrm{CMB}} \left(\frac{k}{k_{\mathrm{CMB}}} \right)^{n_s - 1} \ , \tag{1.5.29}$$

$$n_s - 1 = \left. \frac{d \ln \mathcal{P}_{\mathcal{R}}(k)}{d \ln k} \right|_{k=k_{\mathrm{CMB}}} \ . \tag{1.5.30}$$

As already mentioned, the equations of motion of perturbations in the scalar, vector and tensor sectors are independent from each other up to linear order in the perturbation theory. Hence, one can follow a similar approach to derive the equation of motion for the tensor perturbations (h_{ij}), which propagate as gravitational waves in free space. We will directly provide the equation below

$$h''(k,\tau) + 2\frac{H}{a} h'(k,\tau) + k^2 h(k,\tau) = 0 \ . \tag{1.5.31}$$

Note that Eq. (1.5.31) needs to be solved for two polarization degrees of freedom, namely '+' polarization and '×' polarization. Analogous to the scalar power spectrum, the inflationary tensor power spectrum can be written as

$$\mathcal{P}_h(k,\tau) = \frac{k^3}{2\pi^2} \left| h^2 \right| \tag{1.5.32}$$

where $A = \mathcal{P}_{\mathcal{R}}(k_{\rm CMB})$ and the scalar spectral index n_s tells about the dependency of the power spectrum on the comoving scales. The latest dataset from Planck [5] gives an upper bound on the

$$\ln\left(10^{10}A\right) \leq 2.1 \times 10^{-9} \ , \tag{1.5.33}$$

$$n_s \leq 0.9649 \pm 0.0042 \ , \tag{1.5.34}$$

$$r = \frac{\mathcal{P}_h}{\mathcal{P}_{\mathcal{R}}} < 0.056 \ , \tag{1.5.35}$$

Finally, we note that the vector perturbations do not get sourced if one expresses the stress-energy tensor as a perfect fluid. In such a case, the anisotropic stress (or shear, as known in the literature) $\bar{\pi}$ is zero, and there are no directionalities in the geometry of the linearly perturbed FLRW spacetime [1]. We can then safely ignore vector perturbations.

1.6 Primordial Black Holes

Since Primordial Black Holes or PBHs form an integral aspect of this thesis, it makes sense to give an overview of them at this point. In this section, we will cover the brief history of PBHs' theory development, their mathematical formulation and ultimately their observational status as of today, along with what the future holds for PBHs.

The earliest studies of PBHs date back to the late 1960s, when Zeldovich and Novikov proposed the foundational hypothesis of black holes in the very early universe. Interestingly, the earliest work on PBHs argued against their existence because Zeldovich and Novikov claimed, using a simplified Bondi accretion model, that such black holes would become too massive by the advent of the matter era and alter the structure formation history [45, 46]. However, this simplistic picture was discarded in 1974 by Carr and Hawking, who explained that the increase in PBH mass due to accretion would be much suppressed, thus ruling in favour of PBHs [47]. It was the PBHs that inspired Hawking to come up with the phenomenon of black hole evaporation due to Hawking radiation [48]. In fact, the first-ever constraint on PBHs in the lower mass range came from the Hawking radiation, which states that a black hole of mass smaller than $\sim \mathcal{O}(10^{15})$ g would not have survived today owing to their evaporation [49, 50].

The introduction of cosmic inflation marked a massive step in PBH physics, as inflation provided a natural framework for the origin of density fluctuations that would collapse (if large enough) to become PBHs. Following that, from the 1980s to the 2000s, an extensive groundwork on the theory of PBH formation from gravitationally collapsing inflationary fluctuations was laid by Hawking, Sasaki, Carr, Zeldovich, Starobinsky, Linde, Khlopov, and several others [18, 51–61]. In a similar time frame, work was being done on the primitive analytic estimates for the collapse threshold for PBH formation and numerical estimates by Carr, Novikov, Nadezhin, Polnarev, Harada and Niemeyer [62–67]. In the late 2000s to late 2010s, this was followed by more robust collapse threshold values by Musco, Miller, Harada, Byrnes and Riotto [68–75].

Many other formation mechanisms for PBHs have also been proposed that do not rely on fluctuations from inflation. These novel mechanisms include, but are not limited to, the collapse of cosmic strings [76–78], collisions of true vacuum bubbles [79, 80], topological defects from phase transitions [52, 81] and the production of PBHs in modified gravity and high-energy theories [82, 83]. Nevertheless, to date, PBH formation from inflation remains the most preferred

and well-studied option due to its simplicity and wide acceptance in the community. As we shall see later in Chapter 4, the Gaussian assumption of the scalar fluctuations portrays an oversimplified picture, especially when the perturbations need to be colossally amplified to give rise to a non-negligible PBH population.

From the 1990s to very recently, progress has been made through the works of Sasaki, Matarrese, Riotto, Wands, Byrnes, Bartolo, Malik, and others, who have incorporated primordial non-Gaussianity (PNG) into the calculations of PBH abundance statistics and their astrophysics after formation [84–91]. It is now well known that PNG significantly alters the picture of PBHs and affects their observational constraints depending on their shapes and orders [92, 93]. Although, the CMB observations have put tight bounds on PNG at the scales $0.005\text{Mpc}^{-1} \leq k \leq 0.2\text{Mpc}^{-1}$, the scales leading to PBHs are much smaller and further from the CMB scales (roughly e^{35}), there is a priori no reason to assume that such bounds are justifiable at the PBH scales.

Moreover, the need for observational probes of PBHs arose after Chapline noted in 1975 that PBHs could be viable dark matter candidates [94, 95]. Since then, several observations have imposed various constraints on PBHs for distinct mass ranges, either through direct or indirect non-detections. The most prominent ones are microlensing [96, 97], gravitational waves [98, 99], high-energy emissions from PBH accretion [100, 101], CMB spectral distortions [102, 103] and several astrophysical probes at galaxy scales [104–106]. The bounds from spectral distortions are indirect and are mainly stronger in the supermassive range, as we shall see in detail in the next sections. Currently, gravitational waves have become one of the most powerful tools for hunting PBHs, thanks to the groundbreaking discovery of gravitational waves from merging black hole binaries by the LIGO-VIRGO collaboration in 2015 [107, 108]. After this discovery, the interest in PBHs has inflated, and the field has witnessed tremendous progress in less than a decade.

For example, it was shown by [109] that the merger rate of PBHs ($M_{\text{PBH}} \sim 30M_\odot$) fall within the LIGO of detection, at least for a monochromatic mass distribution and a arbitrary of dark matter fraction. It was, however, argued by [110] that PBH could not be a dominant dark matter fraction, otherwise it would exceed the observed merger rate observed by LIGO. Furthermore, the fact that the third observational run (O3) of the LIGO-VIRGO collaboration did not detect a single subsolar mass binary black hole mergers restricted the $f_{\text{PBH}} \leq 0.06$ for $M_{\text{PBH}} \in [0.2M_\odot, 1M_\odot]$ [111]. More recently, a Bayesian analysis O3 dataset with the PBHs of broader mass functions provided stronger constraints, $f_{\text{PBH}} \leq 10^{-3}$ in the mass range $M_{\text{PBH}} \in [1M_\odot, 300M_\odot]$, with further conclusion that non-Gaussianity does not shift the constraints significantly [112]. For a review on the gravitational wave signatures of PBHs, see [113].

Additionally, the observations from the James Webb Space Telescope (JWST) have also provided important implications for the primordial origin of astrophysical events. For instance, the observations of massive galaxies at high redshifts can be explained with the presence of PBH with an abundance as low as $f_{\text{PBH}} < 0.01$ [114]. Not only do PBHs alter the structure formation, but they could also serve as the seeds of supermassive black holes (SMBHs) if their formation mass if of the order $\mathcal{O}(10^5 M_\odot)$. Moreover, the observations of high redshift quasars UHZ1 and GHZ9 by JWST ($z \sim 11$) can also be explained by efficiently accreting PBHs, without disturbing the existing constraints [115].

For the rest of this thesis, we will focus on the PBHs formed from the collapse of scalar perturbations from inflation unless otherwise stated. In the following section, we explain a

well-established mathematical framework for computing the current PBH abundance as a function of its mass, along with the standard approach to presenting constraints on the PBH abundance.

1.6.1 Statistics of PBH Abundance

Even in the inflationary paradigm, there are multiple ways to obtain large perturbations leading to PBHs. The more sophisticated methods generally involve multi-field models such as Hybrid inflation [116], where a second-order phase transition driven by a secondary waterfall field leads to a significant enhancement in the curvature perturbations. Another example is the curvaton model, in which the curvaton acts as a spectator field during inflation, but after inflation has ended, it predominantly contributes to the total curvature perturbations that would become PBHs [117]. Notably, the curvaton scenario is one of the earliest and most studied cases for non-Gaussian perturbations. There are various single-field models motivated by high-energy physics, for example, the string inflation [118] or DBI inflation [119].

As already seen in the previous section, a slow-roll attractor model predicts perturbations of $\mathcal{O}(10^{-5})$ at nearly all scales and thus, it cannot produce PBHs. Instead, if there is a non-attractor phase in the potential for a short duration, such as a bump [120] or an inflection point [121], then the field would remain in this region for an extended period. The perturbations would have long time to grow as large as $\mathcal{R}_{k,\mathrm{USR}} \sim 10^{-1}$. Such models have gained popularity due to their simplistic nature as well as the freedom to produce PBHs over a wide mass range [122, 123]. However, they are also criticized due to the fine-tuning issue [124].

Nevertheless, we assume that the seeds for PBHs were generated by a single clock (inflaton) with vanishing non-adiabatic perturbations. At the beginning of the radiation era, the super-Hubble curvature perturbations are transferred to the fluctuations in the radiation energy density. When these fluctuations reenter the horizon, they are met with a radiation pressure that tries to dissolve them and thermally equalize the system. This is where the collapse threshold (δ_c) comes into the picture. If the fluctuation is stronger than the threshold value, i.e. $\delta > \delta_c$, the fluctuation will succumb to its gravitational pull and collapse. In the other case, gravity will not be able to withstand the radiation pressure, and the fluctuation will disperse away into the medium.

The threshold for the collapse is a function of the equation of state at the horizon reentry, and an analytic estimate for the threshold in the radiation era gives $\delta_c \sim 0.4$ [95]. More precise values are computed using hydrodynamical simulations [68]. On top of this, one also needs to consider the non-linear relation between the density contrast δ and the comoving curvature perturbation $\mathcal{R}$, which would render intrinsic non-Gaussianity to the density contrast no matter the nature of what $\mathcal{R}$ is.

Overall, studying PBH collapse statistics using only a threshold value is crude, and a more robust approach is to use a compaction function, $\mathcal{C}(r,t)$, as a criterion for gravitational collapse [125]. The compaction function, which is related to the local mass excess in a system, also contains information about the shape of a perturbation, to which a threshold is shown to be significantly sensitive. In such a scenario, the collapse threshold would be identical to the value of the compaction function in the location where it is maximized [126], $\delta_c \equiv \mathcal{C}_{\max}(r_m,t)$. A perturbation will collapse whenever the maximum of the compaction function becomes the order of unity, or $\mathcal{C}_{\max}(r_m,t) \sim 1$. For the sake of simplicity, we proceed with considering $\delta > \delta_c$ as the collapse criterion.

The mass of the PBH at formation is of the order of the horizon mass at the crossing, since the fate of a perturbation is determined at the horizon reentry. Thus we can express the PBH mass at formation as

$$M_{\rm PBH}(t_{\rm fm}) = \gamma M_H|_{k=a\bar{H}} \ , \tag{1.6.1}$$

where $\gamma \simeq 0.2$ is the efficiency factor which depends solely on the equation of state at the time of horizon reentry [127, 128]. We can express the horizon mass as a function of the comoving scales. The advantage of doing so is that it becomes intuitive to map the formed PBH masses with how late their corresponding scales reentered relative to the CMB scales. Consequently, the horizon mass can be expressed as [129]

$$M_{\rm PBH}(k) = 150 M_\odot \gamma \left(\frac{g_*}{106.75}\right)^{-1/6} \left(\frac{k}{3\times 10^5 {\rm Mpc}^{-1}}\right)^{-2} \ , \tag{1.6.2}$$

where $g_*(t)$ is the relativistic degrees of freedom at $t = t_{\rm fm}$. Estimating the fractional energy density (relative to the total energy density) of the formed PBHs becomes quite straightforward if one assumes that the underlying primordial perturbations are Gaussian. In such a case, we can use the Press-Schechter approach to find out the PBH abundance [130]

$$\beta = \frac{\rho_{\rm PBH}}{\rho_{\rm total}} = \int_{\delta_c}^{\infty} d\delta P(\delta) \simeq \frac{1}{2}{\rm Erf}\left[\frac{\delta_c}{\sqrt{2}\sigma}\right]\Big|_{\delta={\rm Gaussian}} \ , \tag{1.6.3}$$

which is simply integrating the probability distribution function of the overdensity contrast, a statistical variable, $P(\delta)$, from its threshold value to an arbitrarily large value. A Gaussian overdensity results in an error function of the collapse threshold.

After its formation in the radiation era, the non-relativistic PBH energy density grows like $\rho_{\rm PBH} \propto a$ relative to the relativistic background energy density. This happens until the matter-radiation equality, so the mass fraction at equality is [131]

$$\beta_{\rm eq} = \beta_{\rm fm}\frac{a_{\rm eq}}{a_{\rm fm}} \ . \tag{1.6.4}$$

The mass fraction is a function of mass, so we have to integrate it over the entire possible PBH masses to get the total energy density of the PBHs at the equality

$$\Omega_{\rm PBH,eq} = \int_{M<}^{M>} d\ln M \beta_{\rm eq} \ . \tag{1.6.5}$$

The evolution from equality to today is not trivial, as it involves a period of matter dominance and a period of dark energy dominance, during which the PBH energy density will, respectively, stay constant and decay as a^{-3}. However, if we normalize the energy density function Eq. (1.6.5) with the dark matter density $\Omega_{\rm DM,eq}$ at equality itself, the ratio will not evolve after equality because both $\Omega_{\rm PBH}$ and $\Omega_{\rm DM}$ are non-relativistic. Therefore, one finds that the PBH abundance can be conveniently expressed normalized to the dark matter density at equality as

$$f_{\rm PBH}(M) = \frac{d\Omega_{\rm PBH}}{d\ln M}\frac{1}{\Omega_{\rm DM}}\Big|_{t_{\rm eq}} \ . \tag{1.6.6}$$

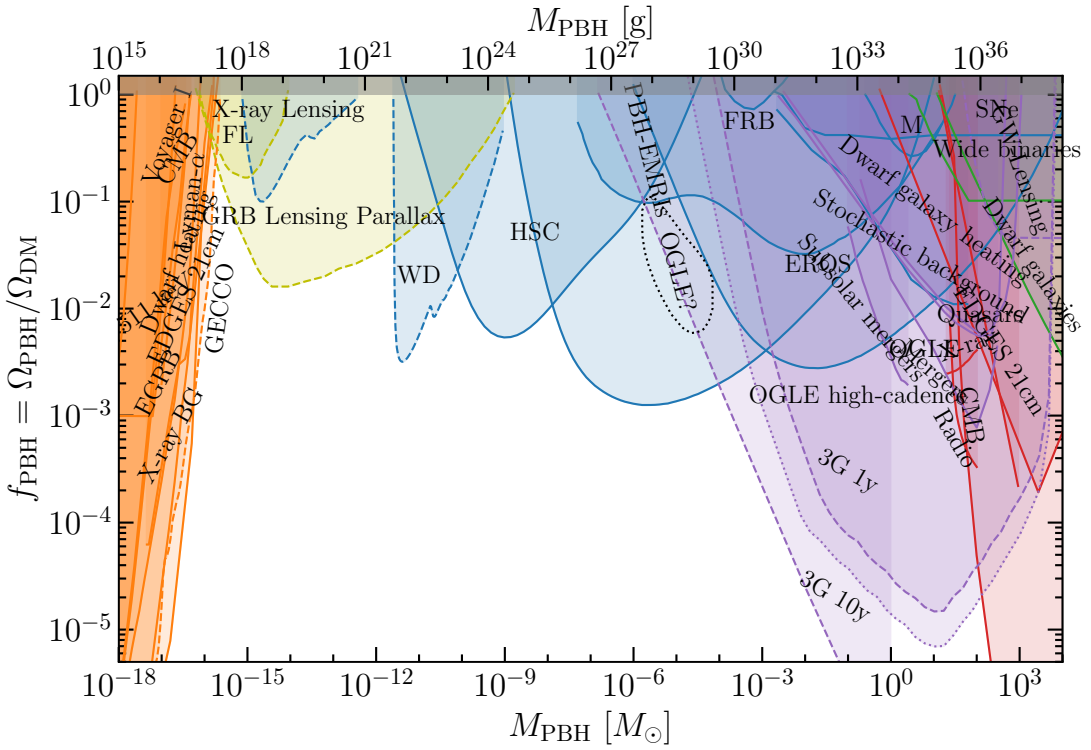

Figure 1.2: *A plot showing the current and forecasted constraints on the PBH energy density relative to the dark matter energy density as a function of the PBH mass at formation. Plotted using the Git repository [132], and the constraints correspond to the measurements from a broad range of experiments [105, 133–147].*

The parameter $f_{\rm PBH}$ is a common way to visualize the constraints on the PBH abundance from various experiments, as evident from Fig. 1.2. The Press-Schechter approach is perhaps the simplest way to model the PBH abundance, however, it might not be the most efficient one.

Peak Theory: The quantity $f_{\rm PBH}$ is very sensitive to the method used to compute the PBH abundance. Peak theory is a more accurate alternative to the Press-Schechter approach [72, 93, 148, 149]. In the Peak theory, the primary object to work with is the local maxima of the overdensity regions or the overdensity "peaks". The PBH abundance is then directly proportional to the number density of such peaks. For a Gaussian overdensity contrast smoothed over a physical scale R[1], one can define a generic spectral moment as

$$\sigma_q^2(R) = \int_0^\infty \frac{{\rm d}k}{k} k^{2q} W^2(k,R) \mathcal{P}_\delta(k) \ , \tag{1.6.7}$$

where $W(k,R)$ is the smoothing window function, $\mathcal{P}_\delta$ is the dimensionless power spectrum of the overdensity contrast δ, and q represents the order of the spectral moment. The zeroth spectral moment is the variance of the density fluctuations, $\sigma_0(R) = \sigma(R)$. For convenience, the density contrast is redefined as $p = \frac{\delta}{\sigma_0}$, which leads us to the following number density of such overdensity

[1]For the extension of the Peak theory to non-Gaussian density fluctuations, see[150].

peaks that will collapse to form the PBHs [151]

$$N(p_c) = \frac{1}{12\sqrt{3}\pi^2} \int_{p_c}^{\infty} \frac{\sigma_2^3}{\sigma_1^3} J(\sigma_0, \sigma_1, \sigma_2, p) e^{-\frac{p^2}{2}} dp \ , \tag{1.6.8}$$

where $p_c = \frac{\delta_c}{\sigma_0}$ is the redefined threshold, and

$$J(\sigma_0, \sigma_1, \sigma_2, p) = \int_0^{\infty} \frac{F(y)}{\sqrt{2\pi(1 - \left(\frac{\sigma_1^2}{\sigma_0 \sigma_2}\right)^2)}} \frac{1}{\exp\left\{\left[\frac{\left(y - \frac{\sigma_1^2 p}{\sigma_0 \sigma_2}\right)^2}{2\left(1 - \left(\frac{\sigma_1^2}{\sigma_0 \sigma_2}\right)^2\right)}\right]\right\}} \ , \tag{1.6.9}$$

$$F(y) = \frac{y^3 - 3y}{2} \left[\text{erf}\left(\sqrt{\frac{5}{2}} y\right) + \text{erf}\left(\sqrt{\frac{5}{8}} y\right)\right] + \tag{1.6.10}$$

$$\sqrt{\frac{2}{5\pi}} \left[\left(\frac{31y^2}{4} + \frac{8}{5}\right) e^{-5y^2/8} + \left(\frac{y^2}{2} - \frac{8}{5}\right) e^{-5y^2/2}\right] \ . \tag{1.6.11}$$

For practical purposes, one usually works with various approximations of the Peak theory by retaining some or all of the spectral moments. Finally, the PBH abundance can be obtained by integrating the peak number density over a given volume

$$\beta = \int_0^V N(p_c) dV \ . \tag{1.6.12}$$

Generally, the Press-Schechter approach has straightforward assumptions, such as spherical collapse, a linear overdensity profile, and ignorance of the profile's shape, which force it to underestimate the PBH abundance compared to the Peak theory. However, the Press-Schechter approach is still widely used when dealing with the PBH statistics owing to its simplicity.

1.7 Reheating to Recombination

Inflation cannot last forever, otherwise, the comoving perturbations would never reenter the horizon, thus preventing the formation of any kind of structures. Moreover, a smooth transition is required, which would ensure a peaceful transfer of energy stored in the field fluctuations to the density fluctuations of the standard model species, while also producing the standard model species. This mechanism is explained by the phase of reheating after inflation, which refers to the heating of the universe after the termination of inflation[2]. Towards the end of inflation, the inflaton has exhausted nearly all of its initial energy, and it sits at the bottom of the potential with a high kinetic energy [156].

The fast-oscillating inflaton features a damping behaviour due to the expansion of the universe. In the Lagrangian of the system, another field θ is introduced, signifying the presence of additional

[2]It is not mandatory that inflation is followed by reheating. There is a class of models called warm inflation, where the energy of the inflaton continuously dissipates into the radiation via interaction with other scalar fields or fermions, thereby, "warming up" the very early universe [152–154]. Towards the end of inflation, the universe is already filled with the thermal bath, which triggers the radiation-dominated era, without requiring the phase of reheating. Moreover, the origin of perturbations is attributed to thermal fluctuations rather than quantum fluctuations, and thermal dissipation also produces tiny tensor perturbations. See [155] for a recent review and current observational status on warm inflation.

species. As the inflaton interacts with the θ field owing to the coupling present in the Lagrangian, it loses its energy to this field, thereby creating new particles. The equation of motion then becomes [157]

$$\ddot{\phi} + (3H + \Gamma)\,\dot{\phi} + \frac{dV}{d\phi} = 0 \ , \tag{1.7.1}$$

where Γ is the interaction rate. Initially, reheating studies involved perturbative treatment of the interaction rate because the interaction rate dominates over the Hubble term in Eq. (1.7.1) only after the expansion of the universe has slowed sufficiently [158]. Hence, the rate of particle production increases gradually. It was later shown that such a perturbative treatment is too simplistic and does not account for the coherent nature of inflation, owing to which, a non-perturbative treatment using parametric resonance was introduced [159, 160].

After the end of reheating, the universe was filled with standard model relativistic species, including the family of bosons, quarks and anti-quarks, leptons and anti-leptons and possibly the yet-to-be-detected beyond standard model (BSM) species [161]. The reheating temperature at the beginning of the radiation era is too high and thus, all the particles are relativistic and in thermal equilibrium[3]. As the universe expanded, it diluted the radiation and cooled down gradually. At the temperature $T \lesssim 150$ GeV, the weak force and electromagnetic force separated due to the spontaneous breaking of electroweak symmetry. As a result of the Higgs mechanism, the W and Z bosons became massive, and photons were rendered massless.

Further cooling of the universe ($T \lesssim 150$ MeV) made it impossible for the quark and gluons to stay unbonded, and they merged to form the hadrons (baryons, mesons) and their anti-particles. This epoch also witnessed an event called Baryogenesis, which explains why the present universe has an abundance of baryons but almost no anti-baryons (since the baryon number conservation requires that the number of baryons and anti-baryons produced after reheating must be equal) [163]. Baryogenesis, believed to have happened at $T \sim 100\text{GeV} - 1\text{TeV}$ (assuming Electroweak baryogenesis, see [164]), required that the baryon number conservation was violated for a short duration that caused a slight excess of baryons, and the rest of the baryon-antibaryon pairs annihilated to form photons.

Until the temperatures $T > 1$ MeV, the three neutrinos $(\nu_\mu, \nu_e, \nu_\tau)$ along with their anti-particles were in equilibrium with the radiation. Below $T \lesssim 1$ MeV, neutrinos decoupled and started free streaming with negligible environmental interaction [165]. Post decoupling, neutrinos contributed independently to the effective relativistic degrees of freedom (N_{eff}) until they became non-relativistic at late times. Thus, we expect to see a cosmic neutrino background (CNB), but we are yet to observe it due to the weakly interacting and non-relativistic behaviour of the neutrinos [166].

Today, except for photons, only neutrinos are known to be relativistic, hence, $N_{\text{eff}} = 3$ according to the standard model of particle physics, corresponding to the three neutrino flavors. The total relativistic energy content of the universe can then be written as the energy stored in

[3]There is a huge uncertainty in the reheating temperature (T_{reh}) since we do not know the energy scale corresponding to inflation. The upper limit is $T_{\text{reh}} \lesssim 10^{15}$GeV, which comes from the overproduction of primordial gravitinos. The lower limit is $T_{\text{reh}} \gtrsim 4$MeV, which comes from the Big Bang Nucleosynthesis. For a review on T_{reh}, refer to [159, 162]

the photons plus the energy stored in neutrinos[4], such that

$$\rho_{\rm rel} = \rho_\gamma \left[1 + \frac{7}{8}\left(\frac{4}{11}\right)^{4/3} N_{\rm eff}\right] . \tag{1.7.2}$$

The actual theoretical value is slightly higher, $N_{\rm eff} = 3.046$, considering the non-instantaneous nature of neutrino decoupling [167, 168]. The measurements from Planck 2018 provides the constraint, $N_{\rm eff} = 2.99 \pm 0.17$, which is in alignment with the standard model predictions [5].

When the temperature dropped below the mass of electron and positron, i.e. $T \lesssim 0.5$ MeV, the pairs became non-relativistic and annihilated to form the radiation $e^+ + e^- \to \gamma$ except for the excess electrons left whose number density should be of the order of baryon excess after Baryogenesis to ensure charge neutrality [169].

The universe now had all the required species (electrons, protons and neutrons) to create the elements through Big Bang Nucleosynthesis (BBN) [170]. Once the temperature was below the binding energy [5] of the deuterium ($T \lesssim 2$ MeV), the neutron-proton pair could trap inside a nucleus to form deuterium $p^+ + n^0 \to D + \gamma$. The formation of a Helium nucleus requires Deuterium formation as an intermediate process, so when the population of Deuterium is sufficiently high, the probability of forming the Helium isotopes increases via the stepwise reaction

$$p^+ + n^0 \to D + \gamma \ , \tag{1.7.3}$$

$$D + D \to {}^3_2He + {}^1_0 n^0 \ , \tag{1.7.4}$$

$$D + D \to {}^4_2He + \gamma \ . \tag{1.7.5}$$

Additionally, heavier elements, such as lithium and beryllium, were produced in very small amounts. The BBN was a short-lasting process because the temperature and energy density dropped quickly, and the environment became unfavourable for further nuclear fusion to occur [171]. It becomes clear from the graph of binding energy per nucleon Fig. 1.3 that the helium nucleus is the most stable among the lighter nuclei. This is why helium was the second most abundant product of BBN after hydrogen [172]. The neutron density was too low, and the temperature kept dropping rapidly so that further nuclear fusion beyond lithium could not occur. BBN ended shortly after $T \sim 0.1$ MeV. The heavier elements were formed much later in the matter era when the cores of stars underwent nuclear fusion [173, 174].

After BBN, radiation still dominated the energy content of the universe; however, there was a tiny fraction of matter (light elements, such as hydrogen and helium) that was in thermal equilibrium with the radiation. The electron-positron production stops when the temperature drops below 0.1 MeV, and any remaining positrons annihilate with the electrons, leaving behind a small electron excess. The relative energy density of the baryonic and dark matter grows

[4] The total number of relativistic degrees of freedom at a given temperature (T) is represented by g_*, which is used in Eq. (1.6.2). The total relativistic energy is thus, $\rho_{\rm rel}(T) = \frac{\pi^2}{30} g_*(T) T^4$. The quantity g_* is a function of temperature and decreases with the expansion as more species decouple and become non-relativistic.

[5] Binding energy of an atom is the minimum energy required to dissociate the constituent neutrons and protons bound inside the nucleus. If a nucleus is bombarded with energy greater than its binding energy, it will break down into protons and neutrons. Conversely, when neutrons and protons join to form a nucleus, the energy equivalent to the binding energy is emitted in the process.

[6] Helium ($^4_2$He) and Oxygen ($^{16}_8$O) are exceptions in this trend because their proton/neutron numbers satisfy the magic numbers. In the nuclear shell model, the doubly magic nuclei are extremely stable because their nuclear shells are completely filled.

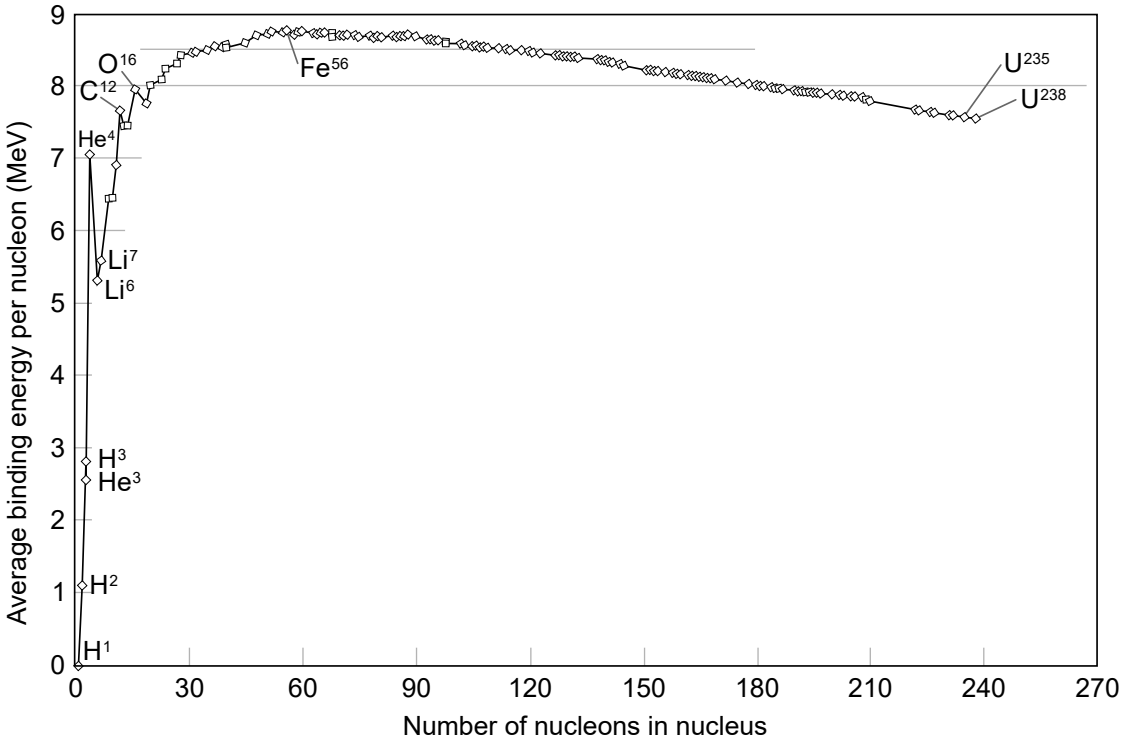

Figure 1.3: *Figure shows the binding energy per nucleon of various elements in the periodic table as a function of the number of nucleons inside the nucleus (equivalently, the mass of the nucleus). The curve shows an overall increasing binding energy per nucleon for lighter elements up to Sodium* $^{23}_{11}$Na *because the strong nuclear force increases with the number of protons and neutrons* [6]*. The increasing trend stabilizes the mass number* 30 *and remains effectively within the same factor until the mass number* 90*. This can be attributed to the fact that the proton-proton repulsive forces begin to become important and counterbalance the strong nuclear force. When the mass number is even heavier, the repulsive forces dominate over the strong nuclear force, so the curve follows a decreasing trend. Graph taken from Wikipedia public archive.*

with expansion, or $\frac{\rho_m}{\rho_\gamma} \propto \frac{a^{-3}}{a^{-4}} = a(t)$. Between the redshifts few $\times\, 10^8 < z <$ few $\times\, 10^3$, the energy exchange between matter and radiation undergoes various levels of efficiency based on how sustainable the photon-producing processes like Bremsstrahlung and double Compton scattering as well as the energy transfer processes like Compton scattering were. This epoch is important for the frequency spectrum of the CMB photons, as we will see in detail in Chapter 3.

At $T \sim 3$ eV or $z \simeq 3400$ the energy densities of matter and radiation equalize [175], that is, $\frac{\rho_\gamma}{\rho_m} \sim 1\Big|_{z=z_{\rm eq}}$. From then on, dark matter begins to dominate the universe's energy content. The origin of dark matter remains a yet-to-be-solved problem in the standard model of physics [176]. The ionization fraction of hydrogen, $I_e = \frac{n_e}{n_e+n_H}$ plays a primary role in driving the efficiency of the Compton scattering. Here n_X stands for the number densities of electrons (e), protons (p) and neutral hydrogen (H). For a system consisting of ionized gases, the ionization fraction is related to its temperature T by the well-known Saha equation given by [177]

$$\frac{I_e^2}{1-I_e} = \frac{1}{n_b}\left(\frac{m_e T}{2\pi}\right)^{3/2} e^{-\frac{E_0}{T}} \tag{1.7.6}$$

where $n_b = n_e + n_H$ is the baryon density assuming electric neutrality $n_p \approx n_e$. A fully ionized (neutral) system will have $I_e \to 1(0)$. $E_0 = 13.6$ eV is the ionization energy of hydrogen. Of course, Eq. (1.7.6) assumes a single-type transition, i.e. when an electron travelling from infinity is captured by a proton, it occupies the ground state of the neutral hydrogen. In reality, hydrogen can also be formed at excited states, and all possible combinations of excited states must be included in Eq. (1.7.6). A higher ionization fraction would mean that the gas has more free electrons that could scatter off the photons. It can be verified using Eq. (1.7.6) that when the temperature of the universe drops to $T \approx 0.3$eV, the ionization fraction becomes extremely small and hydrogen exists in the neutral state. With a similar argument, it can be confirmed that the neutralization of helium, which is the most abundant element after hydrogen, takes place at higher temperatures [177].

Thus, at $T_{\rm rec} = \mathcal{O}(0.3$ eV), the universe is filled with neutral atoms and photons can no longer find free electrons to scatter. This leads to the decoupling of the photons, and they free-stream after being scattered for the last time (the last scattering surface). The universe becomes transparent for the first time and this event is referred to as recombination ($z_{\rm rec} \sim 1100$). The recombination radiation, which fills up the whole sky, lies in the microwave frequency today. Hence, it is known as the Cosmic Microwave Background (CMB) radiation.

1.8 Cosmic Microwave Background

From the last scattering surface to the present day, the CMB has travelled with negligible interaction but a redshifted energy, $T_{\rm CMB} \propto 1/a$. It is easy to compute the present temperature of the CMB, $a_0 T_0 = a_{\rm rec} T_{\rm rec}$ or $T_0 = T_{\rm rec}/(1 + z_{\rm rec}) \approx 2.73\ K$ [178]. This has been verified up to a high precision by various experiments, and we know that $T_0 = 2.72548 \pm 0.00057\ K$.

However, this is not the complete picture. We know how the density perturbations (and possibly, also tensor perturbations) that exited the horizon during inflation reenter one by one after the end of inflation. All the perturbations that reenter the horizon before recombination are passed on to the CMB in the form of temperature anisotropies. These anisotropies are measured relative to the background with approximate magnitude $\frac{\Delta T}{T_0} \sim 10^{-5}$. Fig. 1.4 shows the temperature anisotropy map of the CMB from the latest dataset of the Planck satellite [5, 179].

The quantity $\Theta = \frac{\Delta T}{\bar{T}}$ [7] stores a tremendous amount of information about the universe, from the inflationary fluctuations to sound horizon at recombination and energy density of baryons. A sound horizon is created by the oscillations in the baryon-photon fluid, which propagate with the sound speed in the medium [8]

$$c_s^2 = \frac{\delta p_b + \delta p_\gamma}{\delta \rho_b + \delta \rho_\gamma}\ , \tag{1.8.1}$$

where the subscripts b and γ stand for baryons and photons respectively. The sound horizon is a crucial quantity that determines the amplitude and position of the acoustic peaks of the CMB angular power spectrum Fig. 1.5. For a given sound speed, the sound horizon at recombination is

[7] We have replaced the variable $T_0 \to \bar{T}$ to represent it as a background quantity.

[8] Specifically, these oscillations are sourced by a fight between the radiation pressure of the photons that pushes the fluid radially outwards, and the gravitational pull of the baryons, which acts radially inwards.

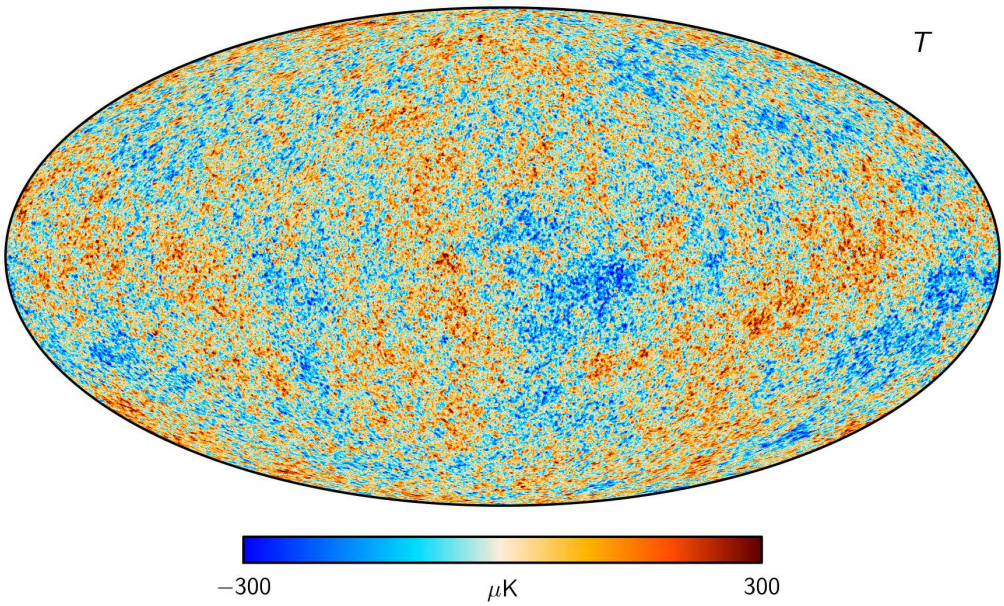

Figure 1.4: *A sky map of the temperature anisotropies in the CMB. The red spots represent a region with slightly higher temperature than the average, and the blue spots represent a region with slightly lower temperature than the average. It is evident from the color gradient that the maximum temperature variation between any two patches in the sky does not exceed* $6 \times 10^{-4} K$*. Figure taken from the ESA Planck archives.*

given by

$$r_s = \int_{z_{\rm rec}}^{\infty} \frac{c_s(z)}{H(z)} dz \ . \tag{1.8.2}$$

During recombination, these oscillations were interrupted by the gradual horizon crossing of the perturbations. Consequently, the temperature variation Θ would have scale-dependent compressions and rarefactions that would freeze at the end of recombination [9]. Additionally, the last oscillation just before the end of recombination would also freeze due to the free-streaming photons. These are referred to as Baryon Acoustic Oscillations and correspond to the physical scale 150 Mpc today [180].

The fact that we are measuring the temperature variation across the sky in all directions encourages us to take the variable Θ to Legendre space. We leave the rest of the details to Appendix A and directly express the following relation

$$\langle \Theta\Theta \rangle_{\vec{x},\hat{n}} = \int \frac{dk\, k^2}{(2\pi)^3} \sum_{\ell} 4\pi (2\ell+1) \Theta_\ell(k) \Theta_\ell(k) P_{\mathcal{R}}(k) \ . \tag{1.8.3}$$

[9] We shall see in Chapter 3 that the phenomenon of acoustic dissipation dampens these oscillations at smaller scales.

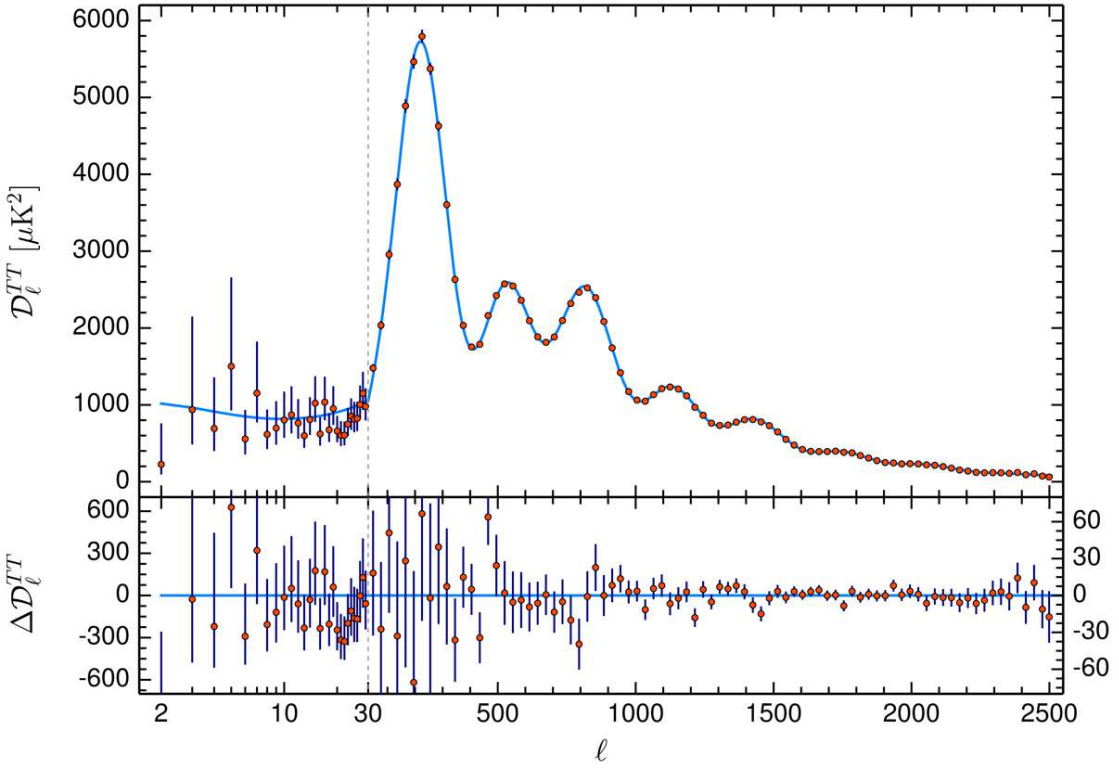

Figure 1.5: *The angular power spectrum of the CMB temperature anisotropies with a slight change of terminology $C_\ell \equiv \mathcal{D}_\ell$. The theoretical prediction made by ΛCDM is shown with the solid blue curve, and the observational data points are shown with the red dots. The vertical bars denote uncertainty in the measurement. At lower multipoles, the high uncertainty is introduced by the cosmic variance[10]. Picture taken from Planck 2018 results [5].*

The Θ's on the right-hand side of Eq. (1.8.3) are the transfer functions that transport the primordial perturbations to the temperature anisotropies. Thanks to the statistical isotropy, there is no overall direction dependency in the transfer functions. The anisotropies imprinted at the last scattering surface can be fully expressed as a sum of the spherical harmonics

$$\Theta(\hat{n}) = \sum_{\ell m} a_{\ell m} Y_{\ell m}(\hat{n}) \ , \qquad -m \leq l \leq m \ , \tag{1.8.4}$$

where we have kept only the direction dependency because we cannot measure the scale-dependency of Θ. By expanding the anisotropies in spherical harmonics, we have decomposed their total

[10]This comes from the fact that we can observe only one statistical realization of the observable universe (or, a single $C_{\ell,\text{obs}}$) and thus, we cannot obtain the theoretical expected value, C_ℓ. This introduces a high uncertainty in knowing the true value C_ℓ, and this uncertainty is expressed as the quantity $\frac{\langle (C_{\ell,\text{obs}} - C_\ell)^2 \rangle}{C_\ell^2} \equiv \sqrt{\frac{2}{2\ell+1}}$, also referred as the cosmic variance. It is noticed that the cosmic variance is inversely proportional to the multipoles. Hence, there is a large uncertainty in knowing the true C_ℓ at smaller multipoles, which explains the large error bars in Fig. 1.5.

strength into several multipoles (ℓ) whose coefficients are given by

$$a_{\ell m} = (-1)^{l+m} \int d\hat{n} Y_{\ell -m} \Theta(\hat{n}) \ . \tag{1.8.5}$$

The random variable $\mathcal{R}$ renders stochasticity to Θ, and this stochasticity propagates into the coefficients $a_{\ell m}$'s, summed over the scales. Assuming Gaussian initial conditions, the variance of $a_{\ell m}$ s stores all the required information about the temperature anisotropies, which is also referred to as the CMB angular power spectrum [34, 181]

$$C_\ell = \langle a_{\ell m} a^*_{\ell m} \rangle = \frac{1}{2\ell + 1} \sum_{-\ell \leq m \leq \ell} |a_{\ell m}|^2 \ , \tag{1.8.6}$$

$$= \int 4\pi \frac{dk}{k} \Theta^2_\ell (t_0, k) \mathcal{P}_\mathcal{R}(k) \ , \tag{1.8.7}$$

where the second step in the above equation can be obtained by substituting temperature anisotropies with the product of the transfer function and primordial curvature power spectrum using Eq. (A.3). The angular power spectrum can actually be observed in the CMB measurement, and we show it for reference in Fig. 1.5 taken from Planck's latest dataset. The observed CMB angular power spectrum predicts a nearly scale-invariant curvature power spectrum with the best-fit parameter and confidence intervals shown in Eq. (1.5.33).

CHAPTER 2

Stochastic Inflation

2.1 Brownian Motion and Langevin Equation

Before proceeding to the stochastic formalism, let us discuss the kinematics of random motion, which is most commonly studied in terms of Brownian motion [182]. Imagine a particle of mass m is suspended in a fluid with a viscosity proportional to the particle velocity v. The equation of motion is governed by the Langevin equation

$$\frac{dv(t)}{dt} = -\frac{1}{\kappa m}v(t) + \frac{1}{m}\xi(t) \ , \tag{2.1.1}$$

where κ is the mobility of the fluid, and $\xi(t)$ is the time-dependent random noise associated with the random forces acting on the particle. It is this noise term that introduces indeterminism to the variable (in this case, particle velocity) and makes it a stochastic variable having certain statistical properties. We will use the same notation for noise when studying stochastic inflation in the forthcoming subsections.

When the fluid is highly viscous, the Reynolds' number is much smaller than one [183]. In such a scenario, the particle moves slowly inside the fluid, and the time variation of the velocity can be ignored. This is referred to as the overdamped limit of fluid motion. In this limit, Eq. (2.1.1) reduces to first order stochastic differential equation

$$\frac{dX(t)}{dt} = \kappa\xi(t) \ , \tag{2.1.2}$$

$$X(t) = X(0) + \kappa\int_0^t \xi(t) \ . \tag{2.1.3}$$

Assuming ergodicity, we can obtain the mean of $X(t)$ by averaging over several realizations of the system Eq. (2.1.3)

$$\langle X(t) - X(0)\rangle = \kappa\int_0^t \langle\xi(t)\rangle \ , \tag{2.1.4}$$

$$= 0. \tag{2.1.5}$$

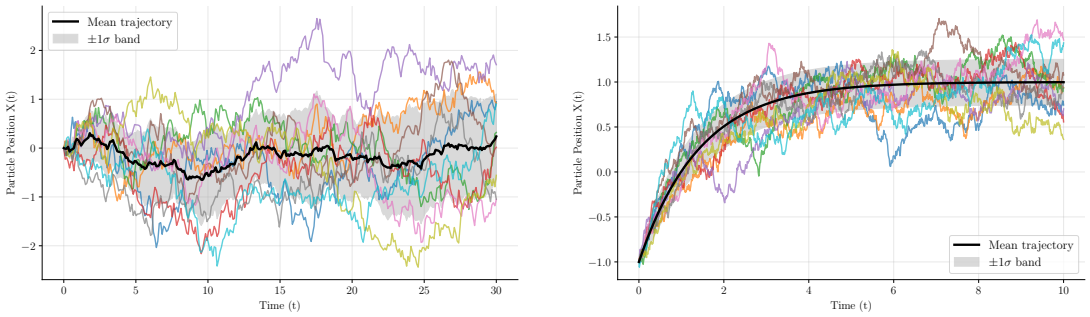

(a) **(b)**

Figure 2.1: ***Left Panel:*** *Motion of a particle in a box in the presence of indeterministic forces modelled as a Gaussian noise in Eq. (2.1.1). The ten trajectories shown in different colors are for ten different realizations.* ***Right Panel:*** *An ensemble of ten stochastic trajectories for a particle following the Ornstein-Uhlenbeck process. It is evident that after a long enough interval, the statistical mean of the system asymptotically approaches a long-term mean, which is unity in this case.*

Here, the noise is modelled as white Gaussian noise with a zero mean, and thus, the mean displacement of the particle is zero. It is easy to show that any additional deterministic force on the right-hand side of Eq. (2.1.1) would have directly shifted the mean displacement Eq. (2.1.5). Moreover, we assume that the noise follows a Markovian property, i.e. its present value is independent of its historical behaviour [184]. This translates to an uncorrelated noise in time $\langle \xi(t)\xi(t')\rangle = 2D\delta(t-t')$, where D is the diffusion coefficient. The variance in the displacement can then be obtained as

$$\langle (X(t) - X(0))^2 \rangle = \int_0^t \langle \xi(t)\xi(t')\rangle dt dt' \ , \tag{2.1.6}$$

$$= 2D \int_0^t \delta(t-t') dt dt' \ , \tag{2.1.7}$$

$$= 2Dt \ . \tag{2.1.8}$$

This is a characteristic Wiener process in which the variance grows proportionally with time. The left panel of Fig. 2.1 shows how a particle following a Brownian motion behaves for an arbitrary number of realizations. Invoking the overdamped condition might seem like an oversimplification, however, we will use the Brownian motion-characterized stochastic process to study inflaton dynamics during inflation, where the field rolls down slowly along the potential. Thus, this assumption is valid in the context of stochastic inflation.

Although not too relevant for stochastic inflation, it is also interesting to understand the mean reversion of a stochastic process. This happens only in the presence of a 'restoring force' in the standard SDE Eq. (2.1.1), which pushes the stochastic variable to converge to its average value infinitely in the future. This characteristic is modelled by adding the restoring force to the

deterministic part of the SDE, such that [185]

$$\frac{dX(t)}{dt} = -\Theta(\mu - X(t)) + \kappa\xi(t) \ , \tag{2.1.9}$$

$$X(t) = \mu - (\mu - X(t_0))e^{-\Theta(t-t_0)} + \kappa \int_0^t \xi(t)e^{-\Theta(t-t_0)} \ , \tag{2.1.10}$$

where $\Theta X(t)$ is the restoring force and t_0 is the initial time. The mean and variance of X are then [186]

$$\langle X(t)\rangle = \mu - (\mu - X(t_0))e^{-\Theta(t-t_0)}, \qquad Var(X) = \frac{\kappa^2}{2\Theta}(1 - e^{-2\Theta t}) \ , \tag{2.1.11}$$

$$\langle X(t)\rangle|_{t\to\infty} = \mu, \qquad Var(X)|_{t\to\infty} = \frac{\kappa^2}{2\Theta}. \tag{2.1.12}$$

It is evident that the particle position continues to fluctuate around the mean; however, as time progresses, there is an increasing probability that the position will approach its long-term mean value more closely. Finally, as time approaches infinity, the particle is expected to be found exactly at its mean position. Moreover, in this limit, the variance also reaches a steady value, inversely proportional to the strength of the restoring force. The higher the restoring force strength, the greater its mean-reverting ability; hence, the corresponding variance would be suppressed. Such mean-reverting stochastic processes find profound applications in Physics, Biology, Finance, and Computer Science and are referred to as Ornstein-Uhlenbeck (OU) processes [185]. The right panel of Fig. 2.1 shows the trajectories of a particle following an OU process.

While the Langevin equation (or OU process) tells us about the random behaviour of the particle position for a single realization, it is also possible to study the collective behaviour of the stochastic system directly using the Fokker-Planck equation. The Fokker-Planck equation controls the evolution of the probability distribution of $X(t)$ so that [187]

$$\frac{\partial P(X,t)}{\partial t} = \frac{\partial}{\partial X}\left[\mu(X,t)P(X,t)\right] + \frac{\partial^2}{\partial X^2}\left[2D(X,t)P(X,t)\right] \ , \tag{2.1.13}$$

which, for either Brownian motion or the OU process, takes the following forms

$$\frac{\partial P(X,t)}{\partial t} = \begin{cases} D\frac{\partial^2 P}{\partial X^2} \ , & \text{Brownian Motion} \ , \\ \Theta\frac{\partial[(X-\mu)P]}{\partial X} + D\frac{\partial^2 P}{\partial X^2} \ , & \text{OU Process} \ , \end{cases} \tag{2.1.14}$$

whose solutions are found to be [188]

$$P(X,t) = \begin{cases} \frac{1}{\sqrt{4\pi Dt}\ e^{-\frac{(X-X_0)^2}{4Dt}}}, & \text{Brownian Motion} \\ \frac{\Theta}{\sqrt{2\pi D}\ e^{-\frac{\Theta(X-X_0)^2}{2D}}}, & \text{OU Process (Stationary solution)} \end{cases} \tag{2.1.15}$$

wherein, the stationary solution refers to the long-term case when the variance has already stabilized to a constant value Eq. (2.1.11). It can be inferred that the particle displacement follows a time-dependent Gaussian distribution, whereas the OU process follows a Gaussian distribution only in the stationary limit.

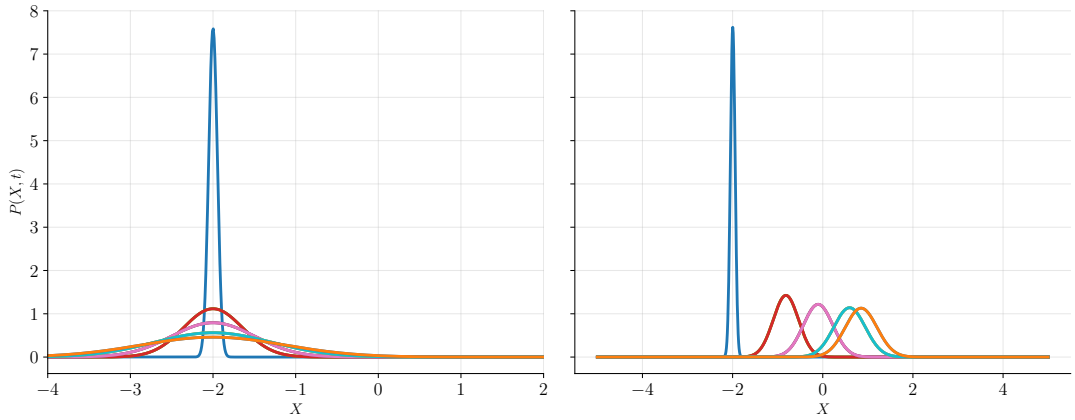

Figure 2.2: ***Left Panel:*** *Snapshots of solution to the Fokker Planck equation Eq. (2.1.13) for a particle following a Brownian motion. The PDFs of different colors represent snapshots of the solution at five different times $t = [0.0, 0.5, 1.0, 2.0, 3.0]$. Notice how the mean of the PDF remains unchanged, as the average over several realizations is independent of time. The variance Eq. (2.1.8), on the other hand, is a time-dependent quantity.* ***Right Panel:*** *Same as the left panel but for an Ornstein-Uhlenbeck process. The mean-reverting behaviour shown in Eq. (2.1.11) is clearly visible.*

2.2 Stochastic Approach to Inflation

An advantage of studying the curvature perturbations in the super-Hubble limit is that the statistical variable $\mathcal{R}_k$ can be treated as a classical quantity despite it being sourced by the quantum fluctuations of the inflaton. Essentially, as a perturbation becomes super-Hubble, the uncertainty in the field momentum becomes extremely small as the conjugate momentum is suppressed exponentially ($\pi \propto e^{-2N}$). Following Heisenberg uncertainty principle $\left[\delta\hat{\phi}, \delta\hat{\pi}\right] \geq \frac{h}{4\pi}$, the uncertainty in the field operator becomes very large, resulting in a squeezed shape in the phase space. This can be understood by quantifying the squeezing of the state in the Schrodinger picture, which can be represented as [189, 190]

$$|\psi\rangle = \exp\left\{-\left\{\frac{r_k}{2}\left(e^{2i\theta_k}\hat{a}^2 - e^{-2i\theta_k}\hat{a}^{\dagger 2}\right)\right\}\right\}|0\rangle \tag{2.2.1}$$

where $\hat{a}$ and $\hat{a}^\dagger$ are respectively, the creation and annihilation operators. The squeezing parameter r_k tells us exactly how much squeezing in phase space the state has undergone, and the squeezing angle θ_k shows the direction of squeezing. It can then be shown that the squeezing parameter, which starts as $r_k = 0$ at the beginning of inflation, reaches high values $r_k \gg 1$ at the super-Hubble scales (see, for example, [191]). This results in a highly squeezed phase-space configuration (see Fig. 2.3), and the expectation values of perturbations expressed as quantum operators closely resemble a statistical ensemble of the classical scalar field over many stochastic realizations [189, 192–195]

$$\langle\psi|\delta\hat{\phi}_k|\psi\rangle\Big|_{\delta\pi\to 0} = \langle\delta\phi_k\rangle_{\rm ens}\ . \tag{2.2.2}$$

Quantum decoherence is another contributor to the quantum-to-classical transition of inflationary perturbations. Consider a system composed of the superposition of two quantum states, $|\phi\rangle =$

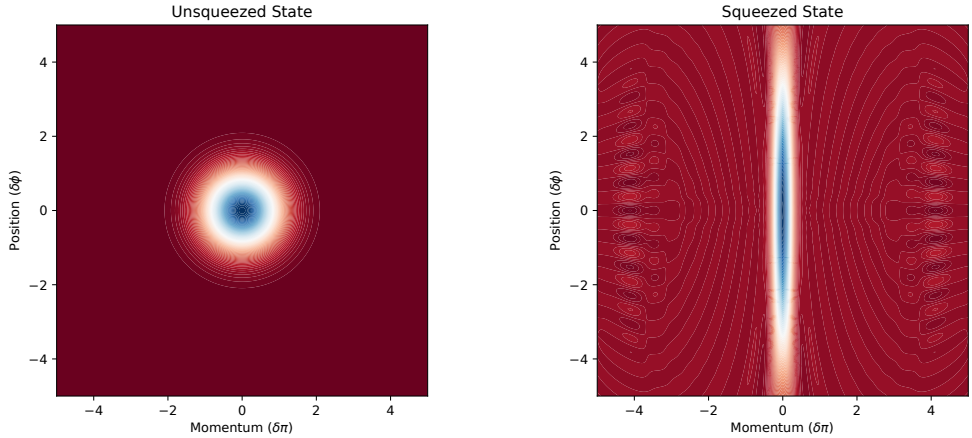

Figure 2.3: ***Left Panel:*** *The configuration in phase space of an arbitrary sub-Hubble perturbation before squeezing.* ***Right Panel:*** *The configuration of the perturbation shown in the left panel at super-Hubble scales. Due to squeezing along the momentum axis, the uncertainty in momentum becomes negligible, while the uncertainty in position becomes extremely large. The figure is created using the Python package Qutip.*

$|\phi_1\rangle + |\phi_2\rangle$. When the system (curvature perturbations, in this case) interacts with the other degrees of freedom that constitute the environment, there is an exchange of information between the system and the environment, mediated by the coupling strength. Such an interaction leads to quantum entanglement between the system and the environment and the superposition of the quantum states now looks like $|\phi\rangle = |\phi_1\rangle \otimes |\psi_{\rm env}\rangle + |\phi_2\rangle \otimes |\psi_{\rm env}\rangle$, where $|\psi_{\rm env}\rangle$ denotes the wavefunction of the environment constituents that could include gravitational waves, perturbations in other fields or additional degrees of freedom from beyond standard model. It can be shown that the off-diagonal elements of the density matrix, which represent the interference between different states, are suppressed exponentially. Consequently, the statistics of stochastic field variables can be explained with the classical probability distribution function.

When analyzing the inflationary fluctuations via a linearized perturbative approach, the equations governing the background are decoupled from the equations governing the perturbations. Any interaction can only be accounted for after going to at least the second order in perturbation theory. An alternative approach to couple the background and perturbations called the stochastic formalism, was carved out for a standard single-field slow roll model by Starobinsky [196] and developed for more complicated models in subsequent works [197–204]. The idea is to split the inhomogeneous universe into short wavelength (SW) modes and long wavelength (LW) modes. The scale that separates the two modes is usually kept significantly larger than the physical horizon and is referred to as the coarse-graining scale $k_{\rm cg}$ ($\gg (aH)^{-1}$). The quantum property of the scalar field is retained by the UV modes ($k > k_{\rm cg}$) and thus, each Fourier mode can be treated as a quantum harmonic oscillator that follows the equation of motion from quantum field theory. The IR modes, on the other hand, are the modes that have crossed the coarse-graining scale ($k < k_{\rm cg}$), which means that they are much larger than the horizon and have had sufficient time to classicalize. Hence, the IR modes are treated as classical variables and they satisfy the equation of motion of the homogeneous background.

The interaction between the classical background (IR modes) and quantum fluctuations (UV modes) is illustrated as follows: Initially, the modes emerge from very small scales, originating from local vacuum fluctuations at the onset of inflation. As the universe undergoes a de Sitter expansion phase, these modes are stretched out and at some point, become super-Hubble. Upon stretching further, they cross the coarse-graining scales and, while merging into the existing classical background, generate a "kick" to modify the evolution of this background. As we shall see, this kick is a central quantity in stochastic formalism, and it is generally modelled as white Gaussian noise.

Moving on to the mathematical formulation for stochastic formalism, the field and its velocity can be split into a short wavelength (SW) field and a long wavelength (LW) field such that

$$[\phi(x,N),\pi(x,N)] = \left[\bar{\phi}(N),\bar{\pi}(N)\right]\big|_{\rm LW} + [\delta\phi(x,N),\delta\pi(x,N)]|_{\rm SW} \ , \tag{2.2.3}$$

$$[\delta\phi(x,N),\delta\pi(x,N)]|_{\rm SW} = \frac{1}{2\pi^{3/2}}\int_{k>k_{\rm cg}} [\phi_{\mathbf{k}}(N),\pi_{\mathbf{k}}(N)]\, e^{-i\mathbf{k}\cdot x} d^3k \ , \tag{2.2.4}$$

$$\left[\bar{\phi}(N),\bar{\pi}(N)\right]\big|_{\rm LW} = \frac{1}{2\pi^{3/2}}\int_{k<k_{\rm cg}} [\phi_{\mathbf{k}}(N),\pi_{\mathbf{k}}(N)]\, e^{-i\mathbf{k}\cdot x} d^3k \ , \tag{2.2.5}$$

where the coarse graining scale is given by $k_{\rm cg} = \sigma aH$ and the field velocity is denoted by $\bar{\pi} = \frac{d\bar{\phi}}{dN}$. The classicalized LW field follows the Klein-Gordon equation for the scalar field in an expanding universe. On the other hand, the quantized SW modes can be explained using the Mukhanov-Sasaki equation

$$\ddot{\bar{\phi}}_{\rm LW} + 3\bar{H}\dot{\bar{\phi}}_{\rm LW} + \frac{\partial V}{\partial\bar{\phi}_{\rm LW}} = 0 \ , \tag{2.2.6}$$

$$\delta\ddot{\phi}_{\mathbf{k},SW} + 3H\delta\dot{\phi}_{\mathbf{k},SW} + \left[\frac{k^2}{a^2} + \frac{\partial^2 V}{\partial\phi^2_{\mathbf{k},LW}} - \frac{8\pi G}{a^3}\frac{d}{dt}\left(\frac{a^3\dot{\phi}^2_{\mathbf{k},LW}}{H}\right)\right]\delta\phi_{\mathbf{k},SW} = 0 \ . \tag{2.2.7}$$

The coarse-graining parameter σ should be sufficiently smaller than unity to ensure that r_k has become significantly large. A relatively large value of $r_k > \frac{1}{2}\cosh^{-1}(100)$ ensures that all the modes have classicalized by the time they cross the coarse-graining scale. This translates to a constant value of $\sigma = 0.01$. Of course, r_k varies with the wavenumber of the modes, and ideally, this should also be the case for σ. However, to keep things simple, we shall use the constant value of σ throughout this section. Further reducing the σ does not change the result since the growing solution of the already classicalized stochastic field does not evolve at very large scales, and the decaying solution has vanished.

This picture is accurate in the SR models, but not necessarily in the USR models. For example, the modes that cross the horizon during the USR phase consist of a constant mode and a growing mode. The choice of σ may be important, as the perturbations could continue to grow as long as the field remains in the USR regime. On top of that, due to the short-term rapid change in the primordial power spectrum at the USR scales, the squeezing tends to reverse itself, meaning that the perturbations may 'unsqueeze' after horizon crossing [205–208]. Although the decoherence of the modes due to entanglement with the environment prevents the unsqueezing of the modes, the decoherence rate plays a crucial role in determining how long the perturbation-environment interaction should occur to achieve an irreversible classical state.

While working with a numerical code, when simulating a high number of stochastic realizations of USR inflation, the fraction of such unsqueezing modes is smaller, and this issue can be overlooked

without significantly compromising the accuracy of the results [191, 209, 210]. For the sake of convenience, we will omit the subscripts LW/SW, except when we need them for clarity. After the coarse-grained variables $\left[\bar{\phi}, \bar{\pi}\right]$ are substituted in the Klein-Gordon equation Eq. (2.2.6), the second-order ordinary differential equation (ODE) decoupled into two first-order ODEs takes the following form

$$\bar{\phi}' = \bar{\pi} + \xi_\phi \ , \tag{2.2.8}$$

$$\bar{\pi}' = -(3-\epsilon)\bar{\pi} - V_{,\bar{\phi}}/H^2 + \xi_\pi \ , \tag{2.2.9}$$

where the derivatives have been switched so as to make the e-folding parameter N as the time variable, $\frac{d}{dN} = \frac{1}{H}\frac{d}{dt}$. We can perform the same change of variable and break-down into two first-order ODEs on the SW equation of motion Eq. (2.2.7) to get

$$\begin{aligned}\delta\psi_{\mathbf{k}}' = &-(3 + H'/H)\delta\psi_{\mathbf{k}} \\ &- \left(k^2/(aH)^2 + \bar{\phi}_{\mathbf{k}}'^{\,2}(3 + H'/H) + 2\phi_{\mathbf{k}}' V_{,\bar{\phi}}/H^2 + V_{,\bar{\phi}\bar{\phi}}/H^2\right)\delta\phi_{\mathbf{k}} \ ,\end{aligned} \tag{2.2.10}$$

$$\delta\phi_{\mathbf{k}}' = \delta\psi_{\mathbf{k}} \ . \tag{2.2.11}$$

The field and momentum noise are respectively, ξ_ϕ and ξ_π.

$$\xi_\phi(N) = \frac{1}{2\pi^{3/2}}\int \beta'(k - \sigma aH)\phi_k(N)e^{-i\mathbf{k}\cdot x}d^3k \ , \tag{2.2.12}$$

$$\xi_\pi(N) = \frac{1}{2\pi^{3/2}}\int \beta'(k - \sigma aH)\pi_k(N)e^{-i\mathbf{k}\cdot x}d^3k \ . \tag{2.2.13}$$

To separate the scales smaller and larger than the coarse-graining scale, generally a Heaviside step function $\beta(k)$ is used. This choice of the window function introduces a sharp slicing that simplifies the equations involved. For a step function, the contribution of the noise to the background evolution is thus instantaneous and a constant value.

In the SR scenario, the choice of the window function — whether a smooth transition, such as a Gaussian function, or a sudden step-like transition — is not essential, as the decaying mode dies out and the growing mode freezes almost immediately after the horizon exit. In the USR case, the super-hubble growth and the number of modes affected by the super-hubble growth depend on the duration of the USR regime. Hence, choosing a smoother window function would imply that the noises defined in Eq. (2.2.12) will be scale-dependent. The scale dependency would then render the Langevin equation Eq. (2.2.8) non-linear. Hence, the noise contribution would vary depending on the choice of the window function. An accurate way of computing the window function requires an in-depth analysis of decoherence and squeezing, which is out of the scope of this thesis. Instead, we will select the step function to split the SW and LW modes. In doing so, we are neglecting the correlations of the noise at different scales ([209, 211–213]).

We will employ the Bunch-Davies vacuum conditions as the initial conditions for the SW modes. Thus, the noise can be modelled as a Gaussian stochastic variable with $\langle\xi_\phi(N)\rangle = \langle\xi_\pi(N)\rangle = 0$. Upon quantizing the field and its conjugate momentum, $\left[\delta\hat{\phi}_{\mathbf{k}}(x,N), \delta\hat{\pi}_{\mathbf{k}}(N)\right] = \hat{a}_{\mathbf{k}}\left[\phi_k(N), \pi_k(N)\right] + \hat{a}_{\mathbf{k}}^\dagger\left[\phi_k(N), \pi_k(N)\right]$, we obtain the two-point correlation functions of Eq. (2.2.12)

[214, 215]

$$\langle 0 \left| \hat{\xi}_\phi(N_x)\hat{\xi}_\phi(N_y) \right| 0\rangle = \frac{d(\sigma aH)^3}{6\pi^2 dN} \left|\delta\phi_{\mathbf{k}}\right|^2\Big|_{k=\sigma aH} \delta(N_x - N_y) \ , \tag{2.2.14}$$

$$\langle 0 \left| \hat{\xi}_\pi(N_x)\hat{\xi}_\pi(N_y) \right| 0\rangle = \frac{d(\sigma aH)^3}{6\pi^2 dN} \left|\delta\phi'_{\mathbf{k}}\right|^2\Big|_{k=\sigma aH} \delta(N_x - N_y) \ , \tag{2.2.15}$$

$$\langle 0 \left| \hat{\xi}_\phi(N_x)\hat{\xi}_\pi(N_y) \right| 0\rangle = \frac{d(\sigma aH)^3}{6\pi^2 dN} \delta\phi_{\mathbf{k}}\delta\phi'_{\mathbf{k}}|_{k=\sigma aH} \delta(N_x - N_y) \ , \tag{2.2.16}$$

$$\langle \delta\phi^2 \rangle = \mathrm{Re}\left(\frac{\delta\phi_{\mathbf{k}}}{\delta\phi'_{\mathbf{k}}}\right) \langle \delta\pi^2 \rangle \ . \tag{2.2.17}$$

Thus, the noise correlators depend on the absolute magnitude of the perturbations, computed at the coarse-graining scale. Moreover, the field and momentum variables become almost perfectly correlated due to the squeezing effect. By definition, the perturbation variable is gauge-dependent, and so are the noise correlators. In general, the statistics of perturbations are studied in the spatially flat gauge, $Q_k = \delta\phi_k|_{\psi=0}$ whereas, our system of stochastic equations Eqs. (2.2.8) and (2.2.9) is a function of the N variable. As we have perturbed the total field and momentum variables with respect to N, keeping the lapse function zero in Eq. (1.5.2), we are explicitly working in the uniform-N gauge. It was shown in [39] that it is necessary to perform a change of gauge on the perturbation variables from spatially flat gauge to uniform N gauge before computing the noise correlators. In doing so, it is found that the correction to the noise coming from the gauge correction, which is related to the non-adiabatic part of the perturbations, is negligible in both attractor-type (SR) and non-attractor-type (USR) models. It was, however, noted from the numerical simulations performed in [191] that in certain cases of a non-attractor, the correction due to the gauge change cannot be disregarded.

To end this subsection, we highlight the recent advancements in the field of stochastic formalism. It has been extensively studied that the effects of quantum diffusion lead to the enhanced probability of large-amplitude perturbations. The non-Gaussian tail of the PDF of curvature perturbations has been obtained numerically by either simulating several stochastic realizations of the Langevin equation to generate a statistical distribution of the perturbations non-perturbatively (see next section) or directly extracting the PDF from solving the Fokker-Planck equation [191, 214, 216–220].

The non-perturbative approach combining stochastic inflation and ΔN formalism has become an attractive alternative to study the abundance statistics of PBHs. The exponential sensitivity of the PBH abundance to the tail of the PDF has become a big motivation for cosmologists to resolve the tail for better precision. Resolving a tail requires simulating many more rare realizations, or equivalently, a large number of total stochastic realizations. In this regard, developments have been made to reduce the computation time required to obtain the PDF, with a resolution extending deep into the tail, by introducing importance sampling to the system of SDEs [221–223]. Importance sampling is a technique widely used in statistics to efficiently sample the realizations that are otherwise rare to catch via direct sampling. Generally, importance sampling can be applied in two ways for a system governed by Brownian-type SDEs: Firstly, a bias can be manually introduced to the Langevin equation Eq. (2.2.8) that will affect only the drift term and shift the mean of the outcome in the (desired) direction of the tail of the PDF. The unbiased solution is then obtained by weighing out the biased solution to the SDE. In the second approach, sampling

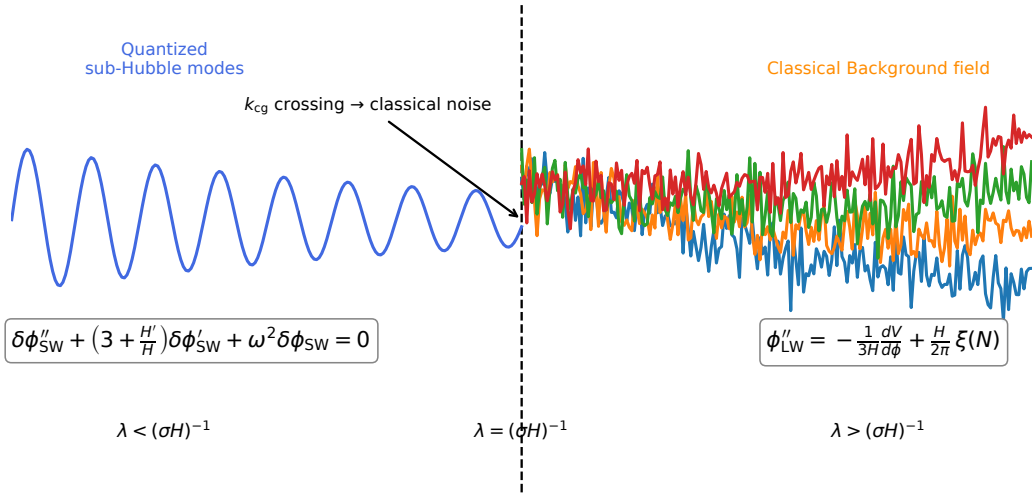

Figure 2.4: *The plot shows how coarse-graining works in stochastic inflation. The SW modes behave as quantum harmonic oscillators at $k > k_{cg}$, and render stochasticity to the classical background upon crossing the coarse-graining scale. The classical trajectories in different colors correspond to independent realizations. Please note that the scales are not intended for use as a reference.*

is performed from a proposal distribution whose standard deviation is broader than that of the target PDF. The associated weights are computed as the ratio of the target PDF and the proposal distribution, and then multiplied by the sample before solving the Langevin equation. In both approaches, it is crucial to select the bias function and the proposal distribution with extreme precaution, otherwise, the statistical properties of the solution would be altered.

Refs. [224–226] introduced a non-perturbative approach to calculate the curvature power spectrum. Since the non-perturbative method does not assume the linearized nature of perturbations, the obtained curvature power spectrum encodes the fully non-linear perturbation characteristics. It is known that quantum diffusion leaves a significant impact on the two-point statistics of curvature perturbations if the field violates the standard slow-roll conditions [227–231]. Finally, the quantum diffusion-induced primordial non-Gaussianity leads to the clustering of PBHs, which has been studied using numerical simulations [232].

2.3 Why a Non-Perturbative Approach?

The real space variance of the stochastic variable $\mathcal{R}$ relates to the dimensionless curvature power spectrum as

$$\left\langle \mathcal{R}^2(\vec{x}) \right\rangle = \int_0^\infty \frac{dk}{k} \mathcal{P}_\mathcal{R}(k) \ . \tag{2.3.1}$$

A perturbative treatment allows for expanding the locally inhomogeneous behaviour of cosmological variables around their homogeneous background counterparts, whose exact solutions are known.

A perturbative expansion of an arbitrary variable $A(x,t)$ can be written as

$$A(x,t) = \bar{A}(t)^{(0)} + A^{(1)}(x,t) + A^{(2)}(x,t) + ... + A^{(n)}(x,t) \ . \tag{2.3.2}$$

Note that $A(x,t)$ denotes a generic perturbed variable and has nothing to do with the lapse function defined in Eq. (1.5.2). The leading-order correction term is assumed to be significantly suppressed compared to the exact background solution, i.e. $\bar{A}(t)^{(0)} \gg A^{(1)}(x,t)$. Similarly, the next-to-leading order corrections are subdominant compared to the leading-order correction and so on, $A^{(n-1)}(x,t) \gg A^{(n)}(x,t)$. Depending on how vital the correction is (or how large the perturbations around the background are), we either keep the higher-order corrections or disregard them, as demonstrated in Section 1.5.

One could justify the small-perturbation assumption from the fact that the CMB anisotropies are $\sim \mathcal{O}(10^{-5})$. However, if one wishes to compute the statistics of $\mathcal{R}$ at the scales much smaller than k where PBHs are predicted to be produced, we expect $\mathcal{R}(k \gg k_*) \lesssim 10^{-1}$. This implies that the density fluctuations (which are proportional to the curvature perturbation) are almost as large as the background energy density at the PBH scales, and either the perturbation theory is unreliable or we must go beyond the first-order terms to account for as much of the full perturbation as possible. In the latter choice, it becomes burdensome to compute the variance of the curvature fluctuation as it involves terms like

$$\left\langle \mathcal{R}^2_{\rm tot}(\vec{x}) \right\rangle = \langle (\mathcal{R}^{(1)}(x,t) + \mathcal{R}^{(2)}(x,t) + ... + \mathcal{R}^{(n)}(x,t))(\mathcal{R}^{(1)}(x,t) + \mathcal{R}^{(2)}(x,t) + \mathcal{R}^{(n)}(x,t)) \rangle \ , \tag{2.3.3}$$

$$\approx \langle (\mathcal{R}^{(1)}(x,t)(\mathcal{R}^{(1)}(x,t) \rangle + 2 \langle (\mathcal{R}^{(1)}(x,t)(\mathcal{R}^{(2)}(x,t) \rangle + ... \ , \tag{2.3.4}$$

where there is no zeroth-order term since the curvature perturbation vanishes in the background. On top of this, we expect non-Gaussianity to play a bigger role beyond first order in perturbation theory owing to the coupling between the scales. This non-Gaussianity exists only in the tail of the PDF of $\mathcal{R}$, but this is enough to hugely impact the PBH statistics since it is exponentially sensitive to the tail Eqs. (1.6.3) and (1.6.6). Thus, we need to go beyond the two-point statistics (power spectrum) to capture the complete information about the curvature perturbations. The two higher correlators $\langle \mathcal{R}_{k_1} \mathcal{R}_{k_2} \mathcal{R}_{k_3} \rangle$ (bispectrum) and $\langle \mathcal{R}_{k_1} \mathcal{R}_{k_2} \mathcal{R}_{k_3} \mathcal{R}_{k_4} \rangle$ (trispectrum) provide information about the asymmetry stored in the tail of the PDF

This suggests how complicated it is to draw the picture of perturbations using the perturbative paintbrush when the perturbations have a large amplitude, and raises the need for a non-perturbative alternative. One of the most common non-perturbative treatments is the separate universe (SU) approach [18]. But first, let us understand gradient expansion, upon which the SU approach is based. As the comoving scales are stretched, the spatial gradients of the corresponding cosmological variables become negligible, $\frac{\partial}{\partial x^i} A(x^i,t) \to 0$. In other words, each point in real space is spatially uncorrelated at super-Hubble scales. The generalized FLRW perturbed metric can be split into $3+1$ using the ADM formalism [233] such that

$$ds^2 = (1+2A)dt^2 + a^2 e^{2\mathcal{R}(x,t)} \gamma_{ij} (dx^i + \partial^i B dt)(dx^j + \partial^j B dt) \ , \tag{2.3.5}$$

where the gradient of the scalar function $\partial^i B$ is a shift vector and γ_{ij} is the background 3-metric on the spatial hypersurface. Gradient expansion asks that the inhomogeneous quantities should be

expanded in the powers of the gradient parameter $\epsilon = \frac{k}{aH}$ (not to be confused with the slow-roll parameter) such that

$$\delta A(x,t) = \delta A^{(0)}(x,t) + \epsilon \delta A^{(1)}(x,t) + \epsilon^2 \delta A^{(2)}(x,t) + \dots \,, \tag{2.3.6}$$

where $\epsilon \ll 1$ at super-Hubble scales. It can be shown that at zeroth order in ϵ, the metric perturbations except for $\mathcal{R}$ perish ($\left[\partial^i B, A, \delta\gamma_{ij}\right] \propto \left[\mathcal{O}(\epsilon), \mathcal{O}(\epsilon^2), \mathcal{O}(\epsilon^2)\right]$) and the metric Eq. (2.3.5) is approximated as [125, 234, 235]

$$ds^2 = dt^2 + a^2 e^{2\mathcal{R}(x,t)} dx_i dx^j \delta_{ij} \,. \tag{2.3.7}$$

If we absorb the scale-dependent prefactor to the 3-metric in Eq. (2.3.7) and define a local scale factor $\tilde{a}(x,t) = a e^{2\mathcal{R}(x,t)}$, we spot that a given point x behaves as a flat FLRW metric and, is independent of any other spatial point. Moreover, at leading order in gradient expansion, the comoving curvature perturbation is conserved because $\dot{\mathcal{R}} = \mathcal{O}(\epsilon^2)$.

It is worth noticing the primary difference between the perturbative expansion Eq. (2.3.2) and the gradient expansion Eq. (2.3.6): the perturbative expansion relies on the smallness of the inhomogenities relative to the zeroth-order (background) term and one would be required to keep more and more terms beyond the leading order, particularly when the perturbations are large, to ensure that the term is as close to the actual curvature perturbation as possible. On the other hand, gradient expansion does not have such an assumption, so the curvature perturbation in Eq. (2.3.7) is, in fact, the total curvature perturbation. However, there is a caveat. Since we are expanding in the powers of ϵ, we essentially ignore the spatial gradients of the perturbed quantities while working at the zeroth order in gradient expansion. Considering that each point in the super-Hubble real space corresponds to a comoving wavenumber in Fourier space ($x \Leftrightarrow k$), it seems candid to neglect the spatial gradients as these scales correspond to the patches much larger than the horizon. However, this assumption overlooks the small-scale characteristics of the perturbations within these super-Hubble-independent patches. In this sense, each order correction in the gradient expansion brings in more information at the microscopic level, where spatial gradients are essential. In this section, we shall not consider such microscopic behaviour and work with the zeroth-order in gradient expansion (See [236] for the details). This sets up the motivation for the ΔN formalism, which we introduce in the following subsection. Although we can already get its intuition from the fact that when we redefine the scale factor by absorbing the curvature perturbation, what we did was store the information about the curvature perturbation corresponding to each point inside the local expansion rate.

2.4 Classical ΔN Formalism

The ΔN formalism has emerged as a powerful non-perturbative choice for studying the large-scale perturbations. The concept was first proposed by Starobinsky, who showed how large-scale perturbations are affected by the stochasticity from the small scales during a de Sitter phase [18, 196]. This was followed by notable works that applied this approach to solve for the one-point statistics of perturbations by analytically solving the Fokker-Planck equation [197, 237], and the study of non-linear evolution of perturbations using spatial gradient expansion in the ADM formalism [202, 238].

The first explicit set-up for ΔN formalism was used in [59] to compute the scalar spectral index. It was Ref. [239] that extended the application of ΔN formalism beyond Gaussianity and computed the primordial curvature bispectrum. In contrast, Ref. [240] developed the ΔN formalism for multifield slow-roll inflation. Before discussing the more recent developments in the ΔN formalism, let us first understand its mathematical formulation. We start by rewriting the generic expression for the perturbed FLRW metric [241–244]

$$ds^2 = (1+2A)dt^2 + 2a^2(t)\partial_\mu B dx^\mu dt + a^2(t)([1-2\psi]\,\gamma_{\mu\nu} + 2\partial_\mu\partial_\nu E)dx^\mu dx^\nu \ , \tag{2.4.1}$$

where we have switched from Greek indices to Latin indices in Eq. (2.4.1) to denote that we are working outside the ADM formalism. The goal is to find the behaviour of the curvature perturbation on a spatial (constant time) hypersurface and map the perturbation to some future spatial hypersurface. It makes sense to introduce a purely timelike 4-vector field v^x orthogonal to the spatial hypersurfaces

$$v^x = (1-A, -\partial^\mu B) \ , \tag{2.4.2}$$

and orthogonal to the spacelike hypersurfaces on which we wish to find the nature of the curvature perturbation. It is possible to obtain the perturbed expansion rate by differentiating v^x with reference to physical time to get

$$\Theta = \nabla_x v^x = 3H - 3\dot{\psi} + \nabla^2(\dot{E} - B) \ , \tag{2.4.3}$$

We can isolate the metric perturbation ψ and subtract the background expansion from Θ to keep only the perturbed part of the expansion rate $\Delta\Theta = \Theta - 3H$, such that

$$\dot{\psi} = -\frac{\Delta\Theta + \nabla^2(\dot{E} - B)}{3} \ . \tag{2.4.4}$$

Let us consider an initial spatial hypersurface $\Lambda(t_1)$ defined in the uniform density gauge (i.e., $\delta\rho = 0$). On this slice, we identify two well-separated regions, denoted as patches M and N, with respective physical sizes λ_M and λ_N, and a separation distance λ satisfying $\lambda \gg \lambda_M, \lambda_N$, as illustrated in Fig. 2.5. These regions can be treated as homogeneous and autonomous FLRW spacetimes on scales larger than the physical horizon. If the difference in the metric perturbation parameter between the two patches on the initial hypersurface is given by $\Delta\psi_1 = \psi_{M_1} - \psi_{N_1}$, then the corresponding difference in the metric perturbation parameter on a later spatial hypersurface $\Lambda(t_2)$ becomes

$$\Delta\psi_2 = \Delta\psi_1 - \Delta N \ , \tag{2.4.5}$$

where ΔN stores the differential expansion rate between the hypersurfaces M and N. Since we are working with the uniform expansion gauge, the field perturbation vanishes and the curvature perturbation $\mathcal{R}$ is equal to the metric perturbation ψ (in the absence of anisotropic stress, $\psi = A$ and there is only one metric perturbation). Thus, we can rewrite Eq. (2.4.5) as

$$\Delta\mathcal{R} = \Delta N \ , \tag{2.4.6}$$

with $\Delta\mathcal{R} = (\Delta\psi_M - \Delta\psi_N)$. We can infer from Eq. (2.4.6) that keeping track of the differential expansion rate across various independent super-Hubble FLRW patches directly gives us the

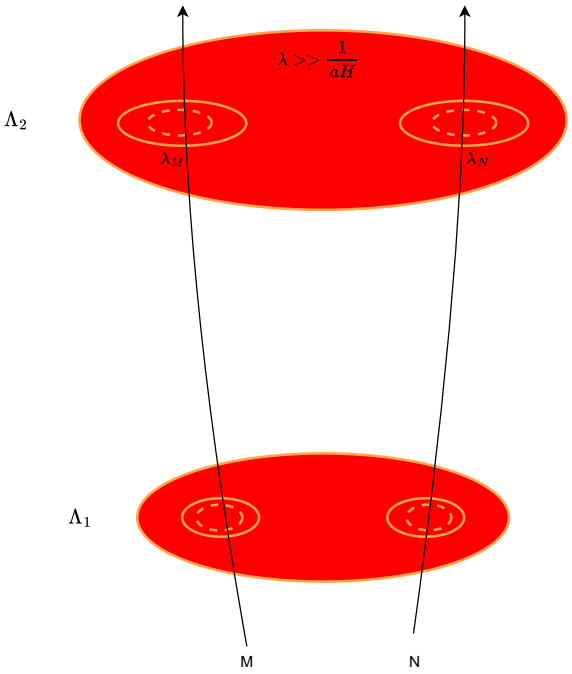

Figure 2.5: *A pictorial representation of worldlines of two independent locally FLRW universes.*

comoving curvature perturbation. It is easy to compute Eq. (2.4.6) in the standard SR scenario. Let us assume that the e-folding parameter is a function of both field and velocity, $N(\bar{\phi}, \bar{\pi})$. The differential element of N is

$$\delta N = \frac{\partial N}{\partial \bar{\phi}} \delta\bar{\phi} + \frac{\partial N}{\partial \bar{\pi}} \delta\bar{\pi} \ . \tag{2.4.7}$$

At the leading order in SR approximation, the kinetic energy is negligible compared to the potential energy $\frac{1}{2}\dot{\bar{\phi}}^2 \ll V(\bar{\phi})$, and hence, the variation in kinetic energy can considered minuscale in comparison with the variation in the field. In other words, we can neglect the second term in Eq. (2.4.7)

$$\delta N \simeq \frac{\partial N}{\partial \bar{\phi}} \delta\bar{\phi} \ , \tag{2.4.8}$$

$$\mathcal{R} = \delta N = \frac{1}{\sqrt{2\epsilon}} \delta\bar{\phi} \ . \tag{2.4.9}$$

From this, we can compute the dimensionless curvature power spectrum

$$\mathcal{P}_{\mathcal{R}}(k)|_{k=\sigma aH} = \frac{k^3}{2\pi^2}\langle\mathcal{R}(k)\mathcal{R}(k')\rangle\delta(k-k') \ , \tag{2.4.10}$$

$$= \frac{k^3}{2\pi^2}\frac{1}{2\epsilon}\langle\delta\phi_k\delta\phi_{k'}\rangle\delta(k-k') \ , \tag{2.4.11}$$

$$= \frac{1}{2\epsilon}\,\mathcal{P}_{\delta\phi}|_{k=\sigma aH} \ , \tag{2.4.12}$$

$$= \frac{1}{4\pi^2}\frac{H^2}{2\epsilon}\bigg|_{k=\sigma aH} \ . \tag{2.4.13}$$

In the last two steps, we used the results from the linear perturbation theory Section 1.5. The subscript below the curvature power spectrum denotes that it is computed at the crossing of the coarse-graining scale $k = k_{\rm cg}$. As expected, the non-perturbative power spectrum coincides with the perturbative power spectrum Eq. (1.5.27) in the slow-roll limit. Even though the perturbative power spectrum is calculated immediately after the horizon exit, the modes are essentially frozen during the interval $N(k = aH)$ to $N(k = \sigma aH)$. In this section, we have utilized the 'Classical ΔN formalism' and found that we can successfully reproduce the perturbative power spectrum.

Thus, we conclude that the separate universe approach applied with the classical ΔN formalism agrees with the linear perturbation theory at zeroth order in the gradient expansion. Moreover, since we did not invoke the quantum diffusion effects while deriving Eq. (2.4.13), we can also deduce that the stochasticity of the SW modes plays a negligible role in the SR limit. We shall use the Stochastic ΔN formalism when we come back to study non-perturbative statistics in the USR model in Section 2.6.2.

Despite being a widely used approach, there are certain limitations of the ΔN formalism that have been studied, particularly when going beyond standard SR models. The non-vanishing nature of the non-adiabatic perturbations makes it important to account for the spatial gradients [245, 246] in the events of sudden transitions. In the non-attractor models, during the SR⇔USR transition, the power spectrum could be as steep as $n_s - 1 = 3$ or $\mathcal{P}_{\mathcal{R}} \propto k^3$ (but no steeper than $n_s - 1 = 4$, see [205]). Although the classical ΔN formalism correctly computes the perturbations statistics in the SR as well as in the USR regimes, one needs numerically-matched corrections to account for the non-linear behaviour of $\mathcal{R}$ during the sudden transitions.

It has been shown that the perturbative curvature power spectrum in the USR regime agrees with the one computed with the stochastic ΔN formalism only at the zeroth order in the SR parameters [229]. The reason is that the Langevin equation Eqs. (2.2.8) and (2.2.9) upon linearization does not reproduce the Mukhanov-Sasaki equation Eq. (1.5.10) in the super-Hubble limit. If one properly accounts for the momentum constraint in the stochastic approach, the linearized Langevin equation correctly reduces to the Mukhanov-Sasaki equation [236, 247].

There have been some instances to extend the classical ΔN formalism in order to generalize it. For example, Ref. [248] considers each super-Hubble patch as an independent non-Flat FLRW universe and assigns a local value of spatial curvature to each patch. This curvature takes into account the corrections to $\mathcal{R}$ from spatial gradient at order $\mathcal{O}(k^2)$. Such corrections are essential in the beyond SR models where $\dot{\mathcal{R}} \neq 0$ even much after Hubble crossing. Another example is an alternative method called the "δM formalism" has also been proposed, which computes the evolution of the tensor perturbations orthogonal to the spatial hypersurfaces by observing the

changes in the Euclidean metric [249]. The ΔN formalism has also been discussed in the case of multi-field inflation at $\mathcal{O}(\epsilon^2)$ in spatial gradients [250].

2.5 Stochastic ΔN Formalism

2.5.1 Derivation

In the previous section, we underlined the need for a non-perturbative approach and how the classical ΔN formalism uses the SU approach to treat the long-wavelength perturbations. In this section, we will incorporate the effects of quantum diffusion into the classical ΔN formalism to understand the small-scale and large-scale correlation non-perturbatively, which is referred to as the stochastic ΔN formalism.

To begin with, the system of Eqs. (2.2.10) and (2.2.11) is used to evolve the SW modes, starting from the Bunch-Davies initial conditions. Simultaneously, the homogeneous and classicalized part of the coarse-grained field is evolved using Eqs. (2.2.8) and (2.2.9), also with some initial conditions. Since we are dealing with second-order ODEs, we require two sets of initial conditions, one for each statistical variable $[\bar{\phi}, \bar{\pi}]$ and $[\delta\phi, \delta\psi]$. Until the largest mode crosses the coarse-graining scale, the background evolves unaffected by quantum diffusion as the noises are off. Once it crosses $k_{\rm cg}$, the amplitude of the perturbation is used to compute the corresponding noise correlators using Eqs. (2.2.14) to (2.2.17). From this moment, the background equations achieve stochasticity because of the noise.

In the same way, smaller modes will also contribute as noise upon crossing $k_{\rm cg}$ and change the trajectory of the classical scalar field. In the context of a numerical simulation, noise refers to a random value drawn from a Gaussian distribution whose variance is determined at the moment of coarse-graining crossing. The system is designed to evolve until it reaches the final configuration N_f, which in this case corresponds to the end of inflation. Clearly, the spatial hypersurface for N_f will not coincide with the spatial hypersurface corresponding to $\bar{N}_f$. We employ the ΔN formalism to compute the comoving curvature perturbation from the difference in the expansion rate recorded at the stochastic final hypersurface to the classical one.

It becomes evident that we are required to perform the first passage time (FPT) analysis when the scalar field reaches the global minimum of the potential for the first time. To capture the statistics of ΔN (or, equivalently, $\mathcal{R}$), we need to generate several stochastic realizations. First, we compute the correlators of $\mathcal{R}$ using the FPT analysis and the ΔN formalism, and then, we construct an algorithm to implement this in a numerical simulation. We are interested in catching the scalar field value when it crosses the final time slicing for the first time, so that[11]

$$\phi_{\rm FPT}(\bar{N}) = \phi_f \ . \tag{2.5.1}$$

Recall that we are working in the uniform expansion gauge, where the lapse function vanishes. This implies that the local time is an unperturbed quantity, the same as the cosmic time. This is why we have not perturbed the e-folding number N starting from Section 2.2. Assuming each

[11] Since the Gaussian noise $\xi(x)$ has vanishing moments greater than the variance, it is symmetric along $x = 0$, owing to which there is equal probability of the noise in negative and positive direction. A negative noise in the final time step might push the field back into the attractor regime. However, in the FPT analysis, this effect is ignored, and the simulation stops after the first time the crossing occurs.

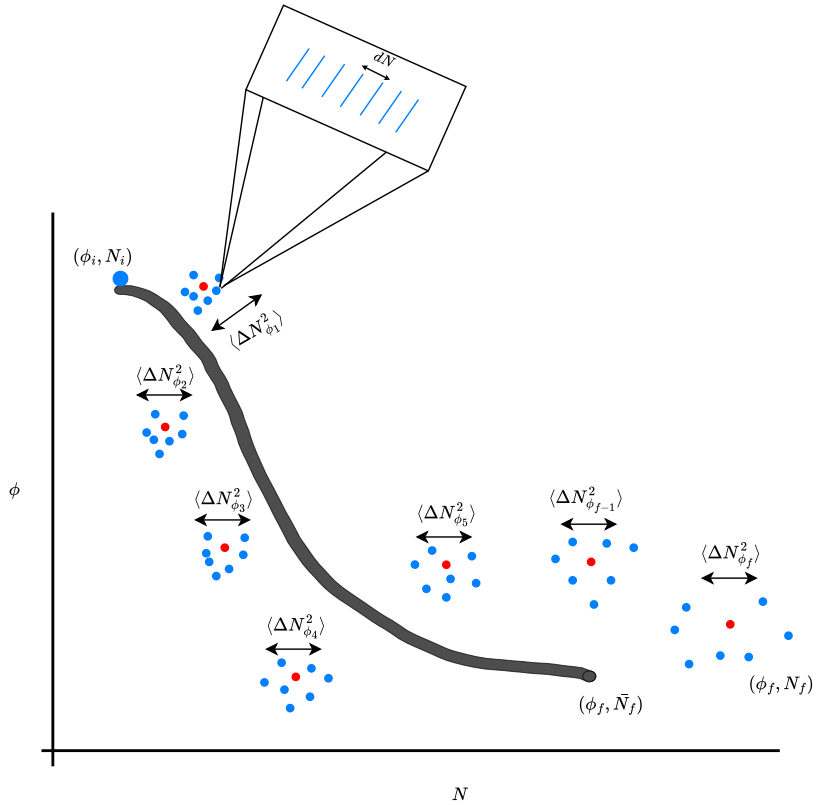

Figure 2.6: *A magnified inflaton-trajectory curve which shows how the stochastic noise from quantum diffusion deviates the paths of the field and the statistical ΔN at each point is used to construct a non-perturbative curvature power spectrum using the algorithm explained in Section 2.5.2.*

point in real space is a separate universe in the long-wavelength limit, we invoke the ΔN formalism and perform the Fourier transform of the curvature perturbation

$$\int_0^\infty dk \mathcal{R}_{\mathbf{k}}(N) e^{i\mathbf{k}\cdot x} = \int_0^\infty dk (N_{\mathbf{k}} - \bar{N}_{\mathbf{k}}) e^{i\mathbf{k}\cdot x} = \int_0^\infty dk \Delta N_{\mathbf{k}} e^{i\mathbf{k}\cdot x} \ , \tag{2.5.2}$$

$$\mathcal{R}_{\mathbf{k}}(N) = \Delta N_{\mathbf{k}} \ . \tag{2.5.3}$$

Because the diffusion terms in the Langevin Eqs. (2.2.8) and (2.2.9) are Gaussian with zero mean, the average or the first moment of the stochastic quantity $N(\phi, \pi)$ overlaps with its value in the classical trajectory, or $\langle N(\phi, \pi) \rangle = \bar{N}(\bar{\phi})$. It is impractical to apply the stochastic ΔN formalism analytically to even the simplest inflation models. Therefore, we run a large number of stochastic realizations using the numerical algorithm introduced in Fig. 2.7 to get a distribution of the

recorded end-of-inflation e-fold $N_f = N(\phi_{\rm FPT})$. The variance of N_f is expressed as

$$\begin{aligned}\langle \Delta N^2_{\mathbf{k}} \rangle &= \langle (N_{f,\mathbf{k}} - \bar{N}^2_{f,\mathbf{k}} \rangle \ , \\ &= \langle N^2_{f,\mathbf{k}} - 2\bar{N}_{f,\mathbf{k}} N_{f,\mathbf{k}} + \bar{N}^2_{f,\mathbf{k}} \rangle \ , \\ &= \langle N^2_{f,\mathbf{k}} - \bar{N}^2_{f,\mathbf{k}} \rangle \ , \end{aligned} \tag{2.5.4}$$

and using Eqs. (2.5.3) and (2.5.4) the dimensionless curvature power spectrum is obtained as

$$\langle \Delta N^2_{\mathbf{k}} \rangle = \int_{k_i}^{k_f} \frac{dk}{k} \mathcal{P}_{\mathcal{R}}(k, \bar{N}) \ , \tag{2.5.5}$$

where, the largest mode k_i starts evolving as soon as the numerical simulation starts and crosses the coarse-graining scale first. The mode k_f is the final mode to cross $k_{\rm cg}$, which means that every mode in the simulation between the interval $[k_i, k_f]$ uniquely deviates the individual super-Hubble FLRW patch from its classical evolution when it crosses $k_{\rm cg}$. Thereafter, the mode classicalizes and merges into the background. To get the power spectrum as the subject, we differentiate Eq. (2.5.5) with respect to $\bar{N}$ with the help of the Leibniz rule

$$\left.\frac{d\langle \Delta N^2_{\mathbf{k}} \rangle}{d\bar{N}}\right|_{\bar{N}=\ln(k_{\rm f}/k)} = \mathcal{P}_{\mathcal{R}}(k, \bar{N})\big|_{\bar{N}=\ln(k_{\rm f}/k)} + \int_{k_i}^{k_f} \left(\frac{\partial \mathcal{P}_{\mathcal{R}}(k, \bar{N})}{\partial \bar{N}}\right) \frac{dk}{k} \ , \tag{2.5.6}$$

where we have omitted the leading order correction from the SR parameter i.e. $k\frac{d}{dk} = \frac{1}{1-\epsilon}\frac{d}{dN} \approx \frac{d}{dN}$. The subscripted variables are calculated at the instant $k_f(N) = \sigma a(N) H(N)$. We notice certain interesting things about Eq. (2.5.6)

- The second term on the right-hand side (time-dependent term) vanishes in the SR limit because the growing mode in the curvature perturbations becomes frozen immediately after the horizon-exit. Consequently, its time variation will have no contribution when the corresponding mode reaches $k_{\rm cg}$. In this case, the differentiation of the variance of ΔN with $\bar{N}$ overlaps with the curvature power spectrum (analytical power spectrum).

- If an inflation model features a regime that violates the SR approximation, such as an USR regime or a bump in the potential, the growing solution of $\mathcal{R}$ does not freeze after Hubble crossing. Depending on the duration of the USR regime, the modes may continue to evolve well beyond $k_{\rm cg}$ crossing. Consequently, the time-dependent term becomes crucial, and its importance depends on the scales (the mode staying in the USR for the longest will be the most affected and vice versa).

- This is a purely mathematical anomaly that arises from working in Fourier space. We will see in Section 2.6.1 that it is trivial to work with the probability distribution function of ΔN as it is defined in real space. The real-space variance in this case can be easily computed by subtracting the square of the expected value of the variable from the expectation value of the squared variable $\mathrm{Var}(X) = E(X^2) - (E(X))^2$. On the other hand, when we perform the time differentiation after taking the quantities to the Fourier space, the time dependence of $\mathcal{P}$ gets separated due to the product rule [226, 247, 251].

- It is unclear how to revive this term in a numerical simulation, as one needs the derivative of the power spectrum before solving Eq. (2.5.6), and this term also varies with the coarse-graining scale. The latter adds a bit of non-reliability to this term because the two different choices of $k_{\rm cg}$ would give rise to two different power spectra, which is not physical.
- Finally, if the power spectrum has sharp features (sudden transitions or steep tilts), this term becomes significant as it stores the scale dependence of the variance in Fourier space. We will come back to this issue in Section 2.6.2.

2.5.2 Numerical Implementation

We present the flowchart of algorithm created for numerically simulating the stochastic realizations for a single-field inflation, and thereby constructing the non-perturbative statistics of perturbations, in Fig. 2.7. The list of abbreviations used in the flowchart is as follows:

- M: Model of Inflation
- ICs: Initial Conditions
- BG: Background
- Pert: Perturbations
- MS Eq.: Mukhanov-Sasaki Equation
- LE: Langevin Equation
- n_R: Number of stochastic realizations
- PDF: Probability Distribution Function
- FPT: First Passage Time

Precomputed Background: In Fourier space, the SW field is decomposed into independent modes, with the associated wavelength $\frac{2\pi}{k}$. Each mode acts as an independent degree of freedom whose equation of motion is given by the Mukhanov-Sasaki equation. When implementing such a system, which has 'n' degrees of freedom, the Mukhanov-Sasaki equation has to be solved $2n \times \frac{dN}{N}$, where dN is the time step of the system running from 0 to N. When a mode crosses the coarse-graining scale, $k = k_{\rm cg}$, the noise correlators are computed from the corresponding amplitude of the perturbations.

A truly stochastic system is non-Markovian, in the sense that the evolution of a mode k_i depends on all the modes larger than k_i or, $\delta\phi_{k_i} \propto f(\delta\phi_{k_{i-1}}, \delta\phi_{k_{i-2}}, \delta\phi_{k_{i-3}}, ..., \delta\phi_{k_0})$. To understand this, we can look at the set of Eqs. (2.2.8), (2.2.9) and (2.2.12): Each time a SW perturbation crosses the coarse-graining scale, it contributes to the background evolution as an instantaneous random noise. Now, for the modes that cross the coarse-graining scale afterwards, the background quantities would be $\left[\bar{\phi}^{\sum_0^{i-1} S_{k_j}}(N), \bar{\pi}^{\sum_0^{i-1} S_{k_j}}(N)\right]$ rather than $\left[\bar{\phi}(N), \bar{\pi}(N)\right]$ where the superscript represents the summed stochasticity introduced by the preceding modes. This is expected as, even though squeezing has classicalized the perturbation, it still has a large uncertainty in the spatial direction, and hence a stochastic variable.

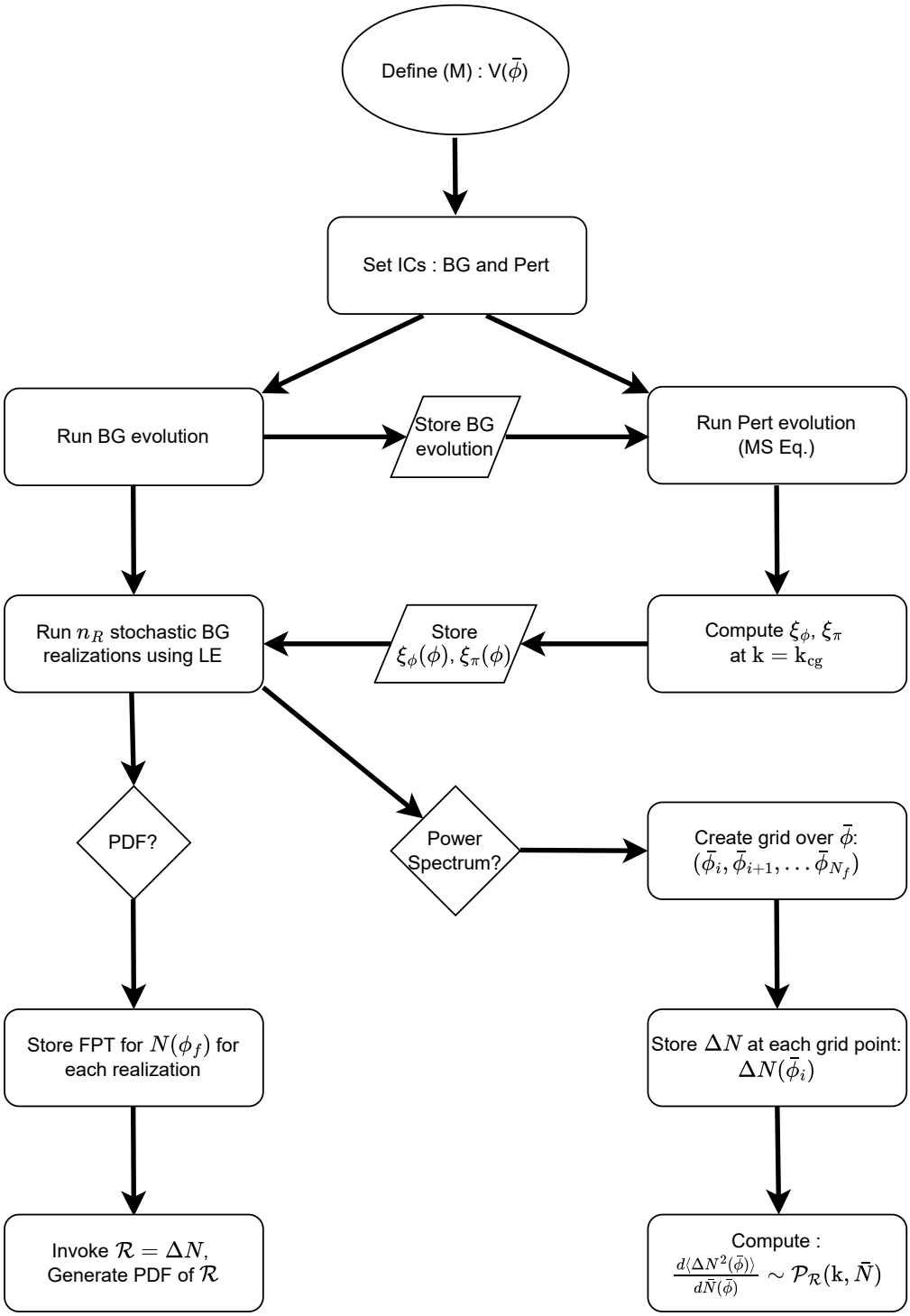

Figure 2.7: *Algorithm to numerically simulation the Stochastic ΔN formalism and generate the Probability Distribution Function, and the curvature power spectrum. The associated abbreviations are listed in this section.*

In terms of a numerical simulation, such a stochastic system would need to perform approximately $\left(2n \times \frac{dN}{N} + 2n \times \frac{dN}{N} + 2R \times \frac{dN}{N}\right)$ integrations. The first term arises from solving the equations of motion for the perturbations, while the second term stems from the fact that, corresponding to each mode crossing $k_{\rm cg}$, the stochastic background must be evolved simultaneously. This causes a backreaction of the kicks through the background. Finally, assuming we want "R" realizations to study the statistics of the associated quantities, the third term comes from simulating the R stochastic realizations. This approach has been applied in the simulations carried out on various single-field SR and USR models in [191, 216, 252–254].

A more straightforward approach, on the other hand, involves omitting the non-Markovian nature of the noise by computing the noise correlators on a fixed background, followed by simulating the stochastic realization via the inclusion of the noise correlators found on the precomputed background. Of course, the computation is less expensive in this case because the background equations have to be simulated only once corresponding to the fixed noise correlators and the method would need to perform approximately $\left(2n \times \frac{dN}{N} + 2 + 2R \times \frac{dN}{N}\right)$ integrations. The 'precomputed background' approach has been shown to agree reasonably well with the fully stochastic results, at least for the two-point statistics of the perturbations [222, 255, 256].

This is not difficult to apprehend: In the attractor regime, noise magnitude is suppressed compared to the deterministic term (background quantities), so the variation in a stochastic realization is not too far from the mean value, which overlaps with the classical trajectory. Thus, choosing to disregard the backreaction of the noise offers an excellent approximation of the otherwise non-Markovian process. This is true even for an USR regime, provided that it does not last for a long duration.

In an extremely rare instance, we expect a large kick that pushes the field significantly away from the classical trajectory, resulting in a significant difference between the fully stochastic and pre-computed noise correlators. However, such rare realizations reside deep inside the tail of a probability distribution function (PDF) and do not affect the two-point statistics. From this, it can also be inferred that the higher correlators that measure the skewness and kurtosis of a PDF will be able to pick up this discrepancy, and thus, the backreaction effects would certainly become important for higher-order statistics

Stochastic Runge-Kutta: An ordinary differential equation (ODE) can be expressed as

$$dX(t) = A(x,t)dt \ , \tag{2.5.7}$$

which can be solved with standard calculus, and has a unique solution for given initial conditions, such that

$$X(t) = \int_0^t A(x,t)dt \ + \ X(t_0) \ . \tag{2.5.8}$$

On the other hand, an arbitrary SDE of the form

$$dX(t) = A(X,t)dt + B(X,t)dW(t) \ , \tag{2.5.9}$$

is governed by stochastic calculus because it features an integral

$$X(t) = \int_0^t A(x,t)dt \ + \ \int_0^t B(X,t)dW(t) \ + \ X(t_0) \ , \tag{2.5.10}$$

where the second term on the right-hand side is a random noise and for a system of Brownian motion, we have $A(X,t) = \mu(t)$, $B(X,t) = Var(X)(t)$, and $dW(t) = dt$. Now, the numerical method, Runge-Kutta of order four (RK4) (or any other iterative method in that regard), works by expanding the solution in a Taylor series and solving for the coefficients of the terms in the series up to the fourth term. This numerical approach is efficient only when the ODE is continuous and differentiable in the domain.

An SDE is generally continuous but not differentiable. It features sharp cusps and random noise, which cannot be accounted for by the RK4 method. This is why, to solve the system of SDEs Eqs. (2.2.8) and (2.2.9), we choose the Stochastic Runge-Kutta of weak order two (SRK2) [257–261]. For a generic SDE Eq. (2.5.9), one can iterate the solution using SRK2 as follows [262, 263]

$$X_{n+1} = X_n + \frac{1}{2}\left(M_1 + M_2\right) \ , \tag{2.5.11}$$

where the coefficients M_1 and M_2 are given by

$$M_1 = A(X(t_n), t_n)\Delta t + (\Delta W(t_n) - Z\sqrt{\Delta t})B(X(t_n), t_n) \ , \tag{2.5.12}$$

$$M_2 = A(X(t_n) + M_1, t_{n+1})\Delta t + (\Delta W(t_n) + Z\sqrt{\Delta t})B(X(t_n) + M_1, t_{n+1}) \ , \tag{2.5.13}$$

which reduces to Runge-Kutta order two method when $B = 0$. Note that for a Brownian motion, the noise takes the form $\Delta W \equiv \sqrt{\Delta t}\ \mathcal{G}(0,1)$, where $\mathcal{G}(\mu, \sigma^2)$ represents a random number picked from a Gaussian distribution having mean μ and variance σ. . The parameter Z takes values ± 1 each with equal probability. This procedure is repeated continuously starting from some initial time t_i to a final time t_f.

The step size plays a key role in numerically solving an SDE because, in addition to accuracy, it also determines the amplitude of noise to be added in each iteration. A coarse stepsize would mean that the stochastic term plays a bigger role than the deterministic term in Eq. (2.5.9) and vice versa for a smaller stepsize. It is evident from the trajectory of the particle following a Geometric Brownian motion in Fig. 2.8 that when we either increase the stepsize or choose a broader noise, the solution obtained using a numerical method for standard ODEs, such as RK4, fails completely, whereas SRK2 accurately takes the noise effects into account. In the small noise and small variance limit, an SDE can be approximated as an ODE, and RK4 converges to the exact solution with reasonably good accuracy. Since the mean of the noise is zero, we expect that the particle goes back to its initial position at a fairly distant final time. However, this convergence of the particle position is observed only for a larger number of timesteps.

The convergence of SRK2 is weak order two. The adjective 'weak' is used explicitly in the context of checking the convergence of SDEs. The weak order methods focus on achieving the accuracy of the statistical moments of the stochastic processes, whereas the strong order methods focus on the accuracy of individual realizations [264]. A weak order two SRK implies that the error in the mean and variance of the distribution of the realizations converges like $\mathcal{O}((\Delta t)^2)$, or quadratic in the timestep. It is apparent that for our case, we want to obtain an accurate estimate of the statistical moments of the Brownian-type stochastic trajectories of the inflaton for a large number of realizations. Hence, a weak-order two method is a more suitable choice.

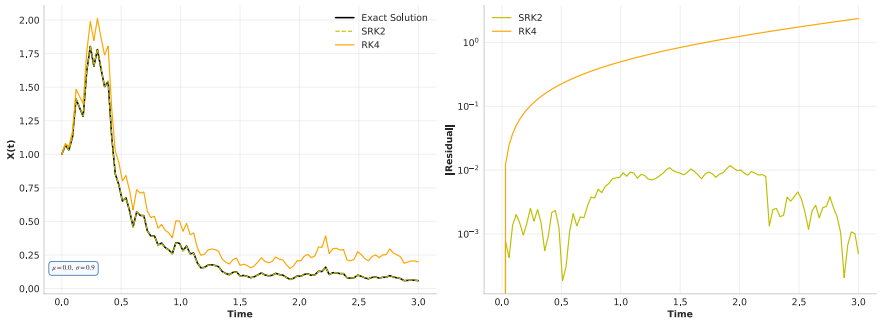

(a)

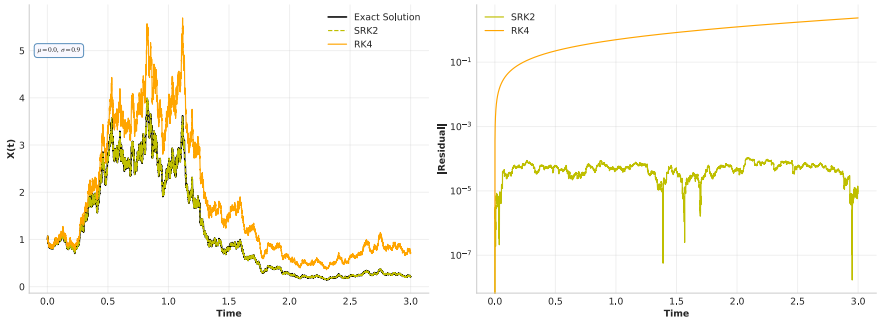

(b)

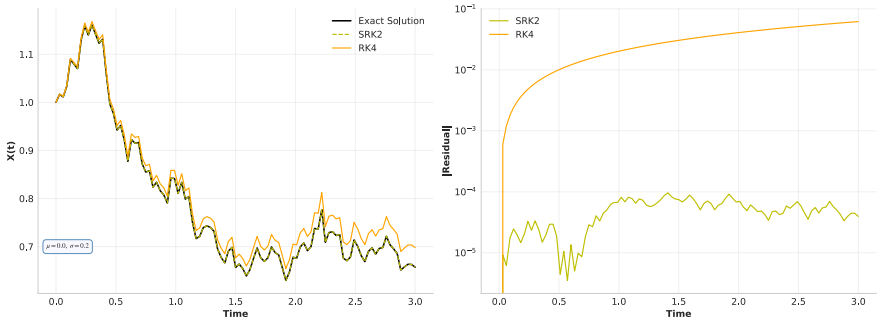

(c)

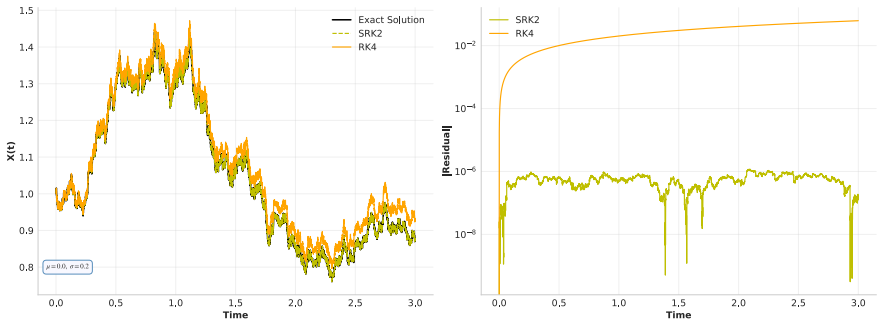

(d)

Figure 2.8: ***Panel (a)****: The plot on the left-hand side shows the particle trajectory for a Geometric Brownian motion with Gaussian noise (mean and variance shown inside the blue box), solved using RK4, SRK2 and a known analytic solution. The timesteps between the final position and the initial position are 100. The absolute residuals of the trajectories relative to the analytic solution are shown in the plot on the right-hand side.* ***Panel (b):*** *Same as in panel (a) but for 10,000 timesteps.* ***Panel (c):*** *Same as in panel (a) but for a Gaussian noise with wider variance.* ***Panel (d):*** *Same as in panel (c) but for 100 timesteps.*

2.6 Obtaining the Statistics

In this section, we list the inflation models that we choose to work with while demonstrating our algorithm defined in the previous section. The first model is the well-known quadratic potential that features a single free parameter, the field mass

$$V(\phi) = \frac{1}{2}m^2\phi^2 \ , \tag{2.6.1}$$

which has already been ruled out by the CMB measurements [265] but still serves as a good starting point due to its polynomial nature and simplicity. From the observed fluctuations at the CMB scales [38], we can infer the free parameter to be $\mathcal{O}(10^{-6})$. We will call this model 'M1' in the rest of the text for convenience.

It is visible from Fig. 2.9b that the SR approximation is obeyed by the scalar field in this model throughout inflation (with $8\pi G$ set to unity)

$$\mathcal{P}_{\mathcal{R}}|_{SR} = \frac{1}{24\pi^2}\left(\frac{V}{\epsilon}\right)\Big|_{k=aH} \ . \tag{2.6.2}$$

The next model is a set of toy potentials, also studied in [191, 217]

$$V(\phi) = V_0\left(1 + \alpha(\phi-\phi_0) + \beta(\phi-\phi_0)^3\right) \ , \tag{2.6.3}$$

which contains four free parameters. The numerical choice of these parameters is provided in Table 2.1. Due to the presence of two terms of unequal powers, this class of model features a tilt depending on whether or not the parameter α is non-zero. The potential is plotted in Fig. 2.9c. We will refer to this model as 'M2'.

Finally, a third inflation model is again a polynomial potential, but motivated by high-energy theory, featuring a non-minimally coupled scalar field [255, 266].

$$V(\phi) = \frac{V_0\phi^4}{4(1+A_1\phi^2)^2}\left[3 + A_1^2\phi_0^4 - 8(1+A_2)\frac{\phi_0}{\phi} + 2(1+A_3)(3+A_1\phi_0^2)\frac{\phi_0^2}{\phi^2}\right] \ , \tag{2.6.4}$$

which contains four free parameters. This model will be referred to as 'M3' and plotted in Fig. 2.9e. We give numerical choices for these parameters in Table 2.1. The parameter V_0 is set from the CMB observations. The position of the inflection point can be adjusted through fine-tuning the parameters. This model is particularly interesting since it is one of the few physically motivated inflationary models that feature an USR regime. However, the scalar field ϕ in Eq. (2.6.4) is non-canonical in the Einstein frame, and it is canonically normalized by changing the variable

$$\Phi = \sqrt{\frac{1+6A_1}{A_1}}\sinh^{-1}\left[\phi\sqrt{A_1(1+6A_1)}\right] - \sqrt{6}\tanh^{-1}\left[\frac{\sqrt{6}A_1\phi}{\sqrt{1+A_1(1+6A_1)\phi^2}}\right] \ , \tag{2.6.5}$$

2.6.1 Probability Distribution Function

The first step in testing the algorithm involves accumulating a large number of stochastic realizations for the FPT analysis of M2 and M3. It does not make sense to simulate M1 because

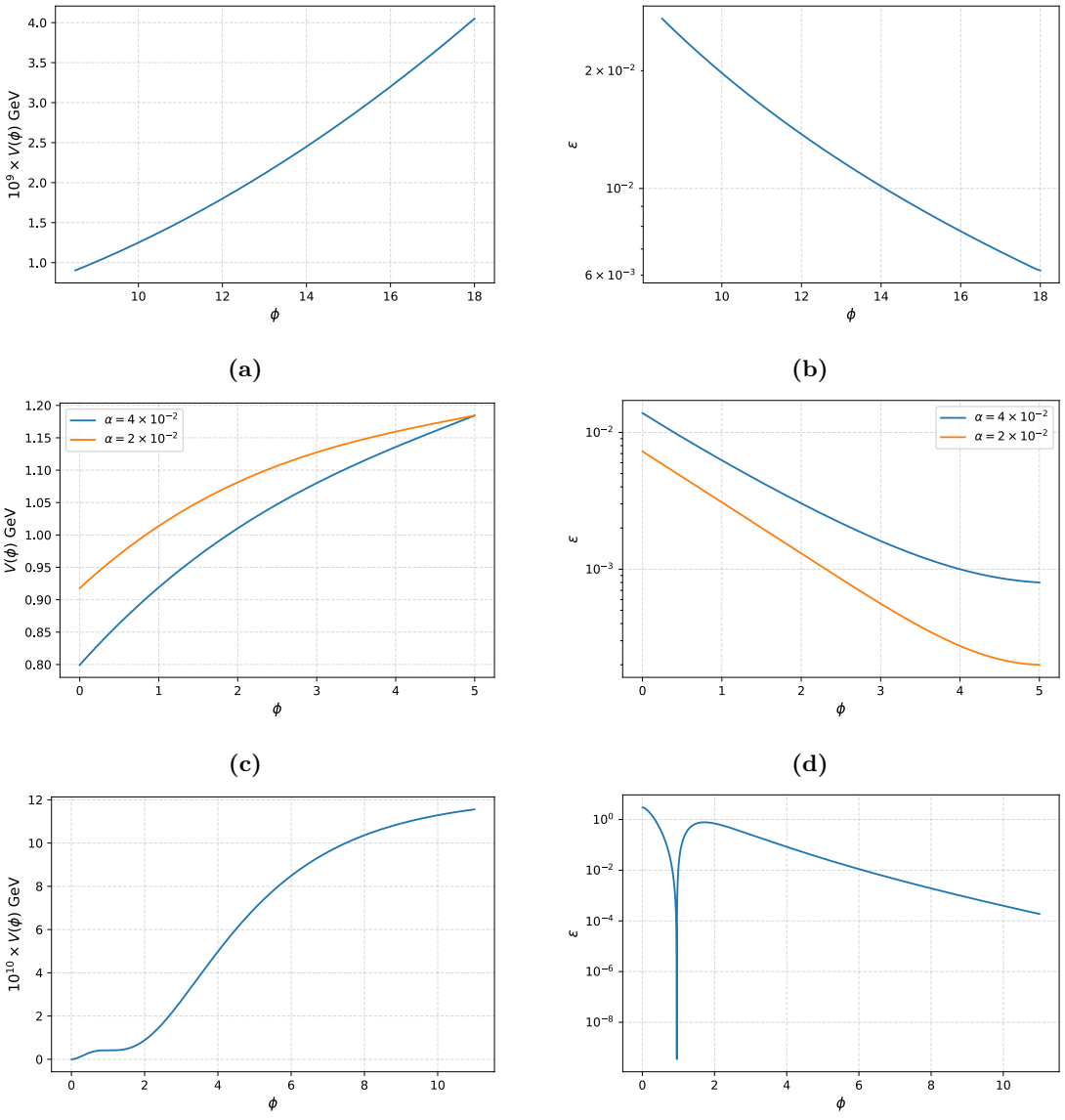

Figure 2.9: ***Top Panel:*** *The left figure shows the potential M1 described in Table 2.1 and the right figure corresponds to the first SR parameter of the same model.* ***Middle Panel:*** *Same as in the top panel but for M2 and for two choices of the parameter α.* ***Bottom Panel:*** *Same as in the top panel but for the model M3.*

Name	Potential	Free Parameters	Numerical Values
M1	Quadratic	$\{m\}$	$\{5 \times 10^{-6}\}$
M2	Toy	$\{V_0, \beta, \alpha, \phi_0\}$	$\left\{\frac{3}{25}\pi^2, 10^{-3}, \{2,4\} \times 10^{-2}, \frac{10^{-1}}{\alpha}\right\}$
M3	Realistic	$\{A_1, A_2, A_3, \phi_0\}$	$\{0.325\,479, 0.0089, 0.011, 1\}$

Table 2.1: *We tabulate the parameters for the three models of inflation, viz. M1, M2, and M3. All values are given in Planck units.*

in a standard SR scenario, the variance of the noise terms is negligible relative to the drift terms of the background. The resulting PDF for ΔN is a narrow Gaussian distribution. More details on the analysis of the noise are provided in Appendix C.

We also include a PDF based on the simplistic approach. In this approach, the correlators Eqs. (2.2.14) to (2.2.16) are not evolved numerically right from the initial conditions. Instead, the super-Hubble attractor solution to Eq. (1.5.10) is directly fed as the solution to the SW mode at the moment of $k_{\rm cg}$ crossing. In other words, it is sufficient to enforce the condition $|\delta\phi_{\mathbf{k}}|^2\Big|_{k\geq aH} = \frac{H^2}{2k^3}$, so the generic correlators Eqs. (2.2.14) to (2.2.16) take the following form

$$\langle 0 \left| \hat{\xi}_\phi(N_x)\hat{\xi}_\phi(N_y) \right| 0\rangle = \frac{H^2}{4\pi^2}\ ,\ \delta(N_x - N_y)\ , \tag{2.6.6}$$

$$\langle 0 \left| \ ,\hat{\xi}_\pi(N_x)\hat{\xi}_\pi(N_y) \right| 0\rangle = 0\ , \tag{2.6.7}$$

$$\langle 0 \left| \hat{\xi}_\phi(N_x)\hat{\xi}_\pi(N_y) \right| 0\rangle = 0\ . \tag{2.6.8}$$

We present the PDF of the stochastic variable N in Fig. 2.10 for the two cases of parameters

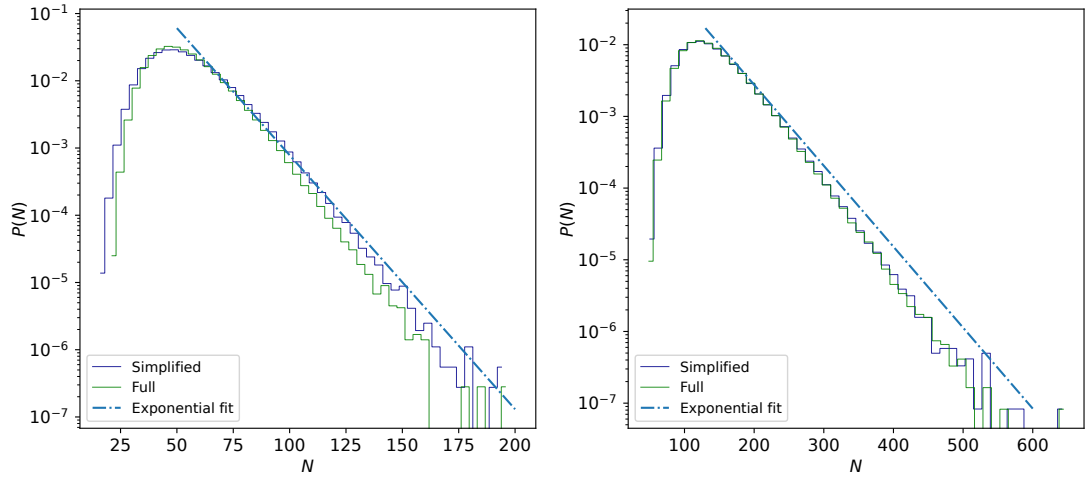

Figure 2.10: ***Left Panel:*** *The figure shows the PDF of N for the model M2 Eq. (2.6.3). The green curve represents the full noise treatment, and the dark blue curve represents the simplified noise treatment computed for $\alpha = 0.04$. The dotted-dashed line corresponds to the exponential fit suggested in [191].* ***Right Panel:*** *Similar analysis as in the left panel but for the case $\alpha = 0.02$.*

mentioned in Table 2.1. In order to construct this PDF, we simulated about 4×10^6 stochastic realizations over the precomputed background. On the other hand, the full treatment refers to the algorithm explained in Section 2.5.2. The dotted-dashed lines represent the exponential fits suggested in [191], which simulated the noise over a stochastic background. We notice a number of interesting points from Fig. 2.10:

- Most importantly, a non-Gaussian tail is clearly visible, reflecting the enhanced probability of having large curvature perturbations. The exponential sensitivity of PBH abundance to this tail makes it important to resolve it as deep inside the PDF as possible.

- For the two cases of M2 discussed in Fig. 2.10, we are able to explore the non-gaussian tails up to $\frac{\Delta N}{\bar{N}} = 3.774|_{\alpha=0.04}$ and $4.286|_{\text{ff}=0.02}$. Going deeper than this requires catching even rarer realizations or a significantly larger number of total realizations.

- The simplified treatment gives an exponential slope $D\left(\alpha = 0.04, \alpha = 0.02\right) \approx [0.086, 0.027]$, where $f(a) \propto e^{-Da}$. In the first case, where $\alpha = 0.04$ and $\bar{N} \sim 53$, the full treatment slightly undermines the variance compared to the simplified treatment. The reason is as follows: In the full treatment, the noise starts acting when the first mode crosses k_{cg} scale, which in our case is when the field enters the flat section of the potential. As a result, we miss out on some important scales that would also have influenced the stochasticity in the background evolution and thus could not be accounted for in the evolution of the super-Hubble separate universes.

- In the other case with $\alpha = 0.02$ and $\bar{N} \sim 140$, the full and simplified treatments agree well within a certain per cent accuracy in contrast to the previous case. This is possible because the mean e-folds is twice as much as the other case and farthest simulated realizations last thrice as much as the other case counterpart, meaning that we are dealing with a much extended duration of the de Sitter phase here. Consequently, a larger number of modes cross k_{cg} in duration and the overall impact due to missing the initial few modes gets dissolved in the integrated stochastic contribution. Thus, both treatments give similar variance.

- When compared with the slope from the PDF computed on a stochastic background (dotted-dashed lines in Fig. 2.10), we find for $\alpha = 0.04$ case that the variance in the precomputed background agrees well with the simplified treatment within a per cent level accuracy. For the case $\alpha = 0.02$, the precomputed variance is lower than the one in the stochastic background. This highlights that accounting for the backreaction of the background on the diffusion terms becomes important, particularly when inflation lasts for a longer duration. We also state that in physical cases, the de Sitter expansion is much lower than this, or around 55-60 e-folds. It is expected that for such a short period, the difference between the variances of the stochastic and the precomputed backgrounds becomes negligible.

- Finally, we note that the momentum noise is switched off in the simplified treatment while it is being accounted for in the full treatment. However, our analysis reveals that in the particular model of inflation, the role of momentum noise is not relevant, as it is orders of magnitude lower than the field noise (see Appendix C).

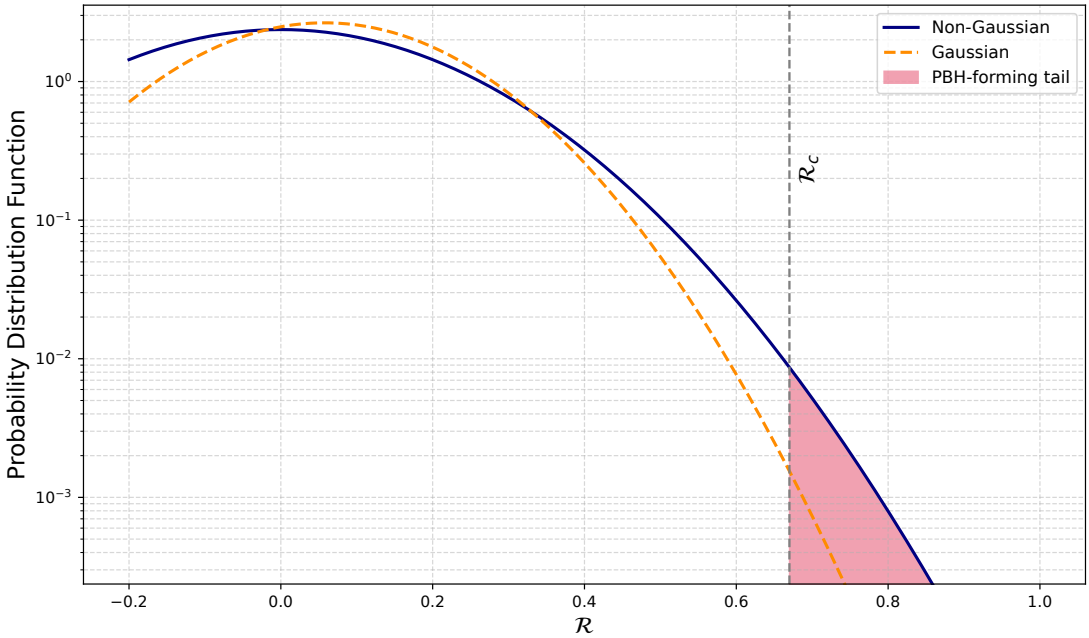

Figure 2.11: *The reference plot shows the sensitivity of the PBH abundance to the tail of the PDF of the total curvature perturbation. A positively non-Gaussian tail could enhance the PBH abundance by several orders of magnitude, since the area under the curve from the threshold $\mathcal{R}_c$ to infinity has increased (see Eq. (1.6.3))*

The PDF generated for the model M3 for about 10^6 stochastic realizations has been shown in Fig. 2.12. Again, we list some important takeaways

- We are able to reach as deep as $\Delta N \simeq 2.5$ inside the non-Gaussian tail.
- The simplified treatment is not included for two reasons: Firstly, there is a super-Hubble growth of perturbations when the field enters the non-attractor regime. Secondly, the momentum noise does not stay suppressed throughout inflation. As shown in the Appendix C, the momentum and field noise become almost of the same order deep inside the USR. Hence, it does not make sense to follow the simplified treatment.

2.6.2 Power Spectrum

We have already discussed why it is challenging to obtain the power spectrum from the PDF in real space. In this section, we chose to work in a time-independent limit such that the second term on the right-hand side of Eq. (2.5.6) vanishes, and we call the resulting curvature power spectrum as Super-Hubble Time-Independent Non-perturbative Spectrum (STINS). We shall see that this assumption has more significance in the USR model when we discuss the two cases below.

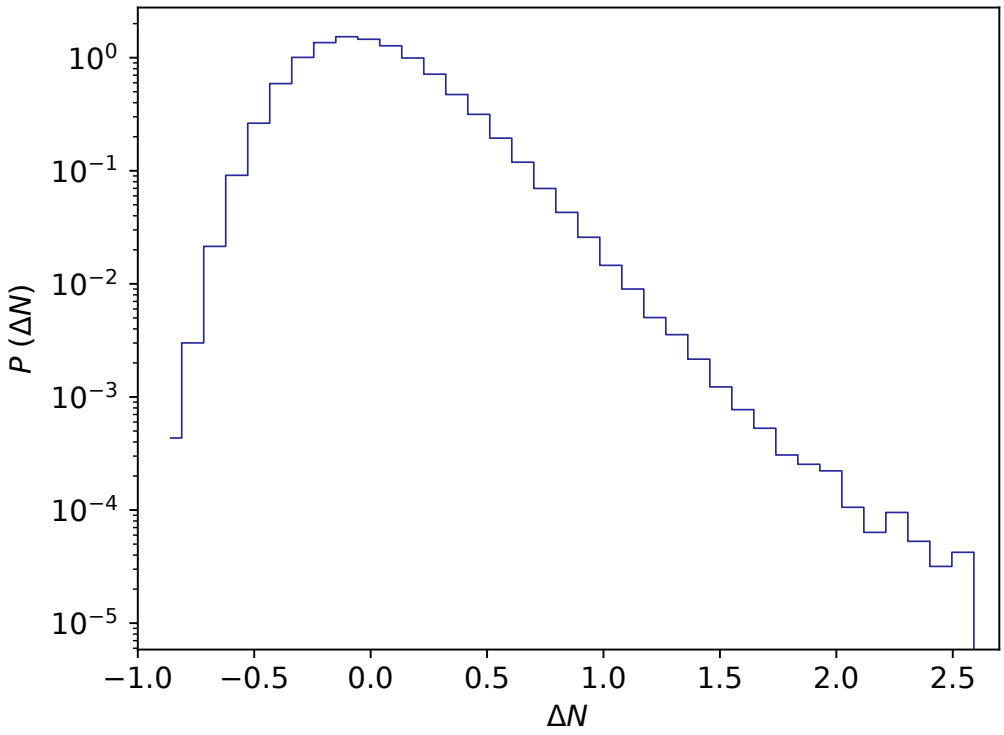

Figure 2.12: *The figure shows the PDF of* $\Delta N = N - \bar{N}$ *(or equivalently, the comoving curvature perturbations) for the model M3 Eq.* (2.6.4)*. The parameter set is mentioned in Table 2.1.*

2.6.2.1 Quadratic Potential

We have to take an important step further in the algorithm to extract the autocorrelation at different scales. We first consider the potential M1 to work with, since it produces a scale-invariant power spectrum in the perturbative approach. We compare it with the non-perturbative STINS in Fig. 2.13 from which we observe a number of details

- The left panel in the figure plots analytic (using Eq. (2.6.2)) and STINS side by side, and the corresponding residual plot is shown in the right panel.
- An individual blue dot in STINS is the spread in the expansion rate of all the simulated stochastic separate universes, corresponding to unique spatial hypersurfaces.
- To store the expansion rate on each spatial hypersurface, we create a grid in the classical value of the scalar field $\bar{\phi}$. More details can be found about the algorithm in Section 2.5.2.
- One can notice the missing readings at the beginning of inflation, when the pivot scale exits the horizon. This is due to the fact that even the largest modes in the simulation are initiated deep inside the physical horizon, and it is only after a certain duration they will

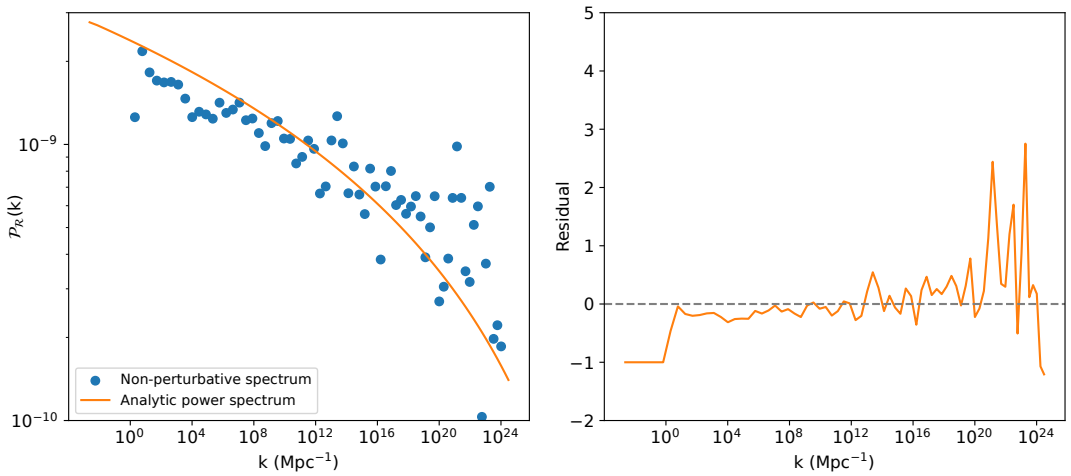

Figure 2.13: ***Left Panel:*** *The figure shows the curvature power spectrum for the model M1 Eq. (2.6.1) as a function of the comoving scales. The blue dots and the orange solid line correspond to the non-perturbative power spectrum and the analytic power spectrum, respectively.* ***Right Panel:*** *The residual of the non-perturbative power spectrum with respect to the analytical spectrum shown in the left panel.*

cross the coarse-graining scale. Suppose the field reading on the initial spatial hypersurface is $\bar{\phi}_\mathrm{i}$ and the first mode crosses k_cg when $\phi = \bar{\phi}_\mathrm{cg1}$, then the evolution of all the super-Hubble patches of the separate universes coincides in the interval $\bar{\phi}_\mathrm{i} - \bar{\phi}_\mathrm{cg1}$ and there is no variation in N.

- It is evident from the left panel of Fig. 2.13 that the blue dots undergo increased spread as the inflation proceeds. This is precisely the property of a Wiener process, as shown in Section 2.1, in which the variance increases linearly with time. We expect the same for the system of Langevin equations Eqs. (2.2.8) and (2.2.9). Although the relation is not exactly linear (owing to the two noise terms in the overall second-order ODE), the variance in ΔN is still proportional to the integral of the diffusion terms

$$\langle \Delta N_k^2 \rangle \big|_{N=\bar{N}_\mathrm{j}} \propto \int_{\phi(\bar{N}_\mathrm{i})}^{\phi(\bar{N}_\mathrm{j})} \xi_{\phi,\pi}(\bar{N}) d\bar{N} \ , \tag{2.6.9}$$

- This effect also shows up in the residual, which stays comfortably below one until $k \approx 10^{20}\ Mpc^{-1}$, but keeps increasing gradually due to the accumulating behaviour of the stochasticity. As the field reaches the end of inflation, the residual goes as high as 3. However, it must be noted that the SR condition $\epsilon \ll 1$ is not strictly followed in this regime, and there are corrections of higher powers of ϵ to the analytic power spectrum Eq. (2.6.2) [267]. We point towards Appendix D to learn about the accuracy check for the analysis.

- Finally, we can infer from the small residual that the time-dependent term in the full non-perturbative power spectrum Eq. (2.5.6) plays an insignificant role in this model.

2.6.2.2 Realistic Potential

We perform a similar analysis but with more sophistication for the model M3 that features an USR regime. The perturbative spectrum has been plotted alongside the STINS, from solving the Mukhanov-Sasaki equation mode by mode (Numerical power spectrum). We also show the analytic power spectrum for reference in Fig. 2.14. The pivot scale is adjusted to $k_* = 0.05\ Mpc^{-1}$. Some interesting things are noticed

- The inflationary regime consists of three subregimes: an USR region highlighted by the grey band and two SR regions outside this band. SR1, USR and SR2.
- In the SR1 region, there is a good agreement between the STINS with the analytic power spectrum (or the numerical spectrum). The residual stays within an order of magnitude before it starts to rise as it reaches the flatter region of the potential.
- Within the USR regime, the analytic solution fails, and we switch the comparison to the numerical (perturbative) spectrum. At the first transition, SR $\Leftrightarrow$ USR, the STINS does not undergo a fall in the amplitude as low as the numerical spectrum and the residual reaches as high as 10^4. This dip signals the transition of the field into the non-attractor USR, where the potential is exactly flat. It has been argued recently that such dips in the power spectra occur only when the field velocity does not change sign at the transition [268]. Moreover, the same Ref. also claims that the dip in the power spectrum is proportional to the inverse square root of the peak that follows it, and this happens to be a universal relation for the single field models.
- As long as the field remains in the USR, the universe remains in a steady state (energy density of the universe remains constant), and the perturbations continue to grow even outside the horizon. This is visible by a sharp rise in the power spectrum amplitude after the dip. This growth in the perturbations is the same in both the STINS and its numerical counterpart. The residual is hardly above a factor of unity in this period. This feature depicts the robustness of the non-perturbative approach to capture an exponentially steep gradient.
- Beyond the peak, the STINS overestimates the steepness of the decay in the perturbations compared to the numerical spectrum, and transitions back to the SR, followed by the end of inflation. Interestingly, at the second transition, the residual spikes again, however, not as high as the first one.
- The disagreement between the STINS and the numerical power spectrum can be traced back to our assumption below Eq. (2.5.6), where we chose to work in the time-independent limit and omitted the term involving the time derivative of $\mathcal{P}_\mathcal{R}$. At the first transition, the power spectrum slope is positive after the dip, $\frac{\partial \mathcal{P}_\mathcal{R}}{\partial N} > 0$, which implies that to get the full curvature power spectrum, the time-dependent term has to be subtracted from the left hand side of Eq. (2.5.6). This is why the dip in the STINS cannot become pronounced as in the perturbative power spectrum near the scales $k \sim 10^{16}\ Mpc^{-1}$. The same argument applies to the second transition (albeit in the other direction), i.e. corresponding to the scales $k \geq 10^{18}\ Mpc^{-1}$. The slope of the power spectrum in this case is negative, $\frac{\partial \mathcal{P}_\mathcal{R}}{\partial N} < 0$

but smaller in magnitude than the slope at the first transition. Thus, there happens the same discrepancy occurs between the two cases (STINS and numerical), and STINS underestimates the amplitude in the power spectrum when compared with the numerical power spectrum.

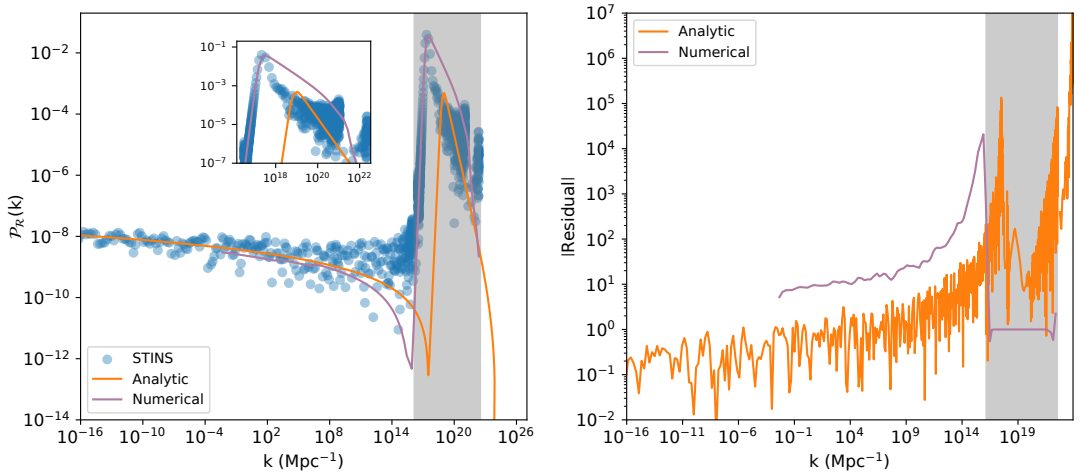

Figure 2.14: ***Left Panel:*** *The figure shows the curvature power spectrum for the model M3 Eq. (2.6.4) as a function of the comoving scales. The blue dots, the orange solid line, and the magenta solid line correspond to the STINS, the analytic power spectrum using the SR approximation, and the numerical solution, respectively. The grey band denotes the USR regime.* ***Right Panel:*** *The absolute residuals for the STINS are shown, both with respect to the SR approximated solution, and the numerical solution.*

These observations lead to the conclusion that it is important to account for the time dependence of the power spectrum, especially in the non-attractor model M3, to construct a fully non-perturbative curvature power spectrum. Furthermore, this term becomes even more crucial in the regions where the power spectrum undergoes sharp transitions. These sharp features are very important in computing the PBH abundance; hence, they should be accounted for in the perturbation statistics. This discussion and the residual plot in Fig. 2.14 also reveal the scale-dependent nature of the omitted term. The accuracy checks for this model have been shown in Appendix D.

Similarly to Eq. (2.5.5), the local bispectrum is related to the third moment of the PDF of ΔN (skewness) such that [269]

$$\mathcal{B} = \frac{d^2\langle \Delta N^3\rangle}{d\tilde{N}^2}\,, \qquad f_{\rm NL} = \frac{5}{72}\frac{d^2\langle \Delta N^3\rangle}{d\tilde{N}^2}\frac{1}{{\mathcal{P}_\mathcal{R}}^2}\,, \tag{2.6.10}$$

where the order of derivative with respect to the mean e-folds is two, and $f_{\rm NL}$ is the non-Gaussianity parameter that quantifies the relative magnitude of bispectrum with respect to power spectrum. It is trivial to compute the skewness of the PDF of ΔN from Section 2.6.1 in real space. However, it is not clear how to transport the scale dependence of the skewness to Fourier space. The fact that bispectrum depends on multiple Fourier modes makes it an even more challenging problem compared to the power spectrum, which depends only on a single Fourier mode Eq. (2.5.6). The analysis of bispectrum is beyond the scope of this thesis.

CHAPTER 3

CMB Spectral Distortions

The temperature anisotropies already bring a wide range of information origin and statistics of the primordial perturbations to the composition, geometry and expansion rate of the present universe. However, there's much more the CMB has to offer than its spatial anisotropies, for example, the distortions in its blackbody spectrum. In this section, we will develop an understanding of spectral distortions (SD) in the CMB. We already had a brief encounter with SD in the CMB in Section 1.6, and in this section, we will expand the discussion around this idea.

Starting from Section Section 3.1, we will see the history and introductory theory on SD, in addition to their classification. In Section 3.2, we will study in detail the distortions induced by the phenomenon of acoustic dissipation in the early universe. We shall provide with a newly developed approximation scheme on top of explaining the existing mathematical formulation of SD. We will also see how these calculations are implemented in the Boltzmann solver `CLASS` [270, 271]. We shall end this section in Section 3.3 by discussing the observational bounds on the SD from acoustic dissipation and how they compare within the different frameworks of accurate (or inaccurate) approximation schemes.

3.1 Background

Historically, it was the seminal works of Zeldovich and Sunyaev that first mentioned the phenomenon of SD [272, 273]. These works showed that distortions could have been induced in the blackbody spectrum of the CMB when it passed through the intergalactic medium, where the relativistic electrons injected additional energy into the photons via Compton scattering. We will see later that such late-time distortions, which leave a specific signature, are identified as y distortions. This was followed by advancements that studied the effects of Bremsstrahlung and double Compton scattering from the perspective of early-time SD [274].

The era of precision cosmology began when Cosmic Background Explorer (COBE) released its data on temperature anisotropies and the frequency spectrum of the CMB [275, 276]. For the latter purpose, COBE used the Far Infrared Absolute Spectrophotometer or the FIRAS. The device is a polarizing Michelson interferometer, sensitive in the wavelengths $\lambda \in [0.1\text{ mm}, 10\text{ mm}]$,

and offers a 7 ° field of view. A crucial component of the FIRAS is an external calibrator which adjusts according to the field of view of the satellite [276]. This calibrator is designed to work as a near-blackbody, which ensures a perfect transfer of energy from outside to inside. We will understand the concept of a blackbody in the coming discussion. The photons pass through the external calibrator and reach a Fourier transform spectrometer, where the frequency spectrum of the incoming CMB photons is matched with an internal reference blackbody. Any deviations between the observed spectrum and the reference spectrum are reported in the form of SD. The bounds on SD from this instrument will be discussed in Section 3.3.

From, early 90s till very recently, we have witnessed tremendous developments in the accurate calculations of SD, distinction between different eras of SD, modelling of various energy injection processes, and analysis of data from COBE (which was awarded a Nobel prize in 2006). Several cosmological codes have also been developed that compute the SD from Einstein-Boltzmann equations, for example, `CLASS` [270, 271], CosmoTherm [277], or SZpack [278]. In the rest of this section, we provide a description of a blackbody, different cosmological processes that are involved in maintaining the blackbody spectrum of the CMB photons, and how inefficiency in these processes results in various types of SD.

3.1.1 Blackbody Radiation

A blackbody is an ideal concept which refers to an object that is a 'perfect absorber' and a 'perfect emitter'. To put simply, a blackbody absorbs all the radiation incident on it, regardless of its frequency, and also emits all the radiation in the entire frequency range of the electromagnetic (EM) spectrum. The emission of EM radiation happens when the blackbody is at thermal equilibrium and depends solely on the temperature (T) of the blackbody. The power of the emitted spectrum per unit area, per unit frequency, per solid angle, is called blackbody radiation ($B_f(T)$). Planck's law, which determines the spectrum of blackbody radiation, is given as

$$B_f(T) = \frac{2hf^3}{c^3} \frac{1}{e^{\frac{hf}{K_b T}} - 1} \ , \tag{3.1.1}$$

where, k_b is the Boltzmann constant, h is the Planck's constant, c is the speed of light and f is the frequency of emitted radiation. The unit of $B_f(T)$ in SI units is $\mathrm{W \cdot m^{-2} \cdot Hz^{-1} \cdot sr^{-1}}$. In real life, there are no perfect blackbodies, but the spectral radiance from several sources, such as the sun, incandescent light, gas stove and the CMB, can be well approximated using Planck's law Eq. (3.1.1). We can also express Planck's law in two extreme limits, viz. high frequency limit (Wien's Law), and low frequency (Rayleigh-Jeans Law) limit

$$B_f(T) = \begin{cases} \frac{2K_b f^2}{c^2} T & f \gg \frac{K_b T}{h} \quad \text{(Wien's Law)} \ , \\ \frac{2hf^3}{c^2} \frac{1}{e^{\frac{hf}{K_b T}}} & f \ll \frac{K_b T}{h} \quad \text{(Rayleigh-Jeans Law)} \ . \end{cases} \tag{3.1.2}$$

The blackbody radiation is a continuous spectrum in frequency, as shown in Fig. 3.1. A unique feature of this spectrum is that the spectral radiance increases with the frequency, peaks at a certain frequency, and then decays exponentially at higher frequencies. The frequency corresponding to the maximum radiation emission is called the peak frequency. The peak frequency depends solely on the blackbody temperature. The relation between the peak wavelength (or inverse of the peak

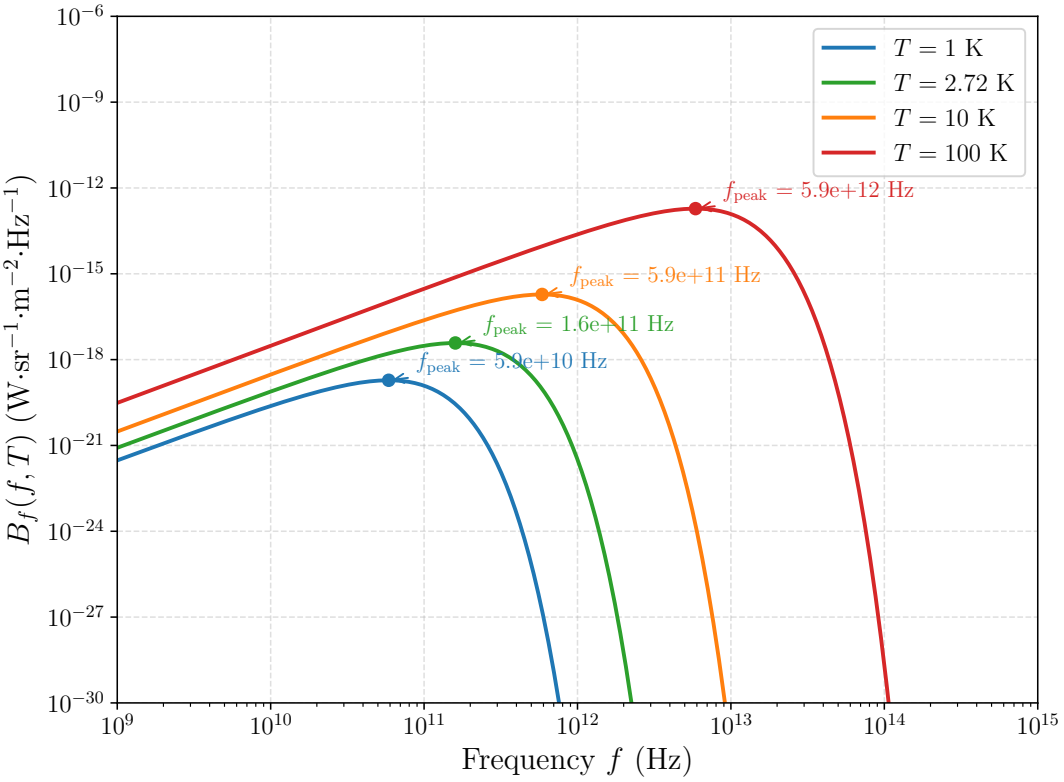

Figure 3.1: *Blackbody distribution curves at different temperatures. The corresponding peak frequencies shown with dots are computed with Wien's displacement law Eq. (3.1.3). Increasing the temperature shifts the intensity of the emitted radiation to higher frequencies.*

frequency) and the blackbody temperature is given by Wien's displacement law

$$\lambda_{\text{peak}} = \frac{2.898 \times 10^{-3}}{T} \text{m} \cdot \text{K} \ . \tag{3.1.3}$$

The peak frequency increases linearly with the temperature, which is also evident from Fig. 3.1. Next, we proceed towards studying the implications on photons as perfect blackbodies. Since, photons follow Bose-Einstein statistics, the occupation number is given as

$$O = \frac{1}{e^x - 1} \ , \tag{3.1.4}$$

where $x = \frac{hf}{K_b T}$. The number density of photons n_γ can be calculated from the fact that the energy of photons is quantized. So, $n_\gamma = \frac{E_n}{hf} \frac{1}{V}$, where E_n is the total energy of n photons, hf is the energy corresponding to a single photon and V being the volume. The total energy can be

obtained by integrating over the spectral radiance Eq. (3.1.1) such that

$$n_\gamma = \frac{E_n}{hf}\frac{1}{V} \,, \tag{3.1.5}$$

$$= \int_0^\infty B_f(T) df d\Omega dV \frac{1}{hfV} \,, \tag{3.1.6}$$

$$= \int_0^\infty \frac{B_f(T)}{hf} df d\Omega \,, \tag{3.1.7}$$

$$= \int_0^\infty \frac{2f^2 O}{c^3} df d\Omega \,, \tag{3.1.8}$$

$$\approx \left(\frac{T}{2.73K}\right)^3 411\mathrm{cm}^{-3} \,. \tag{3.1.9}$$

The number density of photons scales with the third power of the temperature. In the same way, the photon energy density can be computed

$$\rho_\gamma = \frac{E_n}{V} \,, \tag{3.1.10}$$

$$= \int_0^\infty \frac{B_f(T) df d\Omega dV}{V} \,, \tag{3.1.11}$$

$$= \int_0^\infty \frac{2hf^3 O}{c^3} df d\Omega \,, \tag{3.1.12}$$

$$= \sigma T^4 \,, \tag{3.1.13}$$

where σ is called the Stefan-Boltzmann constant and its numerical value in SI units is $5.67 \times 10^{-8}\mathrm{W}\cdot\mathrm{m}^{-2}\cdot\mathrm{K}^{-4}$. The energy density of photons scales with the fourth power of the temperature.

3.1.2 Categorizing the Spectral Distortions

Imagine a thermal bath consisting of matter and photons. At very high redshifts ($z \approx 10^9$), the temperature is much higher than the masses of baryons and fermions; hence, the matter is relativistic and in thermal equilibrium with photons. Three major processes mediate the matter-radiation interaction, namely

- Compton scattering (CS): $\gamma + e^- \leftrightarrow e^- + \gamma$,
- Double Compton Scattering (DCS): $\gamma + e^- \leftrightarrow e^- + \gamma + \gamma$,
- Bremsstrahlung (BS): $e^- + A^+ \leftrightarrow e^-_\downarrow + A^+ + \gamma$,

where A^+ is a positive ion (generally a proton) heavier than electrons. The process of BS involves the production of a photon due to the deflection of an electron under the EM influence of A^+. The moving electron slows down, and the emitted photon of proportionate wavelength compensates for the lost kinetic energy. CS scattering is an inelastic collision that happens when a high frequency photons collides with an electron. The reduced frequency of the scattered photon is given by $\lambda_\downarrow = \lambda + \frac{h}{m_e c}(1 - \cos\theta)$, where θ is the angle between incident and recoil photon directions. DC is also a photon number-changing reaction involving a scattering of low-frequency photons.

The three processes discussed above work in conjunction with each other to ensure that the matter-radiation fluid is fully thermalized. The blackbody distribution of the photons is preserved under the condition that it is an adiabatic system. However, there are certain implications on the blackbody spectrum when the adiabatic assumption is not strictly followed, owing to the injection of external energy onto the fluid. The fact that the universe cools down with the expansion makes it even more interesting because these processes do not remain fully efficient at lower temperatures, as we shall see.

3.1.2.1 Temperature Shift

There are several instances of cosmological and astrophysical processes that could inject energy into the fluid, such as radiation emitted from the mass accreting onto PBHs, adiabatic cooling of the electrons, dissipation of acoustic oscillations, thermal Sunyaev-Zeldovich effect etc. Imagine that at very early times, an external thermodynamic process injects energy and raises the photon temperature from T to T'. Now, depending on whether or not the redistribution of energy is even, the obtained spectral radiance in the new photon configuration could still be a blackbody spectrum. Using Eq. (3.1.13), we can write

$$\frac{\rho'_\gamma}{\rho_\gamma} = \left(\frac{T'}{T}\right)^4 = \left(1+\frac{\Delta T}{T}\right)^4 \approx 1 + 4\frac{\Delta T}{T}\bigg|_{\frac{\Delta T}{T}\ll 1} , \tag{3.1.14}$$

$$\frac{\Delta\rho_\gamma}{\rho_\gamma} \approx 4\frac{\Delta T}{T} , \tag{3.1.15}$$

which denotes the presence of an additional energy. The system is in thermal equilibrium, thanks to the full efficiency of CS, DCS and BS. However, the energy redistribution requires more care than just shifting the temperature. The new spectrum should be able to remember the distribution of photons across the frequency to preserve the shape of the blackbody curve, otherwise, due to CS, the heat would shift the photon population more towards the high-frequency regime. To do that, we must also change the photon occupation number and number density proportionate to the change in temperature.

From Eq. (3.1.9), the change in photon temperature has to be supported by the change in its number density

$$\frac{\Delta n_\gamma}{n_\gamma} \approx 3\frac{\Delta T}{T} = \frac{3}{4}\frac{\Delta\rho_\gamma}{\rho_\gamma} , \tag{3.1.16}$$

which would be taken care of by DCS and BS. However, we have to add/remove the photons throughout the frequency spectrum, as a function of the frequency. This suggests that the photon occupation number Eq. (3.1.4) also undergoes a change to account for the redistribution after the energy injection

$$\Delta O = \frac{1}{e^{\frac{hf}{K_b T(1-\frac{\Delta T}{T})}}-1} - \frac{1}{e^{\frac{hf}{K_b T}}-1} \approx \frac{xe^x}{(e^x-1)^2}\frac{\Delta T}{T} . \tag{3.1.17}$$

Assuming that the conditions Eqs. (3.1.15) to (3.1.17) are met, the difference between the new blackbody spectrum and the original blackbody spectrum, ΔB_f is given by

$$\frac{1}{\frac{2h}{c^3}f^3}\Delta B_f = \Delta O = gG(x) , \tag{3.1.18}$$

where, $G(x) = \frac{xe^x}{(e^x-1)^2}$ and $g = \frac{\Delta T}{T}$. Thus, the resulting spectrum B'_f is also a blackbody spectrum with a shift in its temperature. Although it is not technically a spectral distortion; the temperature shift distortion just shifts the blackbody temperature. To measure the temperature shift, one needs to measure the photon temperature before the injection and after the injection. With the current observations, we have measured the averaged CMB monopole (temperature) at present day or $z = 0$. From a single redshift measurement, it is not possible to separate the photon temperatures before and after the injection. We conclude that during the thermalization era, $z \geq 2 \times 10^6$, CS, responsible for the distribution of the energy via inelastic scattering with electrons, is fully efficient. Simultaneously, DCS and BS, both responsible for changing the photon number density, are also efficient and together, they are able to adjust to the blackbody spectrum but with a shifted temperature.

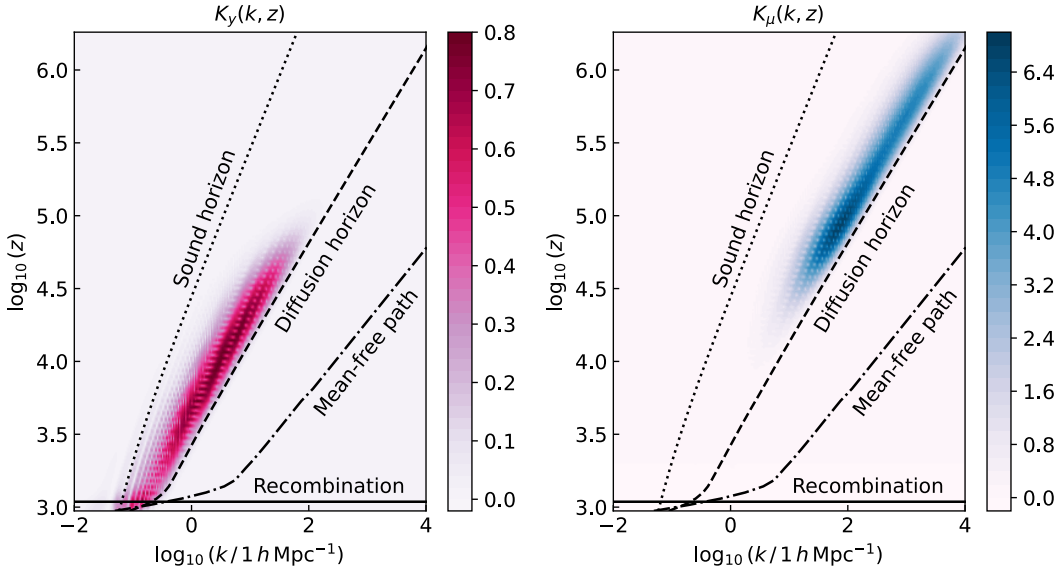

Figure 3.2: ***Left Panel:*** *The contour shows the region in $k-z$ space where the integration kernel for y distortions has the highest contribution, and the colour contrast shows how much a given point will contribute. Alongside the contour, we also plot the scale of the Thomson mean-free path ($k = \frac{2\pi}{\alpha'_T}$) the sound horizon scale ($k = \frac{2\pi}{r_s}$), and the diffusion horizon scale ($k = \frac{2\pi}{r_D}$). The figure is created for standard ΛCDM model using* `CLASS`.

3.1.2.2 Chemical Potential (μ) Distortions

At lower redshifts, $5 \times 10^4 \leq z < 2 \times 10^6$, the universe cools down due to expansion, and the DCS and BS rates have already dropped below the Hubble rate, albeit CS remains efficient. Thus, we cannot alter the photon number. At this point, if external energy is injected into the matter-radiation fluid, the blackbody spectrum undergoes a distortion which cannot be dissolved anymore. The $\gamma \leftrightarrow e^-$ system comes out of the chemical equilibrium, and the chemical potential μ becomes non-zero.

The phase space distribution of photon, $\mathcal{B}(x)$, follows a specific solution of the Boltzmann equation, called the Kompaneets equation. Ignoring the terms involving DCS and BS, we write the Kompaneets equation [279],

$$\frac{\partial \mathcal{B}}{\partial t} = \frac{n_{e^-} s T_{e^-}}{m_{e^-} x^2} \frac{\partial}{\partial x} \left\{ x^4 \frac{\partial \mathcal{B}}{\partial x} + x^4 \frac{T_\gamma}{T_{e^-}} \mathcal{B}(1+\mathcal{B}) \right\} , \tag{3.1.19}$$

which describes the evolution of $\mathcal{B}(x)$ under the influence of Compton interactions with the electrons. The subscript e^- stands for quantities associated with electrons. The cross-section for Thompson scattering is s, and T_γ is the photon temperature. The rate of CS is much faster than the expansion rate, so the system achieves kinetic equilibrium. Consequently, the left-hand side of Eq. (3.1.19) can be neglected. The general solution to Eq. (3.1.19) can be written as

$$\mathcal{O} = \frac{1}{e^{x_{e^-} + \mu} - 1} , \tag{3.1.20}$$

where $x_{e^-} = \frac{T_\gamma}{T_{e^-}} x$ and we get a non-zero chemical potential μ as a constant of integration. The above equation is the photon distribution in Bose-Einstein statistics. We can expand Eq. (3.1.20) such that

$$\mathcal{O}(x_{e^-}) = O(x_{e^-}) - \mu M(x_{e^-}), \tag{3.1.21}$$

where the spectral shape $M(x)$ and amplitude of the μ distortion are [280–282]

$$\mu = 1.401 \left(\frac{\Delta \rho_\gamma}{\rho_\gamma} - \frac{4 \Delta n_\gamma}{3 n_\gamma} \right) , \tag{3.1.22}$$

$$M(x) = 1.401 G(x) \left(0.4561 - \frac{1}{x} \right) , \tag{3.1.23}$$

from which, it is evident that μ distortion vanishes when Eq. (3.1.16) is followed. We shall see in the Section 3.2.2 that μ distortions play a key role in constraining the primordial density fluctuations and also in the abundance of PBHs. We show in Fig. 3.3 how a positive chemical potential affects the photon spectral radiance. Note that DCS and BS are completely absent. Hence, μ distortions are the distortions that could have been a temperature shift, if it were for efficient photon-producing processes.

A distinct feature of μ distortions is visible in Fig. 3.3. There is a shortage of photons at lower frequencies compared to the true blackbody spectrum and vice versa for higher frequencies. The reason is straightforward: no new photons are generated even in the presence of external energy, but CS is fully functional. As a result, the injected energy is circulated among the same number of photons via scattering, which leads to an increase in the number of photons with higher energy.

3.1.2.3 y Distortions

When further expansion of the universe reaches redshifts as late as $z \leq 5 \times 10^4$, the timescale of CS slows down and falls below the Hubble rate. Historically, y distortion was first studied for the energy injection from ionized gas in the galaxy clusters [283]. The electrons present in this gas are relativistic and at, higher temperature than the CMB at $z \leq 10^4$, so the energy transfer via (inefficient) CS releases energy into the photons filling the cosmic background. In addition to

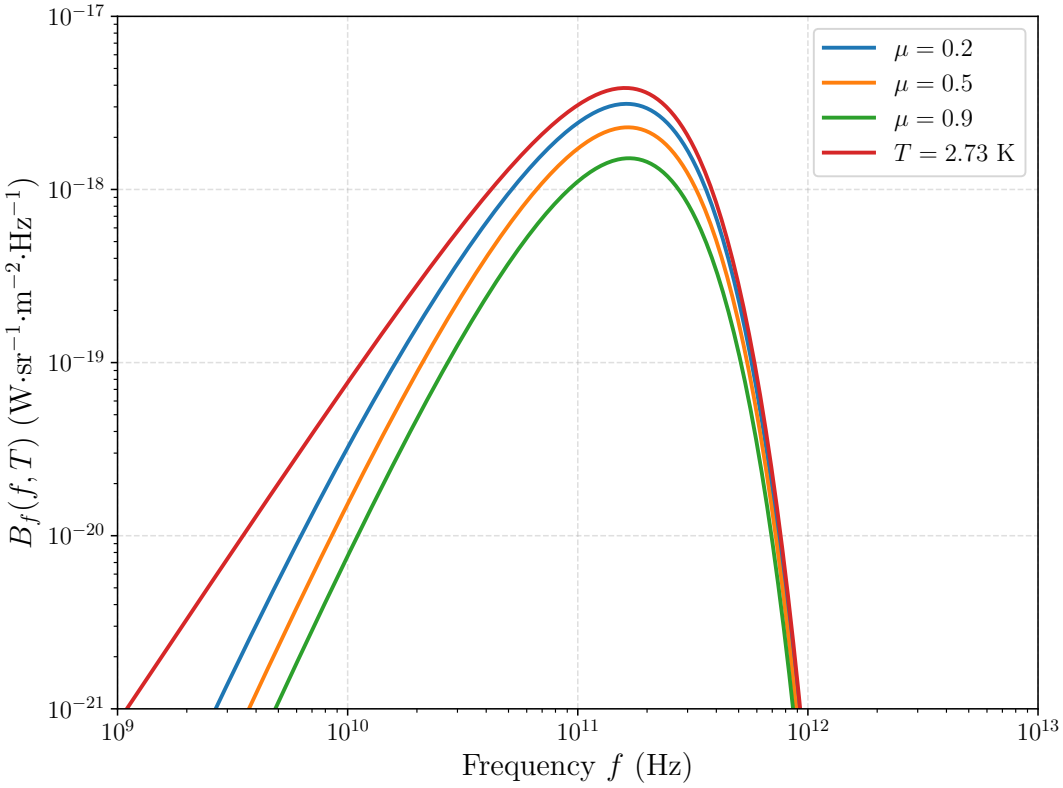

Figure 3.3: *Spectral radiance with non-zero values of the chemical potential μ and photon temperature 2.73 K. The red curve shows the blackbody spectrum at the same temperature. The low-frequency tail of the spectrum is most affected by the variation in the μ amplitude.*

completely switching off DCS and BS at such late times, the inefficiency of CS results in photons emerging out of equilibrium with the electrons. Thus, the energy redistribution cannot happen to its full extent.

The left-hand side of the Kompaneets equation is not zero anymore, and we need to keep track of the time evolution of the full phase distribution of photons $\mathcal{B}(x)$. Rewriting and configuring Eq. (3.1.19), we get [282, 284]

$$\partial\mathcal{B} = \frac{n_{e^-} s T_{e^-}}{m_{e^-} x^2} \frac{\partial}{\partial x} \left\{ x^4 \frac{\partial \mathcal{B}}{\partial x} + x^4 \frac{T_\gamma}{T_{e^-}} \mathcal{B}(1+\mathcal{B}) \right\} \partial t \ , \tag{3.1.24}$$

$$\Delta\mathcal{B} = \frac{n_{e^-} s T_{e^-}}{m_{e^-} x^2} \frac{\partial}{\partial x} \left\{ -x^4 \mathcal{B}(1+\mathcal{B}) + x^4 \frac{T_\gamma}{T_{e^-}} \mathcal{B}(1+\mathcal{B}) \right\} \Delta t \Big|_{dt \to 0} \ , \tag{3.1.25}$$

$$\approx \frac{\Delta T}{m_{e^-}} G(x) \left[x \coth\left(\frac{x}{2}\right) - 4 \right] \Delta t \ , \tag{3.1.26}$$

$$= y Y(x) \ , \tag{3.1.27}$$

where we defined the temperature difference between photons and electrons, the amplitude of y

distortion and its spectral shape, respectively, as

$$\Delta T = T_\gamma - T_{e^-} \ , \tag{3.1.28}$$

$$y = \int_0^t \frac{n_{e^-} s \Delta T}{m_{e^-}} \Delta t \ , \tag{3.1.29}$$

$$Y(x) = G(x) \left[x \coth\left(\frac{x}{2}\right) - 4 \right] \ , \tag{3.1.30}$$

$$G(x) = \mathcal{B}(x)(1 + \mathcal{B}(x)) = -\frac{\partial b}{\partial x} \ . \tag{3.1.31}$$

Also notice that we used the relation Eq. (3.1.31) to reach the expression Eq. (3.1.25) from Eq. (3.1.24). It is evident from Eq. (3.1.29) that if the CS were efficient, the energy redistribution would have nullified any temperature difference between the photons and the electrons. In other words, y distortions are the distortions that could have been μ distortions, if the system were fully Comptonized. It can be further shown that the amplitude of y distortions Eq. (3.1.29) is related to the injected energy in the system as $y = 0.25 \frac{\Delta \rho_\gamma}{\rho_\gamma}$ [272].

The total intensity of the photon spectrum measured by an instrument is the sky average of all the corrections to the blackbody spectrum in the form of distortions $I(x)$. To obtain the purely distorted part, we can subtract from $I(x)$, the theoretical blackbody distribution corresponding to the present photon temperature, $\Delta I(x)$, such that

$$I_f(x) = B_f(2.73K) + gG(x) + \mu M(x) + yY(x) \ , \tag{3.1.32}$$

$$\Delta I_f(x) = gG(x) + \mu M(x) + yY(x) \ . \tag{3.1.33}$$

Since we observe the superposition of all the distortions over the frequency spectrum, it is crucial to isolate the individual distortions for a better analysis of energy injections at different epochs. Fortunately, this is not so difficult to do, thanks to the frequency dependence of μ and y distortions, as depicted in Fig. 3.4. Moreover, both distortions change signs at different frequencies. For μ distortion $f_{0,\mu} \sim 130$ GHz while for y distortions this feature is at higher frequency $f_{0,y} \sim 217$ GHz. The spectral shapes also behave distinctly in the extreme frequency limits [285, 286]

$$M(x) = \begin{cases} 0.64 x e^{-x}, & f \gg \frac{K_b T}{h} \\ -\frac{1.401}{x^2}, & f \ll \frac{K_b T}{h} \end{cases} \tag{3.1.34}$$

$$Y(x) = \begin{cases} x(x-4)e^{-x}, & f \gg \frac{K_b T}{h} \\ -2x^{-1}, & f \ll \frac{K_b T}{h} \end{cases} \tag{3.1.35}$$

3.1.2.4 Residual Distortions

In the above discussion, we assume a sharp transition between μ and y distortion periods. However, in reality, the transition is gradual and spread across a wider range of redshifts. During the transition, the efficiency of CS lies between those in μ and y eras. Other residual distortions could occur after the recombination when the CMB is completely decoupled and starts free-streaming. For the latter case, some injection sources include thermal SZ effect, reionization or decaying dark matter [287]. The computation of residual distortions is non-trivial to perform using analytical

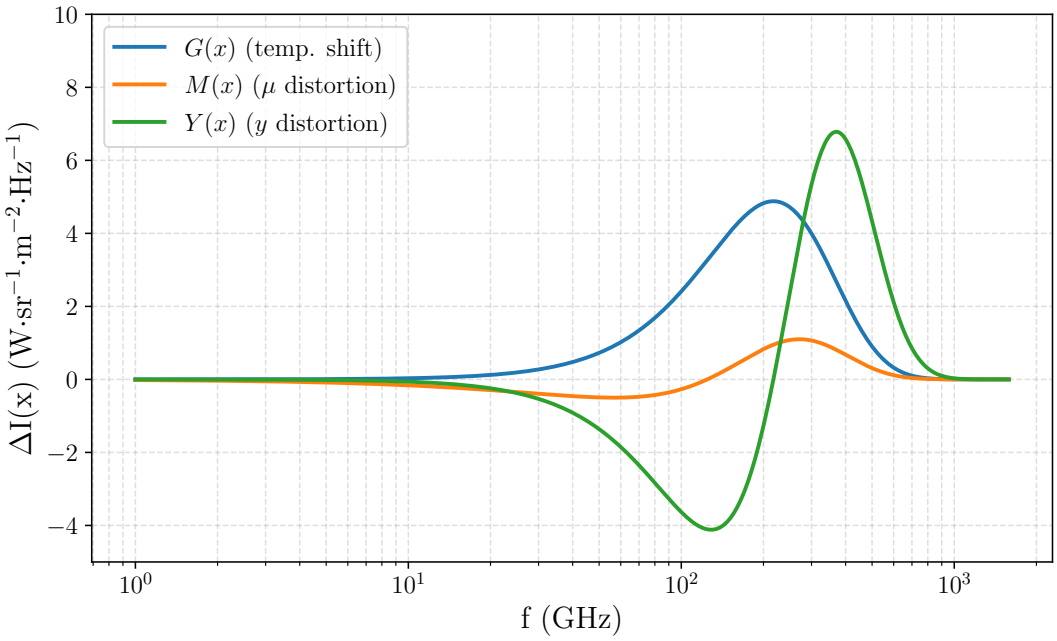

Figure 3.4: *The figure shows the spectral shapes of the distortions in the blackbody as a function of the frequency.*

approximations, since the time dependence of CS efficiency and energy injection has to be considered while solving the Boltzmann equations. This has been implemented using the Green's function approach [288] in the Einstein-Boltzmann solvers `CLASS` [270] and CosmoTherm [277] respectively. The magnitude of residual distortions is significantly suppressed as compared to the other two, so we will neglect them in further analysis.

3.2 Introduction to Acoustic Dissipation

In Section 3.1.2, we painted a rough picture of how the amplitude of the SD can be related to the fractional increase in the photon temperature, or equivalently, the fractional energy injection. In this section, we will provide proper terminology for the heating rate that quantifies the distortion magnitude, particularly sourced by acoustic dissipation.

Under the assumption of adiabatic initial conditions, the density fluctuations in the inflaton are passed on to the photon density perturbations, and both of them can be related at super-Hubble scales as $\frac{\Delta\rho}{\bar{\rho}} = -\frac{4}{3}\mathcal{R}$ [43]. Thus, at the beginning of the radiation-dominated era, the universe is filled with photons with a directional and local temperature field $T(\tau, x, \hat{n})$. At very high temperatures, the photon mean-free path is very short owing to its high-frequency scattering rate. However, as the expansion of the universe proceeds, the mean-free path increases (until it becomes infinite post-recombination). This led to the diffusion of photons from overdensity (hotter) regions to underdensity (colder) regions.

The diffusion creates two important effects. First, mixing of photons at two different tem-

peratures will result in the overall intensity spectrum, which is not a blackbody anymore [289]. Second, exchange of photons between hotter and colder regions will homogenize the temperature fluctuations. Consequently, the remaining density fluctuations would be a damped version of the originally created primordial fluctuations. The result is SD from the dissipation of acoustic (sound) waves. The terminology signifies that the dissipation is governed by the pressure gradient in the plasma. The scale corresponding to the diffusion damping is popularly referred to as the Silk scale, named after the physicist Joseph Silk, who described the acoustic damping of photon perturbations for the first time [290]. Therefore, by observing or not observing the SD, we can extract information about the amplitude of the curvature perturbations from inflation.

Tensor perturbations, unlike scalar perturbations, do not depend on the photon diffusion for the dissipative effect. Instead, the free-streaming GWs release some energy to the plasma during propagation. It has been shown that this effect is suppressed compared to the Silk damping. At the same time, tensor perturbations do not depend on the diffusion damping scales, due to which they have a much longer range of dissipation [291].

In this section, we assume that SD are sourced solely by acoustic dissipation. We denote a generic distortion as s ($= \mu$ or y) and ignore the residual distortions. In our definition, s is the sky-average of the blackbody distortions observed in every spatial direction at a particular time slicing. From the discussion so far, we can write the derivative of s with respect to conformal time τ as

$$s' \propto \frac{d}{d\tau} \left\langle \frac{\Delta\rho|_{\rm b}}{\rho_\gamma|_{\rm b}} \right\rangle_{\rho(\vec{x})} , \tag{3.2.1}$$

where the subscript b means that we are working in the frame of reference where baryons have vanishing velocity. The angular brackets denote a spatial average. The spatial averaged denominator is just the background energy density $\bar{\rho}(x)$ (See [292] and the Appendix therein for the discussion about gauge-invariance of s'). Moreover, the proportionality factor is determined whether or not the energy redistribution causes μ distortions or y distortions, and it can be expressed with a branching ratio, $\mathcal{I}_s(\tau)$, which carries time-dependency [288]

$$s' \propto \frac{d}{d\tau} \frac{\langle \Delta\rho|_{\rm b} \rangle_{\vec{x}}}{\bar{\rho}_\gamma} , \tag{3.2.2}$$

$$= \mathcal{I}_s(\tau) \frac{d}{d\tau} \frac{\langle \Delta\rho|_{\rm b} \rangle_{\vec{x}}}{\bar{\rho}_\gamma} , \tag{3.2.3}$$

$$= \mathcal{I}_s(z) \frac{Q'}{\bar{\rho}_\gamma} , \tag{3.2.4}$$

where, in the last step we define a heating rate function $Q' = \bar{\rho}_\gamma \frac{d}{d\tau} \frac{\langle \Delta\rho|_{\rm b} \rangle_{\vec{x}}}{\bar{\rho}_\gamma}$. A final step involves integrating the contribution from the redshifts at which energy injection occurred until recombination, which gives us the total distortion amplitude in terms of physical time t as

$$\{\mu, y\} = \int dz\, \mathcal{I}_{\{\mu,y\}}(z) \frac{dQ/dz}{\bar{\rho}_\gamma} = -\int dz\, \mathcal{I}_{\{\mu,y\}}(z) \frac{dQ/dt}{(1+z)H\bar{\rho}_\gamma} . \tag{3.2.5}$$

It can be checked that the s distortions vanish during the times of temperature shift (thermalization era) and after recombination. At very early times when CS, DCS and BS are fully functional, the tight-coupling approximation (TCA) holds true for photons and baryons i.e. $v_\gamma = v_b$. Moreover,

in the baryon rest frame, the total temperature anisotropy function $\Theta(\tau, x, \hat{n})$ is just the monopole moment (background temperature). In this case, $\Delta\rho|_b = 0$ and there are no SD. Similarly, at redshifts $z \geq 1100$, photons start free-streaming and travel without much interaction with the environment. The frequency spectrum stays the same throughout the propagation. We can then show that the term $\langle \Delta\rho|_{\rm b} \rangle_{\vec{x}}$ is conserved along time. In other words, the blackbody (or distorted blackbody) spectrum of photons coming from each direction freezes after recombination, as will be shown in the next section.

3.2.1 Expansion into Temperature Anisotropies

Next, we expand the right-hand side of Eq. (3.2.2) in anisotropy multipoles by following the formulation of [292]. First, the local density field is expressed using the local temperature field

$$\rho_\gamma(\tau, \vec{x}) = a_{\rm R} \langle T(\tau, \vec{x}, \hat{n})^4 \rangle_{\hat{n}} = a_{\rm R} \bar{T}^4 \langle (1+\Theta)^4 \rangle_{\hat{n}} \ , \tag{3.2.6}$$

$$n_\gamma(\tau, \vec{x}) = b_{\rm R} \langle T(\tau, \vec{x}, \hat{n})^3 \rangle_{\hat{n}} = b_{\rm R} \bar{T}^3 \langle (1+\Theta)^3 \rangle_{\hat{n}} \ , \tag{3.2.7}$$

where the constants are $a_R = \frac{\pi^2}{15}$, and $b_R = \frac{2\xi(3)}{\pi^2}$. The directional average sums the observable across the whole sky. The foreground temperature is written in terms of the background temperature $\bar{T}$ as a small perturbation Θ, $T(\tau, \vec{x}, \hat{n}) = \bar{T}(\tau)(1+\Theta)$. We work under the assumption that the perturbed part in temperature field is much less than the background i.e. $\Theta \ll 1$. This is justified at the CMB scales (where $\Theta \sim 10^{-5}$); however, we expect higher amplitudes in fluctuations at smaller scales where PBHs are expected to form. Nonetheless, we are still motivated to assume $\Theta \ll 1$ in this regime because of tight constraints on $f_{\rm PBH}$.

Furthermore, the energy excess $\Delta\rho$ can be expressed as a difference between the local density field and the density corresponding to a blackbody at local temperature [293]

$$\Delta\rho(\tau, \vec{x}) = a_{\rm R} \bar{T}^4 \left[\langle (1+\Theta)^4 \rangle_{\hat{n}} - \langle (1+\Theta)^3 \rangle_{\hat{n}}^{4/3} \right] \ , \tag{3.2.8}$$

$$= a_R \bar{T}^4 \left[2\langle \Theta^2 \rangle_{\hat{n}} - 2\Theta_{(0)}^2 + \frac{8}{3} \langle \Theta^3 \rangle_{\hat{n}} - 4\Theta_{(0)} \langle \Theta^2 \rangle_{\hat{n}} + \frac{4}{3} \Theta_{(0)}^3 + \mathcal{O}(\Theta^4) \right] \ , \tag{3.2.9}$$

where the subscript $\Theta_{(0)}$ denotes the monopole. In the second step, we expanded the terms in brackets in the Taylor series and kept the terms up to $\mathcal{O}(\Theta^3)$. We need the energy excess that is normalized to the background energy density to get to the heating rate. Hence, we divide by $\bar{\rho}$

on both sides of Eq. (3.2.9), and differentiate with respect to physical time to reach

$$\begin{aligned}\frac{\Delta\rho(\tau,\vec{x})|_{\rm b}}{\bar{\rho}_\gamma(\tau)} &= \frac{a_{\rm R}\bar{T}^4\left[\langle(1+\Theta)^4\rangle_{\hat{n}} - \langle(1+\Theta)^3\rangle_{\hat{n}}^{4/3}\right]_{\rm b}}{a_{\rm R}\bar{T}^4}\ , \\ &= \left[\left\langle 2\Theta^2 - 2\Theta_{(0)}^2 + \frac{8}{3}\Theta^3 - 4\Theta_{(0)}\Theta^2 + \frac{4}{3}\Theta_{(0)}^3\right\rangle_{\hat{n}} + \mathcal{O}(\Theta^4)\right]_{\rm b}\ , \qquad (3.2.10)\\ \dot{Q} &= \bar{\rho}_\gamma\frac{d}{dt}\frac{\Delta\rho(\tau,\vec{x})|_{\rm b}}{\bar{\rho}_\gamma(\tau)}\ , \\ &= \bar{\rho}_\gamma\frac{d}{dt}\left[\left\langle 2\Theta^2 - 2\Theta_{(0)}^2 + \frac{8}{3}\Theta^3 - 4\Theta_{(0)}\Theta^2 + \frac{4}{3}\Theta_{(0)}^3\right\rangle_{\hat{n},\vec{x}} + \mathcal{O}(\Theta^4)\right]_{\rm b}\ , \\ &= 4\bar{\rho}_\gamma\left[\left\langle\Theta\dot{\Theta} - \Theta_{(0)}\dot{\Theta}_{(0)} + 2\Theta^2\dot{\Theta} - \dot{\Theta}_{(0)}\Theta^2 - 2\Theta_{(0)}\Theta\dot{\Theta} + \Theta_{(0)}^2\dot{\Theta}_{(0)}\right\rangle_{\hat{n},\vec{x}} + \mathcal{O}(\Theta^4)\right]_{\rm b}\ . \qquad (3.2.11)\end{aligned}$$

Notice that the spatial average is over both position and angle. The superscript will be used to show the order of terms in the Taylor expansion, and the subscript will show the order of multipole (order zero is monopole, order one is dipole, and so on).

As already mentioned, the temperature fluctuations are larger than $\mathcal{O}(10^{-5})$ as we seek to explore scales smaller than Planck scales. Hence, it is necessary to go second-order in the Boltzmann equation, which predicts mode-mode coupling between the anisotropy multipoles, the resulting non-Gaussianity in the CMB temperature map and also the existence of the B-modes from scalar perturbations [294]. This information is in addition to the information obtained at the linear order which includes the precise prediction of the CMB angular power spectra (C_ℓ^{TT}, C_ℓ^{TE} and C_ℓ^{EE}). Second-order Boltzmann equations have been widely studied in literature and we will use the results from [295–301] to substitute the terms involving the time derivative of Θ in the baryon rest frame

$$\Theta'|_{\rm b} = \alpha_T'\left[\Theta^{\rm C1} + \Theta^{\rm C2}\right]_{\rm b}\ , \qquad (3.2.12)$$

wherein α_T is the Thomson scattering rate, and the two terms on the right-hand side are

$$\begin{aligned}\Theta^{\rm C1}|_{\rm b} &= -\Theta + \Theta_{(0)} - \Pi_{(2)}^1\ , \\ \Theta^{\rm C2}|_{\rm b} &= (\Theta - \Theta_{(0)})^2 - \Pi_{(2)}^2 + \delta_{\rm b}\Theta^{\rm C1}|_{\rm b}\ , \qquad (3.2.13)\end{aligned}$$

with Π and δ_b being the polarization contribution and dimensionless density perturbations for baryons. We can make use of Eqs. (3.2.12) and (3.2.13) to substitute the time derivative in Eq. (3.2.11) and after simplifying the terms, we get

$$\begin{aligned}\dot{Q} =& 4\bar{\rho}_\gamma\alpha_T'\left[\left\langle(\Theta-\Theta_{(0)})\Theta^{\rm C1} + (\Theta-\Theta_{(0)})\Theta^{\rm C2} + 2(\Theta-\Theta_{(0)})^2\Theta^{\rm C1}\Theta_{(0)}(\Theta-\Theta_{(0)})\Theta^{\rm C1}\right\rangle_{\hat{n},\vec{x}}\right. \\ &\left. + \mathcal{O}(\Theta^4)\right]_{\rm b}\ , \qquad (3.2.14)\end{aligned}$$

where, we also invoked the orthogonal property of the Legendre multipoles, $\langle\Theta_l\Theta_{l'}\rangle \propto \delta(l-l')\frac{2}{2l+1}$. Finally, we note that while switching from baryon rest frame to a arbitrary frame, the photon monopole and dipole terms are shifted by the factors '$\frac{a'}{a}v_b$' and '$-\hat{n}\cdot v_b$' respectively, while

the higher multipoles do not change (See the appendix of [292]). This gives the heating rate expression in another frame so that we can drop the subscript 'b'

$$Q' = 4\bar{\rho}_\gamma \alpha_T' \left[\left\langle \Theta^{\rm G}\Theta^{\rm C1} + \Theta^{\rm G}\Theta^{\rm C2} + 2(\Theta^{\rm G})^2\Theta^{\rm C1} + 2(\Theta_{(0)} + \frac{a'}{a}v_{\rm b})\Theta^{\rm G}\Theta^{\rm C1} \right\rangle_{\hat{n},\vec{x}} + \mathcal{O}(\Theta^4) \right] , \tag{3.2.15}$$

where $\Theta^{\rm G}$ represents that we are working with a generic arbitrary frame with the following expression

$$\Theta^{\rm G} \equiv \Theta - \Theta_{(0)} - \hat{n}\cdot\vec{v}_{\rm b} = \hat{n}\cdot(\vec{v}_\gamma - \vec{v}_{\rm b}) + \Theta_{(l\geq 2)} \ . \tag{3.2.16}$$

In the next subsection, we present the heating rate in a more concise format suitable for implementation in `CLASS` and provide the most accurate approximation scheme for computing the SD. But before finishing this discussion, we note a few important points:

- The redefined heating rate Eq. (3.2.15) depends on three terms broadly; '$\Theta_{(l\geq 2)}$' '$\hat{n}\cdot v_\gamma$' and '$-\hat{n}\cdot v_b$'. The first term is gauge-invariant, while the second and third terms are not. However, the combination '$\hat{n}\cdot v_\gamma - \hat{n}\cdot v_b$' is gauge-invariant [292]. Hence, the heating rate is also gauge-invariant.

- In the TCA, where the Thomson scattering rate is extremely large and the perturbations in density and velocity will be suppressed, leading to vanishing higher multipoles ($l \geq 2$) [293]. Moreover, a polarized pattern is produced in the temperature anisotropies when a GW passes through the quadrupole, stretching the pattern. Since the quadrupole moment is suppressed, the polarization terms also vanish. The result is a vanishing heating rate.

- When the photons free-stream, the Thomson scattering stops or $\alpha_T' \to 0$. The heating rate vanishes again in this limit.

3.2.2 Mathematical Formulation of Acoustic Dissipation

First, we start the analysis by considering only the leading-order terms in the heating rate. By leading order, we mean that the heating rate is second-order in perturbation theory. If we disregard the terms in Eq. (3.2.15) where the overall order is greater than two, we are left with

$$Q' = 4\alpha_T'\bar{\rho}_\gamma \langle \Theta^{\rm G}\Theta^{\rm C1}\rangle_{\hat{n},\vec{x}} \ . \tag{3.2.17}$$

We are interested in studying how the initial conditions from inflation influence this heating rate. To do so, we must trace the temperature anisotropies back to their origin in curvature perturbations. In Appendix A, we show how this is done with the help of the transfer function. We directly use its result to show the two-point correlator of temperature anisotropies

$$\langle \Theta^{\rm G}\Theta^{\rm C1}\rangle_{\hat{n},\vec{x}} = \int \frac{dk\, k^2}{(2\pi)^3} \sum_\ell 4\pi(2\ell+1)\Theta_\ell^{\rm G}(k)\Theta_\ell^{\rm C1}(k)P_{\mathcal{R}}(k) \ . \tag{3.2.18}$$

To recall, the dimensionful and dimensionless power spectra of curvature perturbations are respectively defined as

$$\langle \mathcal{R}(\vec{k})\mathcal{R}^*(\vec{k}')\rangle = P_{\mathcal{R}}(k)\,\delta^{(3)}(\vec{k}-\vec{k}') \ , \tag{3.2.19}$$

$$\mathcal{P}_{\mathcal{R}}(k) \equiv \frac{k^3}{2\pi^2} P_{\mathcal{R}}(k) \ . \tag{3.2.20}$$

The expansion terms Θ in Legendre space are well known, at least for the first few ℓ's. We list them down below

$$\Theta_0^{\rm G} = \Theta_0^{\rm C1} = 0 \ , \tag{3.2.21}$$

$$\Theta_1^{\rm G} = -\Theta_1^{\rm C1} = \Theta_1 - \frac{k}{3}v_{\rm b} = \frac{k}{3}(v_\gamma - v_{\rm b}) \ , \tag{3.2.22}$$

$$\Theta_2^{\rm G} = \Theta_2 \ , \qquad \Theta_2^{\rm C1} = -\Theta_2 + \frac{1}{10}\left(\Theta_2 + \Theta_0^{\rm P} + \Theta_2^{\rm P}\right) \ , \tag{3.2.23}$$

where the superscript 'P' stands for polarization. To compactify the heating rate formula, we define the source function [293]

$$\begin{aligned} S_{\rm ac}(k,\tau) &\equiv -\sum_\ell (2\ell+1)\Theta_\ell^{\rm G}(k)\Theta_\ell^{\rm C1}(k) \ , \\ &= \frac{k^2(v_\gamma - v_{\rm b})^2}{3} + \sum_{l\geq 2}(2\ell+1)\Theta_\ell^2 - \frac{1}{2}\Theta_2(\Theta_2 + \Theta_0^{\rm P} + \Theta_2^{\rm P}) \ , \\ &= \frac{k^2(v_\gamma - v_b)^2}{3} + \frac{9}{2}\Theta_2^2 - \frac{1}{2}\Theta_2(\Theta_0^{\rm P} + \Theta_2^{\rm P}) + \sum_{l\geq 3}(2\ell+1)\Theta_\ell^2 \ , \end{aligned} \tag{3.2.24}$$

using which, Eq. (3.2.15) becomes

$$Q' = -4\bar{\rho}_\gamma \alpha_T' \int \frac{dk\,k^2}{2\pi^2} P_{\mathcal{R}}(k) S_{\rm ac}(k,\tau) \ , \tag{3.2.25}$$

$$= -4\bar{\rho}_\gamma \alpha_T' \int \frac{dk}{k} \mathcal{P}_{\mathcal{R}}(k) S_{\rm ac}(k,\tau) \ . \tag{3.2.26}$$

The subscript 'ac' signifies that it is the dissipation of primordial ACoustic oscillation that sources the heating rate in Eq. (3.2.26). This also implies that the SD (as we shall see later) created from Eq. (3.2.26) are not due to the explicit energy injection process, but rather due to a perturbation losing its energy to the plasma through diffusion. Therefore, we can also classify acoustic dissipation as a "non-injection process" that sources the SD.

It should be noted that the terminology defined in this section or the following sections is just one of the ways to formulate the mathematics behind SD. The chosen way of defining the heating rate that incorporates the k-integral of the product of the curvature power spectrum and the source function, which is followed by the redshift integral of Q' (explained later in this section), fits well with the numerical implementation within the Boltzmann solver `CLASS`. The notations of Ma and Bertschinger have been used in the `CLASS` code, and we shall also use the same notation from here onward [270, 271, 302].

We are working in the epoch much before recombination, and it is reasonable to use the TCA. Higher multipoles ($\ell > 2$) are suppressed by the powers of $\frac{k}{2\alpha_T'}$. Nonetheless, to ensure better

precision, we keep the terms up to the octopole or $\ell = 3$ in the source function

$$S_{\rm ac}^{\rm (A1)}(k,\tau) = \underbrace{\frac{(\theta_\gamma - \theta_b)^2}{3k^2}}_{\rm dipole} + \underbrace{\frac{9}{2}\left(\frac{\sigma_\gamma}{2}\right)^2 - \frac{1}{8}\left(\frac{\sigma_\gamma}{2}\right)(G_{\gamma 0} + G_{\gamma 2})}_{\rm quadrupole} + \underbrace{7\left(\frac{F_{\gamma 3}}{4}\right)^2}_{\rm octopole} \ . \tag{3.2.27}$$

The superscript $A1$ is used to classify different approximation schemes, which will be listed later. Let us list the terminology below and request the user to refer [302] for more details:

$$F_{\gamma\ell} = 4\Theta_\ell \ , \tag{3.2.28}$$

$$G_{\gamma\ell} = 4\Theta_\ell^{\rm P} \ , \tag{3.2.29}$$

$$\sigma_\gamma = \frac{1}{2}F_{\gamma 2} = 2\Theta_2 \ , \tag{3.2.30}$$

$$\theta_\gamma = \frac{3k}{4}F_{\gamma 1} = k^2 v_\gamma = 3k\Theta_1 \ , \tag{3.2.31}$$

$$\theta_{\rm b} = k^2 v_{\rm b} \ , \tag{3.2.32}$$

where the superscript P stands for the polarization multipoles, σ_γ is the photon shear and θ_i are the velocity divergences for photon and baryons ($i = \gamma, b$). As already mentioned, the heating rate contribution Eq. (3.2.26) has to be integrated over redshifts too, because what a spectrophotometer observes is a distortion in the blackbody spectrum of CMB photons combined throughout history, integrated over all the scales of interest. Therefore, we first define an integration kernel $K_\mu(z,k)$ and $K_y(z,k)$ to be integrated over (k,z)

$$K_s(k,z) \equiv -\mathcal{I}_s(z)\,\frac{4\dot{\tau}\,z}{H}\,S_{\rm ac}(k,z) \ , \tag{3.2.33}$$

so that the total s distortion is given by

$$s = \int d\ln z \int d\ln k \ K_s(k,z)\ \mathcal{P}_{\mathcal{R}}(k) \ . \tag{3.2.34}$$

The behaviour of the integration kernel can be better understood from the 2-dimensional contour plot shown in Fig. 3.2. The darker regions within the two subplots tell us at which scales and redshifts the $s = \mu, y$ distortions receive the most contribution from the integration kernel, assuming a scale-invariant curvature power spectrum. A distinction between the contributions from μ distortions and y distortions is clearly visible. The μ distortion acts dominantly at the early times ($10^{4.5} < z < 10^{6.2}$) whereas, the y distortions becomes dominant at late times ($10^{2.9} < z < 10^{4.8}$).

On the other hand, if the power spectrum has a sharply peaked nature, the dark regions would be much more concentrated near the peak wavenumber k_*. Moreover, the position of the peak k_* also determines how far in the past (in terms of redshift) we need to start the integration of Eq. (3.2.34). For example, if $k_* = 10^4 h$ Mpc^{-1}, we need to start from as early as $z = 10^{6.5}$. The reason is straightforward; if the peak of the curvature power spectrum lies at a smaller scale (or larger k's), the corresponding scale would have entered the horizon at very early times, and it would have started dissipating its energy into the photon-baryon fluid earlier. Conversely, if the peak is situated at a larger scale, for example $k_* = 10^2 h$ Mpc^{-1}, the corresponding scale would

have entered the horizon at later times, and that is when it would have provided the dominant contribution to the spectral distortion.

It is important to mention the comoving sound horizon (r_s) and the comoving diffusion horizon (r_D) which are also shown in Fig. 3.2

$$r_s = \int_0^\tau c_{\rm s}(\tilde{\tau}) d\tilde{\tau} \ , \tag{3.2.35}$$

$$r_{\rm D} = \frac{2\pi}{k_{\rm D}} = \left[\int dz \frac{c_s^2}{2\alpha_T' H}\left(\frac{R^2}{1+R} + \frac{16}{15}\right)\right]^{1/2} \ , \tag{3.2.36}$$

where, the sound speed and baryon to photon ratio are respectively, $c_{\rm s}^2 = \frac{1}{3(1+R)}$ and $R = \frac{3\bar{\rho}_{\rm b}}{4\bar{\rho}_\gamma}$. The comoving scales cross the sound horizon at $k = \frac{2\pi}{r_s}$ and the diffusion horizon at $k = \frac{2\pi}{r_{\rm D}}$, whereas the scale corresponding to Thomson mean free path is $k = 2\pi\alpha_T'$. It can be inferred that the scales contribute to the SD when they are considerably sub-Hubble and at the same time are far larger than the Thomson mean free path. This means that the diffusion at those scales will start at a later time when they cross the diffusion scales (since $r_s > r_{\rm D}$).

One can deduce that the ratio '$\frac{k}{\alpha_T'}$' plays a key role in filtering out the scales of interest. Moreover, the TCA is highly efficient at the scales $\alpha_T' \gg k$, where k is the mode which already crossed the physical horizon. Putting together, the higher multipoles ($\ell \geq 3$) are suppressed by the same factor, i.e. $\frac{k}{\alpha_T'} \ll 1$ because at these scales any inhomogeneities are rapidly wiped out.

Even for the term with lower multipoles in Eq. (3.2.27), photon and baryon velocities are nearly identical under the TCA, and quadrupole anisotropies (including the polarization anisotropies) are very small, and the individual terms are given by the following expressions from solving the Boltzmann equation under the TCA,

$$(\theta_\gamma - \theta_b)/k \sim \frac{R}{\sqrt{1+R}}\sigma_\gamma \ , \tag{3.2.37}$$

$$G_{\gamma_0} = \frac{1}{5}G_{\gamma 2} = \frac{\sigma_\gamma}{2} \ , \tag{3.2.38}$$

$$F_{\gamma 3} \simeq \frac{6}{7}\frac{k}{\dot{\alpha}_T'}\sigma_\gamma \ , \tag{3.2.39}$$

which suggests that we can even drop the octopole contribution ($\frac{k}{\alpha_T'} \ll 1$). Using these expressions, we compute Eq. (3.2.27) to obtain

$$S_{\rm ac}(k,\tau) \simeq \frac{9}{2}\left(\frac{\sigma_\gamma}{2}\right)^2 - \frac{1}{8}\left(\frac{\sigma_\gamma}{2}\right)(G_{\gamma 0} + G_{\gamma 2}) \simeq \frac{15}{4}\left(\frac{\sigma_\gamma}{2}\right)^2 \ . \tag{3.2.40}$$

An important point to mention here: The scheme Eq. (3.2.40) under the approximation $\frac{k}{\alpha_T'} \ll 1$ is not necessarily true for very small scales (or very large values of k). It has been demonstrated through analytical calculations that baryonic infall can play a non-negligible role. Baryonic infall is the baryons falling inside the potential well, proportional to the Newtonian potential ψ. On the other hand, photons tend to resist the infall due to their radiation pressure. This leads to an enhanced bulk velocity in the baryon-photon fluid, thus sourcing the dipole $\sim (\theta_\gamma - \theta_b)$. Such an effect is not significant at larger scales because photon radiation pressure also prevents baryons from falling inside the potential well and thus isotropizes the velocities. Consequently, the dipole

term becomes larger than the quadrupole term and the source function becomes [281, 303]

$$S_{\rm ac}(k,\tau) \simeq \frac{(\theta_\gamma-\theta_b)^2}{3k^2} \simeq \frac{(k^2R\psi/\alpha_T')^2}{3k^2}\ . \tag{3.2.41}$$

This effect becomes significant only at large k tails of the source function and at late times, when the baryon energy density is large. This can be seen in Fig. 3.5, where the dipole term leads the large-k tail. One can also notice how accurately the quadrupole term tracks the overall source function $S_{\rm ac}^{(\rm A1)}(k,\tau)$, strengthening our reasoning made so far. From what follows, we briefly discuss the approximation schemes other than Eq. (3.2.27), and point the readers towards [292] for a more elaborate discussion.

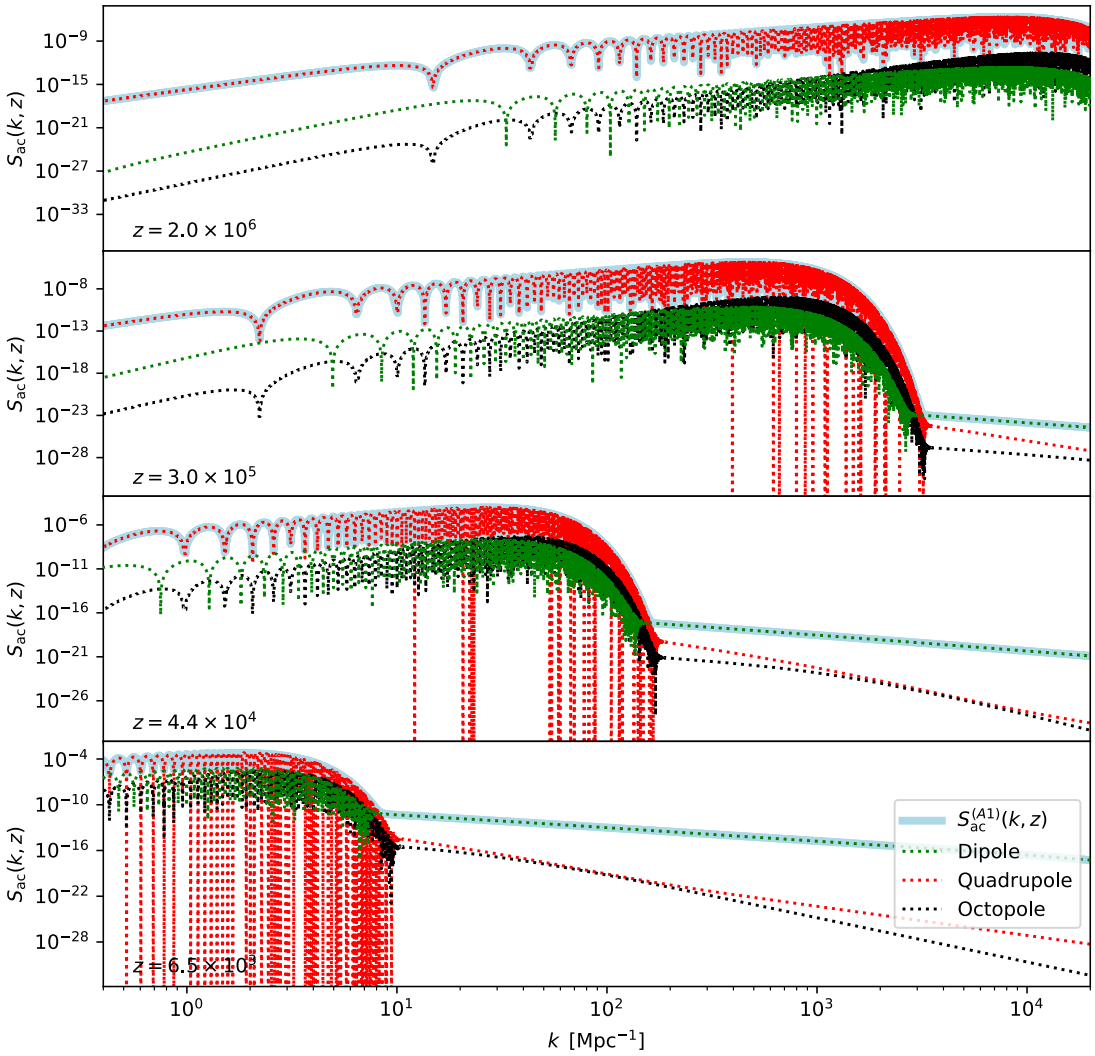

Figure 3.5: *The figure shows how individual terms contribute to the total heating rate Eq. (3.2.27). These individual contributions are shown at four separate redshifts.*

3.2.3 Various Approximation Schemes

Apart from the first approximation scheme discussed in Eq. (3.2.27), we present three additional approximation schemes with varying levels of accuracy and computational efficiency. The main features and assumptions of these schemes are summarized in the bullet points below.

- The next scheme also exploits the TCA and reduces to an analytic expression, which was first studied in [293, 304]. In Newton gauge, the quadrupole moment or photon shear relates to the velocity divergence via $\sigma_\gamma \simeq \frac{16}{45\dot{\tau}}\theta_\gamma^N$, which can be substituted in Eq. (3.2.40) to keep only the dependency on photon velocity divergence

$$S_{\rm ac}(k,\eta) \simeq \frac{16}{135\dot{\tau}^2}(\theta_\gamma^N)^2 \ . \tag{3.2.42}$$

- It is possible to analytically approximate θ_γ using the WKB solution, which in the (sub-sound) super-sound-Horizon limit(s) reads [281, 302]

$$\theta_\gamma^N = \begin{cases} A_{\rm WKB}\frac{3kc_s}{(1+R)^{1/4}}\sin(kr_s)e^{-(k/k_{\rm D})^2}, & k \gg \frac{2\pi}{r_{\rm s}(\tau)} \ , \\ A_{\rm WKB}\frac{kc_s}{(1+R)^{1/4}}\sin(kr_s) \ , & k \ll \frac{2\pi}{r_{\rm s}} \ . \end{cases} \tag{3.2.43}$$

- It was shown in [293, 304] that Eq. (3.2.43) can be further simplified by averaging out the fast oscillations involving the sinusoidal term, since the product with a smooth power spectrum will make only the average around these oscillations relevant. Hence, if we use the average value $\langle\sin^2(kr_s)\rangle = \frac{1}{2}$, we get the next approximation scheme

$$S_{\rm ac}^{(A2)}(k,\tau) \simeq \frac{8A_{\rm WKB}^2k^2}{45{\alpha_T'}^2(1+R)^{3/2}}e^{-2(k/k_{\rm D})^2} \ , \qquad k \gg \frac{2\pi}{r_{\rm s}(\tau)} \ . \tag{3.2.44}$$

  The above simplification saves a good amount of computation because otherwise, we would have to resolve oscillations with frequencies of the order $\mathcal{O}(10^3)$ if we wanted to include scales as small as $k \sim 5\times10^4$ (which we do, as we shall see).

- The Ref. [304] also went a step further in simplification, with the assumption that one is working well within the radiation-dominated era. In such a case, we can approximate the baryon to photon energy density ratio and sound speed as $R \ll 1$ and $c_s^2 \simeq \frac{1}{3}$ to reach the third approximation scheme

$$S_{\rm ac}^{(A3)}(k,\tau) = \frac{A_{\rm WKB}^2k^2}{\alpha_T'}(\partial_\tau r_{{\rm D},R=0}^2)\exp^{-2(k/k_D)^2} \ , \tag{3.2.45}$$

  where $A_{\rm WKB}$ is the WKB normalization constant, which can be computed from the initial conditions.

- Finally, we lay down the fourth approximation, first studied in [292], which also happens to be the most accurate technique for computing the acoustic dissipation source function. The so-called "Hybrid scheme" is provided below with its salient features

$$S_{\rm ac}^{(A4)}(k,\tau) \equiv \begin{cases} \frac{2}{9}\sin^2(kr_{\rm s})\,S_{\rm ac}^{(A2)}(k,\tau) & \text{for } kr_{\rm s} < \frac{\pi}{4} \ , \\ \min\left[S_{\rm ac}^{(A1)}, S_{\rm ac}^{(A2)}\right] & \text{for } \frac{\pi}{4} \le kr_{\rm s} < \pi \ , \\ \max\left[S_{\rm ac}^{(A2)}, \frac{1}{3}(kR\psi/\alpha_T')^2\right] & \text{for } kr_{\rm s} \ge \pi \ . \end{cases} \tag{3.2.46}$$

- We have used three different schemes in three different regimes. Starting from the super-sound horizon regime, the WKB solution described in Eqs. (3.2.43) and (3.2.44) has been used. This is more efficient than using Eq. (3.2.27), where we need to compute the terms up to $\ell \geq 3$. The third (high-k) regime is chosen to incorporate the baryonic infall effect at very small scales, as noted in Eq. (3.2.41). In the intermediate regimes, it is found that Eq. (3.2.44) can be as accurate as the scheme Eq. (3.2.27), and it requires a coarser grid, which makes it faster. Overall, this Hybrid scheme Eq. (3.2.46) has been carefully constructed, striking a balance between processing speed and the accuracy of the result.

3.2.4 Integrating the Source Function over Redshift

One final step remains before we can compute the SD: Integrating every possible contribution from acoustic dissipation from the times as early as the beginning of the radiation era to the end of recombination. This is because when the de Sitter phase lasted for around $55 - 60$ e-folds, the curvature perturbations of varying amplitude were generated on a broad range of comoving scales, from 10^{-2} Mpc^{-1} to 10^{20} Mpc^{-1}. Of course, choosing a narrowly peaked power spectrum, such as a Dirac-Delta spectrum or a lognormal spectrum of narrow width, would mean that the perturbations are enhanced across a small span in Fourier space.

Additionally, we aim to constrain those scales that correspond to the heavy-mass PBHs that result from the collapse of the corresponding perturbations after horizon reentry. The super-solar mass range, i.e. $10^4\ M_\odot$ to $10^{12}\ M_\odot$, is exciting as the PBHs with the mass at formation in this range provide the seeds for the Supermassive black holes (SMBHs) that are present in all the galaxies observed till date. We will come back to the discussion of PBHs as SMBH seeds in detail in Chapter 5.

The key takeaway from this is that we are particularly interested in the range of comoving scales whose perturbations would have generated PBHs in the supermassive range. Turns out that these scales reentered the horizon early in the radiation era. If they had large enough amplitude in perturbations, they would have been imprinted in the μ distortions via acoustic dissipation. In the remaining part of the text, we will keep the discussion of μ distortions in the centre. However, we will regularly retain the relevance of y distortions wherever necessary. With that in mind, we replace the s distortion with the μ distortion, and define the corresponding window function below

$$\begin{aligned} w_\mu(k) &\equiv \int d\ln z\ K_\mu(k,z), \\ &= -\int dz\, \mathcal{I}_\mu(z)\, \frac{4\alpha_T'(z)\, S_{\rm ac}(k,z)}{(1+z)H(z)}\ . \end{aligned} \tag{3.2.47}$$

Using the definition of the window function, we rewrite Eq. (3.2.5) as

$$\mu = \int dk \frac{k^2}{2\pi^2} P_{\mathcal{R}}(k) W_\mu(k) = \int \frac{dk}{k} \mathcal{P}_{\mathcal{R}}(k) W_\mu(k)\ . \tag{3.2.48}$$

A nice way to represent the μ amplitude, after integrating with respect to both k and z, is in the form of a numerical fit. The first numerical fit was introduced in [304] and is equivalent to the

approximation scheme Eq. (3.2.44). It will be referred to as $W_\mu^{(\mathrm{F1})}$ and given by

$$W_\mu^{(\mathrm{F1})}(k) = 2.8 A_{\mathrm{WKB}}^2 \left[\exp\left\{ -\frac{(\hat{k}/1360)^2}{1+(\hat{k}/260)^{0.3}+\hat{k}/340} \right\} - \exp\left\{ -(\hat{k}/32)^2 \right\} \right], \tag{3.2.49}$$

where the wavemode has been made dimensionless, $\hat{k} = k/[1\mathrm{Mpc}^{-1}]$. The numerical fit $W_\mu^{(\mathrm{F1})}$ was further simplified in [305, 306], albeit by compromising the accuracy of the μ window function, which we will denote with $W_\mu^{(\mathrm{F2})}$

$$W_\mu^{(\mathrm{F2})}(k) = 2.8 A_{\mathrm{WKB}}^2 \left[\exp\left\{ -\frac{\hat{k}}{5400} \right\} - \exp\left\{ -(\hat{k}/31.6)^2 \right\} \right] . \tag{3.2.50}$$

It will be shown in Section 3.3 that this numerical fit predicts weaker μ distortion constraints on the curvature power spectrum by roughly an order of magnitude, when compared with the other two numerical fits. The third and final numerical fit was introduced in [292], which uses the hybrid approximation Eq. (3.2.46). This has been obtained for the ΛCDM cosmology, the best-fit parameters from the Planck dataset [307]. The scheme has been implemented in `CLASS` using a second-order Principal Component Analysis (PCA) of SD at the frequencies sensitive to the FIRAS instrument [178] [12].

$$W_\mu^{(\mathrm{F3})}(k) = \exp\left[\sum_{n=0}^{6} w_n \ln\left(\frac{k}{1\,\mathrm{Mpc}^{-1}} \right) \right] , \tag{3.2.51}$$

where the constant coefficients ω_n are given in Table 3.1.

n	ω_n	n	ω_n
0	-2.78	**4**	-1.1864×10^{-2}
1	1.58	**5**	2.0739×10^{-3}
2	-1.33×10^{-1}	**6**	-1.0633×10^{-4}
3	1.477×10^{-2}		

Table 3.1: *We tabulate the coefficients for the numerical fitting of window function $W_\mu(k)$ (see Eq. (3.2.51)).*

3.3 Observational Constraints For a Peaked Spectrum

We are now in a position to determine how to compute the s distortions using the approach explained so far. It is intuitive from Eq. (3.2.48) that the integral is separated into two components: the first component is the curvature power spectrum, which serves as initial conditions for the source. The second component is a time-dependent and scale-dependent transfer function that transports these initial conditions into what we expect to observe today, which in this case is the spectral amplitude of a distorted photon blackbody.

[12] PCA helps to reduce the dimensionality of a dataset by identifying the principal “uncorrelated" or “independent" components that provide the maximum information about the dataset and the rest of the “correlated" components discarded from the analysis.

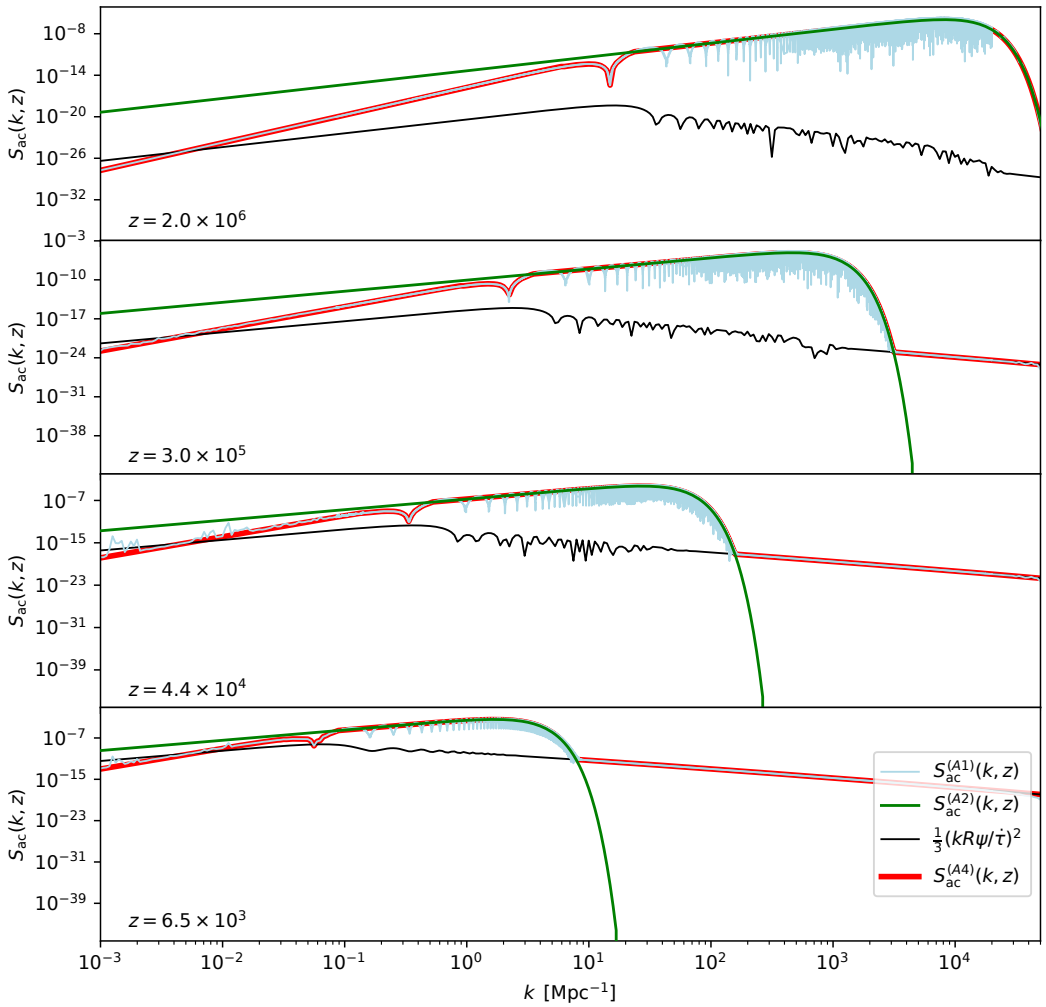

Figure 3.6: *The figure draws a comparison between the source functions computed using the approximation schemes discussed in Section 3.2.2. The scheme (A2) tracks the scheme (A1) accurately in the small-k limit($k \lesssim 10\text{Mpc}^{-1}$), however both the schemes fail to account for the baryonic infall feature at small scales ($k \geq 10\text{Mpc}^{-1}$), shown with the black line. The new scheme (A4) accurately interprets this effect and works at all the scales of interest.*

If the variable corresponding to the initial conditions is a stochastic variable, then a linear transfer function (computed via the linear Boltzmann equation) will simply act as a linear operator that transports the variable on the time axis and causes a shift in the amplitude. However, a linear operation conserves the statistical moments of the probability distribution associated with the stochastic variable. The shape of the initial probability is not conserved if the transfer function non-linearly evolves the initial conditions. This implies that, even if the stochastic variable $\mathcal{R}_k$ were a Gaussian variable, the temperature anisotropies would deviate from Gaussianity if we worked at second-order in the Boltzmann equation. [308]

On the other hand, if we assume the presence of an intrinsic non-Gaussianity in $\mathcal{R}_k$ that is

sourced from inflation, the corresponding non-Gaussian shape of the probability distribution would also be conserved if it is transported via the linear transfer function. This non-Gaussianity in the temperature anisotropies is different from the one introduced by the non-linear transfer function. It is known that the non-Gaussianity from the non-linear relationship between the temperature anisotropy and the curvature perturbations is negligible [308], which is why we shall work with a linear mapping between $\mathcal{R} \to \Theta_\ell$. We leave the discussion of non-Gaussian initial conditions for Chapter 4, and assume Gaussianity in this section.

We consider that the curvature power spectrum is characterized by a Dirac-Delta function, as shown below

$$\mathcal{P}_\mathcal{R}(k) = \frac{k^3}{2\pi^2} P_\mathcal{R}(k) = A k_* \delta(k - k_*) \ , \tag{3.3.1}$$

where A represents the spectral amplitude and k_* is the peak wavemode. In real space, the variance relates to the power spectrum by

$$\left\langle \mathcal{R}^2(\vec{x}) \right\rangle = \int_0^\infty \frac{dk}{k} \mathcal{P}_\mathcal{R}(k) = A \ . \tag{3.3.2}$$

What this means is that the perturbation exists only at a single wavemode k_* and zero elsewhere. This is, of course, not physical because almost every inflation model that predicts an enhanced perturbation predicts it for a range of scales (also recall the steepest allowed power spectrum slope [205]). Nonetheless, this feature simplifies the calculations for us while also providing a picture of what to expect in the presence of a more realistic power spectrum. We can already see Eq. (3.2.48) that $\mu(k_*) = A\, W_\mu(k_*)$.

The constraints on the amplitude A from the non-detection of s distortions are shown in the left panel of Fig. 3.7. Each datapoint in this plot represents the magnitude of the s distortion saturated against the FIRAS upper bound (95 % confidence limit), computed using `CLASS`, corresponding to a single peak wavemode on the X-axis. In other words, the Y-axis in the contour plot stuck to the ceiling represents the quantity $s_{\rm FIRAS}/W_s(k_*)$, where $s_{\rm FIRAS}$ is given by [275, 309]

$$s_{\rm FIRAS} = \begin{cases} 4.7 \times 10^{-5}, & s = \mu \\ 1.5 \times 10^{-5}, & s = y. \end{cases} \tag{3.3.3}$$

The same figure (left panel of Fig. 3.7) depicts the approximation scheme Eq. (3.2.46) alongside the numerical fits $W_\mu^{(\rm F3)}(k)$, $W_\mu^{(\rm F2)}(k)$ and $W_\mu^{(\rm F1)}(k)$. In the right panel of the same figure, we show the fraction of these numerical fits and the approximation scheme Eq. (3.2.46) to check the scale-dependence of the variation between them. It is found that the difference between the schemes Eq. (3.2.44) and Eq. (3.2.46) is negligible for the scales of our interest, hence, we have not shown the constraints from the approximation scheme Eq. (3.2.44). A consequence of this analysis is that the hybrid scheme, which also includes the effects of baryonic infall on the dipole moment at small scales, is insignificant for the s distortions, at least for the range of scales shown here.

It is expected that the difference between these schemes would be noticeable in the extremely large or small k_* values. However, the amplitude of s distortions becomes much smaller at those scales compared to the current sensitivity of FIRAS. When the future-based experiments probe an

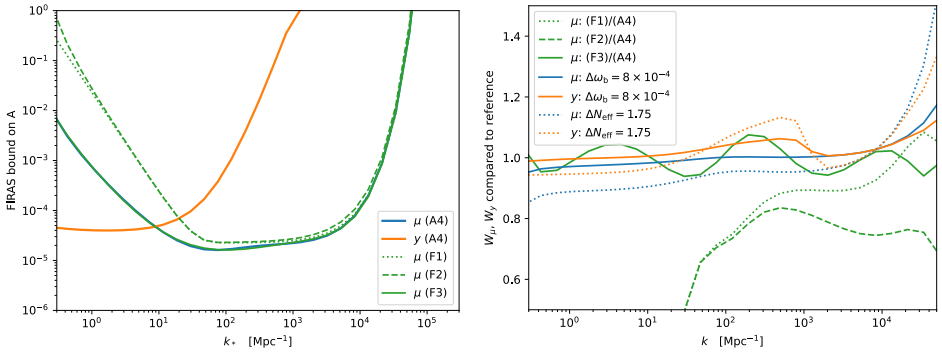

Figure 3.7: ***Left Panel:*** *Bounds on the curvature power spectrum amplitude from FIRAS with respect to the peak of the peak comoving wavenumber of the spectrum. The different discussed cases are for the window functions computed using the accurate scheme (A4), and the three numerical fits to the window function discussed in this section. The fit (F3) agrees very well with the accurate scheme (A4).* ***Right Panel:*** *Apart from the ratio of the numerical fits with the accurate scheme, we also express the change in the window function from the scheme (A4) when varying the most sensitive cosological parameters* $N_{\rm eff}$ *and* ω_b *in dotted lines and solid lines, respectively.*

even smaller range of scales ($k_* \gg 10^4 \mathrm{Mpc}^{-1}$), the deviation in the hybrid scheme compared to the conventional scheme is expected to provide insights into the nature of gravitational potential at such small scales.

The less efficient behaviour of the numerical fits $W_\mu^{(\mathrm{F1})}(k)$ and $W_\mu^{(\mathrm{F2})}(k)$ is clearly visible at the large scales ($k_* < 50$ Mpc^{-1}). Our analysis says that these fits fail to construct accurate branching ratios for the different types of SD, which is achieved in the PCA approach utilized in [292, 310]. On the large-k limit ($k_* > 100$ Mpc^{-1}), these fits are able to reach the accuracy upto 30%, whereas the numerical fit $W_\mu^{(\mathrm{F3})}(k)$ is able to reach an accuracy of less than 10% at all the scales of interest.

Before ending this section, we briefly talk about the dependency of the discussed results on the cosmological parameters. The standard ΛCDM model of cosmology is fully described using the set of six cosmological parameters $\{\omega_{\rm m}, \omega_{\rm b}, N_{\rm eff}, h, T_{\rm cmb}, Y_{\rm He}\}$. Since these parameters govern the growth and evolution of the curvature perturbations, it is necessary to check the sensitivity of the results, particularly within the variation allowed by the confidence intervals from BAO, BBN, FIRAS and Planck. The right panel of Fig. 3.7 shows the result dependency on the most sensitive parameters $\mathrm{N_{eff}}$ and ω_b. The variation in the parameters is very large and the resulting movement in the window functions is about 20% for the interesting scales. It can be concluded that as long as the uncertainty in the cosmological parameters is not too large (which is not at present, thanks to the precision-based observations), the SD of either type do not drastically change with the variation in these parameters. For this analysis, the 1σ intervals taken by us are $\sigma(\omega_{\rm cdm}) = 0.00090$, $\sigma(\omega_{\rm b}) = 0.00012$, $\sigma(N_{\rm eff}) = 0.35$, $\sigma(h) = 0.0038$, $\sigma(Y_{\rm He}) = 0.0006$, and $\sigma(T_{\rm cmb}) = 0.00057$ from [5, 178].

CHAPTER 4

Non-Gaussianity in Spectral Distortions

Our notion that the inflationary fluctuations were Gaussian relies on the assumption that the amplitude of the oscillations of these fluctuations is suppressed relative to the background energy density. However, this notion is strictly challenged at the scales not probed by the CMB measurements ($k \gg 0.05\text{Mpc}^{-1}$), where PBHs are expected to form. A deviation from Gaussianity is automatically expected if the perturbation theory breaks and perturbations at different scales interact. By definition, we can extract all the information about a Gaussian PDF from its first moment (mean) and second moment (variance). Any higher-order moment either vanishes due to symmetry (odd-point correlators) or, is expressible as a function of the second moment (even-point correlators); the latter property is a consequence of Wick's theorem.

This indicates that to detect or quantify the degree of non-Gaussianity associated with a statistical variable, we must look beyond its variance. Looking for non-Gaussianity in arbitrary data requires exploring a virtually infinite number of ways the data could be correlated. One way to distinguish between different types of non-Gaussianities is to look for specific patterns of spatial correlations in the data. This corresponds to different shapes of bispectrum (or trispectrum, to break the degeneracy in the bispectrum) in Fourier space. We summarize the following three popular models of non-Gaussianity with their distinct shapes of the bispectrum [311, 312]:

- **Local non-Gaussianity:** This type of non-Gaussianity is strongly motivated by the fact that the relative temperature fluctuations are significantly smaller than unity, or $\frac{\Delta T}{T} \approx 10^{-5}$, so that a perturbed non-Gaussian variable can be expanded via Taylor series in terms of its Gaussian reference value

$$A_{\text{NG}}(x) = A_{\text{G}}(x) + \frac{3}{5} f_{\text{NL}} (A_{\text{G}}^2(x) - \langle A_{\text{G}}^2(x) \rangle) + \frac{9}{25} g_{\text{NL}} A_{\text{G}}^3(x) + \dots \,, \tag{4.0.1}$$

  where the coefficients $f_{\text{NL}}, g_{\text{NL}}, \dots$ are the non-Gaussianity parameters corresponding to each order in expansion and the prefactors have been set by convention [313]. We have

subtracted the variance from even-point correlators so that the average of $A_{\rm NG}(x)$ is zero. Generally, the covergence is rapid for $A_{\rm NG} \equiv \mathcal{R}$, and thus, it is sufficient to truncate the series by neglecting the terms beyond $f_{\rm NL}$. Local non-Gaussianity is one of the most studied models owing to its simplicity. The bispectrum is related to the local non-Gaussianity parameter via

$$B^{\rm loc}_{\mathcal{R}} = \frac{6}{5} f^{\rm loc}_{\rm NL}\Big(P_{\mathcal{R}}(k_1)P_{\mathcal{R}}(k_2) + P_{\mathcal{R}}(k_2)P_{\mathcal{R}}(k_3) + P_{\mathcal{R}}(k_1)P_{\mathcal{R}}(k_3)\Big)\,, \tag{4.0.2}$$

where the comoving wavenumber form a closed triangle, i.e. $\vec{k}_1 + \vec{k}_2 + \vec{k}_3 = 0$. A well-known model that predicts a local non-Gaussianity is the curvaton model [314, 315]. Other models include hybrid inflation and modulated reheating [316, 317]. We shall come back to local non-Gaussianity when we analyse SD distortions in the presence of primordial non-Gaussianity.

- **Equilateral non-Gaussianity:** An equilateral shape in the bispectrum is expected in the models of inflation that feature a non-canonical kinetic term [318–320]. The bispectrum in this case is given by [321]

$$\begin{aligned} B^{\rm eq}_{\mathcal{R}} = \frac{3}{5} f^{\rm eq}_{\rm NL}\Big(&- 3P_{\mathcal{R}}(k_1)P_{\mathcal{R}}(k_2) - 2P^{2/3}_{\mathcal{R}}(k_1)P^{2/3}_{\mathcal{R}}(k_2)P^{2/3}_{\mathcal{R}}(k_3) \\ &+ 6P^{1/3}_{\mathcal{R}}(k_1)P^{1/3}_{\mathcal{R}}(k_2)P^{1/3}_{\mathcal{R}}(k_3) + (5\text{ perm})\Big)\,, \end{aligned} \tag{4.0.3}$$

which is maximized when when the corresponding wavenumbers form an equilateral triangle, i.e. $k_1 \simeq k_2 \simeq k_3$.

- **Orthogonal non-Gaussianity:** An orthogonal shape is also maximized when $k_1 \simeq k_2 \simeq k_3$ and it is also orthogonal to the equilateral shape [311]. The bispectrum in the orthogonal non-Gaussianity is given as [322]

$$\begin{aligned} B^{\rm orth}_{\mathcal{R}} = \frac{3}{5} f^{\rm orth}_{\rm NL}\Big(&- 9P_{\mathcal{R}}(k_1)P_{\mathcal{R}}(k_2) - 8P^{2/3}_{\mathcal{R}}(k_1)P^{2/3}_{\mathcal{R}}(k_2)P^{2/3}_{\mathcal{R}}(k_3) \\ &+ 18P^{1/3}_{\mathcal{R}}(k_1)P^{1/3}_{\mathcal{R}}(k_2)P^{1/3}_{\mathcal{R}}(k_3) + (5\text{ perm})\Big)\,, \end{aligned} \tag{4.0.4}$$

The single-field inflation models with an attractor-only phase predict negligible non-Gaussianity. This means that a future detection of even a small amount of non-Gaussianity would rule out the single-field slow-roll models. Primordial non-Gaussianity is a fascinating topic and mathematically complicated too. Discussing it in further detail is beyond the scope of this text. Instead, we point towards the standard literature [323–325] for a comprehensive review. We note that the latest data release from Planck 2018 puts the following bounds on $f_{\rm NL}$ at 68% CL [326]

$$\text{Local} : 4.1 \pm 5.1\,, \tag{4.0.5}$$

$$\text{Equilateral} : 4 \pm 67\,, \tag{4.0.6}$$

$$\text{Orthogonal} : -38 \pm 37\,. \tag{4.0.7}$$

4.1 Local Non-Gaussianity and Its Limits

We proceed with the analysis of SD in the presence of a local-type non-Gaussianity. We know from the observations carried out by Planck or its predecessors that at least at the scales near $k = 0.05$ Mpc^{-1}, the curvature perturbations are $\mathcal{R}_k \sim \mathcal{O}(10^{-5})$. Although this is not strictly true at the smaller scales (for the purposes of PBH production), we still expect $\mathcal{R}_k$ to be fairly smaller than unity, $|\mathcal{R}_k| < 1$. Otherwise, this would result in the abundance of PBHs that violates the present DM constraints [120, 121]. We can expand the curvature perturbations in the Taylor series,

$$\mathcal{R}(\vec{x}) = \mathcal{R}_{\rm G}(\vec{x}) + \tilde{f}_{\rm NL}\left(\mathcal{R}_{\rm G}(\vec{x})^2 - \langle \mathcal{R}_{\rm G}(\vec{x})^2\rangle\right) + \tilde{g}_{\rm NL}\mathcal{R}_{\rm G}(\vec{x})^3 + \dots\,, \tag{4.1.1}$$

so that the nth term in expansion is smaller than then the $(n-1)$th term. It is stressed that the non-Gaussianity modelled in this section is present only at the scales relevant for PBHs and vanishes at the CMB scales in order not to violate Planck constraints [326]. Moreover, in this section, we shall use the refurbished non-linear parameters of the leading and next-to-leading order corrections to the Gaussian term ($\mathcal{R}_{\rm G}$), $\tilde{f}_{\rm NL} = 3f_{\rm NL}/5$ and $\tilde{g}_{\rm NL} = 9g_{\rm NL}/25$ respectively, and $\langle \mathcal{R}_{\rm G}\rangle = 0$. Our first analysis will only have the leading-order correction, the one classified with $\tilde{f}_{\rm NL}$. There is a strong inspiration that almost all the models of inflation predict a much smaller $\tilde{g}_{\rm NL}$ compared to $\tilde{f}_{\rm NL}$ [322, 327], except for a few scenarios that involve some degree of fine-tuning [328, 329]. Nonetheless, we shall discuss the case of a dominant $\tilde{g}_{\rm NL}$ in Section 5.3. For the time being, Eq. (4.1.1) becomes

$$\mathcal{R}(\vec{k}) = f_{\rm L}\mathcal{R}_{\rm G}(\vec{q}) + \tilde{f}_{\rm NL}\int \frac{d^3\vec{q}}{(2\pi)^{3/2}}\mathcal{R}_{\rm G}(\vec{q})\mathcal{R}_{\rm G}(\vec{k}-\vec{q})\,. \tag{4.1.2}$$

Even though the parameter $f_{\rm L}$ is trivially placed, it will help in creating a clear distinction. We want to work with dominant and sub-dominant levels of non-Gaussianity to understand the behaviour of SD under both these circumstances. By sub-dominant non-Gaussianity, we mean that the zeroth-order term (or Gaussian part) is the primary contributor to the total curvature perturbation Eq. (4.1.1). We shall refer to this case as "perturbative non-Gaussianity" because the non-Gaussianity can be handled perturbatively. On the other hand, the dominant non-Gaussianity will be referred to as "non-perturbative non-Gaussianity", in which the leading-order correction contribution dominates much more than the Gaussian contribution. All three cases are summarized in Table 4.1.

Gaussian	**Perturbative NG**	**Non-perturbative NG**
$f_{\rm L} = 1,\ f_{\rm NL} = 0$	$f_{\rm L} = 1,\ \lvert\tilde{f}_{\rm NL}\rvert\langle\mathcal{R}_{\rm G}^2\rangle^{1/2} \ll 1$	$f_{\rm L} = 0,\ \lvert\tilde{f}_{\rm NL}\rvert\langle\mathcal{R}_{\rm G}^2\rangle^{1/2} \gg 1$

Table 4.1: *Conditions for Gaussian, perturbative non-Gaussian (NG) and non-perturbative NG cases.*

In the non-perturbative case, the Gaussian term is assumed to be so suppressed that it is non-existent. This is why we refer to this case as purely χ^2 non-Gaussianity. Finally, as mentioned in Section 3.2, our power spectrum peaks at a very narrow range of scales compared to the total range of scales exiting the horizon during inflation. Hence, it is reasonable to take $\tilde{f}_{\rm NL}$ and $\tilde{g}_{\rm NL}$ quantities that do not vary within this short range of scales. However, for more realistic power

spectra featuring broader peaks, the scale-dependence of these parameters becomes crucial for studying the statistics of PBHs [330, 331].

4.2 Spectral Distortions in Perturbative Non-Gaussianity

We have already mentioned in Chapter 3 that when higher powered terms are ignored, the s distortions receive contributions from the terms which are quadratic and cubic in powers of averaged temperature anisotropy multipoles (see the full heating rate formula Eq. (3.2.15)). In such a scenario, it is expected that we treat the quadratic and cubic contributions separately. Intuition tells us that since $|\Theta^B| \ll 1$, we should expect suppression in the amplitude as the power of the multipole rises. This implies that $\Theta^B\Theta^{C1} \gg (\Theta^B)^2\Theta^{C1}$. Let us broaden this idea quantitatively.

For the moment, let us assume that the transfer functions are of order unity. This gives us

$$\langle\Theta^2\rangle \sim f_{\rm L}A_{\rm G} + \tilde{f}^2_{\rm NL}A^2_{\rm G}\ , \quad \langle\Theta^3\rangle \sim f_{\rm L}\tilde{f}_{\rm NL}A^2_{\rm G} + \tilde{f}^3_{\rm NL}A^3_{\rm G}\ . \tag{4.2.1}$$

where we used $f^2_{\rm L} = f_{\rm L}$ and the following approximated magnitude of the curvature perturbation, given $\mathcal{P}_{\mathcal{R}_{\rm G}} \propto A_{\rm G}$,

$$\langle\mathcal{R}^2(\vec{x})\rangle \sim f_{\rm L}A_{\rm G} + \tilde{f}^2_{\rm NL}A^2_{\rm G}\ , \quad \langle\mathcal{R}^3(\vec{x})\rangle \sim f_{\rm L}\tilde{f}_{\rm NL}A^2_{\rm G} + \tilde{f}^3_{\rm NL}A^3_{\rm G}\ , \tag{4.2.2}$$

Following Eq. (4.2.1), we identify three conditions:

1. **Gaussian Limit:** This is a straightforward condition in which $f_{\rm L} = 1$ and $\tilde{f}_{\rm NL} = 0$. We already said that the curvature power spectrum should be much smaller than unity, otherwise, it would overproduce the PBHs. Hence, only the quadratic term is non-zero in Eq. (4.2.1) and $\langle\Theta^2\rangle \ll 1$

2. **Non-Perturbative Non-Gaussian Limit:** In this case, we can absorb the Gaussian term into the χ^2 term so $f_{\rm L} = 0$. Moreover, since $|\tilde{f}_{\rm NL}|A^{1/2}_{\rm G} \gg 1$, the anisotropy terms become

$$\langle\Theta^2\rangle \sim \tilde{f}^2_{\rm NL}A^2_{\rm G}, \qquad \langle\Theta^3\rangle \sim \tilde{f}^3_{\rm NL}A^3_{\rm G} \tag{4.2.3}$$

   Yet again, the total curvature power spectrum must be smaller than unity or $\langle\mathcal{R}(\vec{k})^2\rangle \sim \tilde{f}^2_{\rm NL}A^2_{\rm G} \ll 1$, which constrains the χ^2 coefficient $A^{-1/2}_{\rm G} \ll |\tilde{f}_{\rm NL}| \ll A^{-1}_{\rm G}$. Overall, we find $\langle\Theta^2\rangle \gg \langle\Theta^3\rangle$.

3. **Perturbative Non-Gaussian Limit:** Here we know that $|\tilde{f}_{\rm NL}|A^{1/2}_{\rm G} < 1$ and $f_{\rm L} = 1$. With the same logic as above, it implies that $A_{\rm G} \ll 1$. Thus, the dominant contribution to $\langle\Theta^2\rangle$ comes from $\tilde{f}^2_{\rm NL}A^2_{\rm G}$ whereas the dominant contribution to $\langle\Theta^3\rangle$ comes from $\tilde{f}_{\rm NL}A^2_{\rm G}$. There is a competition between the quadratic and cubic terms where, the quadratic term dominates except when $|\tilde{f}_{\rm NL}| < 1$.

Hence, it is crucial to compute the exact orders of magnitude of the terms $\langle\Theta^2\rangle$ and $\langle\Theta^3\rangle$ in the regime of perturbative non-Gaussianity. In the χ^2 case, we already know that the cubic term should be irrelevant. In this sub-section, we shall assess the perturbative regime, compute the total curvature power spectrum in the presence of a subdominant χ^2 non-Gaussianity and finally, construct the window function to determine the s distortion constraints.

4.2.1 χ^2 Power Spectrum

In the limit $|\tilde{f}_{\rm NL}| > 1$, we have found that the two-point correlator of the temperature anisotropy is the dominant contributor to the s distortions than the three-point correlator. The power spectrum of the full curvature perturbation Eq. (4.1.2) then contains two terms; a Gaussian power spectrum, $P_{\mathcal{R}_{\rm G}}(k)$, and a χ^2 power spectrum, $P_{\mathcal{R}^2_{\rm G}}(k)$, which yields [332],

$$P_{\mathcal{R}}(k) = P_{\mathcal{R}_{\rm G}}(k) + \tilde{f}^2_{\rm NL} P_{\mathcal{R}^2_{\rm G}}(k) = P_{\mathcal{R}_{\rm G}}(k) + 2\tilde{f}^2_{\rm NL} \int \frac{d^3q}{(2\pi)^3} P_{\mathcal{R}_{\rm G}}(q) P_{\mathcal{R}_{\rm G}}(|\vec{k}-\vec{q}|) \ . \tag{4.2.4}$$

If we assume that the Gaussian power spectrum is a Dirac-Delta function, it is possible to analytically integrate Eq. (4.2.4). Using the definition Eq. (3.3.1), we get

$$\begin{aligned} P_{\mathcal{R}^2_{\rm G}}(k) &= 2 \times 2\pi^2 A_{\rm G} k_*^{-2} \times (2\pi) \frac{1}{(2\pi)^3} \int_0^\pi d\theta \sin\theta \int_0^\infty dq q^2 \delta(q-k_*) P_{\mathcal{R}_{\rm G}}(|\vec{k}-\vec{q}|) \ , \\ &= -A_{\rm G} \int_0^\pi d(\cos\theta)\ P_{\mathcal{R}_{\rm G}}(|\vec{k}-k_*\hat{q}|) \ , \\ &= 2\pi^2 A^2_{\rm G} k_*^{-2} \int_{-1}^1 dy\ \delta(|\vec{k}-k_*\hat{q}|-k_*) \ , \end{aligned} \tag{4.2.5}$$

where we have expressed $\vec{q} \equiv (q,\theta,\phi)$, aligned $\vec{k}$ towards z-axis so, $\vec{k}\cdot\vec{q} = kq\cos\theta$. Moreover, the notation is defined as $y \equiv \cos\theta$ and $\hat{q} = \frac{\vec{q}}{|q|}$. The χ^2 power spectrum is

$$P_{\mathcal{R}^2_{\rm G}}(k) = 2\pi^2 A^2_{\rm G} k_*^{-2} \int_{-1}^1 dy\ \delta(f(y)) \ , \tag{4.2.6}$$

where $f(y) \equiv \sqrt{k^2 - 2kk_*y + k_*^2} - k_*$. It is evident that there is a cut-off in $P_{\mathcal{R}^2_{\rm G}}(k)$ such that it is non-vanishing only for $k \leq 2k_*$, $f(y)$. A real root of $f(y)$ is $y = \frac{k}{2k_*}$ and after substituting in Eq. (4.2.6), we get the following expression for the dimensionless curvature power spectrum

$$P_{\mathcal{R}^2_{\rm G}}(k) = 2\pi^2 A^2_{\rm G} k_*^{-2} \int_{-1}^1 dy\ \frac{\delta(y-\frac{k}{2k_*})}{|k|} = 2\pi^2 A^2_{\rm G} k_*^{-2} k^{-1} H(2k_*-k) \ , \tag{4.2.7}$$

$$\mathcal{P}_{\mathcal{R}}(k) \equiv \frac{k^3}{2\pi^2} P_{\mathcal{R}}(k) = \mathcal{P}_{\mathcal{R}_{\rm G}}(k) + \tilde{f}^2_{\rm NL} \mathcal{P}_{\mathcal{R}^2_{\rm G}}(k) \ , \tag{4.2.8}$$

where $H(\theta_0 - \theta)$ is the Heaviside theta function.

4.2.2 Window Function For Leading-Order Correction

A unique feature of the total power spectrum Eq. (4.2.4) is that it peaks at $k = 2k_*$ instead of $k = k_*$ (where the Gaussian spectrum peaks). This happens because of the coupling between the scales introduced by the χ^2 contribution to the total power spectrum. This coupling goes like k^2 until $k = 2k_*$ and then power spectrum cuts off, thanks to the momentum conservation in Eq. (4.2.8). Let us see how this feature translates to the window function for the s distortions when the leading-order correction comes from the $\langle\Theta^2\rangle$ term.

We can directly use Eq. (3.2.48) and substitute the power spectrum Eq. (4.2.8) to get

$$s = A_{\rm G} W_s(k_*) + 2\tilde{f}^2_{\rm NL} A^2_{\rm G}\, W_s^{(\rm NG2)}(k_*) \ , \tag{4.2.9}$$

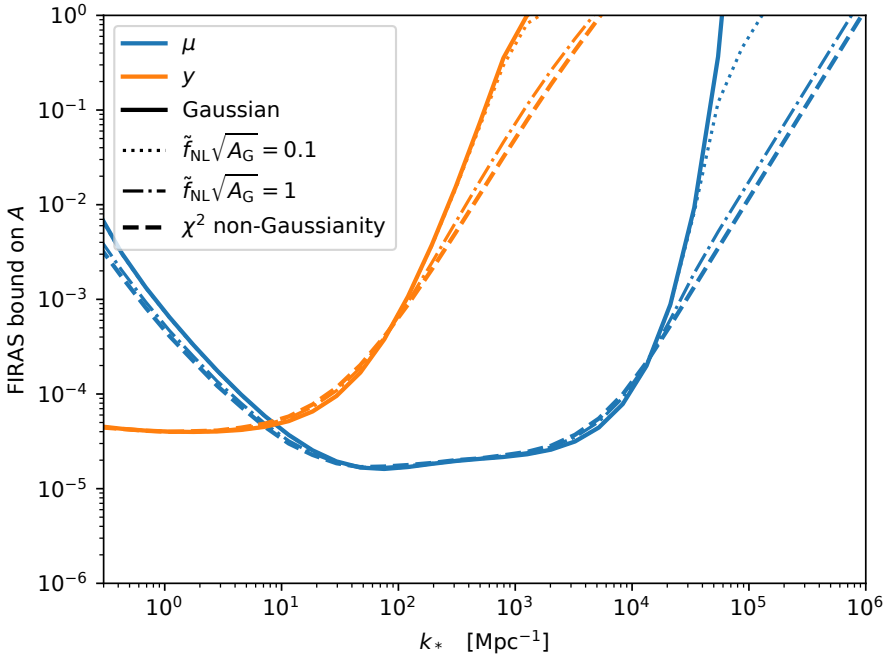

Figure 4.1: *Bounds on the curvature power spectrum amplitude from FIRAS for y distortions (orange lines) and μ distortions (blue lines). The Gaussian case is shown with solid lines, whereas the two perturbative cases, $|\tilde{f}_{\rm NL}|\sqrt{A_{\rm G}} = 0.1$ and $|\tilde{f}_{\rm NL}|\sqrt{A_{\rm G}} = 1$, are shown with dotted and dashed-dotted lines, respectively. The dashed lines correspond to the non-perturbative limit of the χ^2 non-Gaussianity.*

where the subscript “NG2" implies that the window function of the non-Gaussian correction is from the quadratic term in temperature anisotropy. We have used the following definition of the power spectrum amplitude

$$A \equiv \langle \mathcal{R}^2(\vec{x})\rangle = \int_0^\infty \frac{dk}{k}\, \mathcal{P}_{\mathcal{R}}(k) = A_G + 2\tilde{f}_{\rm NL}^2 A_G^2 \ . \tag{4.2.10}$$

Using the definition Eq. (4.2.9), we can set up the constraints on the total amplitude ‘A’ by keeping it as a subject, followed by saturating the s-distortion amplitude with the FIRAS bound Eq. (3.3.3). The result is shown in Fig. 4.1. Along with the Gaussian constraint, two cases of perturbative non-Gaussianity are shown with different relative strength of the non-Gaussian contribution to the total curvature perturbation. For the case $|\tilde{f}_{\rm NL}|\sqrt{A_{\rm G}} = 0.1$, we are well within the perturbative regime since the leading-order correction is 10 times smaller than the Gaussian contribution. The second case, $|\tilde{f}_{\rm NL}|\sqrt{A_{\rm G}} = 1$, is however, the borderline limit of perturbativity because both the Gaussian term and the leading-order correction are of the same magnitude. In reality, perturbation theory fails much earlier than this condition, but we present it as a reference scenario to illustrate how much a constraint can vary within the extreme limits of perturbativity.

The s distortions can be expressed as

$$s = \begin{cases} \frac{A}{1.02}\left[W_s(k_*) + 0.02 W_s^{(\rm NG2)}(k_*)\right] & \text{if } |\tilde{f}_{\rm NL}|\sqrt{A_{\rm G}} = 0.1 \ , \\ \frac{A}{3}\left[W_s(k_*) + 2 W_s^{(\rm NG2)}(k_*)\right] & \text{if } |\tilde{f}_{\rm NL}|\sqrt{A_{\rm G}} = 1 \ . \end{cases} \tag{4.2.11}$$

Moreover, let us write down the coefficients corresponding to the numerical fit for $W_s^{(\mathrm{NG2})}$, which are accurate up to 10%, as follows

n	w_n	n	w_n
0	-2.31	**5**	-7.6855×10^{-3}
1	1.41	**6**	2.70326×10^{-3}
2	-1.25×10^{-1}	**7**	-3.71457×10^{-4}
3	2.443×10^{-2}	**8**	2.31035×10^{-5}
4	-1.405×10^{-3}	**9**	-5.42652×10^{-7}

Table 4.2: *We tabulate the coefficients for the numerical fitting of window function* $W_\mu^{(\mathrm{NG2})}(k)$.

We can infer that as the non-Gaussian term gains significance in magnitude, the curve tends to flatten more in the regime of large k_*. The constraint is stronger than the Gaussian counterpart because in the presence of a positive non-Gaussianity, we expect an additional contribution to the curvature power spectrum (only at the small scales where non-Gaussianity is non-zero). This implies that we should have observed a slightly higher amplitude of the s distortions via acoustic dissipation in this case. The constraints also become mildly stronger at small k, $10^0\ \mathrm{Mpc}^{-1} < k < 10^1\ \mathrm{Mpc}^{-1}$, mainly due to the shift in the peak of the power spectrum $k_* \to 2k_*$.

In the tightest constraint regime, $10^1\ \mathrm{Mpc}^{-1} < k_* < 10^4\ \mathrm{Mpc}^{-1}$, the effect of change in the shape of the power spectrum does not play a role because the window function dominates the integral Eq. (4.2.11). Note that in deriving the constraints from $W_s^{(\mathrm{NG2})}$, we have used the most accurate scheme Eq. (3.2.46). We have not shown the less accurate scheme Eq. (3.2.44) because our analysis shows that at the scales of interest, both schemes do not show any difference even for the non-Gaussian case.

4.2.3 Window Function For Next-to-Leading-Order Correction

Let us come back to the case when $|\tilde{f}_{\mathrm{NL}}| < 1$, i.e. when we anticipate the term $\langle \Theta^3 \rangle$ to dominate over the term $\langle \Theta^2 \rangle$. We have found that for the redshifts and scales that we are interested in ($z \in [10^3, 10^6]$ and $k \in [10^0\ \mathrm{Mpc}^{-1}, 10^5\ \mathrm{Mpc}^{-1}]$), the monopole moment is the most dominant contribution in the heating rate Eq. (3.2.15).

While the higher moments ($\ell \geq 3$) are highly suppressed in the TCA (see the discussion around Eq. (3.2.15)), the quadrupole provides the second dominant contribution after the monopole. We can see this feature in Fig. 4.2 where the quadrupole is comfortably four orders of magnitude at redshifts as early (late) as $z \sim 2 \times 10^6$ (as late as $z \sim 6.5 \times 10^3$). Furthermore, we know from Eq. (3.2.28) that the polarization term contribution is of the same magnitude as the quadrupole term contribution in the TCA. The dipole is also suppressed in the TCA, as explained in the previous section. Combining all of these arguments, the resulting heating rate is

$$Q' \simeq 4\bar{\rho}_\gamma \alpha_T' \left[\langle \Theta^{\mathrm{G}}_{(2)} \Theta^{\mathrm{C1}}_{(2)} \rangle + 2 \langle \tilde{\Theta}_{(0)} \Theta^{\mathrm{G}}_{(2)} \Theta^{\mathrm{C1}}_{(2)} \rangle \right] . \tag{4.2.12}$$

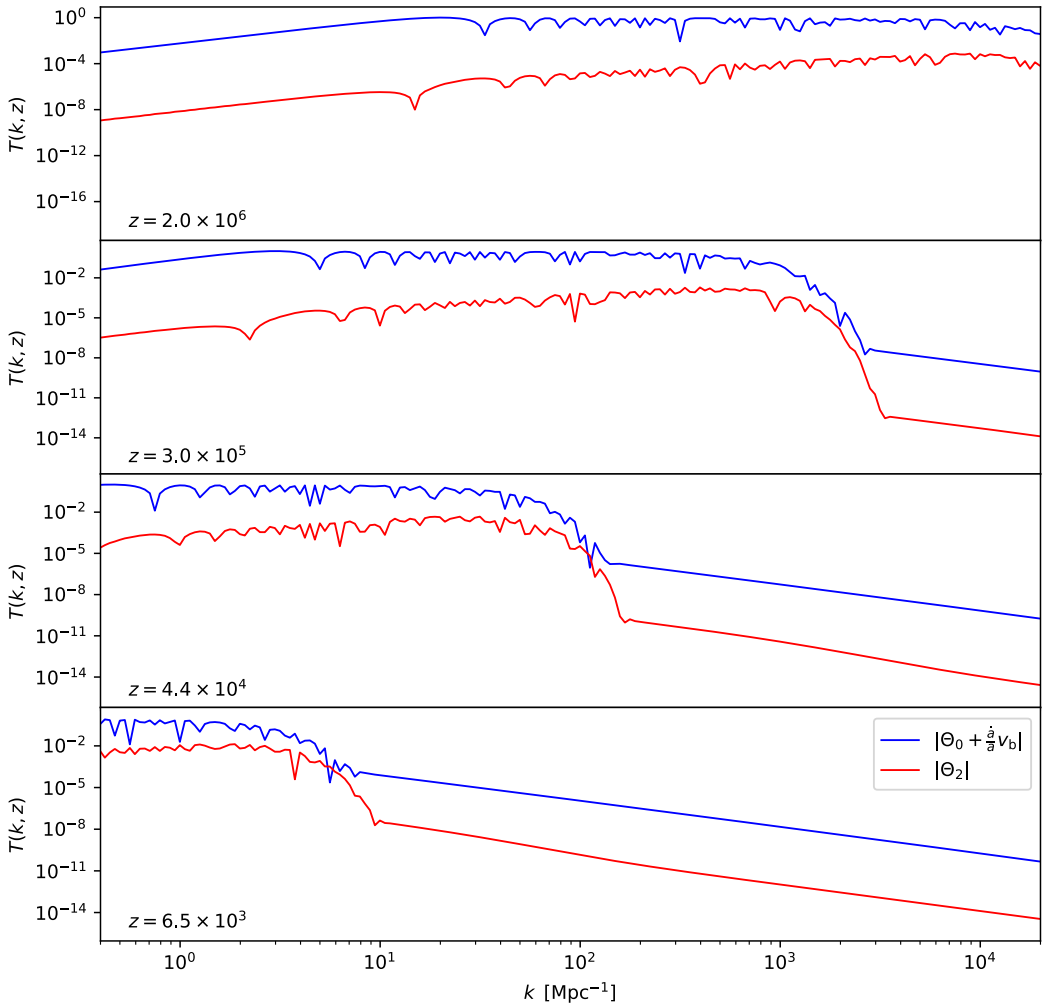

Figure 4.2: *The figure shows the absolute values of the transfer functions, the monopole* $\tilde{\Theta}0 \equiv (\Theta 0 + \frac{\dot{a}}{a} v_b)$ *and the quadrupole* Θ_2 *across four redshift-stamp, plotted as functions of the comoving scales. The monopole is comfortably larger than the quadrupole over all the scales of interest and across all the redshifts. By definition, the transfer functions are gauge invariant.*

Notice how we have retained terms at both quadratic and cubic orders. We can perform the multipole expansion and invoke the TCA such that the terms monopole, “G" subscripted and “C1" subscripted are given as

$$\tilde{\Theta}_{(0)} \equiv (\Theta_{(0)} + \frac{\dot{a}}{a} v_b) \ , \tag{4.2.13}$$

$$\Theta_2^G = -\Theta_2 \ , \tag{4.2.14}$$

$$\Theta_2^{C1} = \Theta_2 - \frac{1}{10}(\Theta_2 + \Theta_0^P + \Theta_2^P) \simeq \Theta_2 - \frac{1}{10}(\Theta_2 + \frac{6}{4}\Theta_2) = \frac{3}{4}\Theta_2 \ , \tag{4.2.15}$$

using which, we get the heating rate

$$Q' \simeq -4\bar{\rho}_\gamma \alpha_T' \ \frac{3}{4} \left[\langle (\Theta_{(2)})^2 \rangle + 2 \langle \tilde{\Theta}_{(0)} (\Theta_{(2)})^2 \rangle \right] \ . \tag{4.2.16}$$

In this discussion, we only need to examine the contribution from the term that is cubic in temperature anisotropy multipole, hence, we neglect the first term on the right-hand side of Eq. (4.2.16). We are required to compute the three-point correlation of the curvature perturbations, as evident from Eqs. (A.2) and (3.2.18). For a χ^2 non-Gaussianity, we can write the three-point correlator of the total curvature perturbation Eq. (4.1.1) becomes

$$\begin{aligned}\langle\mathcal{R}(\vec{k}_1)\mathcal{R}(\vec{k}_2)\mathcal{R}(\vec{k}_3)\rangle &= \langle[\mathcal{R}_{\rm G}(\vec{k}_1)+\mathcal{R}^2_{\rm G}(\vec{k}_1)][\mathcal{R}_{\rm G}(\vec{k}_2)+\mathcal{R}^2_{\rm G}(\vec{k}_2)] \\ &\qquad [\mathcal{R}_{\rm G}(\vec{k}_3)+\mathcal{R}^2_{\rm G}(\vec{k}_3)]\rangle \qquad (4.2.17)\\ &\simeq \tilde{f}_{\rm NL}\langle\mathcal{R}_{\rm G}(\vec{k}_1)\mathcal{R}_{\rm G}(\vec{k}_2)\mathcal{R}^2_{\rm G}(\vec{k}_3)\rangle + \text{permutations}\ , \qquad (4.2.18)\end{aligned}$$

where we ignored the terms of the form $\langle\mathcal{R}^2_{\rm G}\mathcal{R}^2_{\rm G}\mathcal{R}^2_{\rm G}\rangle$ and the odd correlator of $\mathcal{R}_{\rm G}$ is zero by definition. If we apply Wick's theorem to Eq. (4.2.18), we can expand the overall four-point correlator of $\mathcal{R}_{\rm G}$ as the product of its two-point correlators, followed by replacing them with the power spectrum

$$\begin{aligned}\langle\mathcal{R}(\vec{k}_1)\mathcal{R}(\vec{k}_2)\mathcal{R}(\vec{k}_3)\rangle \;=\; & \tilde{f}_{\rm NL}\,[P_{\mathcal{R}_{\rm G}}(k_1)P_{\mathcal{R}_{\rm G}}(k_2)+P_{\mathcal{R}_{\rm G}}(k_2)P_{\mathcal{R}_{\rm G}}(k_3)\\ & +P_{\mathcal{R}_{\rm G}}(k_3)P_{\mathcal{R}_{\rm G}}(k_1)]\,\delta^{(3)}(\vec{k}_1+\vec{k}_2+\vec{k}_3)\ . \qquad (4.2.19)\end{aligned}$$

We directly write the cubic anisotropy term "022" as a final expression and leave the further computation of Section 4.2.3 to Appendix B,

$$\begin{aligned}\langle\tilde{\Theta}_{(0)}(\Theta_{(2)})^2\rangle = \frac{15\sqrt{2}\tilde{f}_{\rm NL}}{\pi^{7/2}}\int_0^\infty dr\,r^2\left[\int_0^\infty dk_1 P_{\mathcal{R}_{\rm G}}(k_1)k_1^2\Theta_2(k_1)j_2(rk_1)\right]^2 \\ \int_0^\infty dk_2 k_2^2\tilde{\Theta}_0(k_2)j_0(rk_2)\ . \qquad (4.2.20)\end{aligned}$$

We choose a Dirac-Delta power spectrum Eq. (3.3.1) so that Eq. (4.2.20) simplifies to give

$$\langle\tilde{\Theta}_{(0)}(\Theta_{(2)})^2\rangle = 60\sqrt{2\pi}\tilde{f}_{\rm NL}A^2_{\rm G}\int_0^\infty dr\,r^2\,[\Theta_2(k_*)j_2(rk_*)]^2\int_0^\infty dk\,k^2\tilde{\Theta}_0(k)j_0(rk)\ , \qquad (4.2.21)$$

which can be further simplified if we deploy an analytical estimate of the integration with respect to 'r' using Eq. (B.8) to get

$$\langle\tilde{\Theta}_{(0)}(\Theta_{(2)})^2\rangle = \frac{15\pi\sqrt{2\pi}\,[\Theta_2(k_*)]^2}{k_*^2}\int_0^{\sqrt{2}k_*} dk\,k\,\tilde{\Theta}_0(k)\,P_2\left(1-\frac{k^2}{2k_*^2}\right)\ . \qquad (4.2.22)$$

It is now possible to write the cubic contribution to the s distortion (denoted as s_{Θ^3})

$$s_{\Theta^3} = \int dz\,\mathcal{I}_s(z)\,\frac{4\alpha_T'(z)}{a_0H(z)}\,\frac{3}{2}\langle\tilde{\Theta}_{(0)}(\Theta_{(2)})^2\rangle\ . \qquad (4.2.23)$$

Finally, the total magnitude of s distortion, including up to the cubic contribution, should be

$$\begin{aligned}s &= A_{\rm G}W_s(k_*)+s_{\Theta^2}+s_{\Theta^3}\ , \qquad (4.2.24)\\ &= A_{\rm G}W_s(k_*)+2\tilde{f}^2_{\rm NL}A^2_{\rm G}W_s^{(\rm NG2)}(k_*)+\tilde{f}_{\rm NL}A^2_{\rm G}W_s^{(\rm NG3)}(k_*)\ . \qquad (4.2.25)\end{aligned}$$

Note that the term $j_\ell(x)$ in Eq. (4.2.20) is the spherical Bessel function, and s_{Θ^2} in Eq. (4.2.24) is the s distortion contribution from the term quadratic in temperature anisotropy. We have

introduced a new quantity, $W_s^{(\rm NG3)}(k_*)$ in Eq. (4.2.25) which is the window function from the non-Gaussian contribution via the cubic term (Θ^3) and its expression is given as

$$W_s^{(\rm NG3)}(k_*) \equiv \int dz\, \mathcal{I}_s(z)\, \frac{4\alpha_T'(z)}{a_0 H(z)}\, \frac{45}{2}\pi\sqrt{2\pi}\, \left[\Theta_2(k_*, z)\right]^2 \int_0^{\sqrt{2}k_*} d\ln k\, \frac{k^2}{k_*^2}\tilde{\Theta}_0(k, z)\, P_2\left(1 - \frac{k^2}{2k_*^2}\right) \,. \tag{4.2.26}$$

`CLASS` Implementation: Now our job is to feed the 'NG3' powered s_Θ^3 distortion in order to quantify its magnitude. For this purpose, we reformulate the equations to make them compatible with the structure of the code within `CLASS`. The redefined source function from acoustic dissipation and the power spectrum, respectively, are

$$\begin{aligned} S_{\rm ac}(k, z) &\longrightarrow \frac{45}{2}\pi\sqrt{2\pi}\, \left[\Theta_2(k_*, z)\right]^2\, \tilde{\Theta}_0(k, z) \,, \\ \mathcal{P}_{\mathcal{R}}(k) &\longrightarrow \tilde{f}_{\rm NL} A_{\rm G}^2\, \frac{k^2}{k_*^2}\, P_2\left(1 - \frac{k^2}{2k_*^2}\right) H(\sqrt{2}k_* - k) \,, \end{aligned} \tag{4.2.27}$$

where, the term $H(\sqrt{2}k_* - k)$ represents the Heaviside theta function. We note that this change of definitions have nothing to do with the physics of the problem. It is just a way to add $W_s^{(\rm NG3)}(k_*)$ in `CLASS` efficiently. It is important to highlight the following points while performing the numerical integration of Eq. (4.2.26)

- It is trickier to compute $W_s^{(\rm NG3)}(k_*)$ compared to $W_s^{(\rm NG2)}(k_*)$. This happens because unlike $W_s^{(\rm NG2)}(k_*)$, which features squared oscillatory term and thus, can be averaged as $\langle \sin^2 x \rangle \approx \frac{1}{2}$, the new window function $W_s^{(\rm NG3)}(k_*)$ has an odd oscillatory term (thanks to $\Theta_0\Theta_2^2$). Since the oscillations are in both k-space and z-space, we need to work with a finer grid in the variables (k, z), which is computationally expensive.

- We compute the window function $W_s^{(\rm NG3)}(k_*)$ for a Dirac-Delta power spectrum using Eq. (4.2.26) and for a log-normal type power spectrum using Eq. (4.2.20)(For the log-normal case and accuracy check, see the Appendix in [292]). The result for the Dirac-Delta function power spectrum is shown in Fig. 4.3.

- It can be seen from the figure that the window function $W_s^{(\rm NG3)}$ is significantly suppressed than $W_s^{(\rm NG2)}$ at all the scales of interest, which becomes increasingly suppressed at smaller scales. Moreover, assuming the non-Gaussianity parameter lies in the range $0 < \tilde{f}_{\rm NL} < 1$, the window function is negative on top of being suppressed. This implies that in the perturbative regime of non-Gaussianity, the cubic term should contribute towards erasing the SD.

- Although we qualitatively argued at the beginning of this section that a contribution from $W_s^{(\rm NG3)}(k_*)$ over $W_s^{(\rm NG2)}(k_*)$, the physical situation is more complicated because the transfer functions are not of the same order at all the multipoles, as assumed in Eq. (4.2.1).

- For instance, the monopole moment is a fast oscillating function, and its oscillations are zero-centred. Averaging them over different scales would suppress the magnitude of the

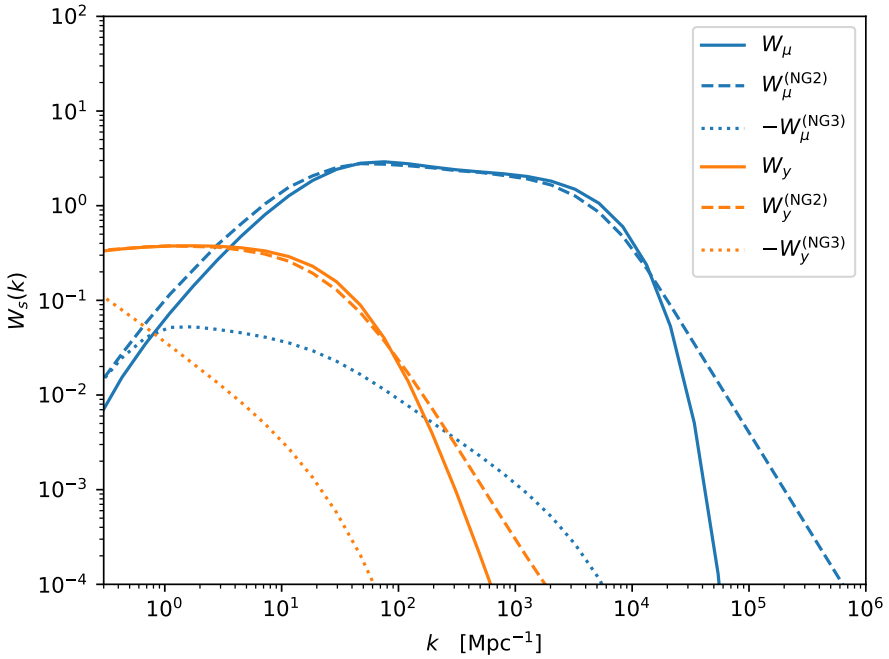

Figure 4.3: *The figure compares the Gaussian window functions for s distortions, denoted by $W_s(k)$, and those arising from a local non-Gaussian contribution generated by a Dirac-delta curvature power spectrum. The window function $W^{(\rm NG3)}$ corresponding to the contribution $\langle\Theta^3\rangle$ is largely subdominant, barring the small-k regime.*

monopole term. The dependence of the two window functions on the multipoles can be written as

$$W_s^{(\rm NG3)}(k_*) \propto \tilde{f}_{\rm NL} A_{\rm G}^2 \tilde{\Theta}_0 [\Theta_2]^2 \ , \qquad W_s^{(\rm NG2)}(k_*) \propto 2\tilde{f}_{\rm NL}^2 A_{\rm G}^2 [\Theta_2]^2 \ . \tag{4.2.28}$$

Clearly, $W_s^{(\rm NG3)}(k_*)$ is suppressed when $\langle\Theta_0\rangle_k \ll 1$. The only way for $W_s^{(\rm NG3)}(k_*)$ to be larger than $W_s^{(\rm NG2)}(k_*)$ would be to have $|\tilde{f}_{\rm NL}| \ll 1$ but then the non-Gaussian term would not be important at all. Thus, we find that, in any case, the non-Gaussian contribution to the heating rate from the cubic term should be negligible compared to the quadratic term.

4.3 Spectral Distortions in Non-Perturbative Non-Gaussianity

Finally, we consider a strongly non-Gaussian regime i.e. the non-perturbative non-Gaussianity, where the total curvature perturbation is $\mathcal{R} = \mathcal{R}_{\rm G}^2$. We recall the discussion in the beginning of Section 4.2 that in this regime, the quadratic terms in temperature anisotropy is the primary contributor to the s distortions. This implies that we are only interested in the two-point correlator of $\mathcal{R}_{\rm G}^2$. We have already computed the total power spectrum in Eq. (4.2.8) and for this case we absorb the Gaussian spectrum such that $\mathcal{P}_{\mathcal{R}}(k) \equiv \mathcal{P}_{\mathcal{R}_{\rm G}^2}(k)$. Consequently, the amplitude of this power spectrum results

$$A \equiv \langle \mathcal{R}^2(\vec{x})\rangle = \int_0^\infty \frac{dk}{k}\, \mathcal{P}_{\mathcal{R}}(k) = 2A_G^2 \ , \tag{4.3.1}$$

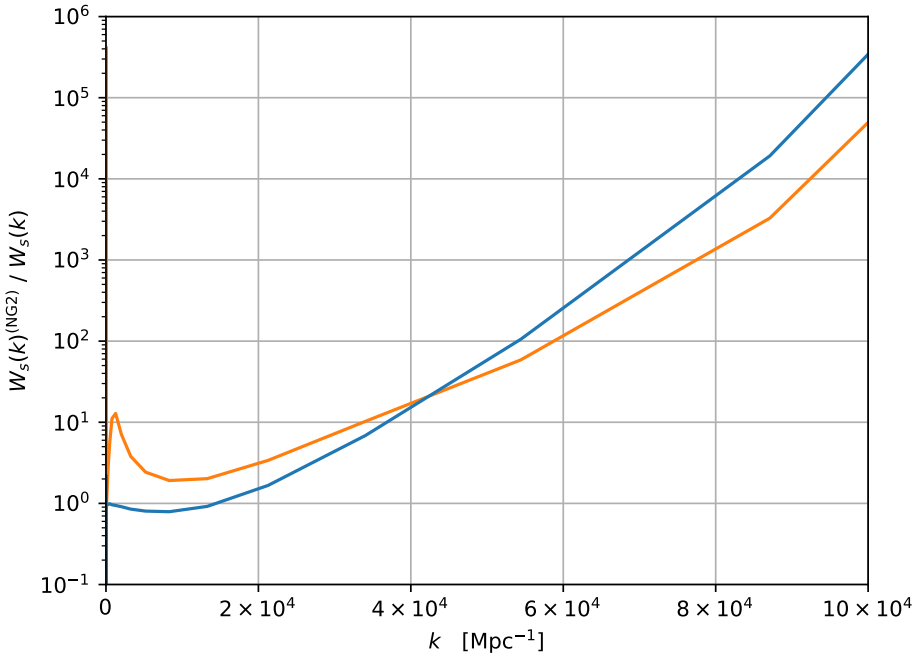

Figure 4.4: *The figure shows the strength of the window functions for s distortions of non-perturbative χ^2 non-Gaussianity, relative to the Gaussian window functions. The orange and blue curves are, respectively, for y distortions and μ distortions.*

from which we find that the s distortion receives a single contribution from the 'NG2' window function in Eq. (4.2.11) or

$$s = A\, W_s^{(\mathrm{NG2})}(k_*) \ . \tag{4.3.2}$$

We have already seen the constraint on 'A' from non-perturbative non-Gaussianity in Fig. 4.1. The curve is even more flattened than the perturbative non-Gaussian case. This is expected since this behaviour at large k, which comes from the coupling between the scales, is a result of the χ^2 contribution. Moreover, in their tightest regime, the constraints in the $s = \mu, y$ distortions coincide with the Gaussian constraints. As the peak of the power spectrum has shifted to $k = 2k_*$, the constraints have become slightly stronger at small-k.

We also plot the ratio of the χ^2 and the Gaussian window functions in Fig. 4.4. It is evident that the ratios rise consistently for $k \geq 10^4$ Mpc^{-1}. For example, beyond $k = 4 \times 10^4$ Mpc^{-1} the χ^2 window function of μ distortion has already become stronger than the Gaussian counterpart by an order of unity. Further than this, the slope is even steeper and for $k \geq 7 \times 10^4$Mpc^{-1} the μ distortion constraint has become three orders of magnitude stronger in the χ^2 case.

CHAPTER 5

PBH Constraints From Spectral Distortions

We already noted in Section 1.6 the most important experiments that have constrained the PBH population, ranging from GWs measurements to CMB anisotropies as well as CMB SD. These experiments have different sensitivities at different scales in the sky, and thus, most of the constraints are unique to a specific range of PBH masses. Furthermore, the constraints are also sensitive to the initial mass distribution of the PBHs. For example, a monochromatic PBH mass function is widely used due to its simplified assumption that all the PBHs that form after the horizon reentry of large perturbations essentially correspond to the same mass. Under this assumption Eq. (1.6.6) reduces to

$$f_{\rm PBH} \equiv \left.\frac{\rho_{\rm PBH}}{\rho_{\rm DM}}\right|_{\rm today} \simeq 2.4\beta \left(\frac{M_{\rm eq}}{M}\right)^{1/2} . \tag{5.0.1}$$

The horizon mass at equality in standard ΛCDM cosmology is $M_{\rm eq} \simeq 2.7 \times 10^{17} M_\odot$ and the normalizing prefactor comes from the total energy density to the dark matter energy density ratio at equality [5]. Of course, a monochromatic mass distribution is an impractical concept because in reality, most of the non-attractor inflation models predict an enhancement in the power spectrum that affects a finite range of comoving scales and thus, we expect PBH production for the corresponding finite range of masses according to Eq. (1.6.2).

Moreover, the relation Eq. (5.0.1) assumes that the fractional energy density of PBHs stays constant between the time of formation and today. This is not entirely true because accretion plays a key role in adding mass to the PBHs throughout the radiation and matter eras. Accretion onto PBHs is a highly complex process to model due to its numerous dependencies, including the initial PBH mass, the dark matter fraction comprised of PBHs, the density profile of the surrounding halos, and the accretion model (such as disk accretion or spherical accretion, see [101] for details). The radiation emitted from PBH accretion spans a broad range of frequencies in the electromagnetic spectrum, allowing a large number of observations from cosmology to astrophysics

to be used to constrain the PBH abundance (e.g., X-ray background, radio background, and CMB background). Furthermore, a strong presence of primordial non-Gaussianity could result in a highly clustered population of PBHs, leading to a more complicated accretion model.

The effect of accretion history on the PBH seeds (along with other seeds) of different masses is shown in the left panel of Fig. 5.1. It can be seen that the quasars at $z \approx 6$ can be traced back to PBH seeds as massive as $M_{\rm PBH} \approx 6 \times 10^4 M_\odot$, if they accrete with the average Eddington ratio $\langle \lambda_E \rangle \sim 0.5$. However, if the accretion is less efficient, a more massive PBH seed is required. Overall, it shows that an efficiently accreting PBH seed can gain mass as much as four orders of magnitude.

The constraints on the $f_{\rm PBH}$ are shown in the right panel of the same figure (albeit, for a different accretion model and DM halo profile). The cut-off redshift (roughly around $z \sim 10$) exists for the PBH accretion because of various factors such as higher peculiar PBH velocity due to gravitational wells from structures at late times, enhanced radiation pressure due to reionization from the earliest stars and galaxies, and feedback from heating of the accreting matter due to friction. If the cut-off happens as late as $z = 7$, one can expect the $f_{\rm PBH}$ constraints to be relaxed by up to eight orders of magnitude at $M_{\rm PBH} \sim 10^4 M_\odot$ compared to the case where there is no accretion ('No evolution') [333]. It highlights how sensitive the PBH constraints are to the accretion rate. We choose to neglect all these interesting effects and refer to a vast literature for more details [101, 334–338].

In this section, we aim to understand the PBH constraints derived from SD sourced by the dissipation of the associated acoustic oscillations. An interesting mass regime here is the supermassive range. The origin of Supermassive Black Holes (SMBHs) remains an open issue in astronomy, with a number of potential candidates from astrophysics and cosmology. Some of these candidates on the astrophysical side include a direct gravitational collapse of large mass gas clouds [339], stellar mass black holes undergoing mergers [340], and a gravitational collapse of the population III stars which form from the lightest metals [341].

Recently, PBHs have gained attention as a cosmological candidate for SMBHs. PBHs can seed the present-day SMBHs with or without accretion. If mass addition due to accretion is considered, the PBHs with formation mass as low as $10^4 M_\odot$ could become SMBHs today. On the other hand, considering an inefficient or no accretion onto PBHs, it is challenging to have PBHs as SMBHs with formation mass smaller than $10^5 M_\odot$. The primordial scalar perturbations corresponding to the supermassive mass range $[10^4 M_\odot, 10^{13} M_\odot]$ reentered the horizon during μ era and if present, they would have created a signature on the μ distortions via acoustic oscillation explained in Section 3.2.2.

Unfortunately, the constraints on PBHs from μ distortions are too strong to allow even a single SM-PBH of formation mass $M \geq 10^4 M_\odot$[293, 304, 342, 343]. These constraints apply to the PBHs formed from the gravitational collapse of Gaussian primordial density fluctuations. The presence of a positive non-Gaussianity in the density fluctuation would imply a heavier tail of the PDF of curvature perturbations and thus, an enhanced abundance of PBHs due to their exponential tail sensitivity Eq. (1.6.3). In this case, a smaller amplitude in the power spectrum is also sufficient to generate a sizable population of PBHs due to the enhanced probability of large fluctuations. We have already computed the framework for incorporating χ^2 and cubic non-Gaussianities into the computations of SD up to next-to-leading order in temperature anisotropies.

In this section, we will introduce the current status of the PBH constraints from μ distortions, which are computed using the Gaussian assumption. Thereafter, we will assess the renewed stature of PBHs as SMBH candidates for locally non-Gaussian perturbations of χ^2 type in perturbative and non-perturbative limits. For this, we will also use the results from Chapter 4 to check the intersection of the non-Gaussian μ constraints and PBH constraints. We will continue this discussion to explore stronger cubic non-Gaussianity and speculate on the results for even stronger cases of non-Gaussianity in the forthcoming subsections.

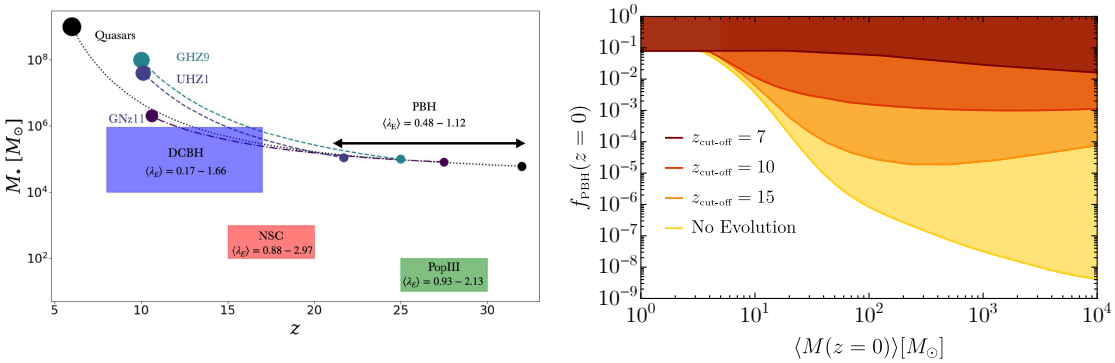

Figure 5.1: ***Left Panel:*** *The figure shows the mass evolution of different black hole (BH) seeds as a function of redshift. DCBHs stand for direct collapse BHs, NSCs stand for nuclear star clusters, PopIII stands for population III stars, and λ_E is the accretion rate of the BH normalized to its Eddington accretion rate. Dotted and dashed lines correspond to two different average accretion rates between $0.48 \leq \langle\lambda_E\rangle \leq 1.12$. The heavy PBH seeds are formed from runaway mergers of lighter PBHs residing in DM halos, and their subsequent accretion history is modelled via a semi-analytic method. Figure taken from [333].* ***Right Panel:*** *The constraint on the f_{PBH} as a function of the PBH mass for an extended mass distribution at $z = 0$. The contours of different colours represent different accretion cut-off redshifts. Figure taken from [336, 344, 345].*

5.1 Gaussian Constraints

With the help of the Press-Schechter formalism, the PBH abundance for Gaussian density fluctuations is already computed in Eq. (1.6.3), but we rewrite it in terms of curvature perturbation instead of density contrast, such that

$$\beta = \frac{1}{2}\text{ErfC}\left[\frac{\mathcal{R}_c}{\sqrt{2A}}\right] , \tag{5.1.1}$$

where we explicitly work with the Dirac-Delta power spectrum Eq. (3.3.1). A power spectrum featuring a narrow spike is unphysical but, as mentioned earlier, it serves as a signatory example for broader spectra. Moreover, it is known that the threshold amplitude required for PBH formation is only slightly reduced when the featured peak is relatively wider, like a thin log-normal power spectrum [346]. For SD, broad power spectra should also broaden the constraints, meaning that we get even more conservative limits on how massive the PBHs can be without evading the SD constraints [347]. Thus, a Dirac-Delta power spectrum provides the least conservative estimate of the heaviest allowed SM-PBH. The variance of the power spectrum is related to its peak

amplitude via

$$A = \sigma^2 = \int_0^\infty \frac{dk}{k} \mathcal{P}_\mathcal{R}(k) \ . \tag{5.1.2}$$

Earlier in Section 1.6, we briefly mentioned the PBH threshold and how the compaction function is related to the threshold. A trade-off between the gravitational pull and the radiation pressure determines the formation threshold at the particular time. A precise way to compute the PBH formation threshold is through numerical hydrodynamical simulations, and it should be a more sophisticated function rather than a constant. For the sake of simplicity, we shall consider a constant value of threshold $\mathcal{R}_c = 0.67$ in line with the literature [346, 348]. The non-linear relationship between overdensity contrast and curvature perturbation requires correcting the PBH abundance in terms of curvature perturbations threshold Eq. (5.1.1) by a factor of two, such that [73, 346, 349]

$$\beta = \frac{1}{2} \text{ErfC}\left[\frac{\mathcal{R}_c}{\sqrt{A}}\right] \ . \tag{5.1.3}$$

The minimum peak amplitude of the power spectrum should be the amplitude which produces a single PBH in the entire universe at a specific comoving scale. We shall refer to this lowest amplitude of interest as “1−PBH" limit. Any magnitude of β smaller than this limit will result in no PBHs. Therefore [350, 351],

$$\beta < \beta_{1-\text{PBH}}(k) \simeq 1.2 \times 10^{-11} (k\,\text{Mpc})^{-3}, \tag{5.1.4}$$

The PBH abundance is exponentially sensitive to the threshold, but the power spectrum is sensitive to the abundance via a mere logarithmic relation (see Eq. (1.6.6)). Thus, what may appear to be a minor difference in terms of power spectrum amplitude is exaggerated for abundance amplitude. We choose to express the PBH constraints on the amplitude for three different cases of $f_{\text{PBH}}(= [10^{-10}, 10^{-5}, 1-\text{PBH}])$. For reference, $f_{\text{PBH}} \simeq 10^{-16}$ corresponds to $\beta_{1-\text{PBH}}(k)$ for $M_{\text{PBH}} = 10^6 M_\odot$.

It is not clearly understood how small f_{PBH} needs to be in order to have all the SMBHs as SM-PBHs. We do know from the observation of extremely high-energy jet emissions that SMBHs accrete massively. Furthermore, observations also tell us that the mass range of SMBHs is quite wide, $M_{\text{SMBH}} \in \left[10^5 M_\odot, 10^{12} M_\odot\right]$, so, if we were to start with a monochromatic primordial curvature power spectrum, the accretion would have to play its role at varying efficiencies across the sky. Keeping in mind such variability, it is a reasonable choice to use $f_{\text{PBH}} = 10^{-5}$ that is in line with the present bounds on PBH abundance and also leads to non-negligible SMBH seeds.

Our PBH constraint plot for the Gaussian case is shown in Fig. 5.2. Notably, the difference between 1−PBH and $f_{\text{PBH}} = 1$ is barely one order of magnitude even at the smallest k values. To compute the μ distortion constraint, we have utilized our most accurate scheme for the acoustic dissipation source function Eq. (3.2.46). The amplitude of the power spectrum has been saturated via the FIRAS bound Eq. (3.3.3).

The intersection between the PBH constraint and the μ constraint provides the maximal limit of M_{PBH} up to which, for a given f_{PBH}, we can expect the PBHs to form without disrespecting the distortion bounds. In Gaussian case, it is visible from Fig. 5.2 that this intersection happens roughly at similar scales for 1−PBH and $f_{\text{PBH}} = 1$ limits not only because these lines are quite

near to each other, but also because the μ constraint cuts off steeply at $k \geq 10^4 \text{Mpc}^{-1}$, owing to the sharply peaked power spectrum. We find that at best only a single PBH can be formed of maximum allowed mass $M_{\text{PBH}} \approx 10^4 \text{Mpc}^{-1}$. If the power spectrum features a broader peak, this intersection would happen at slightly smaller mass values, putting an even more stringent limit on the maximum mass. Furthermore, this maximum mass reduces slightly for higher f_{PBH}. It is concluded that for Gaussian perturbations with arbitrarily wide power spectrum, the μ distortion constraints do not allow PBHs to source even a single SMBH with an initial seed $M_{\text{PBH}} 10^4 M_\odot$.

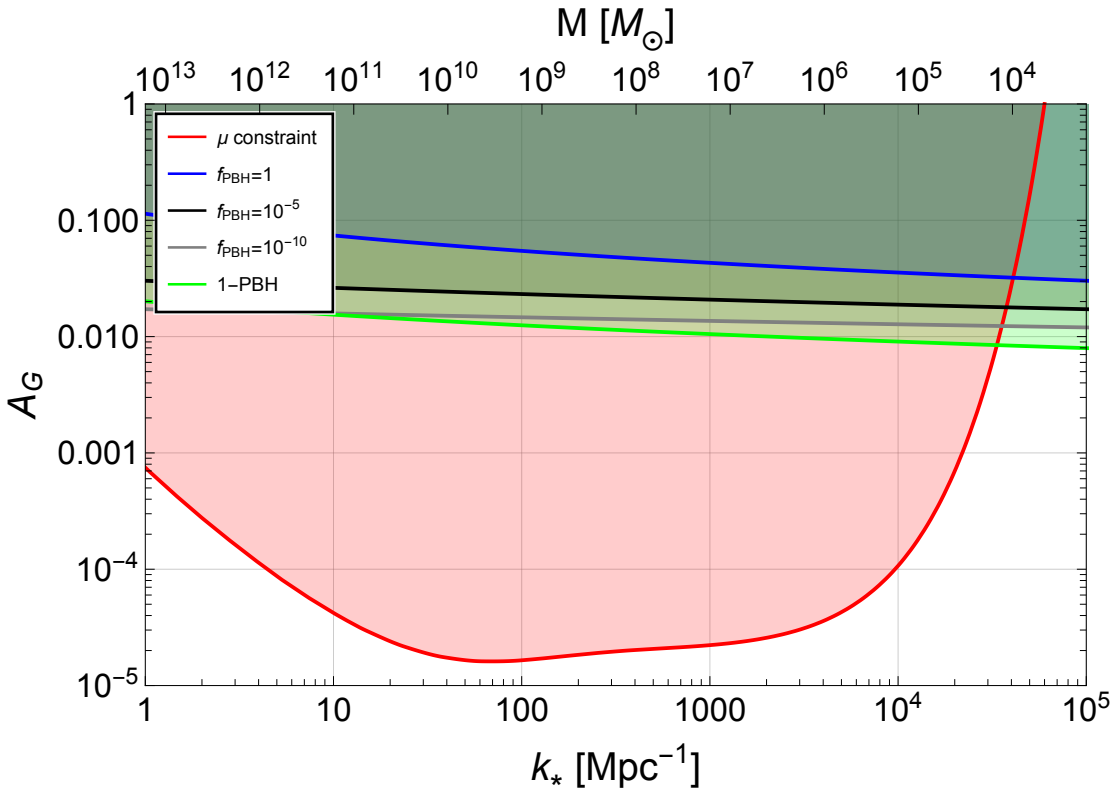

Figure 5.2: *Constraints on the power spectrum amplitude assuming Gaussian curvature perturbations and a Dirac delta power spectrum. The upper x-axis shows the horizon mass in solar mass units (which is approximately the PBH mass) corresponding to each k_* value.*

5.2 Constraints From χ^2 Non-Gaussianity

We shall return to the non-Gaussianity of local type with the total curvature receiving corrections via Taylor series expansion:

$$\mathcal{R}(\vec{x}) = \mathcal{R}_{\text{G}}(\vec{x}) + \tilde{f}_{\text{NL}} \left(\mathcal{R}_{\text{G}}(\vec{x})^2 - \langle \mathcal{R}_{\text{G}}(\vec{x})^2 \rangle \right) + \tilde{g}_{\text{NL}} \mathcal{R}_{\text{G}}(\vec{x})^3 + ... \tag{5.2.1}$$

where we shall work with χ^2 non-Gaussianity ($\tilde{f}_{\text{NL}} \neq 0, \tilde{g}_{\text{NL}} = 0$) in this subsection and consider the case of cubic non-Gaussianity ($\tilde{g}_{\text{NL}} \neq 0, \tilde{f}_{\text{NL}} = 0$) in Section 5.3. As we shall see later, the implications of non-Gaussianity are more significant for PBHs compared to SD.

Like in the case of SD, we shall consider χ^2 non-Gaussianity in two limits: perturbative and non-perturbative. Recall that the perturbative limit satisfies the condition $|\tilde{f}_{\rm NL}|\langle\mathcal{R}^2_{\rm G}\rangle^{1/2} \ll 1$ such that the Gaussian term in the expansion dominates the total curvature perturbation and the non-Gaussian χ^2 term subdominantly contributes. On the other hand, in the non-perturbative limit, we have $|\tilde{f}_{\rm NL}|\langle\mathcal{R}^2_{\rm G}\rangle^{1/2} \gg 1$ such that the χ^2 contribution is so dominant in the total curvature perturbation that we can switch off the Gaussian contribution. The constraints on PBHs as SMBH seeds in these two limits were first studied in [352], and we shall discuss them in the remaining part of this subsection.

5.2.1 Perturbative Limit

Similar to the case of s distortions, we will study and visualize the behaviour of the PBH constraints for two perturbative instances, namely $|\tilde{f}_{\rm NL}|\langle\mathcal{R}^2_{\rm G}\rangle^{1/2} = 0.1$, for which we are deep inside the perturbative regime, and $|\tilde{f}_{\rm NL}|\langle\mathcal{R}^2_{\rm G}\rangle^{1/2} = 1$, which is just the extreme perturbative limit as discussed in Chapter 4.

We recall that the variance corresponding to the total curvature perturbation Eq. (5.2.1) and the associated μ distortion amplitude are given respectively by

$$A \equiv \langle\mathcal{R}^2\rangle = A_G + 2\tilde{f}^2_{\rm NL}A^2_G. \ , \tag{5.2.2}$$

$$\mu = \mu_G + \mu_{\chi^2} = A_G W_\mu(k_*) + 2\tilde{f}^2_{\rm NL}A^2_G W^{(\rm NG2)}_\mu(k_*) \ , \tag{5.2.3}$$

where the definitions of the window functions are the same as in Chapter 3. To plot the μ constraint, we saturate the μ amplitude with the FIRAS bound by taking the two limits of perturbativity. As for the PBH constraints, we use the technique from [87] (also summarized in Appendix E) to compute the variance from the PBH abundance in the presence of arbitrary-ordered non-Gaussianity. Expressing the total variance in terms of the Gaussian variance, we get

$$A = \frac{A_G}{2}\left(1+\sqrt{1+8\kappa}\right)\begin{cases}\approx A_{\rm G}, & \kappa = 0.01\\ = 2A_{\rm G}, & \kappa = 1 \ ,\end{cases} \tag{5.2.4}$$

where $\kappa = A\tilde{f}^2_{\rm NL}$ is the perturbativity quantifier. As expected, the variance of the total perturbation is approximately equal to the Gaussian counterpart when $\kappa = 0.01$. On the other hand, the variance doubles in the extreme perturbative limit, $\kappa = 1$, as it receives equal contributions from the purely Gaussian and the purely χ^2 terms.

We show the results for both the μ constraints and the PBH constraints in Fig. 5.3. The regime where μ constraints are stronger than the PBH constraints is the disapproved regime for the existence of PBHs. Although the μ constraint barely changes when $\kappa = 1$ (except for the very small scales where it flattens), the 1−PBH line comes down by a factor of two. However, this has hardly any implication for the SM-PBHs because the intersection of these constraints (which provides the maximum allowed mass of a PBH corresponding to a certain $f_{\rm PBH}$) happens roughly at the same mass value ($\approx 10^4 M_\odot$) as in the Gaussian case.

In the extreme perturbative scenario, the flattening of μ constraints is more significant, but still not substantial enough to make the intersection happen at a higher mass. A necessary caution here: Since the 1−PBH line shifts down by almost an order of magnitude (compared

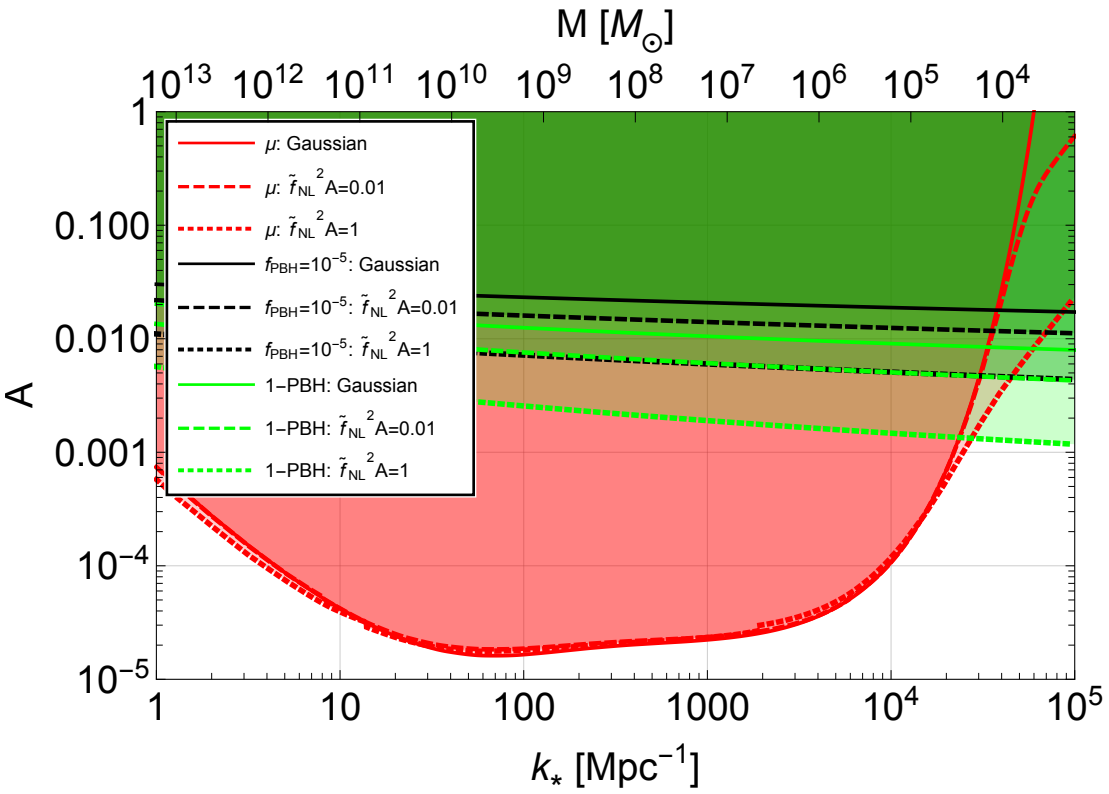

Figure 5.3: *The PBH and μ constraints are shown for Gaussian perturbations in solid lines, perturbative non-Gaussianity in dashed lines ($\tilde{f}_{\rm NL}^2 A = 0.01$), and for the case representing the extreme limit of the perturbative non-Gaussianity in dotted lines. Noteably, the PBH constraint for $f_{\rm PBH} = 10^{-5}$ with $\tilde{f}_{\rm NL}^2 A = 1$ (dashed black) is not too far from the constraint corresponding to a single PBH abundance for $\tilde{f}_{\rm NL}^2 A = 0.01$ (dotted green).*

to the Gaussian line), it would be inaccurate to consider the intersection with the Gaussian μ constraint, as done in the conventional literature. In this case, the intersection shifts by a factor of two on the higher mass side, implying that even in the extreme perturbative limit, μ constraints on SM-PBHs are not evaded significantly. In the following subsection, we will push the χ^2 non-Gaussianity to its strongest non-perturbative limit and check the relaxation in the SM-PBH constraints.

5.2.2 Non-Perturbative Limit

The non-perturbative limit demands that we neglect the Gaussian part of the curvature perturbation such that the full curvature perturbation Eq. (5.2.1) is equal to the χ^2 term

$$\mathcal{R}(\vec{x}) = \mathcal{R}_{\rm G}^2(\vec{x}) - \langle \mathcal{R}_{\rm G}^2 \rangle \ , \tag{5.2.5}$$

where we absorbed the non-Gaussianity parameter $\tilde{f}_{\rm NL}$ in the definition of the amplitude ($\sqrt{A}\tilde{f}_{\rm NL} \to \sqrt{A}$) since it only scales the results. It is worth recalling that in our analysis, $\tilde{f}_{\rm NL}$ is scale-independent across all the scales shown in the plots and at the same time it vanishes at the

scales measured by Planck to avoid the tight constraints from the CMB [5]. This is why we can absorb this parameter without worrying about changing the scale dependence of the power spectrum. We caution that certain models of inflation inspire a scale-dependent $\tilde{f}_{\rm NL}$, which have been studied in the context of both PBHs and SIGWs [330, 331]. This interesting study is beyond the scope of this text, and we restrict ourselves to a constant value of $\tilde{f}_{\rm NL}$(also for the higher-order non-Gaussianity parameters). The expression for the one-loop corrected power spectrum has already been derived in Eq. (4.2.8), which we rewrite below

$$\mathcal{P}_{\mathcal{R}}(k) \equiv \frac{k^3}{2\pi^2} P_{\mathcal{R}}(k) = \mathcal{P}_{\mathcal{R}^2_{\rm G}}(k) \ , \tag{5.2.6}$$

$$= \frac{A_{\rm G^2}}{2} \frac{k^2}{k_*^2} H(2k_* - k) \ , \tag{5.2.7}$$

and the corresponding variance is

$$A_{\rm G^2} = \int_0^\infty \mathcal{P}_{\mathcal{R}_{\rm G^2}} \, d\ln k = 2A_{\rm G^2} \ . \tag{5.2.8}$$

Notice how we have changed the convention for the power spectrum amplitude in contrast to Chapter 4. We shall use the notation $A_{\rm G^n}$ to indicate the variance of the power spectrum associated with the non-perturbative non-Gaussianity of nth order, for example, a non-perturbative cubic non-Gaussianity has variance $A_{\rm G^3}$ and so on. This is more convenient for this section because we will be dealing with the non-Gaussianities up to $n = 5$.

The μ constraint in the non-perturbative case, already shown in Fig. 4.1, is plotted alongside the PBH constraint in Fig. 5.4. The constraint flattens only at small scales where $k \geq 10^4$ Mpc^{-1} and otherwise, it remains in agreement with the Gaussian constraints in its tightest regime. In comparison, the PBH constraint is more sensitive to the non-perturbative non-Gaussianity. Albeit for the cases $f_{\rm PBH} = 10^{-10}, 10^{-5}$, the intersection of these two constraints is hardly different from the one in their Gaussian counterparts. For the 1−PBH case, the intersection is relatively distant from the intersection in the Gaussian counterpart, differing by almost an order of magnitude in $M_{\rm PBH}$ scales. In the latter scenario, we observe a relaxation in the maximum allowed PBH mass from $10^4 M_\odot$ to nearly $10^5 M_\odot$.

We can better examine the scale dependency of both μ and PBH constraints by plotting the ratio of the constraints (relative to the Gaussian constraints) in the perturbative and non-perturbative limits, as shown in Fig. 5.5. As expected, the PBH constraints always weaken in the presence of non-Gaussianity for a given $f_{\rm PBH}$. The ratio of the PBH constraints also exhibits a slight scale-dependence, where they become more relaxed at smaller scales (or smaller masses). However, the μ constraint ratio is mostly scale-independent except for the small k values where the saw-tooth tail of the one-loop power spectrum Eq. (5.2.7) dominates. What's more, the μ constraint ratio is also independent of the μ values and only becomes μ dependent at small k values, for the same reason as before. Conversely, the PBH constraint ratio is sensitive to $f_{\rm PBH}$ because the PBH abundance is linearly proportional to the total power spectrum amplitude. Finally, it can also be inferred that the PBH constraint moves significantly only in the non-perturbative regime of non-Gaussianity.

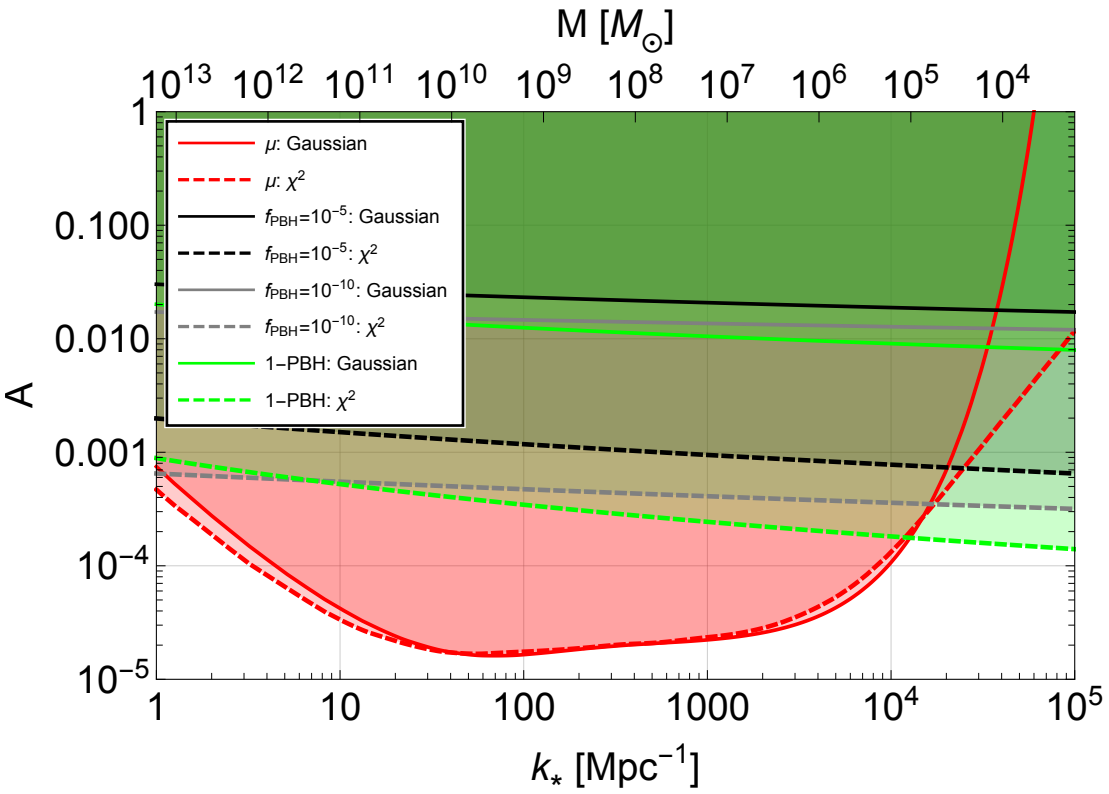

Figure 5.4: *The figure shows both the PBH constraints and the μ distortion constraints on the power spectrum amplitude. The solid and dashed lines correspond to the Gaussian perturbations and χ^2 non-Gaussian perturbations, respectively.*

5.3 Constraints From Cubic Non-Gaussianity

With the inference that even a non-perturbative χ^2 non-Gaussianity is insufficient to relax the μ distortions bounds on the PBH in the supermassive range, we are motivated to study the local non-Gaussianity with a stronger magnitude. We know from the Taylor expansion of the total curvature perturbation Eq. (4.1.1), that the next-to-leading-order correction should come from the term which is cubic in the Gaussian term, or

$$\mathcal{R}(\vec{x}) = \mathcal{R}_{\rm G}(\vec{x}) + \tilde{g}_{\rm NL}\mathcal{R}^3_{\rm G}(\vec{x}) \ , \tag{5.3.1}$$

where we remind about the rescaled cubic non-gaussianity parameter $\tilde{g}_{\rm NL} \equiv 9g_{\rm NL}/25$. Note that we set $\tilde{f}_{\rm NL} = 0$ in order to work in the purely cubic non-Gaussian regime. To put the amplitude or notation to be used in this section on the same platform as the previous sections, let us compute the two-point correlator of $\mathcal{R}$ such that

$$\langle \mathcal{R}\mathcal{R} \rangle = \langle (\mathcal{R}_{\rm G} + \tilde{g}_{\rm NL}\mathcal{R}_{\rm G^3})(\mathcal{R}_{\rm G} + \tilde{g}_{\rm NL}\mathcal{R}_{\rm G^3}) \rangle \ , \tag{5.3.2}$$

$$= \langle \mathcal{R}_{\rm G^2} \rangle + 2\tilde{g}_{\rm NL}\langle \mathcal{R}_{\rm G^4} \rangle + \tilde{g}^2_{\rm NL}\langle \mathcal{R}_{\rm G^6} \rangle \tag{5.3.3}$$

$$= A_{\rm G} + 6\tilde{g}_{\rm NL}A^2_{\rm G} + 15\tilde{g}^2_{\rm NL}A_{\rm G^3} \tag{5.3.4}$$

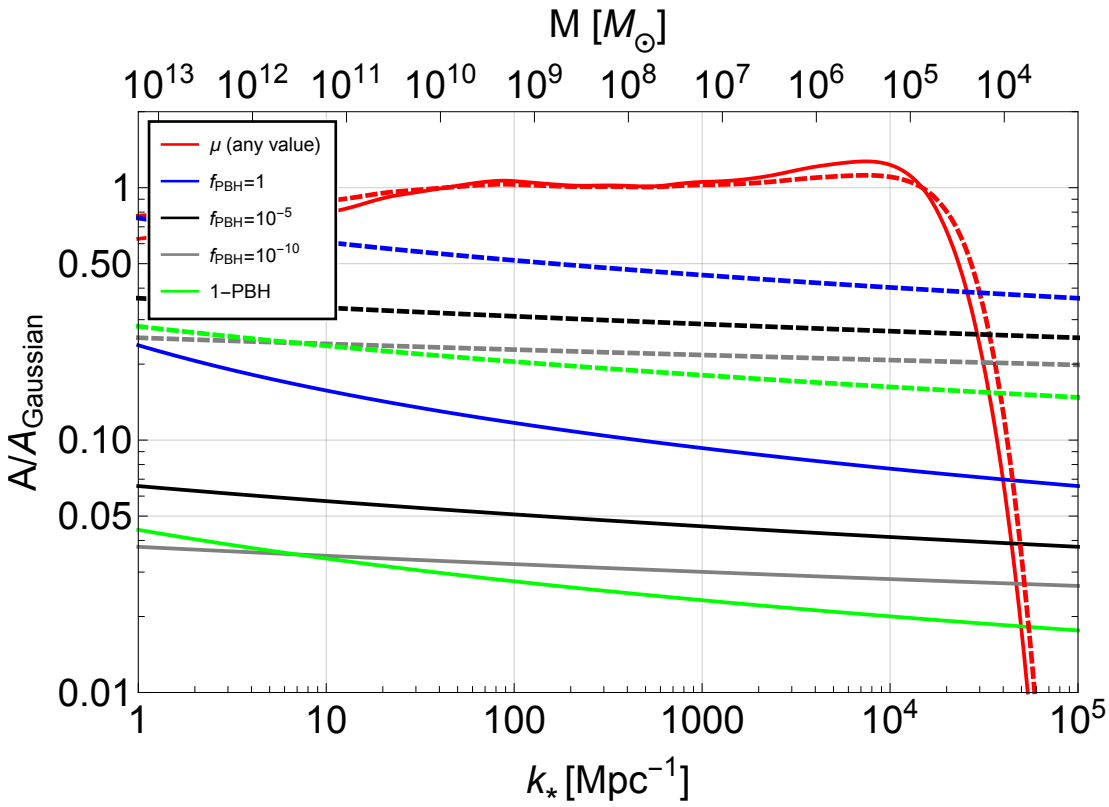

Figure 5.5: *The figure shows the ratio of variances, comparing the constraint on the variance for a χ^2 non-Gaussian perturbation relative to the Gaussian case (solid lines), and for the perturbative non-Gaussian case ($\tilde{f}_{\rm NL}^2 A = 1$) relative to the Gaussian variance (dashed lines, with matching color schemes). The μ constraint ratio does not depend on the μ spectral amplitude. On the contrary, the PBH constraints vary with the assumed value of $f_{\rm PBH}$, though they show only a light sensitivity to k_*.*

Furthermore, we will only show the analysis in the non-perturbative regime of cubic non-Gaussianity, which corresponds to the limit $\tilde{g}_{\rm NL} \to \infty$, for reasons that will become clear later. This gives the definition $A = 15A_{\rm G}^3$, which we shall replace after obtaining the total curvature power spectrum. As before, we neglect the Gaussian contribution in Eq. (5.3.1) and rewrite it in Fourier space

$$\begin{aligned}\mathcal{R}(\vec{k}) &= \mathcal{R}_{\rm G^3}(\vec{k}) \ , \\ &= \tilde{g}_{\rm NL} \int \frac{d^3\vec{q}_1}{(2\pi)^{3/2}} \frac{d^3\vec{q}_2}{(2\pi)^{3/2}} \mathcal{R}_G(\vec{q}_1)\mathcal{R}_G(\vec{q}_2)\mathcal{R}_G(\vec{k}-\vec{q}_1-\vec{q}_2) \ . \end{aligned} \tag{5.3.5}$$

The next task is to characterize the shape of the Gaussian curvature power spectrum, and we choose to work with the Dirac-Delta function again

$$\mathcal{P}_G(k) \equiv \frac{k^3}{2\pi^2} P_G(k) = A_G k_* \delta(k - k_*) \ , \tag{5.3.6}$$

where the notations have the same meaning as in the earlier discussion. As already mentioned, choosing a broader power spectrum would only lead to an extended flattening in the μ constraints

and only a slight difference in the PBH constraints. Eventually, one will get the same conclusion as the Dirac-Delta case, but with a smaller value of the maximum allowed PBH mass, since the intersection of the constraints (see Fig. 5.4 for an intuition) would shift towards the smaller scales. This conclusion was recently verified by [347], who performed a similar analysis using broader power spectra and more complex calculations, ultimately leading to the same conclusion.

The two-loop power spectrum for the curvature perturbation Eq. (5.3.5) has been computed for the first time in [353] using the technique formulated in [332]. We shall summarize the individual contributions in the two-loop integral and point towards the original reference [353] for the complicated (but analytic) integration. The two terms are

- **Dressed Vertex Diagram (DV):** It can be written as

$$P_{G^3,DV} = 6^2 \frac{1}{4} \int \frac{d^3q_1}{(2\pi)^3} \frac{d^3q_2}{(2\pi)^3} P_G(q_1) P_G(q_2) P_G(k) \ , \tag{5.3.7}$$

$$\mathcal{P}_{G^3,DV} = \frac{k^3}{2\pi^2} P_{G^3,DV} = 9 A_G^3 k_* \delta(k - k_*) \ , \tag{5.3.8}$$

  which corresponds to a Gaussian power spectrum rescaled by a factor of $9A_{\rm G}^2$. The factor '6^2' occurs due to our choice of defining the curvature perturbation with Eq. (5.2.1). We can also compute the corresponding variance

$$\sigma^2_{\mathcal{R}_{G^3,DV}} = \int \mathrm{dln}\tilde{k} \frac{\mathcal{P}_{G^3,DV}}{A_G^3} = 9 \ , \tag{5.3.9}$$

  where $\tilde{k} = \frac{k}{k_*}$.

- **Sunset Diagram (S):** It is more complicated to calculate analytically; however, thanks to a series of simplifications, it has been done in [353]. The Sunset contribution is given by

$$P_{G^3,S} = 6 \int \frac{d^3q_1}{(2\pi)^3} \int \frac{d^3q_2}{(2\pi)^3} P_G(\vec{q}_1) P_G(\vec{q}_2) P_G(|\vec{k} - \vec{q}_1 - \vec{q}_2|) \ , \tag{5.3.10}$$

  which, after a lengthy procedure, results in the following term

$$\mathcal{P}_{G^3,S} = \begin{cases} 3\left(\frac{A_G k}{k_*}\right)^3 \ , & 0 \leq \tilde{k} \leq 1 \\ \frac{3A_G^3 k^2}{2k_*^3}(3k_* - k) \ , & 1 < \tilde{k} \leq 3 \ , \end{cases} \tag{5.3.11}$$

  The spectrum cuts off at $k = 3k_*$ due to momentum conservation. Similarly, the variance for the sunset term gives

$$\sigma^2_{\mathcal{R}_{G^3,S}} = \int \mathrm{dln}\tilde{k} \frac{\mathcal{P}_{G^3,S}}{A_G^3} = 6 \ . \tag{5.3.12}$$

We can add both the contributions (Dressed Vertex and Sunset) to get the total two-loop power spectrum, whose variance is

$$\begin{aligned} \sigma_{\mathcal{R}^2_{G^3}} &= \sigma^2_{\mathcal{R}_{G^3,DV}} + \sigma^2_{\mathcal{R}_{G^3,S}} \ , \\ &= 9A_G^3 + 6A_G^3 \ , \\ &= 15A_G^3 \ , \end{aligned} \tag{5.3.13}$$

which coincides with the amplitude redefinition $A = 15A_{\rm G}^3$ as expected. Using the redefined power spectrum amplitude and combining Eqs. (5.3.8) and (5.3.11), we can write the total power spectrum as

$$\mathcal{P}_{G^3}(k) = 3A_G^3 \left[\tilde{k}^3 p(\tilde{k}) + 3k_* \delta(k - k_*)\right] \ , \tag{5.3.14}$$

wherein the piecewise function is defined as

$$p(\tilde{k}) = \begin{cases} 1 & \tilde{k} \leq 1 \ , \\ \frac{3-\tilde{k}}{2\tilde{k}} & 1 < \tilde{k} < 3 \ . \end{cases} \tag{5.3.15}$$

5.3.1 Spectral Distortion Constraints

In analogy with the s distortion in χ^2 non-Gaussianity Eq. (4.2.9), we define the s distortion in cubic non-Gaussianity to be

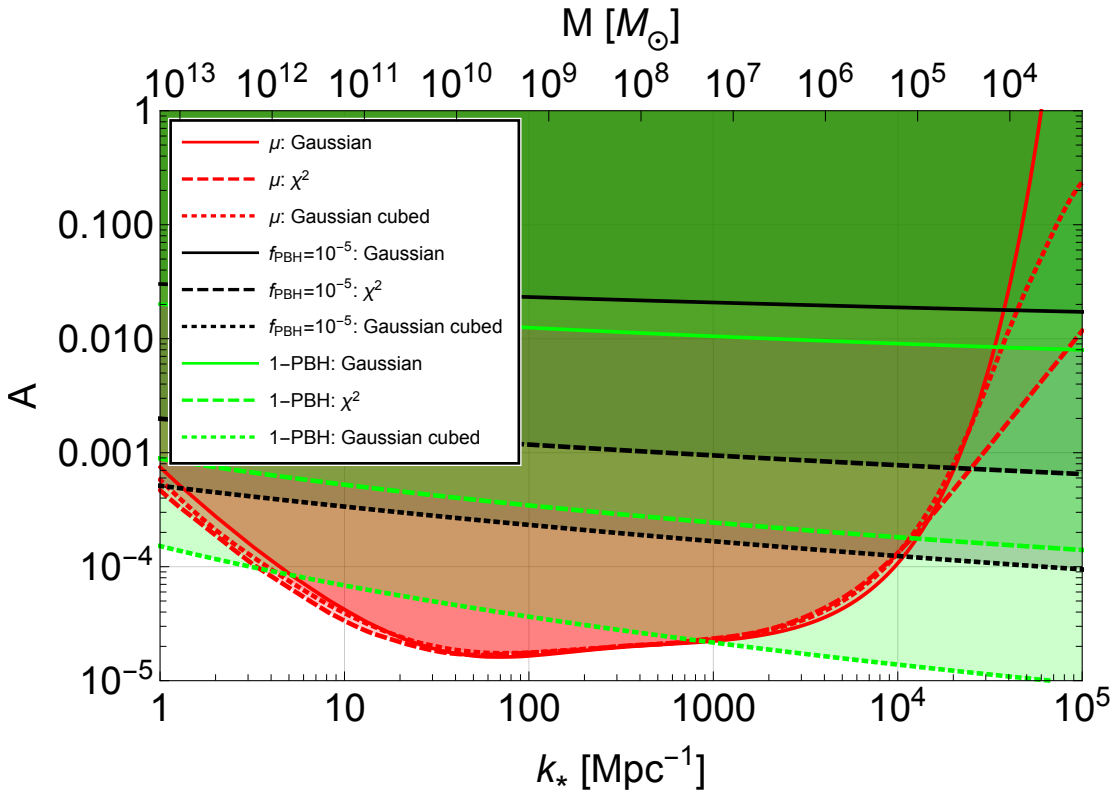

Figure 5.6: *The figure shows the constraints on the amplitude of the power spectrum for three types of perturbations: Gaussian (solid lines), χ^2 non-Gaussian (dashed lines), and cubic non-Gaussian (dotted lines). The $f_{\rm PBH} = 10^{-10}$ constraint is omitted to avoid visual comotion.*

$$s = 9A_G^3 \, W_s(k_*) + 6A_G^3 \, W_s^{(CNG)}(k_*) = \frac{9}{15} A \, W_s(k_*) + \frac{6}{15} A \, W_s^{(CNG)}(k_*) \ , \tag{5.3.16}$$

where the window function corresponding to the Gaussian contribution $W_s(k_*)$ is derived for the accurate hybrid approximation scheme Eq. (3.2.51) using the PCA. The newly introduced

window function $W_s^{(CNG)}(k_*)$ represents the contribution from the two-loop power spectrum of the non-perturbative cubic non-Gaussian curvature perturbation Eq. (5.3.5), and the abbreviated superscript "CNG" stands for cubic non-Gaussianity. The mathematical expression for $W_s^{(CNG)}(k_*)$ is

$$W_s^{(\mathrm{CNG})}(k_*) = \frac{1}{2}\int_0^{3k_*} \frac{dk}{k}\frac{k^3}{k_*^3}\, p(\tilde{k})\, W_s(k)\ , \tag{5.3.17}$$

Finally, we implement the above window function in `CLASS` and perform the same numerical analysis as in Chapter 4 to extract the $s = \mu$ distortion saturated with the FIRAS limit Eq. (3.3.3). The constraint is shown in Fig. 5.7 alongside the PBH constraint, which we explain in the following section.

5.3.2 PBH Constraints

We use the formalism explained in Appendix E to compute the power spectrum amplitude from the PBH abundance (and in turn, f_{PBH}). Similar to the χ^2 case Fig. 5.4, we plot the PBH constraints for ($f_{\mathrm{PBH}} = [10^{-10}, 10^{-5}, 1-\mathrm{PBH}]$) and show the results in Fig. 5.7. As expected, the PBH constraint is even more sensitive to the cubic case than the χ^2 case, as it comes down to as much as two orders of magnitude for the $1-$PBH abundance. This situation is similar to the other two cases of f_{PBH}.

On the other hand, the μ constraints are notably aligned with the Gaussian constraints, except for very large k values (or equivalently, very small scales). This is precisely the reason why we do not consider the perturbative case for the cubic non-Gaussianity, since a perturbative limit here would be even closer to the Gaussian constraint than the one in Fig. 5.7. Coming to the maximum allowed PBH mass, the intersection of the μ constraint and the PBH constraint in the non-perturbative cubic case happens at $M_{\mathrm{PBH}} \approx 10^7 M_\odot$, which is roughly three orders of magnitude relaxed than the Gaussian case ($M_{\mathrm{PBH}} \approx 10^4 M_\odot$) and two orders of magnitude relaxed than the χ^2 case ($M_{\mathrm{PBH}} \approx 10^5 M_\odot$). The results are less relaxed for larger PBH abundance because the intersection of the constraints in the cases $f_{\mathrm{PBH}} = [10^{-10}, 10^{-5}]$ happens at smaller masses, $10^6 M_\odot$ and $10^5 M_\odot$ respectively.

However, this relaxation is mostly attributed to the weakened PBH constraint and has hardly anything to do with the μ constraint, which nearly coincides with the Gaussian case in the tightest-constraint regime ($10\ \mathrm{Mpc}^{-1} \lesssim k_* \lesssim 10^4\ \mathrm{Mpc}^{-1}$). As a reference, we also plot the constraints for the non-perturbative χ^2 case in Fig. 5.6. In the discrepant regime (large k regime), the cubic μ constraint is closer to the Gaussian μ constraint than the χ^2 μ constraint. This is expected because if we look at the total power spectrum in the cubic case Eq. (5.3.14), it scales with a cubic power in k or $\mathcal{P}_{\mathrm{G}^3} \propto \tilde{k^3}$ if we ignore the amplitude shift due to the second term (the Dressed Vertex term). Whereas, we know from Eq. (5.2.7) that the total power spectrum in the χ^2 case varies as $\mathcal{P}_{\mathrm{G}^2} \propto \tilde{k^2}$. Hence, a steeper slope is anticipated for the cubic μ constraint as in the flattened regime in Fig. 5.6 (which corresponds to $10^4\ \mathrm{Mpc}^{-1} \leq k_* \leq 10^5\ \mathrm{Mpc}^{-1}$).

In summary, we can infer from Section 5.3 and Section 5.2 that the μ constraint is insensitive to even a non-perturbative non-Gaussianity in its tightest regime and flattens only at very small comoving scales. Consequently, even in the presence of such strong non-Gaussianities, we expect a very small population of present-day SMBHs to be seeded by PBHs without evading the SD bounds. This should not come as a surprise because we already saw in Chapter 4 how the

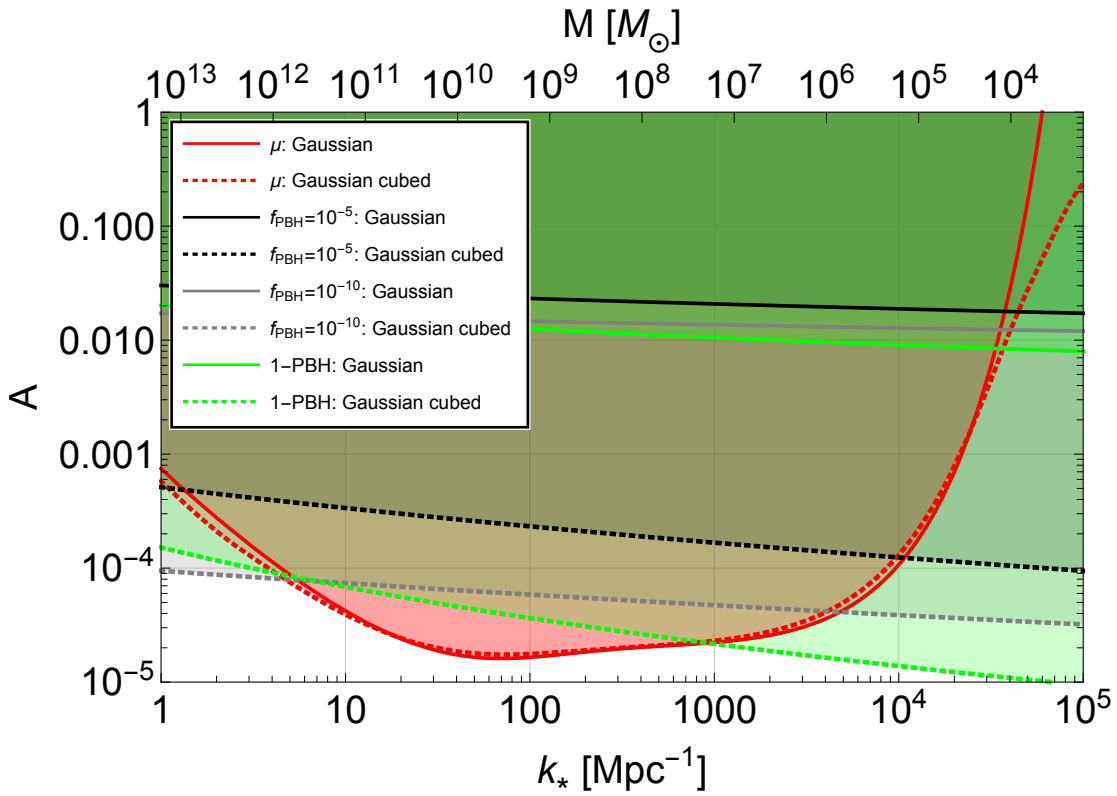

Figure 5.7: *The bounds on μ-distortion on the amplitude of the power spectrum are shown for Gaussian perturbations (solid lines) and cubic non-Gaussian perturbations (dotted lines). Additionally, we display the power spectrum amplitudes necessary to produce various PBH abundances for both Gaussian and cubic cases.*

leading-order correction to the s distortions comes from the quadratic term in anisotropy or $\langle\Theta^2\rangle$ and the next-to-leading order correction from the cubic anisotropy $\langle\Theta^3\rangle$ is relatively suppressed. This quadratic anisotropy depends only on the curvature power spectrum; thus, higher moments of $\mathcal{R}$ do not play a role at the leading order. In the last discussion of this section, we discuss the cases of stronger non-Gaussianities with a caution that it is physically challenging to motivate such non-Gaussianities in the early universe.

5.4 Stronger Non-Gaussianities

This discussion follows from the results of [352, 353]. We have explicitly shown how the tightest-constraint regime remains mostly unbothered regardless of how we classify the primordial initial fluctuations Eq. (E.1) up to $n = 3$. Despite incorporating the one-loop correction to the curvature power spectrum in the χ^2 case and two-loop correction in the cubic case, only the large-k tail behaviour of the μ constraint is affected. Furthermore, the power spectrum, the bispectrum and

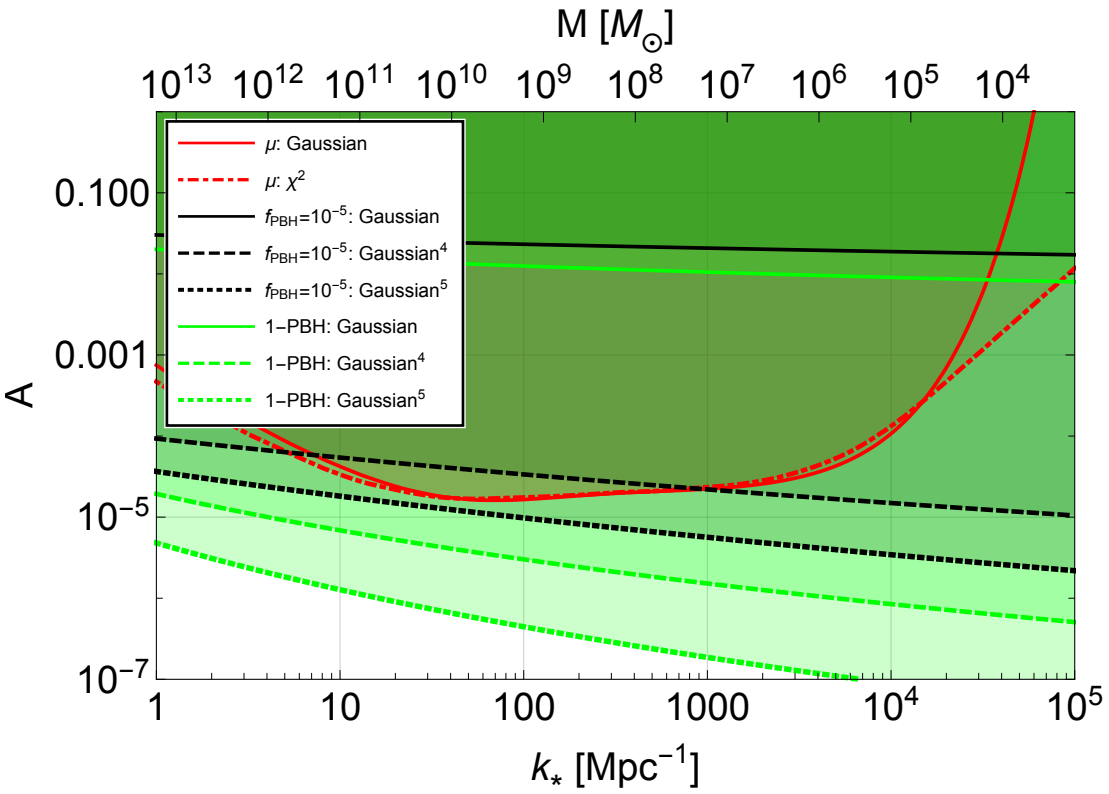

Figure 5.8: *The constraints on $f_{\rm PBH}$ parameter for a non-perturbative non-Gaussianity. The dashed curves correspond to the non-Gaussianity, which is the power four of the Gaussian perturbations, and the dotted curves correspond to the non-Gaussianity, which is the power five of the Gaussian perturbations. The solid curves correspond to the Gaussian perturbations. To analyse the intersection points, the μ constraints are also plotted for the χ^2 and Gaussian cases in dashed-dotted and solid linestyles, respectively.*

the trispectrum manifest the following proportionality to the Gaussian curvature perturbation

$$\mathcal{P}_\mathcal{R} \sim A_G^n \,, \tag{5.4.1}$$

$$\mathcal{B}_\mathcal{R} \sim \begin{cases} A_G^{3n/2} \,, & \text{for even } n \\ 0 \,, & \text{otherwise} \,, \end{cases} \tag{5.4.2}$$

$$\mathcal{T}_\mathcal{R} \sim A_G^{2n} \,. \tag{5.4.3}$$

To circumvent the overproduction of PBHs, $A_{\rm G}$ is always smaller than unity, which implies that in any case, the bispectrum and trispectrum are subdominant compared to the power spectrum. This remains true at an arbitrary order n in non-Gaussianity. However, constructing a model that predicts non-Gaussianities for large values of n requires a significant amount of fine-tuning [328, 354–356]. Although it is challenging to calculate the exact expression for the Sunset diagrams corresponding to the stronger non-Gaussianities ($n > 2$), a semi-analytic approximation has been penned in the appendix of [353], which shows that the relative significance of the Sunset diagram keeps decreasing with increasing the order of non-Gaussianity. This is shown in Fig. 5.9. It strengthens the reasoning that at large values of n, the μ constraint should be very similar to its

Gaussian counterpart.

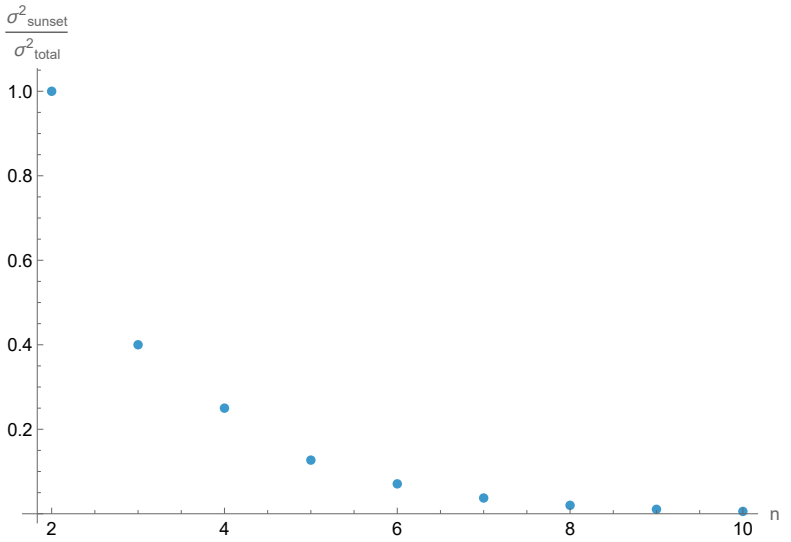

Figure 5.9: *The points in the figure show the relative significance of the sunset diagram to the variance corresponding to the full curvature power spectrum. The x-axis represents the order 'n' of non-Gaussianity in the non-perturbative limit.*

In Appendix E we compute the power spectrum amplitude required to generate an arbitrary PBH abundance, in the presence of non-Gaussianity with $n = 4, 5$. The resulting constraint is plotted in Fig. 5.8 alongside the μ constraint for the χ^2 case[13]. For the first time, we are able to produce a single PBH of any mass without disturbing the μ constraints ($n = 4$). Even for a higher PBH abundance, $f_{\text{PBH}} = 10^{-5}$, we expect the maximum allowed mass to be $\sim 10^7 M_\odot$. This situation further improves for the 5th order non-Gaussianity, where we see the PBH bound lower than the μ constraint for all masses, even when $f_{\text{PBH}} = 10^{-5}$.

[13]We could also have plotted the μ constraint for the cubic non-Gaussianity, but in the end the conclusion remains independent of either of them, as already explained before.

CHAPTER 6

Conclusions

This thesis investigates the perturbations originating from the inflationary epoch in the early universe by developing dedicated numerical tools. In addition, it explores the observable imprints of these perturbations, specifically the Cosmic Microwave Background (CMB) and Primordial Black Holes (PBHs). PBHs are often regarded as leading dark matter candidates and are increasingly considered potential seeds for the formation of supermassive black holes in the present-day universe. While the temperature anisotropies in the CMB have been extensively studied and have unveiled a wealth of information about the early universe, the spectral distortions of the CMB remain relatively underexplored. This is primarily due to the stringent upper bounds on their magnitude from the FIRAS experiment.

Following a review of the foundational physics of the early universe up to the epoch of recombination, we introduced the stochastic approach to inflation in Chapter 2. Using a Brownian-like stochastic framework, we modeled the influence of quantized short-wavelength (SW) perturbation modes on the classicalized long-wavelength (LW) background. The SW modes act as random white noise, modifying the dynamics of LW modes whenever they undergo quantum-to-classical transitions through squeezing and decoherence.

In Section 2.5.2, we presented our numerical algorithm to generate stochastic realizations for arbitrary single-field inflation models. This algorithm includes the effects of noise via a Wiener process and uses a stochastic Runge-Kutta weak order two method. It outputs either the probability distribution function (PDF) or the power spectrum of curvature perturbations using the ΔN formalism. We demonstrated the algorithm on three inflationary models, one of which exhibits an ultra-slow-roll (USR) regime, and generated the PDF and power spectrum in Section 2.6.1 and Section 2.6.2, respectively. From the PDFs of the fully non-linear curvature perturbation in Figs. 2.10 and 2.12, we report a significant presence of non-Gaussianity in the distribution tails. Although we recover a nearly scale-invariant power spectrum in the attractor model, we observe that for the USR case, mapping the real-space variance to the Fourier-space power spectrum is nontrivial due to the strong scale dependence, as discussed in Section 2.6.2. Nevertheless, our algorithm is capable of computing higher-order statistical moments, such as the bispectrum and trispectrum, and can be readily extended to multi-field inflation scenarios.

In Chapter 3, we begin by introducing the concept of a blackbody and proceed in Section 3.1.2 to explain how the relative efficiency of the three dominant photon-matter interaction processes—Compton scattering, double Compton scattering, and Bremsstrahlung—gives rise to various categories of spectral distortions, namely temperature shifts, μ distortions, y distortions, and residual distortions. In Section 3.2, we narrow our focus to distortions caused by the dissipation of primordial perturbations and outline the standard framework to compute s distortions, where $s = \mu, y$. We also introduce a new and more accurate scheme to calculate the source function for s distortions. This scheme is implemented in the Einstein-Boltzmann solver `CLASS` to compute the amplitude and shape of s distortions numerically, leading to observational constraints on the primordial power spectrum in Section 3.3.

In Chapter 4, we motivate the study of primordial non-Gaussianity, especially at scales much smaller than those probed by the CMB. We consider local-type non-Gaussianity by retaining the leading-order correction in Eq. (4.1.1). In Section 4.2.2, we construct the window function corresponding to this correction, which arises from the one-loop corrected power spectrum. We find that within the perturbative regime, the constraints on the power spectrum nearly align with their Gaussian counterparts, except in the extreme limit of perturbativity. We also examine the non-perturbative (χ^2) regime and find that constraints flatten significantly at small scales due to mode coupling, as shown in Fig. 4.1. To assess the relevance of next-to-leading-order corrections, we construct the window function for the cubic contribution, arising from the bispectrum of anisotropy multipoles, in Section 4.2.3. We find this contribution to be subdominant across all non-Gaussianity regimes, as demonstrated in Fig. 4.3.

The significance of non-Gaussianity in the context of PBHs is further highlighted in Fig. 2.11, which illustrates the sensitivity of PBH abundance to the PDF tail. In Chapter 5, we apply the same model of non-Gaussianity from Chapter 4 to compute the PBH constraints and intersect them with the μ distortion bounds to determine the implications for $f_{\rm PBH}$. Since μ constraints impact supermassive PBHs, any relaxation of these intersecting constraints would be promising for the hypothesis that PBHs seed supermassive black holes (SMBHs). We find that in the perturbative limit, the maximum allowed PBH mass remains essentially unchanged, as shown in Fig. 5.3. However, in the non-perturbative χ^2 case, a relaxation of up to one order of magnitude is observed—though only for very small PBH abundances (Fig. 5.4).

Furthermore, in Section 5.3, we analytically compute the two-loop power spectrum associated with the next-to-leading-order non-Gaussian correction in Eq. (4.1.1), and construct the corresponding non-Gaussian window function in Eq. (5.3.17), which receives contributions from both dressed vertex and sunset diagrams. When intersecting PBH and μ constraints in the non-perturbative $\tilde{g}_{\rm NL}$ limit, we find minimal increases in both maximum PBH mass and allowed $f_{\rm PBH}$ compared to the χ^2 case. This is attributed to the steeper scaling of the μ constraint in the cubic case, $\mu \propto k^3$, versus $\mu \propto k^2$ in the χ^2 scenario, as illustrated in Fig. 5.6. As a result, the cubic non-Gaussian constraint curve lies closer to the Gaussian curve and nearly overlaps with it in the most constrained regime.

In Section 5.4, we explore the implications of even stronger non-Gaussianities—specifically Gaussian^4 and Gaussian^5—for the formation of supermassive PBHs. We find that, in these cases, it is possible to produce PBHs of any mass without violating μ constraints, although only for PBH abundances as small as $f_{\rm PBH} = 10^{-5}$, as evident from Fig. 5.8. While analytical

computation of the corresponding window functions is challenging, our findings from the χ^2 and cubic non-Gaussian analyses suggest that μ constraints in these stronger cases would lie even closer to the Gaussian curve than in the cubic case. Although this raises the possibility of generating a small fraction of SMBHs without requiring accretion, it is important to note that such strong non-Gaussianities currently lack theoretical support from known inflationary models.

Our results open several avenues for future work. One potential extension of the stochastic inflation algorithm is to map the scale dependence of the non-perturbative power spectrum, Eq. (2.5.6). This could be achieved by discretizing the system and treating the scale-dependent term as the dependent variable. With suitable initial conditions, one could solve for $\frac{d\mathcal{P}_{\mathcal{R}}}{dN}(k, \bar{N})$, and subsequently compute higher-order spectral moments via peak theory. This would allow for an extremely accurate calculation of $f_{\rm PBH}$ through a fully non-perturbative method using Eq. (1.6.12).

On a parallel front, our analysis of spectral distortions from non-Gaussian curvature perturbations can be extended to study second-order induced gravitational waves (SIGWs), enabling bounds on SIGWs in the presence of strong non-Gaussianity. Given that SIGWs are emerging as viable candidates for the stochastic gravitational wave background observed by Pulsar Timing Array and NANOGrav collaborations [357], a combined analysis using μ distortion and PTA constraints could offer novel insights into the permissible ranges of non-Gaussianity parameters.

Appendices

Appendix A: Two Point Correlators in Legendre Space

Let X be the generic superscript to denote the temperature anisotropies $\Theta^X \equiv \Theta^B, \Theta^{C1}$. We switch to Fourier space from real space

$$\Theta^X(\eta, \vec{x}, \hat{n}) = \int \frac{d^3\vec{k}}{(2\pi)^{3/2}} e^{-i\vec{k}\cdot\vec{x}} \Theta^X(\vec{k}, \hat{n}, t) \ . \tag{A.1}$$

We know that in the ΛCDM model, the CMB anisotropies were seeded by the inflationary perturbations, including the scalar and tensor perturbations. Scalar perturbations played a dominant role in generating the spatial temperature variations, so we shall neglect the contribution of tensor modes to Θ^X. We can store the evolution history of the scalar curvature perturbations (from the time they were super-Horizon at the end of inflation till they transformed into Θ^X) into the transfer function Θ^X,

$$\Theta^X(\vec{k}, \hat{n}, t) = \Theta^X(k, \mu, t)\mathcal{R}(\vec{k}) \ . \tag{A.2}$$

We have denoted the transfer function of Θ^X with the same variable to go with the convention and $\cos\mu = \frac{\vec{k}}{|\vec{k}|} \cdot \hat{n}$. The linear relation between the curvature perturbation and temperature anisotropy is also valid in the presence of non-Gaussianity. Moving on, we switch to the Legendre space so that

$$\Theta^X(\tau, \vec{x}, \hat{n}) = \int \frac{d^3\vec{k}}{(2\pi)^{3/2}} e^{-i\vec{k}\cdot\vec{x}} \sum_\ell (-i)^\ell (2\ell+1)\Theta_\ell^X(k) P_\ell(\mu)\mathcal{R}(\vec{k}) \ , \tag{A.3}$$

where

$$\Theta^X(k, \mu, t) = \sum_\ell (-i)^\ell (2\ell+1)\Theta_\ell^X(k) P_\ell(\mu) \ , \tag{A.4}$$

and $P_\ell(\mu)$ is the Legendre polynomial of degree l. Using Eq. (A.3), we write the two-point correlator of the temperature anisotropy as

$$\begin{aligned}\Theta^{\rm G}\Theta^{\rm C1} = \int \frac{d^3\vec{k}d^3\vec{k}'}{(2\pi)^3} e^{-i(\vec{k}-\vec{k}')\cdot\vec{x}} \sum_{\ell,\ell'} (-i)^{(\ell-\ell')}(2\ell+1)(2\ell'+1) \\ \Theta_\ell^{\rm G}(k)\Theta_{\ell'}^{\rm C1}(k') P_\ell(\mu)P_{\ell'}(\mu') \times \mathcal{R}(\vec{k})\mathcal{R}^*(\vec{k}') \ ,\end{aligned} \tag{A.5}$$

where we have taken a product of Eq. (A.3) with its complex conjugate. The left-hand side of Eq. (A.5) is a real and measurable quantity when we take its average over position and direction. Since the curvature perturbation is a stochastic variable, we invoke ergodicity to claim that the variance of the average of $\mathcal{R}_{\vec{k}}$ over many random outcomes is equal to taking the variance of the real variable Θ_X averaged over the entire sky. We can substitute the variance of $\mathcal{R}_{\vec{k}}$ with the power spectrum in Fourier space

$$\begin{aligned}\langle\Theta^{\rm G}\Theta^{\rm C1}\rangle = \int \frac{d^3\vec{k}}{(2\pi)^3} \sum_{\ell,\ell'} (-i)^{(\ell-\ell')}(2\ell+1)(2\ell'+1)\Theta_\ell^{\rm G}(k)\Theta_{\ell'}^{\rm C1}(k) \\ P_\ell(\mu)P_{\ell'}(\mu)P_{\mathcal{R}}(k) \ ,\end{aligned} \tag{A.6}$$

where we have integrated the dependency over the Fourier mode $d^3\vec{k}$, thanks to the Dirac delta function resulting from the homogeneity and statistical isotropy of the power spectrum. To integrate the remaining part of the integral in Eq. (A.6), we can use the orthogonality of Legendre polynomials

$$\int d\hat{k} P_\ell(\mu) P_{\ell'}(\mu) = \int_0^\pi d\theta \, \sin\theta \int_0^{2\pi} d\phi P_\ell(\cos\theta) P_{\ell'}(\cos\theta) \ , \tag{A.7}$$

$$= 2\pi \int_{-1}^{1} dx P_\ell(x) P_{\ell'}(x) \ , \tag{A.8}$$

$$= 2\pi \frac{2}{2\ell+1} \delta_{\ell\ell'} \ , \tag{A.9}$$

such that the directional spatial average of Eq. (A.6) reduces to

$$\langle \Theta^{\rm G} \Theta^{\rm C1} \rangle_{\vec{x},\hat{n}} = \int \frac{dk\, k^2}{(2\pi)^3} \sum_\ell 4\pi (2\ell+1) \Theta_\ell^{\rm G}(k) \Theta_\ell^{\rm C1}(k) P_{\mathcal{R}}(k) \ . \tag{A.10}$$

Appendix B: Locally Non-Gaussian Bispectrum

We are interested in computing the bispectrum of the temperature anisotropies, which is the Fourier counterpart of the three-point correlation function in real space

$$B_{\ell_1\ell_2\ell_3} \equiv \langle \Theta_{(\ell 1)}(\vec{x},\hat{n},\eta)\, \Theta_{(\ell 2)}(\vec{x},\hat{n},\eta)\, \Theta_{(\ell 3)}(\vec{x},\hat{n},\eta) \rangle_{\vec{x},\hat{n}} \ . \tag{B.1}$$

We can expand this expression in Legendre multipoles. Similar to Section 3.2, we can invoke ergodicity to average over many random realizations in a specific direction to obtain the average of space and direction, i.e. $\langle ... \rangle|_{(\vec{x},\hat{n})}$. We can rewrite Eq. (B.1) as

$$\begin{aligned} B_{\ell_1\ell_2\ell_3} = \Bigg\langle \int \frac{d^3\vec{k}_1 d^3\vec{k}_2 d^3\vec{k}_3}{(2\pi)^{9/2}} e^{-i(\vec{k}_1+\vec{k}_2+\vec{k}_3)\cdot\vec{x}} (-i)^{\ell_1+\ell_2+\ell_3} \\ (2\ell_1+1)(2\ell_2+1)(2\ell_3+1) \times \Theta_{\ell_1}(k_1)\Theta_{\ell_2}(k_2)\Theta_{\ell_3}(k_3) \\ P_{\ell_1}(\hat{k}_1\cdot\hat{n}) P_{\ell_2}(\hat{k}_2\cdot\hat{n}) P_{\ell_3}(\hat{k}_3\cdot\hat{n}) \mathcal{R}(\vec{k}_1)\mathcal{R}(\vec{k}_2)\mathcal{R}(\vec{k}_3) \Bigg\rangle \ . \end{aligned} \tag{B.2}$$

A fancy expression for the 3-dimensional Dirac-Delta function has been used to simplify the higher-order correlators [358], which works on substituting δ^3 with a function involving spherical Bessel functions (first kind) and Wigner 3j-symbols

$$\begin{aligned} \delta^3(\vec{k}_1+\vec{k}_2+\vec{k}_3) \quad = \quad & 8 \sum_{L_i,M_i} i^{L_1+L_2+L_3} \sqrt{\frac{\prod_i (2L_i+1)}{4\pi}} \\ & \begin{pmatrix} L_1 & L_2 & L_3 \\ 0 & 0 & 0 \end{pmatrix} \begin{pmatrix} L_1 & L_2 & L_3 \\ M_1 & M_2 & M_3 \end{pmatrix} \\ & \times Y_{L_1}^{M_1}(\hat{k}_1) Y_{L_2}^{M_2}(\hat{k}_2) Y_{L_3}^{M_3}(\hat{k}_3) \\ & \int dr r^2 j_{L_1}(rk_1) j_{L_2}(rk_2) j_{L_3}(rk_3) \ . \end{aligned} \tag{B.3}$$

We can sum up the three permutation terms of the bispectrum by considering them as equal. Upon replacing the Delta function in Eq. (B.2) with its new definition, we get the following bulky expression

$$
\begin{aligned}
B_{\ell_1\ell_2\ell_3} &= 24\tilde{f}_{\rm NL}\int \frac{d^3\vec{k}_1 d^3\vec{k}_2 d^3\vec{k}_3}{(2\pi)^{9/2}}(-i)^{\ell_1+\ell_2+\ell_3}(2\ell_1+1)(2\ell_2+1)(2\ell_3+1) \\
&\times \Theta_{\ell_1}(k_1)\Theta_{\ell_2}(k_2)\Theta_{\ell_3}(k_3)P_{\ell_1}(\hat{k}_1\cdot\hat{n})P_{\ell_2}(\hat{k}_2\cdot\hat{n})P_{\ell_3}(\hat{k}_3\cdot\hat{n})P_{\mathcal{R}}(k_1)P_{\mathcal{R}}(k_2) \\
&\times \sum_{L_i,M_i} i^{L_1+L_2+L_3}\sqrt{\frac{(2L_1+1)\,(2L_2+1)\,(2L_3+1)}{4\pi}} \\
&\begin{pmatrix} L_1 & L_2 & L_3 \\ 0 & 0 & 0 \end{pmatrix}\begin{pmatrix} L_1 & L_2 & L_3 \\ M_1 & M_2 & M_3 \end{pmatrix} \\
&\times Y_{L_1}^{M_1}(\hat{k}_1)Y_{L_2}^{M_2}(\hat{k}_2)Y_{L_3}^{M_3}(\hat{k}_3)\int dr r^2 j_{L_1}(rk_1)j_{L_2}(rk_2)j_{L_3}(rk_3)\ . \qquad \text{(B.4)}
\end{aligned}
$$

Furthermore, the Legendre polynomials P_{ℓ_i}, with i running from 1 to 3, can be expanded into spherical harmonics, and if we also note that spherical harmonics follow the orthogonal property, we get

$$
\begin{aligned}
\int d\hat{k}_i\, P_{\ell_i}(\hat{k}_i\cdot\hat{n})\, Y_{L_i}^{M_i}(\hat{k}_i) &= \int d\hat{k}_i \left(\sum_{m_i=-l_i}^{l_i}\frac{4\pi}{(2\ell_i+1)}Y_{\ell_i}^{m_i}(\hat{n})Y_{\ell_i}^{m_i*}(\hat{k}_i)\right)Y_{L_i}^{M_i}(\hat{k}_i) \\
&= \sum_{m_i=-l_i}^{l_i}\frac{4\pi}{(2\ell_i+1)}Y_{\ell_i}^{m_i}(\hat{n})\delta_{\ell_i,L_i}\delta_{m_i,M_i}\ . \qquad \text{(B.5)}
\end{aligned}
$$

To simplify things, we can align the direction vector with $\hat{n}$ towards $\theta = 0$ that gives $Y_{\ell_i}^{m_i}(\hat{n}) = \sqrt{(2\ell_i+1)/4\pi}\ \delta_{m_i,0}$ and the bulky expression is compressed

$$
\begin{aligned}
B_{\ell_1\ell_2\ell_3} &= 24\tilde{f}_{\rm NL}(4\pi)\int \frac{dk_1 dk_2 dk_3}{(2\pi)^{9/2}}k_1^2k_2^2k_3^2\Theta_{\ell_1}(k_1)\Theta_{\ell_2}(k_2)\Theta_{\ell_3}(k_3) \\
&P_{\mathcal{R}}(k_1)P_{\mathcal{R}}(k_2)\times(2\ell_1+1)\,(2\ell_2+1)\,(2\ell_3+1)\begin{pmatrix} \ell_1 & \ell_2 & \ell_3 \\ 0 & 0 & 0 \end{pmatrix}^2 \\
&\int dr r^2 j_{\ell_1}(rk_1)j_{\ell_2}(rk_2)j_{\ell_3}(rk_3)\ . \qquad \text{(B.6)}
\end{aligned}
$$

The above equation can be written in a more convenient form that facilitates its numerical implementation. There are three integrals with respect to (k_1, k_2, k_3) and one integral with respect to r. The integrals with respect to the wavemodes k_1 and k_2 are the same, so we can

integrate the expression for the k_1 integral and square it to obtain the following expression

$$\begin{aligned} B_{\ell_1\ell_2\ell_3} &= \frac{48\tilde{f}_{\rm NL}}{(2\pi)^{7/2}}\left[\prod_i(2\ell_i+1)\right]\begin{pmatrix}\ell_1 & \ell_2 & \ell_3\\ 0 & 0 & 0\end{pmatrix}^2 \\ &\int dr\, r^2\left[\int dk_1\, k_1^2 P_{\mathcal{R}}(k_1)\Theta_{\ell_1}(k_1)j_{\ell_1}(rk_1)\right] \\ &\times\left[\int dk_2\, k_2^2 P_{\mathcal{R}}(k_2)\Theta_{\ell_2}(k_2)j_{\ell_2}(rk_2)\right]\left[\int dk_3\, k_3^2\Theta_{\ell_3}(k_3)j_{\ell_3}(rk_3)\right]\,. \end{aligned} \tag{B.7}$$

It turns out that the only component of the bispectrum which is of interest to us is the $022 = 202 = 220$th component. In the case where one of the indices is zero, the r-integral, $J_{220}(k_1,k_2,k_3) \equiv \int drr^2 j_2(rk_1)j_2(rk_2)j_0(rk_3)$, obeys an analytic expression

$$J_{220}(k_1,k_2,k_3) = \begin{cases} \frac{\pi}{4k_1k_2k_3}P_2(\Delta) & \text{if } 0\le\Delta\le 1, \\ 0 & \text{otherwise.}\end{cases} \tag{B.8}$$

where, $\Delta = \frac{k_1^2+k_2^2-k_3^2}{2k_1k_2}$. Finally, we write the version of the bispectrum that is in the same format as the one implemented in `CLASS`, as

$$\begin{aligned} B_{220} &= \frac{15\sqrt{2}\tilde{f}_{\rm NL}}{\pi^{7/2}}\int dk_1\, k_1^2\Theta_2(k_1)P_{\mathcal{R}}(k_1)\int dk_2\, k_2^2\Theta_2(k_2)P_{\mathcal{R}}(k_2) \\ &\int dk_3\, k_3^2\Theta_0(k_3)\times J_{220}(k_1,k_2,k_3)\,. \end{aligned} \tag{B.9}$$

Appendix C: Noise Plots For Stochastic Inflation

This appendix shows the evolution of stochastic noise for the inflation models studied in Chapter 2. First, we show the noise treatment for model M2 Eq. (2.6.3) in Fig. C.1 for two different cases. The left panel shows the variance of the field noise. We have also compared the full noise treatment via Eq. (2.2.14) and the simplified noise treatment via Eq. (2.6.8). It is clear from the right panel of Fig. C.1 that the momentum noise variance is at least five orders of magnitude smaller than the field noise variance for either case.

Furthermore, we plot the noise evolution of the model M3 Eq. (2.6.4) in Fig. C.2. The left panel of the same figure shows that the sudden features starting from the SR $\rightarrow$ USR, which are smoothened out by the simplified treatment, are accurately tracked by the full treatment. Moreover, the failure of the simplified treatment becomes more evident from the right panel of Fig. C.2, where the momentum noise is nearly comparable to the field noise in the USR region.

Appendix D: Accuracy Check of Stochastic Inflation

Whenever a numerical simulation is involved in the treatment of differential equations, it is necessary to highlight its sensitivity to sampling. As a supplement to the algorithm and results

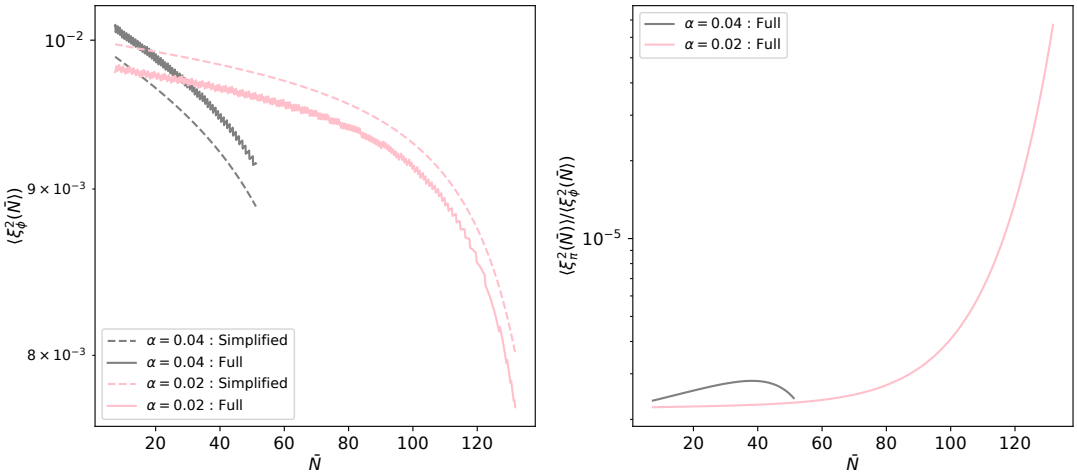

Figure C.1: ***Left Panel:*** *The figure shows the evolution of the variance of the field noise for the model M2 Eq. (2.6.3), and for $\alpha = 0.02, 0.04$. The solid lines represent computation using the full calculation Eq. (2.2.14), whereas the dashed lines represent computation using the simplified treatment given in Eq. (2.6.6).* ***Right Panel:*** *Similar analysis to the left panel but for the variance of the momentum noise, which is normalized to the variance of the field noise. Note that the momentum noise is switched off in the simplified treatment.*

explained in Chapter 2, we perform a sensitivity check for models M2 and M3. The graph of the inflaton's trajectory Fig. 2.6 makes it clear that two parameters play a key role, viz. the time step dN between two consecutive spatial hypersurfaces, and the number of stochastic realizations n_R. The former parameter is responsible for activity at the micro-level, controlling the precision with which each stochastic realization occurs. The latter, on the other hand, is accountable for the macro-level activity because a larger number of realizations would narrow down the uncertainty in the variance at each grid point in the field space.

D.1 M1 Model

We vary dN and n_R first for the attractor potential M1. The sensitivity to these parameters for this model is shown in Fig. D.1. In the left panel, where we have kept n_R constant and varied the time step dN, it is observed that for a larger time step, the amplitude of the oscillations in the residual is also larger. On the contrary, these oscillations in the residual are restricted to less than two for the smallest time step in the analysis. In the right panel of the same figure, we have kept dN constant and varied n_R. The residual is least (less than two) in uncertainty amplitude when n_R is largest, as expected.

D.2 M3 Model

We perform a similar analysis but for the more complicated model M3, which features an USR regime. The residual plotted is for the STINS rather than the full non-perturbative power spectrum. First glimpse on Fig. D.2 tells us that the precision in dN needs to be better than the M1 model by around one order of magnitude. Similar to the case of M1, there is an increasing

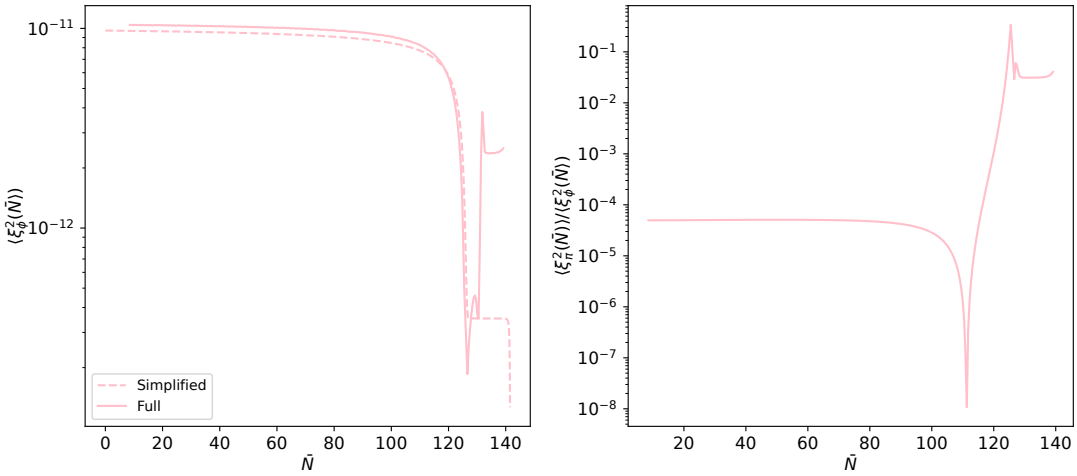

Figure C.2: ***Left Panel:*** *The figure shows the evolution of the variance of the field noise for the model M3 Eq. (2.6.4). The solid lines represent computation using the full calculation Eq. (2.2.14), whereas the dashed lines represent computation using the simplified treatment given in Eq. (2.6.6).* ***Right Panel:*** *Similar analysis to the left panel but for the variance of the momentum noise, which is normalized to the variance of the field noise. Note that the momentum noise is switched off in the simplified treatment.*

scale-dependence in the residual. The left and right panels of the figure correspond to instances with $n_R = 750$ and $n_R = 5000$, respectively. The attractor regime remains primarily insensitive to the increased number of realizations, although increasing n_R does make this insensitivity more independent of the time step.

There is an improvement in the residual by more than an order of magnitude at the SR $\rightarrow$ USR transition when n_R is increased to 5000. Finally, it is worth mentioning that the field grid is unequally spaced in this model to compensate for the extremely small changes in the field evolution in the USR regime. For this purpose, we adjust this grid length from a minimum of 2000 points to a maximum of 3500 points, in order to minimize the residual fluctuation amplitude.

Appendix E: Large Non-Gaussianity and PBH Abundance

This appendix provides a summary of computing the constraints on the amplitude 'A' of the curvature power spectrum, in the presence of arbitrary-ordered non-Gaussianities. This method was introduced in [87], and the constraints for non-Gaussianities characterized by up to the fifth power of Gaussian perturbations were first calculated in [352]. We are interested in the non-perturbative limit where the non-Gaussianity parameters reach infinity ($\tilde{f}_{\rm NL}, \tilde{g}_{\rm NL}, \tilde{h}_{\rm NL}, \tilde{i}_{\rm NL} \rightarrow \infty$). The total curvature perturbation in the non-perturbative limit is

$$\mathcal{R} \equiv h(\mathcal{R}_{\rm G}) = \mathcal{R}^n_{\rm G} - \langle \mathcal{R}^n_{\rm G} \rangle, \tag{E.1}$$

where $n \in [2, 5]$ in this text. With the help of the following change of variable, one can write a non-Gaussian PDF in terms of a Gaussian PDF

$$P_{\rm NG} d\mathcal{R} = \sum_i \left| \frac{dh_i^{-1}(\mathcal{R})}{d\mathcal{R}} \right| P_{\rm G}(h^{-1}) d\mathcal{R} \ . \tag{E.2}$$

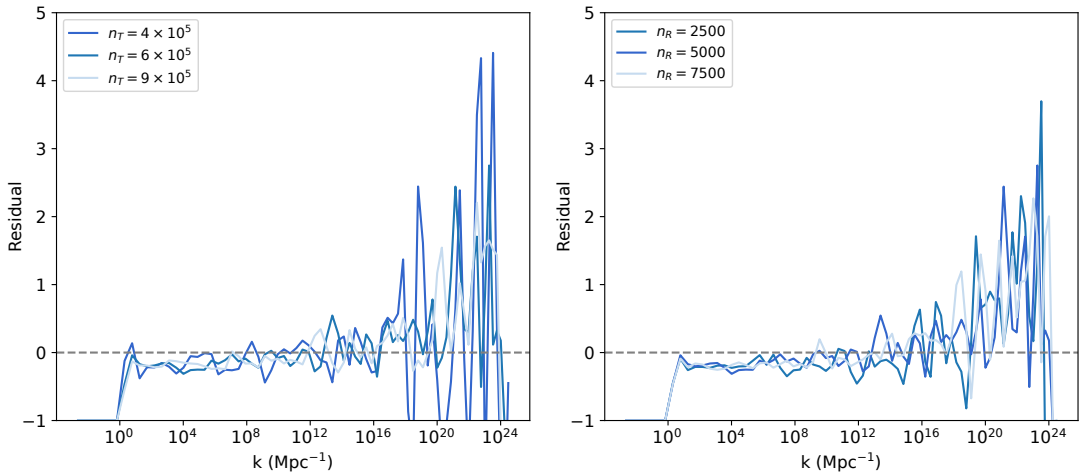

Figure D.1: ***Left Panel:*** *The figure compares the residuals of the non-perturbative power spectrum as a function of the comoving scales for the model M1 Eq. (2.6.1), and for the case* $n_{\rm R} = 5000$*. The parameter* n_T *is defined as* $n_T = \frac{\bar{N}}{dN}$*.* ***Right Panel:*** *Similar analysis as in the left panel but for the case* $n_T = 6 \times 10^5$*.*

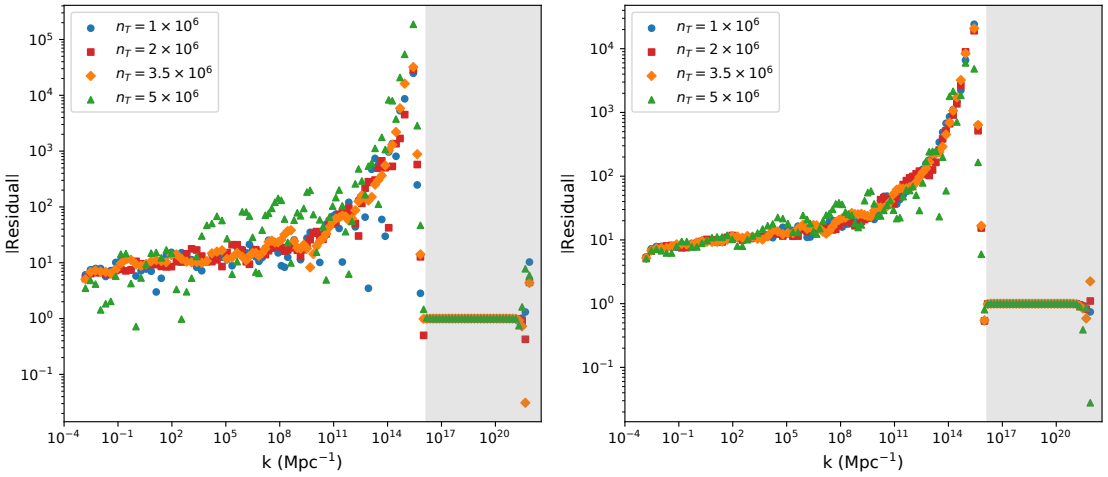

Figure D.2: ***Left Panel:*** *The figure compares the residuals of the STINS as a function of the comoving scales for the model M3 Eq. (2.6.4), and for the case* $n_{\rm R} = 750$*. The grey band shows the USR regime.* ***Right Panel:*** *Similar analysis as in the left panel but for the case* $n_{\rm R} = 5000$*.*

The terms $P_{\rm G}$ and $P_{\rm NG}$ stand for Gaussian PDF and non-Gaussian PDF, respectively, and the index 'i' sums all the solutions to $h(\mathcal{R}_{\rm G}) = \mathcal{R}$. The number of solutions is two (both solutions are the same) or one when n is an even or odd number , respectively.

When n is an odd number, the second term in the final expression of Eq. (E.1) vanishes as

the odd moment of a Gaussian variable is zero. This results in

$$h^{-1}(\mathcal{R}) = \mathcal{R}^{1/n} \,, \tag{E.3}$$

$$\Rightarrow y \equiv \frac{h^{-1}(\mathcal{R})}{\sigma_{\rm G}} = \frac{\mathcal{R}^{1/n}}{\sigma_{\rm G}}, \qquad y_c = \frac{\mathcal{R}_c^{1/n}}{\sigma_{\rm G}} \,. \tag{E.4}$$

With the help of the Press-Schechter formalism explained in Section 1.6, we write the PBH abundance up to arbitrary order in non-Gaussianity

$$\beta_{{\rm G}^n} = \frac{1}{2}{\rm ErfC}\left(\frac{y_c}{\sqrt{2}}\right). \tag{E.5}$$

To make the power spectrum amplitude a subject, the above equation can be reversed

$$A_G = \sigma_{\rm G}^2 = \frac{\mathcal{R}_c^{2/n}}{2{\rm InvErfC}^2(2\beta_{{\rm G}^n})} \,, \tag{E.6}$$

where ErfC and InvErfC are respectively the error function and inverse error function. From this, the variance is computed as follows

$$(n-1)!!A_{\rm G}^n = \frac{(n-1)!!}{2^n}\frac{\mathcal{R}_c^2}{{\rm InvErfC}^n(2\beta_{{\rm G}^n})} \,. \tag{E.7}$$

When n is an odd number, the nth moment does not vanish, and instead of a generic solution, we need to find the solutions for specific values of n. The specific values of interest to us are $n = 2$ and $n = 4$. For $n = 2$,

$$\langle \mathcal{R}_{\rm G}^2 \rangle = \sigma_{\rm G}^2 \Rightarrow h^{-1} = \pm\sqrt{\mathcal{R} + \sigma_{\rm G}^2} \,, \tag{E.8}$$

$$\Rightarrow y = \frac{\pm\sqrt{\mathcal{R} + \sigma_{\rm G}^2}}{\sigma_{\rm G}}, \qquad y_c = \frac{\pm\sqrt{\mathcal{R}_c + \sigma_{\rm G}^2}}{\sigma_{\rm G}} \,. \tag{E.9}$$

Using the Press-Schechter formalism again, we get

$$\beta_{{\rm G}^2} = {\rm ErfC}\left(\frac{|y_c|}{\sqrt{2}}\right), \qquad \Rightarrow \ |y_c| = \sqrt{2}\,{\rm InvErfC}\left(\beta_{{\rm G}^2}\right), \tag{E.10}$$

which is reversed to get the power spectrum amplitude

$$A_{G^2} = 2\sigma_{\rm G}^4 = \frac{2\,\mathcal{R}_c^2}{\left(2\,{\rm InvErfC}^2\left(\beta_{{\rm G}^2}\right) - 1\right)^2}. \tag{E.11}$$

In the same way, for the $n = 4$ case,

$$\langle \mathcal{R}_{\rm G}^4 \rangle = 3\sigma_{\rm G}^4 \Rightarrow h^{-1} = \pm\left(\mathcal{R} + 3\sigma_{\rm G}^4\right)^{1/4} \,, \tag{E.12}$$

$$y = \frac{\pm\sqrt{\mathcal{R} + 3\sigma_{\rm G}^4}}{\sigma_{\rm G}}, \qquad y_c = \frac{\pm\sqrt{\mathcal{R}_c + 3\sigma_{\rm G}^4}}{\sigma_{\rm G}}, \tag{E.13}$$

and invoking the Press-Schechter formula for the final time

$$\beta_{{\rm G}^4} = {\rm ErfC}\left(\frac{|y_c|}{\sqrt{2}}\right), \qquad \Rightarrow \ |y_c| = \sqrt{2}{\rm InvErfC}\left(\beta_{{\rm G}^4}\right), \tag{E.14}$$

which is followed by finding the corresponding variance

$$A_{G^4} = 96A_{\rm G}^4 = \frac{96\,\mathcal{R}_c^2}{\left(4\,{\rm InvErfC}^4\left(\beta_{{\rm G}^4}\right) - 3\right)^2} \,, \tag{E.15}$$

where we have used the relation $\langle \mathcal{R}_{\rm G}^8 \rangle = 7!!\sigma_{\rm G}^8$.

Bibliography

[1] Sean M. Carroll. *Spacetime and Geometry: An Introduction to General Relativity*. Cambridge University Press, July 2019. ISBN: 978-0-8053-8732-2, 978-1-108-48839-6, 978-1-108-77555-7. DOI: 10.1017/9781108770385.

[2] George Efstathiou and Steven Gratton. "The evidence for a spatially flat Universe". In: *Mon. Not. Roy. Astron. Soc.* 496.1 (2020), pp. L91–L95. DOI: 10.1093/mnrasl/slaa093. arXiv: 2002.06892 [astro-ph.CO].

[3] Albert Einstein. "The Field Equations of Gravitation". In: *Sitzungsber. Preuss. Akad. Wiss. Berlin (Math. Phys.)* 1915 (1915), pp. 844–847.

[4] Will J. Percival et al. "Baryon Acoustic Oscillations in the Sloan Digital Sky Survey Data Release 7 Galaxy Sample". In: *Mon. Not. Roy. Astron. Soc.* 401 (2010), pp. 2148–2168. DOI: 10.1111/j.1365-2966.2009.15812.x. arXiv: 0907.1660 [astro-ph.CO].

[5] N. Aghanim et al. "Planck 2018 results. VI. Cosmological parameters". In: *Astron. Astrophys.* 641 (2020). [Erratum: Astron.Astrophys. 652, C4 (2021)], A6. DOI: 10.1051/0004-6361/201833910. arXiv: 1807.06209 [astro-ph.CO].

[6] A. Friedmann. "On the Possibility of a world with constant negative curvature of space". In: *Z. Phys.* 21 (1924), pp. 326–332. DOI: 10.1007/BF01328280.

[7] Andrew L Friedman. "On the Curvature of Space". In: *General Relativity and Gravitation* 31 (1999), pp. 1991–2000.

[8] Laird A. Thompson. *Vesto Slipher and the First Galaxy Redshifts*. 2011. arXiv: 1108.4864 [physics.hist-ph].

[9] Robert P. Kirshner. "Hubble's diagram and cosmic expansion". In: *Proceedings of the National Academy of Science* 101.1 (Jan. 2004), pp. 8–13. DOI: 10.1073/pnas.2536799100.

[10] Jean-Pierre Luminet. "Lemaitre's Big Bang". In: *PoS* FFP14 (2016), p. 214. DOI: 10.22323/1.224.0214. arXiv: 1503.08304 [physics.hist-ph].

[11] V. N. Lukash, E. V. Mikheeva and A. M. Malinovsky. "Formation of the large-scale structure of the Universe". In: *Phys. Usp.* 54 (2011), pp. 983–1005. DOI: 10.3367/UFNe.0181.201110a.1017. arXiv: 1209.0371 [astro-ph.CO].

[12] S. Perlmutter et al. "Measurements of Ω and Λ from 42 High Redshift Supernovae". In: *Astrophys. J.* 517 (1999), pp. 565–586. DOI: 10.1086/307221. arXiv: astro-ph/9812133.

[13] Adam G. Riess et al. "Observational evidence from supernovae for an accelerating universe and a cosmological constant". In: *Astron. J.* 116 (1998), pp. 1009–1038. DOI: 10.1086/300499. arXiv: astro-ph/9805201.

[14] R. A. Alpher, H. Bethe and G. Gamow. "The origin of chemical elements". In: *Phys. Rev.* 73 (1948), pp. 803–804. DOI: 10.1103/PhysRev.73.803.

[15] Fred Hoyle. "THE STEADY-STATE UNIVERSE". In: *Scientific American* 195.3 (1956), pp. 157–169. ISSN: 00368733, 19467087.

[16] Hua-Hui Xiong et al. "Oscillating universe with quintom matter". In: *Phys. Lett. B* 666 (2008), pp. 212–217. DOI: 10.1016/j.physletb.2008.07.053. arXiv: 0805.0413 [astro-ph].

[17] Alan H. Guth. "The Inflationary Universe: A Possible Solution to the Horizon and Flatness Problems". In: *Phys. Rev. D* 23 (1981). Ed. by Li-Zhi Fang and R. Ruffini, pp. 347–356. DOI: 10.1103/PhysRevD.23.347.

[18] Alexei A. Starobinsky. "Dynamics of Phase Transition in the New Inflationary Universe Scenario and Generation of Perturbations". In: *Phys. Lett. B* 117 (1982), pp. 175–178. DOI: 10.1016/0370-2693(82)90541-X.

[19] Andreas Albrecht and Paul J. Steinhardt. "Cosmology for Grand Unified Theories with Radiatively Induced Symmetry Breaking". In: *Phys. Rev. Lett.* 48 (1982). Ed. by Li-Zhi Fang and R. Ruffini, pp. 1220–1223. DOI: 10.1103/PhysRevLett.48.1220.

[20] George F. Smoot et al. "Structure in the COBE differential microwave radiometer first year maps". In: *Astrophys. J. Lett.* 396 (1992), pp. L1–L5. DOI: 10.1086/186504.

[21] Fotini Markopoulou. "Planck scale models of the universe". In: *Science and Ultimate Reality: Celebrating the Vision of John Archibald Wheeler and Taking it Forward into a New Century of Discovery*. Oct. 2002, pp. 550–563. arXiv: gr-qc/0210086.

[22] Hans Peter Nilles. "Supersymmetry, Supergravity and Particle Physics". In: *Phys. Rept.* 110 (1984), pp. 1–162. DOI: 10.1016/0370-1573(84)90008-5.

[23] John C. Baez and John Huerta. "The Algebra of Grand Unified Theories". In: *Bull. Am. Math. Soc.* 47 (2010), pp. 483–552. DOI: 10.1090/S0273-0979-10-01294-2. arXiv: 0904.1556 [hep-th].

[24] M. Tanabashi et al. "Review of Particle Physics". In: *Phys. Rev. D* 98.3 (2018), p. 030001. DOI: 10.1103/PhysRevD.98.030001.

[25] Aron J. Beekman, Louk Rademaker and Jasper van Wezel. "An Introduction to Spontaneous Symmetry Breaking". In: *SciPost Phys. Lect. Notes* 11 (2019), p. 1. DOI: 10.21468/SciPostPhysLectNotes.11. arXiv: 1909.01820 [hep-th].

[26] Gerard 't Hooft. "Magnetic Monopoles in Unified Gauge Theories". In: *Nucl. Phys. B* 79 (1974). Ed. by J. C. Taylor, pp. 276–284. DOI: 10.1016/0550-3213(74)90486-6.

[27] T. W. B. Kibble. "Topology of Cosmic Domains and Strings". In: *J. Phys. A* 9 (1976), pp. 1387–1398. DOI: 10.1088/0305-4470/9/8/029.

[28] Alexander Vilenkin. "Cosmic Strings and Domain Walls". In: *Phys. Rept.* 121 (1985), pp. 263–315. DOI: 10.1016/0370-1573(85)90033-X.

[29] N. Seiberg and Edward Witten. "Monopoles, duality and chiral symmetry breaking in N=2 supersymmetric QCD". In: *Nucl. Phys. B* 431 (1994), pp. 484–550. DOI: 10.1016/0550-3213(94)90214-3. arXiv: hep-th/9408099.

[30] Timur Doumler and Alexander Knebe. "Investigating the influence of magnetic fields upon structure formation with amiga- a c code for cosmological magnetohydrodynamics". In: *Monthly Notices of the Royal Astronomical Society* 403.1 (Mar. 2010), pp. 453–473. ISSN: 1365-2966. DOI: 10.1111/j.1365-2966.2009.16144.x.

[31] Chen Zhang et al. "On the cosmological abundance of magnetic monopoles". In: *JHEP* 08 (2024), p. 220. DOI: 10.1007/JHEP08(2024)220. arXiv: 2404.04926 [hep-ph].

[32] Samuel Kim. "Astrophysical Indirect Magnetic Monopole Searches and the Monopole Parameter Space". In: ().

[33] Alan H. Guth and S. H. H. Tye. "Phase Transitions and Magnetic Monopole Production in the Very Early Universe". In: *Phys. Rev. Lett.* 44 (1980). [Erratum: Phys.Rev.Lett. 44, 963 (1980)], p. 631. DOI: 10.1103/PhysRevLett.44.631.

[34] Julien Lesgourgues. "Cosmological Perturbations". In: *Theoretical Advanced Study Institute in Elementary Particle Physics: Searching for New Physics at Small and Large Scales*. 2013, pp. 29–97. DOI: 10.1142/9789814525220_0002. arXiv: 1302.4640 [astro-ph.CO].

[35] Swagat S. Mishra. "Cosmic Inflation: Background dynamics, Quantum fluctuations and Reheating". In: (Mar. 2024). arXiv: 2403.10606 [gr-qc].

[36] Christian T. Byrnes and Philippa S. Cole. "Lecture notes on inflation and primordial black holes". In: Dec. 2021. arXiv: 2112.05716 [astro-ph.CO].

[37] H. V. Peiris et al. "First year Wilkinson Microwave Anisotropy Probe (WMAP) observations: Implications for inflation". In: *Astrophys. J. Suppl.* 148 (2003), pp. 213–231. DOI: 10.1086/377228. arXiv: astro-ph/0302225.

[38] Y. Akrami et al. "Planck 2018 results. X. Constraints on inflation". In: *Astron. Astrophys.* 641 (2020), A10. DOI: 10.1051/0004-6361/201833887. arXiv: 1807.06211 [astro-ph.CO].

[39] Chris Pattison, Vincent Vennin, Hooshyar Assadullahi and David Wands. "Stochastic inflation beyond slow roll". In: *JCAP* 07 (2019), p. 031. DOI: 10.1088/1475-7516/2019/07/031. arXiv: 1905.06300 [astro-ph.CO].

[40] Christopher Gordon, David Wands, Bruce A. Bassett and Roy Maartens. "Adiabatic and entropy perturbations from inflation". In: *Phys. Rev. D* 63 (2000), p. 023506. DOI: 10.1103/PhysRevD.63.023506. arXiv: astro-ph/0009131.

[41] Viatcheslav F. Mukhanov. "Quantum Theory of Gauge Invariant Cosmological Perturbations". In: *Sov. Phys. JETP* 67 (1988), pp. 1297–1302.

[42] Misao Sasaki. "Large Scale Quantum Fluctuations in the Inflationary Universe". In: *Prog. Theor. Phys.* 76 (1986), p. 1036. DOI: 10.1143/PTP.76.1036.

[43] Daniel Baumann. "Inflation". In: *Theoretical Advanced Study Institute in Elementary Particle Physics: Physics of the Large and the Small*. 2011, pp. 523–686. DOI: 10.1142/9789814327183_0010. arXiv: 0907.5424 [hep-th].

[44] Scott Dodelson. "Coherent phase argument for inflation". In: *AIP Conf. Proc.* 689.1 (2003). Ed. by J. F. Nieves and R. R. Volkas, pp. 184–196. DOI: 10.1063/1.1627736. arXiv: hep-ph/0309057.

[45] Ya. B. Zeldovich and I. D. Novikov. "The Hypothesis of Cores Retarded during Expansion and the Hot Cosmological Model". In: *Sov. Astron.* 10 (1967), p. 602.

[46] Ya. B. Zeldovich. "Gravitational instability: An Approximate theory for large density perturbations". In: *Astron. Astrophys.* 5 (1970), pp. 84–89.

[47] Bernard J. Carr and S. W. Hawking. "Black holes in the early Universe". In: *Mon. Not. Roy. Astron. Soc.* 168 (1974), pp. 399–415. DOI: 10.1093/mnras/168.2.399.

[48] S. W. Hawking. "Black hole explosions". In: *Nature* 248 (1974), pp. 30–31. DOI: 10.1038/248030a0.

[49] Bernard Carr, Kazunori Kohri, Yuuiti Sendouda and Jun'ichi Yokoyama. "Constraints on primordial black holes". In: *Rept. Prog. Phys.* 84.11 (2021), p. 116902. DOI: 10.1088/1361-6633/ac1e31. arXiv: 2002.12778 [astro-ph.CO].

[50] Bernard J. Carr. "Some cosmological consequences of primordial black-hole evaporations". In: *Astrophys. J.* 206 (1976), pp. 8–25. DOI: 10.1086/154351.

[51] Andrei D. Linde. "Scalar Field Fluctuations in Expanding Universe and the New Inflationary Universe Scenario". In: *Phys. Lett. B* 116 (1982), pp. 335–339. DOI: 10.1016/0370-2693(82)90293-3.

[52] Hideo Kodama, Misao Sasaki and Katsuhiko Sato. "Abundance of Primordial Holes Produced by Cosmological First Order Phase Transition". In: *Prog. Theor. Phys.* 68 (1982), p. 1979. DOI: 10.1143/PTP.68.1979.

[53] Bernard J. Carr. "The Origin of Cosmological Density Fluctuations". In: *Nucl. Phys. B* 252 (1985). Ed. by R. Baier and H. Satz, pp. 81–111. DOI: 10.1016/0550-3213(85)90427-4.

[54] Alexei A. Starobinsky. "Multicomponent de Sitter (Inflationary) Stages and the Generation of Perturbations". In: *JETP Lett.* 42 (1985), pp. 152–155.

[55] A. G. Polnarev and M. Yu. Khlopov. "COSMOLOGY, PRIMORDIAL BLACK HOLES, AND SUPERMASSIVE PARTICLES". In: *Sov. Phys. Usp.* 28 (1985), pp. 213–232. DOI: 10.1070/PU1985v028n03ABEH003858.

[56] M. Yu. Khlopov, B. A. Malomed, Ia. B. Zeldovich and Ya. B. Zeldovich. "Gravitational instability of scalar fields and formation of primordial black holes". In: *Mon. Not. Roy. Astron. Soc.* 215.4 (1985), pp. 575–589. DOI: 10.1093/mnras/215.4.575.

[57] Bernard J. Carr and James E. Lidsey. "Primordial black holes and generalized constraints on chaotic inflation". In: *Phys. Rev. D* 48 (1993), pp. 543–553. DOI: 10.1103/PhysRevD.48.543.

[58] Bernard J. Carr, J. H. Gilbert and James E. Lidsey. "Black hole relics and inflation: Limits on blue perturbation spectra". In: *Phys. Rev. D* 50 (1994), pp. 4853–4867. DOI: 10.1103/PhysRevD.50.4853. arXiv: astro-ph/9405027.

[59] Misao Sasaki and Ewan D. Stewart. "A General analytic formula for the spectral index of the density perturbations produced during inflation". In: *Prog. Theor. Phys.* 95 (1996), pp. 71–78. DOI: 10.1143/PTP.95.71. arXiv: astro-ph/9507001.

[60] Juan Garcia-Bellido, Andrei D. Linde and David Wands. "Density perturbations and black hole formation in hybrid inflation". In: *Phys. Rev. D* 54 (1996), pp. 6040–6058. DOI: 10.1103/PhysRevD.54.6040. arXiv: astro-ph/9605094.

[61] M. Yu. Khlopov, R. V. Konoplich, S. G. Rubin and A. S. Sakharov. "Formation of black holes in first order phase transitions". In: (July 1998). arXiv: hep-ph/9807343.

[62] Bernard J. Carr. "The Primordial black hole mass spectrum". In: *Astrophys. J.* 201 (1975), pp. 1–19. DOI: 10.1086/153853.

[63] D. K. Nadezhin, I. D. Novikov and A. G. Polnarev. "The hydrodynamics of primordial black hole formation". In: *"Soviet Astronomy"* 22 (Apr. 1978), pp. 129–138.

[64] I. D. Novikov and A. G. Polnarev. "The Hydrodynamics of Primordial Black Hole Formation - Dependence on the Equation of State". In: *"Soviet Astronomy"* 24 (Apr. 1980), pp. 147–151.

[65] Jens C. Niemeyer and K. Jedamzik. "Near-critical gravitational collapse and the initial mass function of primordial black holes". In: *Phys. Rev. Lett.* 80 (1998), pp. 5481–5484. DOI: 10.1103/PhysRevLett.80.5481. arXiv: astro-ph/9709072.

[66] Jens C. Niemeyer and K. Jedamzik. "Dynamics of primordial black hole formation". In: *Phys. Rev. D* 59 (1999), p. 124013. DOI: 10.1103/PhysRevD.59.124013. arXiv: astro-ph/9901292.

[67] Tomohiro Harada and B. J. Carr. "Upper limits on the size of a primordial black hole". In: *Phys. Rev. D* 71 (10 May 2005), p. 104009. DOI: 10.1103/PhysRevD.71.104009.

[68] Ilia Musco, John C. Miller and Luciano Rezzolla. "Computations of primordial black hole formation". In: *Class. Quant. Grav.* 22 (2005), pp. 1405–1424. DOI: 10.1088/0264-9381/22/7/013. arXiv: gr-qc/0412063.

[69] Ilia Musco, John C. Miller and Alexander G. Polnarev. "Primordial black hole formation in the radiative era: Investigation of the critical nature of the collapse". In: *Class. Quant. Grav.* 26 (2009), p. 235001. DOI: 10.1088/0264-9381/26/23/235001. arXiv: 0811.1452 [gr-qc].

[70] Ilia Musco and John C. Miller. "Primordial black hole formation in the early universe: critical behaviour and self-similarity". In: *Class. Quant. Grav.* 30 (2013), p. 145009. DOI: 10.1088/0264-9381/30/14/145009. arXiv: 1201.2379 [gr-qc].

[71] Tomohiro Harada, Chul-Moon Yoo and Kazunori Kohri. "Threshold of primordial black hole formation". In: *Phys. Rev. D* 88.8 (2013). [Erratum: Phys.Rev.D 89, 029903 (2014)], p. 084051. DOI: 10.1103/PhysRevD.88.084051. arXiv: 1309.4201 [astro-ph.CO].

[72] Sam Young, Christian T. Byrnes and Misao Sasaki. "Calculating the mass fraction of primordial black holes". In: *JCAP* 07 (2014), p. 045. DOI: 10.1088/1475-7516/2014/07/045. arXiv: 1405.7023 [gr-qc].

[73] Sam Young, Ilia Musco and Christian T. Byrnes. "Primordial black hole formation and abundance: contribution from the non-linear relation between the density and curvature perturbation". In: *JCAP* 11 (2019), p. 012. DOI: 10.1088/1475-7516/2019/11/012. arXiv: 1904.00984 [astro-ph.CO].

[74] Alex Kehagias, Ilia Musco and Antonio Riotto. "Non-Gaussian Formation of Primordial Black Holes: Effects on the Threshold". In: *JCAP* 12 (2019), p. 029. DOI: 10.1088/1475-7516/2019/12/029. arXiv: 1906.07135 [astro-ph.CO].

[75] Valerio De Luca, Alex Kehagias and Antonio Riotto. "How well do we know the primordial black hole abundance: The crucial role of nonlinearities when approaching the horizon". In: *Phys. Rev. D* 108.6 (2023), p. 063531. DOI: 10.1103/PhysRevD.108.063531. arXiv: 2307.13633 [astro-ph.CO].

[76] S.W. Hawking. "Black holes from cosmic strings". In: *Physics Letters B* 231.3 (1989), pp. 237–239. ISSN: 0370-2693. DOI: 10.1016/0370-2693(89)90206-2.

[77] Alexander Polnarev and Robert Zembowicz. "Formation of primordial black holes by cosmic strings". In: *Phys. Rev. D* 43 (4 Feb. 1991), pp. 1106–1109. DOI: 10.1103/PhysRevD.43.1106.

[78] R. R. Caldwell and Paul Casper. "Formation of black holes from collapsed cosmic string loops". In: *Physical Review D* 53.6 (Mar. 1996), pp. 3002–3010. ISSN: 1089-4918. DOI: 10.1103/physrevd.53.3002.

[79] Matt Crawford and David N. Schramm. "Spontaneous Generation of Density Perturbations in the Early Universe". In: *Nature* 298 (1982), pp. 538–540. DOI: 10.1038/298538a0.

[80] Heling Deng, Jaume Garriga and Alexander Vilenkin. "Primordial black hole and wormhole formation by domain walls". In: *Journal of Cosmology and Astroparticle Physics* 2017.04 (Apr. 2017), pp. 050–050. ISSN: 1475-7516. DOI: 10.1088/1475-7516/2017/04/050.

[81] M. Yu. Khlopov, R. V. Konoplich, S. G. Rubin and A. S. Sakharov. *Formation of Black Holes in First Order Phase Transitions*. 1998. arXiv: hep-ph/9807343 [hep-ph].

[82] Ryotaro Ishikawa and Sergei V. Ketov. "Exploring the parameter space of modified supergravity for double inflation and primordial black hole formation". In: *Class. Quant. Grav.* 39.1 (2022), p. 015016. DOI: 10.1088/1361-6382/ac3bd9. arXiv: 2108.04408 [astro-ph.CO].

[83] Yermek Aldabergenov and Sergei V. Ketov. "Primordial Black Holes from Volkov–Akulov–Starobinsky Supergravity". In: *Fortsch. Phys.* 71.6-7 (2023), p. 2300039. DOI: 10.1002/prop.202300039. arXiv: 2301.12750 [hep-th].

[84] N. Bartolo, Sabino Matarrese and A. Riotto. "Evolution of second - order cosmological perturbations and non-Gaussianity". In: *JCAP* 01 (2004), p. 003. DOI: 10.1088/1475-7516/2004/01/003. arXiv: astro-ph/0309692.

[85] Karim A. Malik and David H. Lyth. "A numerical study of non-gaussianity in the curvaton scenario". In: *JCAP* 09 (2006), p. 008. DOI: 10.1088/1475-7516/2006/09/008. arXiv: astro-ph/0604387.

[86] Misao Sasaki, Jussi Valiviita and David Wands. "Non-Gaussianity of the primordial perturbation in the curvaton model". In: *Phys. Rev. D* 74 (2006), p. 103003. DOI: 10.1103/PhysRevD.74.103003. arXiv: astro-ph/0607627.

[87] Christian T. Byrnes, Edmund J. Copeland and Anne M. Green. "Primordial black holes as a tool for constraining non-Gaussianity". In: *Phys. Rev. D* 86 (2012), p. 043512. DOI: 10.1103/PhysRevD.86.043512. arXiv: 1206.4188 [astro-ph.CO].

[88] Sam Young and Christian T. Byrnes. "Primordial black holes in non-Gaussian regimes". In: *JCAP* 08 (2013), p. 052. DOI: 10.1088/1475-7516/2013/08/052. arXiv: 1307.4995 [astro-ph.CO].

[89] G. Franciolini, A. Kehagias, S. Matarrese and A. Riotto. "Primordial Black Holes from Inflation and non-Gaussianity". In: *JCAP* 03 (2018), p. 016. DOI: 10.1088/1475-7516/2018/03/016. arXiv: 1801.09415 [astro-ph.CO].

[90] Alba Kalaja et al. "From Primordial Black Holes Abundance to Primordial Curvature Power Spectrum (and back)". In: *JCAP* 10 (2019), p. 031. DOI: 10.1088/1475-7516/2019/10/031. arXiv: 1908.03596 [astro-ph.CO].

[91] Andrew D. Gow et al. "Non-perturbative non-Gaussianity and primordial black holes". In: *EPL* 142.4 (2023), p. 49001. DOI: 10.1209/0295-5075/acd417. arXiv: 2211.08348 [astro-ph.CO].

[92] P. A. Klimai and E. V. Bugaev. "Primordial black hole formation from non-Gaussian curvature perturbations". In: *17th International Seminar on High Energy Physics*. Vol. 2. Moscow, Russia: INR, Oct. 2012, pp. 163–174. arXiv: 1210.3262 [astro-ph.CO].

[93] Chul-Moon Yoo, Tomohiro Harada, Jaume Garriga and Kazunori Kohri. "Primordial black hole abundance from random Gaussian curvature perturbations and a local density threshold". In: *PTEP* 2018.12 (2018). [Erratum: PTEP 2024, 049202 (2024)], 123E01. DOI: 10.1093/ptep/pty120. arXiv: 1805.03946 [astro-ph.CO].

[94] George F. Chapline. "Cosmological effects of primordial black holes". In: *Nature* 253.5489 (1975), pp. 251–252. DOI: 10.1038/253251a0.

[95] Bernard Carr, Florian Kuhnel and Marit Sandstad. "Primordial Black Holes as Dark Matter". In: *Phys. Rev. D* 94.8 (2016), p. 083504. DOI: 10.1103/PhysRevD.94.083504. arXiv: 1607.06077 [astro-ph.CO].

[96] Hiroko Niikura et al. "Microlensing constraints on primordial black holes with Subaru/HSC Andromeda observations". In: *Nature Astron.* 3.6 (2019), pp. 524–534. DOI: 10.1038/s41550-019-0723-1. arXiv: 1701.02151 [astro-ph.CO].

[97] Hiroko Niikura et al. "Constraints on Earth-mass primordial black holes from OGLE 5-year microlensing events". In: *Phys. Rev. D* 99.8 (2019), p. 083503. DOI: 10.1103/PhysRevD.99.083503. arXiv: 1901.07120 [astro-ph.CO].

[98] Misao Sasaki, Teruaki Suyama, Takahiro Tanaka and Shuichiro Yokoyama. "Primordial black holes—perspectives in gravitational wave astronomy". In: *Class. Quant. Grav.* 35.6 (2018), p. 063001. DOI: 10.1088/1361-6382/aaa7b4. arXiv: 1801.05235 [astro-ph.CO].

[99] Juan Garcia-Bellido, Marco Peloso and Caner Unal. "Gravitational Wave signatures of inflationary models from Primordial Black Hole Dark Matter". In: *JCAP* 09 (2017), p. 013. DOI: 10.1088/1475-7516/2017/09/013. arXiv: 1707.02441 [astro-ph.CO].

[100] Yacine Ali-Haımoud and Marc Kamionkowski. "Cosmic microwave background limits on accreting primordial black holes". In: *Phys. Rev. D* 95.4 (2017), p. 043534. DOI: 10.1103/PhysRevD.95.043534. arXiv: 1612.05644 [astro-ph.CO].

[101] Vivian Poulin et al. "CMB bounds on disk-accreting massive primordial black holes". In: *Phys. Rev. D* 96.8 (2017), p. 083524. DOI: 10.1103/PhysRevD.96.083524. arXiv: 1707.04206 [astro-ph.CO].

[102] Sandeep Kumar Acharya and Rishi Khatri. *CMB spectral distortions constraints on primordial black holes, cosmic strings and long lived unstable particles revisited*. 2020. arXiv: 1912.10995 [astro-ph.CO].

[103] David Zegeye, Keisuke Inomata and Wayne Hu. "Spectral distortion anisotropy from inflation for primordial black holes". In: *Phys. Rev. D* 105.10 (2022), p. 103535. DOI: 10.1103/PhysRevD.105.103535. arXiv: 2112.05190 [astro-ph.CO].

[104] Anne M Green. "Astrophysical uncertainties on stellar microlensing constraints on multi-Solar mass primordial black hole dark matter". In: *Phys. Rev. D* 96.4 (2017), p. 043020. DOI: 10.1103/PhysRevD.96.043020. arXiv: 1705.10818 [astro-ph.CO].

[105] Ranjan Laha. "Primordial Black Holes as a Dark Matter Candidate Are Severely Constrained by the Galactic Center 511 keV γ -Ray Line". In: *Phys. Rev. Lett.* 123.25 (2019), p. 251101. DOI: 10.1103/PhysRevLett.123.251101. arXiv: 1906.09994 [astro-ph.HE].

[106] Siyu Chen, Hong-Hao Zhang and Guangbo Long. "Revisiting the constraints on primordial black hole abundance with the isotropic gamma-ray background". In: *Phys. Rev. D* 105.6 (2022), p. 063008. DOI: 10.1103/PhysRevD.105.063008. arXiv: 2112.15463 [astro-ph.CO].

[107] B. P. Abbott et al. "Observation of Gravitational Waves from a Binary Black Hole Merger". In: *Phys. Rev. Lett.* 116.6 (2016), p. 061102. DOI: 10.1103/PhysRevLett.116.061102. arXiv: 1602.03837 [gr-qc].

[108] B. P. Abbott et al. "Binary Black Hole Mergers in the first Advanced LIGO Observing Run". In: *Phys. Rev. X* 6.4 (2016). [Erratum: Phys.Rev.X 8, 039903 (2018)], p. 041015. DOI: 10.1103/PhysRevX.6.041015. arXiv: 1606.04856 [gr-qc].

[109] Simeon Bird et al. "Did LIGO detect dark matter?" In: *Phys. Rev. Lett.* 116.20 (2016), p. 201301. DOI: 10.1103/PhysRevLett.116.201301. arXiv: 1603.00464 [astro-ph.CO].

[110] Misao Sasaki, Teruaki Suyama, Takahiro Tanaka and Shuichiro Yokoyama. "Primordial Black Hole Scenario for the Gravitational-Wave Event GW150914". In: *Phys. Rev. Lett.* 117.6 (2016). [Erratum: Phys.Rev.Lett. 121, 059901 (2018)], p. 061101. DOI: 10.1103/PhysRevLett.117.061101. arXiv: 1603.08338 [astro-ph.CO].

[111] R. Abbott et al. "Search for Subsolar-Mass Binaries in the First Half of Advanced LIGO's and Advanced Virgo's Third Observing Run". In: *Phys. Rev. Lett.* 129.6 (2022), p. 061104. DOI: 10.1103/PhysRevLett.129.061104. arXiv: 2109.12197 [astro-ph.CO].

[112] M. Andrés-Carcasona et al. "Constraints on primordial black holes from LIGO-Virgo-KAGRA O3 events". In: *Phys. Rev. D* 110.2 (2024), p. 023040. DOI: 10.1103/PhysRevD.110.023040. arXiv: 2405.05732 [astro-ph.CO].

[113] Eleni Bagui et al. "Primordial black holes and their gravitational-wave signatures". In: *Living Rev. Rel.* 28.1 (2025), p. 1. DOI: 10.1007/s41114-024-00053-w. arXiv: 2310.19857 [astro-ph.CO].

[114] P. E. Colazo, F. Stasyszyn and N. Padilla. "Structure formation with primordial black holes to alleviate early star formation tension revealed by JWST". In: *Astron. Astrophys.* 685 (2024), p. L8. DOI: 10.1051/0004-6361/202449565. arXiv: 2404.13110 [astro-ph.CO].

[115] Pratika Dayal. "Exploring a primordial solution for early black holes detected with JWST". In: *Astron. Astrophys.* 690 (2024), A182. DOI: 10.1051/0004-6361/202451481. arXiv: 2407.07162 [astro-ph.GA].

[116] Sébastien Clesse and Juan Garcıa-Bellido. "Massive Primordial Black Holes from Hybrid Inflation as Dark Matter and the seeds of Galaxies". In: *Phys. Rev. D* 92.2 (2015), p. 023524. DOI: 10.1103/PhysRevD.92.023524. arXiv: 1501.07565 [astro-ph.CO].

[117] Kazunori Kohri, Chia-Min Lin and Tomohiro Matsuda. "Primordial black holes from the inflating curvaton". In: *Phys. Rev. D* 87.10 (2013), p. 103527. DOI: 10.1103/PhysRevD.87.103527. arXiv: 1211.2371 [hep-ph].

[118] Michele Cicoli, Victor A. Diaz and Francisco G. Pedro. "Primordial Black Holes from String Inflation". In: *JCAP* 06 (2018), p. 034. DOI: 10.1088/1475-7516/2018/06/034. arXiv: 1803.02837 [hep-th].

[119] Ogan Özsoy, Susha Parameswaran, Gianmassimo Tasinato and Ivonne Zavala. "Mechanisms for Primordial Black Hole Production in String Theory". In: *JCAP* 07 (2018), p. 005. DOI: 10.1088/1475-7516/2018/07/005. arXiv: 1803.07626 [hep-th].

[120] Swagat S. Mishra and Varun Sahni. "Primordial Black Holes from a tiny bump/dip in the Inflaton potential". In: *JCAP* 04 (2020), p. 007. DOI: 10.1088/1475-7516/2020/04/007. arXiv: 1911.00057 [gr-qc].

[121] Mayukh R. Gangopadhyay, Jayesh C. Jain, Devanshu Sharma and Yogesh. "Production of primordial black holes via single field inflation and observational constraints". In: *Eur. Phys. J. C* 82.9 (2022), p. 849. DOI: 10.1140/epjc/s10052-022-10796-x. arXiv: 2108.13839 [astro-ph.CO].

[122] Guillermo Ballesteros and Jesús Gambın Egea. "One-loop power spectrum in ultra slow-roll inflation and implications for primordial black hole dark matter". In: *JCAP* 07 (2024), p. 052. DOI: 10.1088/1475-7516/2024/07/052. arXiv: 2404.07196 [astro-ph.CO].

[123] Bao-Min Gu, Fu-Wen Shu and Ke Yang. "Inflation with shallow dip and primordial black holes". In: *Phys. Dark Univ.* 47 (2025), p. 101744. DOI: 10.1016/j.dark.2024.101744. arXiv: 2307.00510 [astro-ph.CO].

[124] Philippa S. Cole, Andrew D. Gow, Christian T. Byrnes and Subodh P. Patil. "Primordial black holes from single-field inflation: a fine-tuning audit". In: *JCAP* 08 (2023), p. 031. DOI: 10.1088/1475-7516/2023/08/031. arXiv: 2304.01997 [astro-ph.CO].

[125] Masaru Shibata and Misao Sasaki. "Black hole formation in the Friedmann universe: Formulation and computation in numerical relativity". In: *Phys. Rev. D* 60 (1999), p. 084002. DOI: 10.1103/PhysRevD.60.084002. arXiv: gr-qc/9905064.

[126] Tomohiro Harada, Chul-Moon Yoo and Yasutaka Koga. "Revisiting compaction functions for primordial black hole formation". In: *Phys. Rev. D* 108.4 (2023), p. 043515. DOI: 10.1103/PhysRevD.108.043515. arXiv: 2304.13284 [gr-qc].

[127] Ilia Musco. "Threshold for primordial black holes: Dependence on the shape of the cosmological perturbations". In: *Physical Review D* 100.12 (Dec. 2019). ISSN: 2470-0029. DOI: 10.1103/physrevd.100.123524.

[128] Ilia Musco, Valerio De Luca, Gabriele Franciolini and Antonio Riotto. "Threshold for primordial black holes. II. A simple analytic prescription". In: *Phys. Rev. D* 103.6 (2021), p. 063538. DOI: 10.1103/PhysRevD.103.063538. arXiv: 2011.03014 [astro-ph.CO].

[129] Albert Escrivà. "PBH Formation from Spherically Symmetric Hydrodynamical Perturbations: A Review". In: *Universe* 8.2 (2022), p. 66. DOI: 10.3390/universe8020066. arXiv: 2111.12693 [gr-qc].

[130] Joaquin Sureda, Juan Magana, Ignacio J. Araya and Nelson D. Padilla. "Press–Schechter primordial black hole mass functions and their observational constraints". In: *Mon. Not. Roy. Astron. Soc.* 507.4 (2021), pp. 4804–4825. DOI: 10.1093/mnras/stab2450. arXiv: 2008.09683 [astro-ph.CO].

[131] Christian T. Byrnes, Mark Hindmarsh, Sam Young and Michael R. S. Hawkins. "Primordial black holes with an accurate QCD equation of state". In: *JCAP* 08 (2018), p. 041. DOI: 10.1088/1475-7516/2018/08/041. arXiv: 1801.06138 [astro-ph.CO].

[132] Bradley J. Kavanagh. *bradkav/PBHbounds: Release version.* Version 1.0. Nov. 2019. DOI: 10.5281/zenodo.3538999. URL: https://doi.org/10.5281/zenodo.3538999.

[133] B. J. Carr, Kazunori Kohri, Yuuiti Sendouda and Jun'ichi Yokoyama. "New cosmological constraints on primordial black holes". In: *Phys. Rev. D* 81 (2010), p. 104019. DOI: 10.1103/PhysRevD.81.104019. arXiv: 0912.5297 [astro-ph.CO].

[134] A. Barnacka, J. F. Glicenstein and R. Moderski. "New constraints on primordial black holes abundance from femtolensing of gamma-ray bursts". In: *Phys. Rev. D* 86 (2012), p. 043001. DOI: 10.1103/PhysRevD.86.043001. arXiv: 1204.2056 [astro-ph.CO].

[135] Steven Clark et al. "Planck Constraint on Relic Primordial Black Holes". In: *Phys. Rev. D* 95.8 (2017), p. 083006. DOI: 10.1103/PhysRevD.95.083006. arXiv: 1612.07738 [astro-ph.CO].

[136] Timothy D. Brandt. "Constraints on MACHO Dark Matter from Compact Stellar Systems in Ultra-Faint Dwarf Galaxies". In: *Astrophys. J. Lett.* 824.2 (2016), p. L31. DOI: 10.3847/2041-8205/824/2/L31. arXiv: 1605.03665 [astro-ph.GA].

[137] Sunghoon Jung and Chang Sub Shin. "Gravitational-Wave Fringes at LIGO: Detecting Compact Dark Matter by Gravitational Lensing". In: *Phys. Rev. Lett.* 122.4 (2019), p. 041103. DOI: 10.1103/PhysRevLett.122.041103. arXiv: 1712.01396 [astro-ph.CO].

[138] Miguel Zumalacarregui and Uros Seljak. "Limits on stellar-mass compact objects as dark matter from gravitational lensing of type Ia supernovae". In: *Phys. Rev. Lett.* 121.14 (2018), p. 141101. DOI: 10.1103/PhysRevLett.121.141101. arXiv: 1712.02240 [astro-ph.CO].

[139] Mathieu Boudaud and Marco Cirelli. "Voyager 1 $e^{\pm}$ Further Constrain Primordial Black Holes as Dark Matter". In: *Phys. Rev. Lett.* 122.4 (2019), p. 041104. DOI: 10.1103/PhysRevLett.122.041104. arXiv: 1807.03075 [astro-ph.HE].

[140] B. P. Abbott et al. "Search for Subsolar Mass Ultracompact Binaries in Advanced LIGO's Second Observing Run". In: *Phys. Rev. Lett.* 123.16 (2019), p. 161102. DOI: 10.1103/PhysRevLett.123.161102. arXiv: 1904.08976 [astro-ph.CO].

[141] Yi-Fan Wang, Qing-Guo Huang, Tjonnie G. F. Li and Shihong Liao. "Searching for primordial black holes with stochastic gravitational-wave background in the space-based detector frequency band". In: *Phys. Rev. D* 101.6 (2020), p. 063019. DOI: 10.1103/PhysRevD.101.063019. arXiv: 1910.07397 [astro-ph.CO].

[142] Shikhar Mittal, Anupam Ray, Girish Kulkarni and Basudeb Dasgupta. "Constraining primordial black holes as dark matter using the global 21-cm signal with X-ray heating and excess radio background". In: *JCAP* 03 (2022), p. 030. DOI: 10.1088/1475-7516/2022/03/030. arXiv: 2107.02190 [astro-ph.CO].

[143] Hyungjin Kim. "A constraint on light primordial black holes from the interstellar medium temperature". In: *Mon. Not. Roy. Astron. Soc.* 504.4 (2021), pp. 5475–5484. DOI: 10.1093/mnras/stab1222. arXiv: 2007.07739 [hep-ph].

[144] Vicky Kalogera et al. "The Next Generation Global Gravitational Wave Observatory: The Science Book". In: (Nov. 2021). arXiv: 2111.06990 [gr-qc].

[145] Alexander H. Nitz and Yi-Fan Wang. "Broad search for gravitational waves from subsolar-mass binaries through LIGO and Virgo's third observing run". In: *Phys. Rev. D* 106.2 (2022), p. 023024. DOI: 10.1103/PhysRevD.106.023024. arXiv: 2202.11024 [astro-ph.HE].

[146] A. Esteban-Gutiérrez, E. Mediavilla, J. Jiménez-Vicente and J. A. Muñoz. "Constraints on the Abundance of Primordial Black Holes from X-Ray Quasar Microlensing Observations: Substellar to Planetary Mass Range". In: *Astrophys. J.* 954.2 (2023), p. 172. DOI: 10.3847/1538-4357/ace62f. arXiv: 2307.07473 [astro-ph.CO].

[147] Przemek Mróz et al. "Limits on Planetary-mass Primordial Black Holes from the OGLE High-cadence Survey of the Magellanic Clouds". In: *Astrophys. J. Lett.* 976.1 (2024), p. L19. DOI: 10.3847/2041-8213/ad8e68. arXiv: 2410.06251 [astro-ph.CO].

[148] James M. Bardeen, J. R. Bond, Nick Kaiser and A. S. Szalay. "The Statistics of Peaks of Gaussian Random Fields". In: *Astrophys. J.* 304 (1986), pp. 15–61. DOI: 10.1086/164143.

[149] Anne M. Green, Andrew R. Liddle, Karim A. Malik and Misao Sasaki. "A New calculation of the mass fraction of primordial black holes". In: *Phys. Rev. D* 70 (2004), p. 041502. DOI: 10.1103/PhysRevD.70.041502. arXiv: astro-ph/0403181.

[150] Chul-Moon Yoo, Jinn-Ouk Gong and Shuichiro Yokoyama. "Abundance of primordial black holes with local non-Gaussianity in peak theory". In: *JCAP* 09 (2019), p. 033. DOI: 10.1088/1475-7516/2019/09/033. arXiv: 1906.06790 [astro-ph.CO].

[151] Qing Wang, Yi-Chen Liu, Bing-Yu Su and Nan Li. "Primordial black holes from the perturbations in the inflaton potential in peak theory". In: *Phys. Rev. D* 104.8 (2021), p. 083546. DOI: 10.1103/PhysRevD.104.083546. arXiv: 2111.10028 [astro-ph.CO].

[152] Arjun Berera. "Warm inflation". In: *Phys. Rev. Lett.* 75 (1995), pp. 3218–3221. DOI: 10.1103/PhysRevLett.75.3218. arXiv: astro-ph/9509049.

[153] Arjun Berera and Li-Zhi Fang. "Thermally induced density perturbations in the inflation era". In: *Phys. Rev. Lett.* 74 (1995), pp. 1912–1915. DOI: 10.1103/PhysRevLett.74.1912. arXiv: astro-ph/9501024.

[154] Arjun Berera, Marcelo Gleiser and Rudnei O. Ramos. "A First principles warm inflation model that solves the cosmological horizon / flatness problems". In: *Phys. Rev. Lett.* 83 (1999), pp. 264–267. DOI: 10.1103/PhysRevLett.83.264. arXiv: hep-ph/9809583.

[155] Vahid Kamali, Meysam Motaharfar and Rudnei O. Ramos. "Recent Developments in Warm Inflation". In: *Universe* 9.3 (2023), p. 124. DOI: 10.3390/universe9030124. arXiv: 2302.02827 [hep-ph].

[156] Rouzbeh Allahverdi, Robert Brandenberger, Francis-Yan Cyr-Racine and Anupam Mazumdar. "Reheating in Inflationary Cosmology: Theory and Applications". In: *Ann. Rev. Nucl. Part. Sci.* 60 (2010), pp. 27–51. DOI: 10.1146/annurev.nucl.012809.104511. arXiv: 1001.2600 [hep-th].

[157] D. Boyanovsky, H. J. de Vega and R. Holman. "Erice lectures on inflationary reheating". In: *International School of Astrophysics, D. Chalonge: 5th Course: Current Topics in Astrofundamental Physics*. Sept. 1996, pp. 183–270. arXiv: hep-ph/9701304.

[158] Richard Watkins and Lawrence M. Widrow. "Aspects of reheating in first order inflation". In: *Nucl. Phys. B* 374 (1992), pp. 446–468. DOI: 10.1016/0550-3213(92)90362-F.

[159] Mustafa A. Amin, Mark P. Hertzberg, David I. Kaiser and Johanna Karouby. "Nonperturbative Dynamics Of Reheating After Inflation: A Review". In: *Int. J. Mod. Phys. D* 24 (2014), p. 1530003. DOI: 10.1142/S0218271815300037. arXiv: 1410.3808 [hep-ph].

[160] Swagat S. Mishra, Varun Sahni and Alexei A. Starobinsky. "Curing inflationary degeneracies using reheating predictions and relic gravitational waves". In: *JCAP* 05 (2021), p. 075. DOI: 10.1088/1475-7516/2021/05/075. arXiv: 2101.00271 [gr-qc].

[161] Mathias Becker et al. "Confronting dark matter freeze-in during reheating with constraints from inflation". In: *JCAP* 01 (2024), p. 053. DOI: 10.1088/1475-7516/2024/01/053. arXiv: 2306.17238 [hep-ph].

[162] Anupam Mazumdar and Bryan Zaldivar. "Quantifying the reheating temperature of the universe". In: *Nucl. Phys. B* 886 (2014), pp. 312–327. DOI: 10.1016/j.nuclphysb.2014.07.001. arXiv: 1310.5143 [hep-ph].

[163] Antonio Riotto and Mark Trodden. "Recent progress in baryogenesis". In: *Ann. Rev. Nucl. Part. Sci.* 49 (1999), pp. 35–75. DOI: 10.1146/annurev.nucl.49.1.35. arXiv: hep-ph/9901362.

[164] Benedict von Harling, Oleksii Matsedonskyi and Geraldine Servant. "High-temperature electroweak baryogenesis with composite Higgs". In: *JHEP* 12 (2023), p. 138. DOI: 10.1007/JHEP12(2023)138. arXiv: 2307.14426 [hep-ph].

[165] Douglas Scott. "The Cosmic Neutrino Background". In: *International School of Physics "Enrico Fermi" in collaboration with the summer schools ISAPP: Neutrino Physics, Astrophysics and Cosmology*. Feb. 2024. arXiv: 2402.16243 [astro-ph.CO].

[166] Andreas Ringwald. "Prospects for the direct detection of the cosmic neutrino background". In: *Nucl. Phys. A* 827 (2009). Ed. by Itzhak Tserruya, Avraham Gal and Daniel Ashery, pp. 501C–506C. DOI: 10.1016/j.nuclphysa.2009.05.109. arXiv: 0901.1529 [astro-ph.CO].

[167] G. Mangano, G. Miele, S. Pastor and M. Peloso. "A Precision calculation of the effective number of cosmological neutrinos". In: *Phys. Lett. B* 534 (2002), pp. 8–16. DOI: 10.1016/S0370-2693(02)01622-2. arXiv: astro-ph/0111408.

[168] Pablo F. de Salas and Sergio Pastor. "Relic neutrino decoupling with flavour oscillations revisited". In: *JCAP* 07 (2016), p. 051. DOI: 10.1088/1475-7516/2016/07/051. arXiv: 1606.06986 [hep-ph].

[169] Luke C. Thomas, Ted Dezen, Evan B. Grohs and Chad T. Kishimoto. "Electron-positron annihilation freeze-out in the early universe". In: *Phys. Rev. D* 101 (6 Mar. 2020), p. 063507. DOI: 10.1103/PhysRevD.101.063507.

[170] Brian D. Fields, Paolo Molaro and Subir Sarkar. "Big-Bang Nucleosynthesis". In: *Chin. Phys. C* 38 (2014), pp. 339–344. arXiv: 1412.1408 [astro-ph.CO].

[171] Richard H. Cyburt, Brian D. Fields, Keith A. Olive and Tsung-Han Yeh. "Big Bang Nucleosynthesis: 2015". In: *Rev. Mod. Phys.* 88 (2016), p. 015004. DOI: 10.1103/RevModPhys.88.015004. arXiv: 1505.01076 [astro-ph.CO].

[172] Craig J. Hogan. "Big bang nucleosynthesis and the observed abundances of light elements". In: (Sept. 1996). arXiv: astro-ph/9609138.

[173] Anna Frebel and Timothy C. Beers. "The formation of the heaviest elements". In: *Phys. Today* 71 (2018), p. 0130. DOI: 10.1063/PT.3.3815. arXiv: 1801.01190 [astro-ph.SR].

[174] John J. Cowan et al. "Origin of the heaviest elements: The rapid neutron-capture process". In: *Rev. Mod. Phys.* 93.1 (2021), p. 15002. DOI: 10.1103/RevModPhys.93.015002. arXiv: 1901.01410 [astro-ph.HE].

[175] Benedict Bahr-Kalus, David Parkinson and Eva-Maria Mueller. "Measurement of the matter-radiation equality scale using the extended baryon oscillation spectroscopic survey quasar sample". In: *Mon. Not. Roy. Astron. Soc.* 524.2 (2023). [Erratum: Mon.Not.Roy.Astron.Soc. 526, 3248–3249 (2023)], pp. 2463–2476. DOI: 10.1093/mnras/stad1867. arXiv: 2302.07484 [astro-ph.CO].

[176] Gianfranco Bertone and Dan Hooper. "History of dark matter". In: *Rev. Mod. Phys.* 90.4 (2018), p. 045002. DOI: 10.1103/RevModPhys.90.045002. arXiv: 1605.04909 [astro-ph.CO].

[177] Aritra Das, Ritesh Ghosh and S. Mallik. "Saha ionization equation in early universe". In: *Astrophys. J.* 881 (2019), p. 40. DOI: 10.3847/1538-4357/ab2d2f. arXiv: 1812.10686 [hep-ph].

[178] D. J. Fixsen. "The Temperature of the Cosmic Microwave Background". In: *Astrophys. J.* 707 (2009), pp. 916–920. DOI: 10.1088/0004-637X/707/2/916. arXiv: 0911.1955 [astro-ph.CO].

[179] N. Aghanim et al. "Planck 2018 results. V. CMB power spectra and likelihoods". In: *Astron. Astrophys.* 641 (2020), A5. DOI: 10.1051/0004-6361/201936386. arXiv: 1907.12875 [astro-ph.CO].

[180] Bruce A. Bassett and Renee Hlozek. "Baryon Acoustic Oscillations". In: (Oct. 2009). arXiv: 0910.5224 [astro-ph.CO].

[181] Matteo Lucca. "The future of cosmology? A case for CMB spectral distortions". PhD thesis. U. Brussels, 2023. arXiv: 2307.08513 [astro-ph.CO].

[182] Ioannis Karatzas and Steven E. Shreve. "Brownian Motion". In: *Brownian Motion and Stochastic Calculus*. Springer New York, 1998, pp. 47–127. ISBN: 978-1-4612-0949-2. DOI: 10.1007/978-1-4612-0949-2_2. URL: https://doi.org/10.1007/978-1-4612-0949-2_2.

[183] A. Paglietti. *The laminar-to-turbulent transition in viscous fluid flow*. 2017. arXiv: 1703.07223 [physics.gen-ph].

[184] Philippe Carmona and Laure Coutin. *Fractional Brownian motion and the Markov Property*. 1998. arXiv: math/9809123 [math.PR].

[185] Pece Trajanovski et al. "Ornstein-Uhlenbeck process and generalizations: Particle dynamics under comb constraints and stochastic resetting". In: *Physical Review E* 107.5 (May 2023). ISSN: 2470-0053. DOI: 10.1103/physreve.107.054129.

[186] Martin Jacobsen. "Laplace and the origin of the Ornstein-Uhlenbeck process". In: *Bernoulli* 2.3 (1996), pp. 271–286. DOI: 10.3150/bj/1178291723.

[187] Nicholas M. Boffi and Eric Vanden-Eijnden. *Probability flow solution of the Fokker-Planck equation*. 2023. arXiv: 2206.04642 [cs.LG].

[188] A. V. Plyukhin. "Generalized Fokker-Planck equation, Brownian motion, and ergodicity". In: *Physical Review E* 77.6 (June 2008). ISSN: 1550-2376. DOI: 10.1103/physreve.77.061136.

[189] David Polarski and Alexei A. Starobinsky. "Semiclassicality and decoherence of cosmological perturbations". In: *Class. Quant. Grav.* 13 (1996), pp. 377–392. DOI: 10.1088/0264-9381/13/3/006. arXiv: gr-qc/9504030.

[190] Julien Grain and Vincent Vennin. "Canonical transformations and squeezing formalism in cosmology". In: *JCAP* 02 (2020), p. 022. DOI: 10.1088/1475-7516/2020/02/022. arXiv: 1910.01916 [astro-ph.CO].

[191] Daniel G. Figueroa, Sami Raatikainen, Syksy Rasanen and Eemeli Tomberg. "Implications of stochastic effects for primordial black hole production in ultra-slow-roll inflation". In: *JCAP* 05.05 (2022), p. 027. DOI: 10.1088/1475-7516/2022/05/027. arXiv: 2111.07437 [astro-ph.CO].

[192] Claus Kiefer and David Polarski. "Why do cosmological perturbations look classical to us?" In: *Adv. Sci. Lett.* 2 (2009), pp. 164–173. DOI: 10.1166/asl.2009.1023. arXiv: 0810.0087 [astro-ph].

[193] Claus Kiefer, Ingo Lohmar, David Polarski and Alexei A. Starobinsky. "Pointer states for primordial fluctuations in inflationary cosmology". In: *Class. Quant. Grav.* 24 (2007), pp. 1699–1718. DOI: 10.1088/0264-9381/24/7/002. arXiv: astro-ph/0610700.

[194] Claus Kiefer, David Polarski and Alexei A. Starobinsky. "Quantum to classical transition for fluctuations in the early universe". In: *Int. J. Mod. Phys. D* 7 (1998), pp. 455–462. DOI: 10.1142/S0218271898000292. arXiv: gr-qc/9802003.

[195] Jerome Martin, Vincent Vennin and Patrick Peter. "Cosmological Inflation and the Quantum Measurement Problem". In: *Phys. Rev. D* 86 (2012), p. 103524. DOI: 10.1103/PhysRevD.86.103524. arXiv: 1207.2086 [hep-th].

[196] Alexei A. Starobinsky. "STOCHASTIC DE SITTER (INFLATIONARY) STAGE IN THE EARLY UNIVERSE". In: *Lect. Notes Phys.* 246 (1986), pp. 107–126. DOI: 10.1007/3-540-16452-9_6.

[197] Yasusada Nambu and Misao Sasaki. "Stochastic Stage of an Inflationary Universe Model". In: *Phys. Lett. B* 205 (1988), pp. 441–446. DOI: 10.1016/0370-2693(88)90974-4.

[198] Yasusada Nambu. "Stochastic Dynamics of an Inflationary Model and Initial Distribution of Universes". In: *Prog. Theor. Phys.* 81 (1989), p. 1037. DOI: 10.1143/PTP.81.1037.

[199] Henry E. Kandrup. "STOCHASTIC INFLATION AS A TIME DEPENDENT RANDOM WALK". In: *Phys. Rev. D* 39 (1989), p. 2245. DOI: 10.1103/PhysRevD.39.2245.

[200] Ken-ichi Nakao, Yasusada Nambu and Misao Sasaki. "Stochastic Dynamics of New Inflation". In: *Prog. Theor. Phys.* 80 (1988), p. 1041. DOI: 10.1143/PTP.80.1041.

[201] Silvia Mollerach, Sabino Matarrese, Antonello Ortolan and Francesco Lucchin. "Stochastic inflation in a simple two field model". In: *Phys. Rev. D* 44 (1991), pp. 1670–1679. DOI: 10.1103/PhysRevD.44.1670.

[202] D. S. Salopek and J. R. Bond. "Stochastic inflation and nonlinear gravity". In: *Phys. Rev. D* 43 (1991), pp. 1005–1031. DOI: 10.1103/PhysRevD.43.1005.

[203] Salman Habib. "Stochastic inflation: The Quantum phase space approach". In: *Phys. Rev. D* 46 (1992), pp. 2408–2427. DOI: 10.1103/PhysRevD.46.2408. arXiv: gr-qc/9208006.

[204] Alexei A. Starobinsky and Junichi Yokoyama. "Equilibrium state of a selfinteracting scalar field in the De Sitter background". In: *Phys. Rev. D* 50 (1994), pp. 6357–6368. DOI: 10.1103/PhysRevD.50.6357. arXiv: astro-ph/9407016.

[205] Christian T. Byrnes, Philippa S. Cole and Subodh P. Patil. "Steepest growth of the power spectrum and primordial black holes". In: *JCAP* 06 (2019), p. 028. DOI: 10.1088/1475-7516/2019/06/028. arXiv: 1811.11158 [astro-ph.CO].

[206] Samuel Passaglia, Wayne Hu and Hayato Motohashi. "Primordial black holes and local non-Gaussianity in canonical inflation". In: *Phys. Rev. D* 99.4 (2019), p. 043536. DOI: 10.1103/PhysRevD.99.043536. arXiv: 1812.08243 [astro-ph.CO].

[207] Ogan Özsoy and Gianmassimo Tasinato. "On the slope of the curvature power spectrum in non-attractor inflation". In: *JCAP* 04 (2020), p. 048. DOI: 10.1088/1475-7516/2020/04/048. arXiv: 1912.01061 [astro-ph.CO].

[208] Pedro Carrilho, Karim A. Malik and David J. Mulryne. "Dissecting the growth of the power spectrum for primordial black holes". In: *Phys. Rev. D* 100.10 (2019), p. 103529. DOI: 10.1103/PhysRevD.100.103529. arXiv: 1907.05237 [astro-ph.CO].

[209] H. Casini, R. Montemayor and P. Sisterna. "Stochastic approach to inflation. 2. Classicality, coarse graining and noises". In: *Phys. Rev. D* 59 (1999), p. 063512. DOI: 10.1103/PhysRevD.59.063512. arXiv: gr-qc/9811083.

[210] Sabino Matarrese, Marcello A. Musso and Antonio Riotto. "Influence of superhorizon scales on cosmological observables generated during inflation". In: *JCAP* 05 (2004), p. 008. DOI: 10.1088/1475-7516/2004/05/008. arXiv: hep-th/0311059.

[211] S. Winitzki and A. Vilenkin. "Effective noise in stochastic description of inflation". In: *Phys. Rev. D* 61 (2000), p. 084008. DOI: 10.1103/PhysRevD.61.084008. arXiv: gr-qc/9911029.

[212] Julien Grain and Vincent Vennin. "Stochastic inflation in phase space: Is slow roll a stochastic attractor?" In: *JCAP* 05 (2017), p. 045. DOI: 10.1088/1475-7516/2017/05/045. arXiv: 1703.00447 [gr-qc].

[213] Masahiro Morikawa. "Dissipation and fluctuation of quantum fields in expanding universes". In: *Phys. Rev. D* 42 (4 Aug. 1990), pp. 1027–1034. DOI: 10.1103/PhysRevD.42.1027.

[214] Chris Pattison, Vincent Vennin, David Wands and Hooshyar Assadullahi. "Ultra-slow-roll inflation with quantum diffusion". In: *JCAP* 04 (2021), p. 080. DOI: 10.1088/1475-7516/2021/04/080. arXiv: 2101.05741 [astro-ph.CO].

[215] Swagat S. Mishra, Edmund J. Copeland and Anne M. Green. "Primordial black holes and stochastic inflation beyond slow roll. Part I. Noise matrix elements". In: *JCAP* 09 (2023), p. 005. DOI: 10.1088/1475-7516/2023/09/005. arXiv: 2303.17375 [astro-ph.CO].

[216] Daniel G. Figueroa, Sami Raatikainen, Syksy Rasanen and Eemeli Tomberg. "Non-Gaussian Tail of the Curvature Perturbation in Stochastic Ultraslow-Roll Inflation: Implications for Primordial Black Hole Production". In: *Phys. Rev. Lett.* 127.10 (2021), p. 101302. DOI: 10.1103/PhysRevLett.127.101302. arXiv: 2012.06551 [astro-ph.CO].

[217] Jose Maria Ezquiaga, Juan García-Bellido and Vincent Vennin. "The exponential tail of inflationary fluctuations: consequences for primordial black holes". In: *JCAP* 03 (2020), p. 029. DOI: 10.1088/1475-7516/2020/03/029. arXiv: 1912.05399 [astro-ph.CO].

[218] Chiara Animali and Vincent Vennin. "Primordial black holes from stochastic tunnelling". In: *JCAP* 02 (2023), p. 043. DOI: 10.1088/1475-7516/2023/02/043. arXiv: 2210.03812 [astro-ph.CO].

[219] Eemeli Tomberg. "Stochastic constant-roll inflation and primordial black holes". In: *Phys. Rev. D* 108.4 (2023), p. 043502. DOI: 10.1103/PhysRevD.108.043502. arXiv: 2304.10903 [astro-ph.CO].

[220] Shi Pi and Misao Sasaki. "Logarithmic Duality of the Curvature Perturbation". In: *Phys. Rev. Lett.* 131.1 (2023), p. 011002. DOI: 10.1103/PhysRevLett.131.011002. arXiv: 2211.13932 [astro-ph.CO].

[221] Joseph H. P. Jackson et al. "Numerical simulations of stochastic inflation using importance sampling". In: *JCAP* 10 (2022), p. 067. DOI: 10.1088/1475-7516/2022/10/067. arXiv: 2206.11234 [astro-ph.CO].

[222] Joseph H. P. Jackson et al. "Stochastic inflation beyond slow roll: noise modelling and importance sampling". In: (Oct. 2024). arXiv: 2410.13683 [astro-ph.CO].

[223] Eemeli Tomberg. "Numerical stochastic inflation constrained by frozen noise". In: *JCAP* 04 (2023), p. 042. DOI: 10.1088/1475-7516/2023/04/042. arXiv: 2210.17441 [astro-ph.CO].

[224] Tomohiro Fujita, Masahiro Kawasaki, Yuichiro Tada and Tomohiro Takesako. "A new algorithm for calculating the curvature perturbations in stochastic inflation". In: *JCAP* 12 (2013), p. 036. DOI: 10.1088/1475-7516/2013/12/036. arXiv: 1308.4754 [astro-ph.CO].

[225] Tomohiro Fujita, Masahiro Kawasaki and Yuichiro Tada. "Non-perturbative approach for curvature perturbations in stochastic δN formalism". In: *JCAP* 10 (2014), p. 030. DOI: 10.1088/1475-7516/2014/10/030. arXiv: 1405.2187 [astro-ph.CO].

[226] Kenta Ando and Vincent Vennin. "Power spectrum in stochastic inflation". In: *JCAP* 04 (2021), p. 057. DOI: 10.1088/1475-7516/2021/04/057. arXiv: 2012.02031 [astro-ph.CO].

[227] Matteo Biagetti, Gabriele Franciolini, Alex Kehagias and Antonio Riotto. "Primordial Black Holes from Inflation and Quantum Diffusion". In: *JCAP* 07 (2018), p. 032. DOI: 10.1088/1475-7516/2018/07/032. arXiv: 1804.07124 [astro-ph.CO].

[228] Jose Marıa Ezquiaga and Juan Garcıa-Bellido. "Quantum diffusion beyond slow-roll: implications for primordial black-hole production". In: *JCAP* 08 (2018), p. 018. DOI: 10.1088/1475-7516/2018/08/018. arXiv: 1805.06731 [astro-ph.CO].

[229] Diego Cruces, Cristiano Germani and Tomislav Prokopec. "Failure of the stochastic approach to inflation beyond slow-roll". In: *JCAP* 03 (2019), p. 048. DOI: 10.1088/1475-7516/2019/03/048. arXiv: 1807.09057 [gr-qc].

[230] Aritra De and Rafid Mahbub. "Numerically modeling stochastic inflation in slow-roll and beyond". In: *Phys. Rev. D* 102.12 (2020), p. 123509. DOI: 10.1103/PhysRevD.102.123509. arXiv: 2010.12685 [astro-ph.CO].

[231] Diego Cruces and Cristiano Germani. "Stochastic inflation at all order in slow-roll parameters: Foundations". In: *Phys. Rev. D* 105.2 (2022), p. 023533. DOI: 10.1103/PhysRevD.105.023533. arXiv: 2107.12735 [gr-qc].

[232] Chiara Animali and Vincent Vennin. "Clustering of primordial black holes from quantum diffusion during inflation". In: *JCAP* 08 (2024), p. 026. DOI: 10.1088/1475-7516/2024/08/026. arXiv: 2402.08642 [astro-ph.CO].

[233] Eric Gourgoulhon. *3+1 Formalism in General Relativity*. Lecture Notes in Physics. Springer, 2012. DOI: 10.1007/978-3-642-24525-1.

[234] David H. Lyth, Karim A. Malik and Misao Sasaki. "A General proof of the conservation of the curvature perturbation". In: *JCAP* 05 (2005), p. 004. DOI: 10.1088/1475-7516/2005/05/004. arXiv: astro-ph/0411220.

[235] Yoshiharu Tanaka and Misao Sasaki. "Gradient expansion approach to nonlinear superhorizon perturbations. II. A Single scalar field". In: *Prog. Theor. Phys.* 118 (2007), pp. 455–473. DOI: 10.1143/PTP.118.455. arXiv: 0706.0678 [gr-qc].

[236] Diego Cruces. "Review on Stochastic Approach to Inflation". In: *Universe* 8.6 (2022), p. 334. DOI: 10.3390/universe8060334. arXiv: 2203.13852 [gr-qc].

[237] James M. Bardeen and Guillermo J. Bublik. "Quantum Fluctuations and Inflation". In: *Class. Quant. Grav.* 4 (1987), p. 573. DOI: 10.1088/0264-9381/4/3/015.

[238] D. S. Salopek and J. R. Bond. "Nonlinear evolution of long wavelength metric fluctuations in inflationary models". In: *Phys. Rev. D* 42 (1990), pp. 3936–3962. DOI: 10.1103/PhysRevD.42.3936.

[239] David H. Lyth and Yeinzon Rodriguez. "The Inflationary prediction for primordial non-Gaussianity". In: *Phys. Rev. Lett.* 95 (2005), p. 121302. DOI: 10.1103/PhysRevLett.95.121302. arXiv: astro-ph/0504045.

[240] Hyun-Chul Lee et al. "A New delta N formalism for multi-component inflation". In: *JCAP* 10 (2005), p. 004. DOI: 10.1088/1475-7516/2005/10/004. arXiv: astro-ph/0506262.

[241] Viatcheslav F. Mukhanov, H. A. Feldman and Robert H. Brandenberger. "Theory of cosmological perturbations. Part 1. Classical perturbations. Part 2. Quantum theory of perturbations. Part 3. Extensions". In: *Phys. Rept.* 215 (1992), pp. 203–333. DOI: 10.1016/0370-1573(92)90044-Z.

[242] Hideo Kodama and Misao Sasaki. "Cosmological Perturbation Theory". In: *Prog. Theor. Phys. Suppl.* 78 (1984), pp. 1–166. DOI: 10.1143/PTPS.78.1.

[243] James M. Bardeen. "Gauge Invariant Cosmological Perturbations". In: *Phys. Rev. D* 22 (1980), pp. 1882–1905. DOI: 10.1103/PhysRevD.22.1882.

[244] E. Lifshitz. "Republication of: On the gravitational stability of the expanding universe". In: *J. Phys. (USSR)* 10.2 (1946), p. 116. DOI: 10.1007/s10714-016-2165-8.

[245] Joseph H. P. Jackson et al. "The separate-universe approach and sudden transitions during inflation". In: *JCAP* 05 (2024), p. 053. DOI: 10.1088/1475-7516/2024/05/053. arXiv: 2311.03281 [astro-ph.CO].

[246] Samuel M Leach, Misao Sasaki, David Wands and Andrew R Liddle. "Enhancement of superhorizon scale inflationary curvature perturbations". In: *Phys. Rev. D* 64 (2001), p. 023512. DOI: 10.1103/PhysRevD.64.023512. arXiv: astro-ph/0101406.

[247] Diego Cruces, Cristiano Germani, Amin Nassiri-Rad and Masahide Yamaguchi. "Small noise expansion of stochastic inflation". In: (Oct. 2024). arXiv: 2410.17987 [astro-ph.CO].

[248] Danilo Artigas, Shi Pi and Takahiro Tanaka. "Extended δN formalism". In: (Aug. 2024). arXiv: 2408.09964 [astro-ph.CO].

[249] Alireza Talebian-Ashkezari, Nahid Ahmadi and Ali Akbar Abolhasani. "δ M formalism: a new approach to cosmological perturbation theory in anisotropic inflation". In: *JCAP* 03 (2018), p. 001. DOI: 10.1088/1475-7516/2018/03/001. arXiv: 1609.05893 [gr-qc].

[250] Atsushi Naruko, Yu-ichi Takamizu and Misao Sasaki. "Beyond δN formalism". In: *PTEP* 2013 (2013), 043E01. DOI: 10.1093/ptep/ptt008. arXiv: 1210.6525 [astro-ph.CO].

[251] Tomislav Prokopec and Gerasimos Rigopoulos. "ΔN and the stochastic conveyor belt of ultra slow-roll inflation". In: *Phys. Rev. D* 104.8 (2021), p. 083505. DOI: 10.1103/PhysRevD.104.083505. arXiv: 1910.08487 [gr-qc].

[252] Laurence Perreault Levasseur, Vincent Vennin and Robert Brandenberger. "Recursive Stochastic Effects in Valley Hybrid Inflation". In: *Phys. Rev. D* 88 (2013), p. 083538. DOI: 10.1103/PhysRevD.88.083538. arXiv: 1307.2575 [hep-th].

[253] Laurence Perreault Levasseur. "Lagrangian formulation of stochastic inflation: Langevin equations, one-loop corrections and a proposed recursive approach". In: *Phys. Rev. D* 88.8 (2013), p. 083537. DOI: 10.1103/PhysRevD.88.083537. arXiv: 1304.6408 [hep-th].

[254] Laurence Perreault Levasseur and Evan McDonough. "Backreaction and Stochastic Effects in Single Field Inflation". In: *Phys. Rev. D* 91.6 (2015), p. 063513. DOI: 10.1103/PhysRevD.91.063513. arXiv: 1409.7399 [hep-th].

[255] Guillermo Ballesteros et al. "Non-Gaussian tails without stochastic inflation". In: (June 2024). arXiv: 2406.02417 [astro-ph.CO].

[256] Devanshu Sharma. "Stochastic inflation and non-perturbative power spectrum beyond slow roll". In: *JCAP* 03 (2025), p. 017. DOI: 10.1088/1475-7516/2025/03/017. arXiv: 2411.08854 [astro-ph.CO].

[257] Peter E. Kloeden and Eckhard Platen. *Numerical Solution of Stochastic Differential Equations*. Vol. 23. Stochastic Modelling and Applied Probability. Springer-Verlag Berlin Heidelberg, 1992. ISBN: 978-3-540-54062-5. DOI: 10.1007/978-3-662-12616-5. URL: https://doi.org/10.1007/978-3-662-12616-5.

[258] Yoshio Komori. "Multi-colored rooted tree analysis of the weak order conditions of a stochastic Runge–Kutta family". In: *Applied Numerical Mathematics* 57.2 (2007), pp. 147–165. ISSN: 0168-9274. DOI: 10.1016/j.apnum.2006.02.002.

[259] Kristian Debrabant and Andreas Rossler. "Classification of stochastic Runge–Kutta methods for the weak approximation of stochastic differential equations". In: *Mathematics and Computers in Simulation* 77.4 (Apr. 2008), pp. 408–420. ISSN: 0378-4754. DOI: 10.1016/j.matcom.2007.04.016.

[260] Andreas Rossler. "Second Order Runge–Kutta Methods for Itô Stochastic Differential Equations". In: *SIAM Journal on Numerical Analysis* 47.3 (2009), pp. 1713–1738. DOI: 10.1137/060673308. eprint: https://doi.org/10.1137/060673308.

[261] Andreas Rossler. "Runge–Kutta Methods for the Strong Approximation of Solutions of Stochastic Differential Equations". In: *SIAM Journal on Numerical Analysis* 48.3 (2010), pp. 922–952. DOI: 10.1137/09076636X. eprint: https://doi.org/10.1137/09076636X.

[262] A. J. Roberts. *Modify the Improved Euler scheme to integrate stochastic differential equations*. 2012. arXiv: 1210.0933 [math.NA].

[263] A. Samsudin, N. Rosli and A. N. Ariffin. "Stability analysis of explicit and implicit stochastic Runge–Kutta methods for stochastic differential equations". In: *Journal of Physics: Conference Series* 890 (2017), p. 012084. DOI: 10.1088/1742-6596/890/1/012084.

[264] A. Tocino and J. Vigo-Aguiar. "Weak Second Order Conditions for Stochastic Runge–Kutta Methods". In: *SIAM Journal on Scientific Computing* 24.2 (2002), pp. 507–523. DOI: 10.1137/S1064827501387814. eprint: https://doi.org/10.1137/S1064827501387814.

[265] P. A. R. Ade et al. "Planck 2015 results. XX. Constraints on inflation". In: *Astron. Astrophys.* 594 (2016), A20. DOI: 10.1051/0004-6361/201525898. arXiv: 1502.02114 [astro-ph.CO].

[266] Guillermo Ballesteros, Julián Rey, Marco Taoso and Alfredo Urbano. "Primordial black holes as dark matter and gravitational waves from single-field polynomial inflation". In: *JCAP* 07 (2020), p. 025. DOI: 10.1088/1475-7516/2020/07/025. arXiv: 2001.08220 [astro-ph.CO].

[267] Ewan D. Stewart and David H. Lyth. "A More accurate analytic calculation of the spectrum of cosmological perturbations produced during inflation". In: *Phys. Lett. B* 302 (1993), pp. 171–175. DOI: 10.1016/0370-2693(93)90379-V. arXiv: gr-qc/9302019.

[268] Vadim Briaud et al. "How deep is the dip and how tall are the wiggles in inflationary power spectra?" In: (Jan. 2025). arXiv: 2501.14681 [astro-ph.CO].

[269] Vincent Vennin and Alexei A. Starobinsky. "Correlation Functions in Stochastic Inflation". In: *Eur. Phys. J. C* 75 (2015), p. 413. DOI: 10.1140/epjc/s10052-015-3643-y. arXiv: 1506.04732 [hep-th].

[270] Julien Lesgourgues. "The Cosmic Linear Anisotropy Solving System (CLASS) I: Overview". In: (Apr. 2011). arXiv: 1104.2932 [astro-ph.IM].

[271] Diego Blas, Julien Lesgourgues and Thomas Tram. "The Cosmic Linear Anisotropy Solving System (CLASS) II: Approximation schemes". In: *JCAP* 07 (2011), p. 034. DOI: 10.1088/1475-7516/2011/07/034. arXiv: 1104.2933 [astro-ph.CO].

[272] Ya. B. Zeldovich and R. A. Sunyaev. "The Interaction of Matter and Radiation in a Hot-Model Universe". In: *Astrophys. Space Sci.* 4 (1969), pp. 301–316. DOI: 10.1007/BF00661821.

[273] R. A. Sunyaev and Ya. B. Zeldovich. "Small-scale fluctuations of relic radiation". In: *Astrophys. Space Sci.* 7.1 (1970), pp. 3–19. DOI: 10.1007/BF00653471.

[274] Wayne Hu and Joseph Silk. "Thermalization and spectral distortions of the cosmic background radiation". In: *Phys. Rev. D* 48 (1993), pp. 485–502. DOI: 10.1103/PhysRevD.48.485.

[275] D. J. Fixsen et al. "The Cosmic Microwave Background spectrum from the full COBE FIRAS data set". In: *Astrophys. J.* 473 (1996), p. 576. DOI: 10.1086/178173. arXiv: astro-ph/9605054.

[276] John C. Mather et al. "Calibrator design for the COBE far infrared absolute spectrophotometer (FIRAS)". In: *Astrophys. J.* 512 (1999), pp. 511–520. DOI: 10.1086/306805. arXiv: astro-ph/9810373.

[277] J. Chluba and R. A. Sunyaev. "The evolution of CMB spectral distortions in the early Universe". In: *Mon. Not. Roy. Astron. Soc.* 419 (2012), pp. 1294–1314. DOI: 10.1111/j.1365-2966.2011.19786.x. arXiv: 1109.6552 [astro-ph.CO].

[278] Jens Chluba, Daisuke Nagai, Sergey Sazonov and Kaylea Nelson. "A fast and accurate method for computing the Sunyaev–Zeldovich signal of hot galaxy clusters: Computation of SZ signal". In: *Monthly Notices of the Royal Astronomical Society* 426.1 (Sept. 2012), pp. 510–530. ISSN: 0035-8711. DOI: 10.1111/j.1365-2966.2012.21741.x.

[279] A. S. Kompaneets. "The Establishment of Thermal Equilibrium between Quanta and Electrons". In: *Soviet Journal of Experimental and Theoretical Physics* 4.5 (May 1957), pp. 730–737.

[280] R. A. Sunyaev and Ya. B. Zeldovich. "Small-Scale Fluctuations of Relic Radiation". In: *"Astrophys. Space Sci."* 7.1 (Apr. 1970), pp. 3–19. DOI: 10.1007/BF00653471.

[281] Wayne T. Hu. "Wandering in the Background: A CMB Explorer". Other thesis. Aug. 1995. arXiv: astro-ph/9508126.

[282] Matteo Lucca et al. "The synergy between CMB spectral distortions and anisotropies". In: *JCAP* 02 (2020), p. 026. DOI: 10.1088/1475-7516/2020/02/026. arXiv: 1910.04619 [astro-ph.CO].

[283] Ya. B. Zeldovich, V. G. Kurt and R. A. Sunyaev. "Recombination of hydrogen in the hot model of the universe". In: *Zh. Eksp. Teor. Fiz.* 55 (1968), pp. 278–286.

[284] Jens Chluba. *Science with Spectral Distortions of the Cosmic Microwave Background*. CUSO Lectures 2014. Lecture notes available at https://www.jb.man.ac.uk/~jchluba/Science/CUSO_Lecture_Notes_JC.pdf. 2014.

[285] S. A. Balashev et al. "SPECTRAL DISTORTIONS OF THE CMB DIPOLE". In: *The Astrophysical Journal* 810.2 (Sept. 2015), p. 131. ISSN: 1538-4357. DOI: 10.1088/0004-637x/810/2/131.

[286] Suvodip Mukherjee, Joseph Silk and Benjamin D. Wandelt. "FSD: Frequency Space Differential measurement of CMB spectral distortions". In: *Mon. Not. Roy. Astron. Soc.* 477.4 (2018), pp. 4473–4482. DOI: 10.1093/mnras/sty888. arXiv: 1801.05120 [astro-ph.CO].

[287] Jens Chluba. "Which spectral distortions does ΛCDM actually predict?" In: *Mon. Not. Roy. Astron. Soc.* 460.1 (2016), pp. 227–239. DOI: 10.1093/mnras/stw945. arXiv: 1603.02496 [astro-ph.CO].

[288] Jens Chluba and Donghui Jeong. "Teasing bits of information out of the CMB energy spectrum". In: *Mon. Not. Roy. Astron. Soc.* 438.3 (2014), pp. 2065–2082. DOI: 10.1093/mnras/stt2327. arXiv: 1306.5751 [astro-ph.CO].

[289] Jens Chluba, Jan Hamann and Subodh P. Patil. "Features and New Physical Scales in Primordial Observables: Theory and Observation". In: *Int. J. Mod. Phys. D* 24.10 (2015), p. 1530023. DOI: 10.1142/S0218271815300232. arXiv: 1505.01834 [astro-ph.CO].

[290] Joseph Silk. "Cosmic black body radiation and galaxy formation". In: *Astrophys. J.* 151 (1968), pp. 459–471. DOI: 10.1086/149449.

[291] Thomas Kite, Andrea Ravenni, Subodh P. Patil and Jens Chluba. "Bridging the gap: spectral distortions meet gravitational waves". In: *Mon. Not. Roy. Astron. Soc.* 505.3 (2021), pp. 4396–4405. DOI: 10.1093/mnras/stab1558. arXiv: 2010.00040 [astro-ph.CO].

[292] Devanshu Sharma, Julien Lesgourgues and Christian T. Byrnes. "Spectral distortions from acoustic dissipation with non-Gaussian (or not) perturbations". In: *JCAP* 07 (2024), p. 090. DOI: 10.1088/1475-7516/2024/07/090. arXiv: 2404.18474 [astro-ph.CO].

[293] Jens Chluba, Rishi Khatri and Rashid A. Sunyaev. "CMB at 2x2 order: The dissipation of primordial acoustic waves and the observable part of the associated energy release". In: *Mon. Not. Roy. Astron. Soc.* 425 (2012), pp. 1129–1169. DOI: 10.1111/j.1365-2966.2012.21474.x. arXiv: 1202.0057 [astro-ph.CO].

[294] M. Beneke and C. Fidler. "Boltzmann hierarchy for the cosmic microwave background at second order including photon polarization". In: *Phys. Rev. D* 82 (2010), p. 063509. DOI: 10.1103/PhysRevD.82.063509. arXiv: 1003.1834 [astro-ph.CO].

[295] Nicola Bartolo, Sabino Matarrese and Antonio Riotto. "CMB Anisotropies at Second Order I". In: *JCAP* 06 (2006), p. 024. DOI: 10.1088/1475-7516/2006/06/024. arXiv: astro-ph/0604416.

[296] Nicola Bartolo, Sabino Matarrese and Antonio Riotto. "CMB anisotropies at second-order II: analytical approach". In: *Journal of Cosmology and Astroparticle Physics* 2007.01 (Jan. 2007), pp. 019–019. ISSN: 1475-7516. DOI: 10.1088/1475-7516/2007/01/019.

[297] Cyril Pitrou. "The radiative transfer at second order: a full treatment of the Boltzmann equation with polarization". In: *Classical and Quantum Gravity* 26.6 (Feb. 2009), p. 065006. ISSN: 1361-6382. DOI: 10.1088/0264-9381/26/6/065006.

[298] Cyril Pitrou. "The radiative transfer for polarized radiation at second order in cosmological perturbations". In: *General Relativity and Gravitation* 41.11 (Mar. 2009), pp. 2587–2595. ISSN: 1572-9532. DOI: 10.1007/s10714-009-0782-1.

[299] Cyril Pitrou, Jean-Philippe Uzan and Francis Bernardeau. "The cosmic microwave background bispectrum from the non-linear evolution of the cosmological perturbations". In: *Journal of Cosmology and Astroparticle Physics* 2010.07 (July 2010), pp. 003–003. ISSN: 1475-7516. DOI: 10.1088/1475-7516/2010/07/003.

[300] M. Beneke and C. Fidler. "Boltzmann hierarchy for the cosmic microwave background at second order including photon polarization". In: *Phys. Rev. D* 82 (2010), p. 063509. DOI: 10.1103/PhysRevD.82.063509. arXiv: 1003.1834 [astro-ph.CO].

[301] Atsushi Naruko, Cyril Pitrou, Kazuya Koyama and Misao Sasaki. "Second-order Boltzmann equation: gauge dependence and gauge invariance". In: *Class. Quant. Grav.* 30 (2013), p. 165008. DOI: 10.1088/0264-9381/30/16/165008. arXiv: 1304.6929 [astro-ph.CO].

[302] Chung-Pei Ma and Edmund Bertschinger. "Cosmological perturbation theory in the synchronous and conformal Newtonian gauges". In: *Astrophys. J.* 455 (1995), pp. 7–25. DOI: 10.1086/176550. arXiv: astro-ph/9506072.

[303] Wayne Hu and Naoshi Sugiyama. "Small scale cosmological perturbations: An Analytic approach". In: *Astrophys. J.* 471 (1996), pp. 542–570. DOI: 10.1086/177989. arXiv: astro-ph/9510117.

[304] Jens Chluba and Daniel Grin. "CMB spectral distortions from small-scale isocurvature fluctuations". In: *Mon. Not. Roy. Astron. Soc.* 434 (2013), pp. 1619–1635. DOI: 10.1093/mnras/stt1129. arXiv: 1304.4596 [astro-ph.CO].

[305] Jens Chluba, Adrienne L. Erickcek and Ido Ben-Dayan. "Probing the inflaton: Small-scale power spectrum constraints from measurements of the CMB energy spectrum". In: *Astrophys. J.* 758 (2012), p. 76. DOI: 10.1088/0004-637X/758/2/76. arXiv: 1203.2681 [astro-ph.CO].

[306] Joaquim Iguaz Juan, Pasquale D. Serpico and Guillermo Franco Abellán. "The QCD phase transition behind a PBH origin of LIGO/Virgo events?" In: *JCAP* 07.07 (2022), p. 009. DOI: 10.1088/1475-7516/2022/07/009. arXiv: 2204.07027 [astro-ph.CO].

[307] M. Tristram et al. "Cosmological parameters derived from the final Planck data release (PR4)". In: *Astron. Astrophys.* 682 (2024), A37. DOI: 10.1051/0004-6361/202348015. arXiv: 2309.10034 [astro-ph.CO].

[308] Guido W. Pettinari et al. "The intrinsic bispectrum of the Cosmic Microwave Background". In: *JCAP* 04 (2013), p. 003. DOI: 10.1088/1475-7516/2013/04/003. arXiv: 1302.0832 [astro-ph.CO].

[309] Federico Bianchini and Giulio Fabbian. "CMB spectral distortions revisited: A new take on μ distortions and primordial non-Gaussianities from FIRAS data". In: *Phys. Rev. D* 106.6 (2022), p. 063527. DOI: 10.1103/PhysRevD.106.063527. arXiv: 2206.02762 [astro-ph.CO].

[310] Bryce Cyr et al. "Disentangling the primordial nature of stochastic gravitational wave backgrounds with CMB spectral distortions". In: *Mon. Not. Roy. Astron. Soc.* 528.1 (2024), pp. 883–897. DOI: 10.1093/mnras/stad3861. arXiv: 2309.02366 [astro-ph.CO].

[311] Leonardo Senatore, Kendrick M. Smith and Matias Zaldarriaga. "Non-Gaussianities in Single Field Inflation and their Optimal Limits from the WMAP 5-year Data". In: *JCAP* 01 (2010), p. 028. DOI: 10.1088/1475-7516/2010/01/028. arXiv: 0905.3746 [astro-ph.CO].

[312] E. Komatsu et al. "Seven-Year Wilkinson Microwave Anisotropy Probe (WMAP) Observations: Cosmological Interpretation". In: *Astrophys. J. Suppl.* 192 (2011), p. 18. DOI: 10.1088/0067-0049/192/2/18. arXiv: 1001.4538 [astro-ph.CO].

[313] Eiichiro Komatsu and David N. Spergel. "Acoustic signatures in the primary microwave background bispectrum". In: *Phys. Rev. D* 63 (2001), p. 063002. DOI: 10.1103/PhysRevD.63.063002. arXiv: astro-ph/0005036.

[314] David H. Lyth and David Wands. "Generating the curvature perturbation without an inflaton". In: *Phys. Lett. B* 524 (2002), pp. 5–14. DOI: 10.1016/S0370-2693(01)01366-1. arXiv: hep-ph/0110002.

[315] Takeo Moroi and Tomo Takahashi. "Effects of cosmological moduli fields on cosmic microwave background". In: *Phys. Lett. B* 522 (2001). [Erratum: Phys.Lett.B 539, 303–303 (2002)], pp. 215–221. DOI: 10.1016/S0370-2693(01)01295-3. arXiv: hep-ph/0110096.

[316] Francis Bernardeau and Jean-Philippe Uzan. "Inflationary models inducing non-Gaussian metric fluctuations". In: *Phys. Rev. D* 67 (2003), p. 121301. DOI: 10.1103/PhysRevD.67.121301. arXiv: astro-ph/0209330.

[317] Gia Dvali, Andrei Gruzinov and Matias Zaldarriaga. "A new mechanism for generating density perturbations from inflation". In: *Phys. Rev. D* 69 (2004), p. 023505. DOI: 10.1103/PhysRevD.69.023505. arXiv: astro-ph/0303591.

[318] Jaume Garriga and Viatcheslav F. Mukhanov. "Perturbations in k-inflation". In: *Phys. Lett. B* 458 (1999), pp. 219–225. DOI: 10.1016/S0370-2693(99)00602-4. arXiv: hep-th/9904176.

[319] Eva Silverstein and David Tong. "Scalar speed limits and cosmology: Acceleration from D-cceleration". In: *Phys. Rev. D* 70 (2004), p. 103505. DOI: 10.1103/PhysRevD.70.103505. arXiv: hep-th/0310221.

[320] Mohsen Alishahiha, Eva Silverstein and David Tong. "DBI in the sky". In: *Phys. Rev. D* 70 (2004), p. 123505. DOI: 10.1103/PhysRevD.70.123505. arXiv: hep-th/0404084.

[321] Paolo Creminelli et al. "Limits on non-gaussianities from wmap data". In: *JCAP* 05 (2006), p. 004. DOI: 10.1088/1475-7516/2006/05/004. arXiv: astro-ph/0509029.

[322] Tomo Takahashi. "Primordial non-Gaussianity and the inflationary Universe". In: *PTEP* 2014.6 (2014), 06B105. DOI: 10.1093/ptep/ptu060.

[323] N. Bartolo, E. Komatsu, Sabino Matarrese and A. Riotto. "Non-Gaussianity from inflation: Theory and observations". In: *Phys. Rept.* 402 (2004), pp. 103–266. DOI: 10.1016/j.physrep.2004.08.022. arXiv: astro-ph/0406398.

[324] David Wands. "Local non-Gaussianity from inflation". In: *Class. Quant. Grav.* 27 (2010), p. 124002. DOI: 10.1088/0264-9381/27/12/124002. arXiv: 1004.0818 [astro-ph.CO].

[325] Christian T. Byrnes. "Lecture notes on non-Gaussianity". In: *Astrophys. Space Sci. Proc.* 45 (2016). Ed. by Júlio C. Fabris et al., pp. 135–165. DOI: 10.1007/978-3-319-44769-8_3. arXiv: 1411.7002 [astro-ph.CO].

[326] Y. Akrami et al. "Planck 2018 results. IX. Constraints on primordial non-Gaussianity". In: *Astron. Astrophys.* 641 (2020), A9. DOI: 10.1051/0004-6361/201935891. arXiv: 1905.05697 [astro-ph.CO].

[327] Teruaki Suyama, Tomo Takahashi, Masahide Yamaguchi and Shuichiro Yokoyama. "On Classification of Models of Large Local-Type Non-Gaussianity". In: *JCAP* 12 (2010), p. 030. DOI: 10.1088/1475-7516/2010/12/030. arXiv: 1009.1979 [astro-ph.CO].

[328] Sami Nurmi, Christian T. Byrnes and Gianmassimo Tasinato. "A non-Gaussian landscape". In: *JCAP* 06 (2013), p. 004. DOI: 10.1088/1475-7516/2013/06/004. arXiv: 1301.3128 [astro-ph.CO].

[329] Teruaki Suyama, Tomo Takahashi, Masahide Yamaguchi and Shuichiro Yokoyama. "Implications of Planck results for models with local type non-Gaussianity". In: *JCAP* 06 (2013), p. 012. DOI: 10.1088/1475-7516/2013/06/012. arXiv: 1303.5374 [astro-ph.CO].

[330] Christian T. Byrnes et al. "Scale-dependent non-Gaussianity probes inflationary physics". In: *JCAP* 10 (2010), p. 004. DOI: 10.1088/1475-7516/2010/10/004. arXiv: 1007.4277 [astro-ph.CO].

[331] Theodoros Papanikolaou et al. "New probe of non-Gaussianities with primordial black hole induced gravitational waves". In: *Phys. Lett. B* 857 (2024), p. 138997. DOI: 10.1016/j.physletb.2024.138997. arXiv: 2403.00660 [astro-ph.CO].

[332] Christian T. Byrnes, Kazuya Koyama, Misao Sasaki and David Wands. "Diagrammatic approach to non-Gaussianity from inflation". In: *JCAP* 11 (2007), p. 027. DOI: 10.1088/1475-7516/2007/11/027. arXiv: 0705.4096 [hep-th].

[333] Francesco Ziparo, Simona Gallerani and Andrea Ferrara. "Primordial black holes as supermassive black hole seeds". In: *JCAP* 04 (2025), p. 040. DOI: 10.1088/1475-7516/2025/04/040. arXiv: 2411.03448 [astro-ph.CO].

[334] Massimo Ricotti, Jeremiah P. Ostriker and Katherine J. Mack. "Effect of Primordial Black Holes on the Cosmic Microwave Background and Cosmological Parameter Estimates". In: *Astrophys. J.* 680 (2008), p. 829. DOI: 10.1086/587831. arXiv: 0709.0524 [astro-ph].

[335] G. Hasinger. "Illuminating the dark ages: Cosmic backgrounds from accretion onto primordial black hole dark matter". In: *JCAP* 07 (2020), p. 022. DOI: 10.1088/1475-7516/2020/07/022. arXiv: 2003.05150 [astro-ph.CO].

[336] V. De Luca, G. Franciolini, P. Pani and A. Riotto. "Constraints on Primordial Black Holes: the Importance of Accretion". In: *Phys. Rev. D* 102.4 (2020), p. 043505. DOI: 10.1103/PhysRevD.102.043505. arXiv: 2003.12589 [astro-ph.CO].

[337] Pasquale D. Serpico, Vivian Poulin, Derek Inman and Kazunori Kohri. "Cosmic microwave background bounds on primordial black holes including dark matter halo accretion". In: *Phys. Rev. Res.* 2.2 (2020), p. 023204. DOI: 10.1103/PhysRevResearch.2.023204. arXiv: 2002.10771 [astro-ph.CO].

[338] C. Casanueva-Villarreal et al. "Primordial black holes as dark matter candidates: Multi-frequency constraints from cosmic radiation backgrounds". In: (May 2025). arXiv: 2505.10706 [astro-ph.CO].

[339] Andika, Irham T. et al. "Tracing the rise of supermassive black holes - A panchromatic search for faint, unobscured quasars at z $\geq$ 6 with COSMOS-Web and other surveys". In: *"Astronomy & Astrophysics"* 685 (2024), A25. DOI: 10.1051/0004-6361/202349025.

[340] Fabio Pacucci and Abraham Loeb. "Separating Accretion and Mergers in the Cosmic Growth of Black Holes with X-ray and Gravitational Wave Observations". In: *Astrophys. J.* 895.2 (2020), p. 95. DOI: 10.3847/1538-4357/ab886e. arXiv: 2004.07246 [astro-ph.GA].

[341] Zijian Wang et al. "The Role of Population III Star Tidal Disruption Events in Black Hole Growth at the Cosmic Dawn". In: (Apr. 2025). arXiv: 2504.18144 [astro-ph.HE].

[342] Rishi Khatri, Rashid A Sunyaev and Jens Chluba. "Mixing of blackbodies: entropy production and dissipation of sound waves in the early Universe". In: *"Astronomy & Astrophysics"* 543 (2012), A136.

[343] Enrico Pajer and Matias Zaldarriaga. "A hydrodynamical approach to CMB μ-distortion from primordial perturbations". In: *JCAP* 02 (2013), p. 036. DOI: 10.1088/1475-7516/2013/02/036. arXiv: 1206.4479 [astro-ph.CO].

[344] Bernard Carr et al. "Primordial black hole constraints for extended mass functions". In: *Phys. Rev. D* 96.2 (2017), p. 023514. DOI: 10.1103/PhysRevD.96.023514. arXiv: 1705.05567 [astro-ph.CO].

[345] Albert Escrivà, Florian Kuhnel and Yuichiro Tada. "Primordial Black Holes". In: (Nov. 2022). DOI: 10.1016/B978-0-32-395636-9.00012-8. arXiv: 2211.05767 [astro-ph.CO].

[346] Andrew D. Gow, Christian T. Byrnes, Philippa S. Cole and Sam Young. "The power spectrum on small scales: Robust constraints and comparing PBH methodologies". In: *JCAP* 02 (2021), p. 002. DOI: 10.1088/1475-7516/2021/02/002. arXiv: 2008.03289 [astro-ph.CO].

[347] Zhan-He Wang, Hai-Long Huang and Yun-Song Piao. "Broad primordial power spectrum and μ-distortion constraints on primordial black holes". In: *Phys. Rev. D* 111.8 (2025), p. 083553. DOI: 10.1103/PhysRevD.111.083553. arXiv: 2501.08542 [astro-ph.CO].

[348] Tomohiro Nakama, Teruaki Suyama, Kazunori Kohri and Nagisa Hiroshima. "Constraints on small-scale primordial power by annihilation signals from extragalactic dark matter minihalos". In: *Phys. Rev. D* 97.2 (2018), p. 023539. DOI: 10.1103/PhysRevD.97.023539. arXiv: 1712.08820 [astro-ph.CO].

[349] V. De Luca et al. "The Ineludible non-Gaussianity of the Primordial Black Hole Abundance". In: *JCAP* 07 (2019), p. 048. DOI: 10.1088/1475-7516/2019/07/048. arXiv: 1904.00970 [astro-ph.CO].

[350] Bernard J. Carr and M. Sakellariadou. "Dynamical constraints on dark compact objects". In: *Astrophys. J.* 516 (1999), pp. 195–220. DOI: 10.1086/307071.

[351] Philippa S. Cole and Christian T. Byrnes. "Extreme scenarios: the tightest possible constraints on the power spectrum due to primordial black holes". In: *JCAP* 02 (2018), p. 019. DOI: 10.1088/1475-7516/2018/02/019. arXiv: 1706.10288 [astro-ph.CO].

[352] Christian T. Byrnes, Julien Lesgourgues and Devanshu Sharma. "Robust μ-distortion constraints on primordial supermassive black holes from non-Gaussian perturbations". In: *JCAP* 09 (2024), p. 012. DOI: 10.1088/1475-7516/2024/09/012. arXiv: 2404.18475 [astro-ph.CO].

[353] Xavier Pritchard, Christian T. Byrnes, Julien Lesgourgues and Devanshu Sharma. "Robust μ-distortion constraints on primordial supermassive black holes from cubic (gNL) non-Gaussian perturbations". In: (May 2025). arXiv: 2505.08442 [astro-ph.CO].

[354] Lotfi Boubekeur and David. H. Lyth. "Detecting a small perturbation through its non-Gaussianity". In: *Phys. Rev. D* 73 (2006), p. 021301. DOI: 10.1103/PhysRevD.73.021301. arXiv: astro-ph/0504046.

[355] Elliot Nelson and Sarah Shandera. "Statistical Naturalness and non-Gaussianity in a Finite Universe". In: *Phys. Rev. Lett.* 110.13 (2013), p. 131301. DOI: 10.1103/PhysRevLett.110.131301. arXiv: 1212.4550 [astro-ph.CO].

[356] Sam Young and Christian T. Byrnes. "Long-short wavelength mode coupling tightens primordial black hole constraints". In: *Phys. Rev. D* 91.8 (2015), p. 083521. DOI: 10.1103/PhysRevD.91.083521. arXiv: 1411.4620 [astro-ph.CO].

[357] John Ellis et al. "What is the source of the PTA GW signal?" In: *Phys. Rev. D* 109.2 (2024), p. 023522. DOI: 10.1103/PhysRevD.109.023522. arXiv: 2308.08546 [astro-ph.CO].

[358] Guido Walter Pettinari. "The intrinsic bispectrum of the Cosmic Microwave Background". PhD thesis. Portsmouth U., ICG, Sept. 2013. DOI: 10.1007/978-3-319-21882-3. arXiv: 1405.2280 [astro-ph.CO].